

Chapter 1. Introduction

1.1. Research Background

The motivation of this research is to meet the growing demand for the high measurand resolution, high spatial resolution, attenuation insensitive and low-cost quasi-distributed temperature and strain sensors that can reliably work under harsh environment or in extended structures.

Optical fiber sensors are essentially a means whereby light guided within an optical fiber can be modified in response to an external physical, chemical, biological, biomedical or similar influence [1]. Optical fiber sensors have been under research for over three decades and a wide body of knowledge has been accumulated. Fiber sensors that can measure tens of different parameters, such as temperature, strain, pressure, acoustic field, flow rate, electric field, magnetic field, current, and voltage, can be found in literature. Some of them are available on market. Fiber sensors have the advantages of small size, low weight, and immunity from electromagnetic interference, chemical passivity and capability of distant measurement. These make them a good candidate for applications that are inaccessible using alternative technologies, such as down-hole oil well temperature and pressure monitoring, current and voltage measurements in highly electromagnetic interfered environments, chemical constituents in the blood of patients undergoing surgical treatment, etc.

There are two main drives for distributed fiber sensor research. The first is to lower cost-per-sensor so that fiber sensors could hopefully become price-competitive against electrical sensors in order to gain widespread acceptance. The second is to obtain spatial distribution of the measurand.

Single point sensors seldom utilize the very high intrinsic bandwidth of the optical fiber transmission medium and, when a large number of points is to be measured, many fibers must be used to connect the sensor heads and the terminal electronics, thus negative some of the advantages of the fiber transmission medium. There is therefore an opportunity to save cost by multiplexing a number of sensing elements onto a single fiber or fiber pair and thus to form a fiber-optic sensor network distributed in space. The benefits are not

simply sharing terminal equipment, but simplified wiring and reduced installation cost as well. In the case of the York DTS-800 (released in 1996), 10,000 points are measured simultaneously on a single optical fiber, and six fibers can be addressed by a single instrument, increasing the number of measurement points that are accessible by a single instrument to 60,000. The cost of the measurement is dominated by the cost of the fiber and its installation [2].

Obtaining spatial distribution of a measurand is important in a number of applications. In the power supply industry, power generator coil temperature should be monitored. The cost of a single generator failure induced by cooling pipe malfunction has been put at over \$3M. In the power transmission industry, when distributed temperature sensors are used to real-time monitor the high-voltage transmission lines, the ability to carry additional peak loads is considered to be a real benefit. It has been estimated [3] that the value of an additional capacity of 100 MW over 10 miles at 230 kV is around \$3.5M per year. Distributed temperature sensors can also be incorporated into a building as a fire-alarm system. Distributed strain sensors can be used for health monitoring of in civil structures, such as bridges, dams, and buildings. Distributed pressure sensors find their niche in down-hole oil well and undersea acoustic array applications.

1.2. Review of Distributed Fiber Sensor

Distributed optical fiber sensing is a technique which utilizes the very special properties of the optical fiber to make simultaneous measurements of both the spatial and temporal behavior of a measurand field [4-5]. Based on the continuity of spatial measurement, distributed fiber sensors can be divided into two categories: fully-distributed fiber sensor and quasi-distributed fiber sensor.

1.2.1. Fully Distributed Fiber Sensor

Optical Time-Domain Reflectometry (OTDR) is used routinely in optical communications industry for the evaluations of fibers and installed links. It is adopted in distributed fiber sensing as well. The OTDR typically consists of a laser source, a directional coupler connected to the fiber under test, an optical receiver followed by further electronic circuitry used for data acquisition, signal averaging and processing, measurement control and display of the results. A schematic diagram of the system is

shown in Figure 1.1. A short, high-intensity optical pulse is launched into the fiber and a measurement is made of its backscatter as a function of time. The signal consists of light scattered during the progress of the pulse down the fiber and re-captured by the waveguide in the return direction [2]; it takes the following well-known form as a function of the position z of the scattering element du [6]

$$P_s(z) = P_0 W v_g \alpha_s S \exp\left[\int_0^z -2\alpha(u) du\right] \quad (0.1)$$

where P_0 , W , and v_g are the power launched, the pulse width and the group velocity, respectively. α_s and α are the scattering and total loss coefficients. S is the capture fraction, i.e. the proportion of the scattered light collected by the optical system. In order to use OTDR in a distributed sensor, it is clear from Equation (1.1) that the scattering loss α_s [7], the local capture fraction S , both of which affect the signal directly, or the local fiber attenuation α [8], which affects the derivative of the signal, must be functions of the quantity to be measured. Based on this principle, various fully distributed fiber sensors have been developed, such as the Rayleigh scattering type based on local fiber attenuation α variation, or Raman scattering and the Brillouin scattering type based on scattering loss α_s .

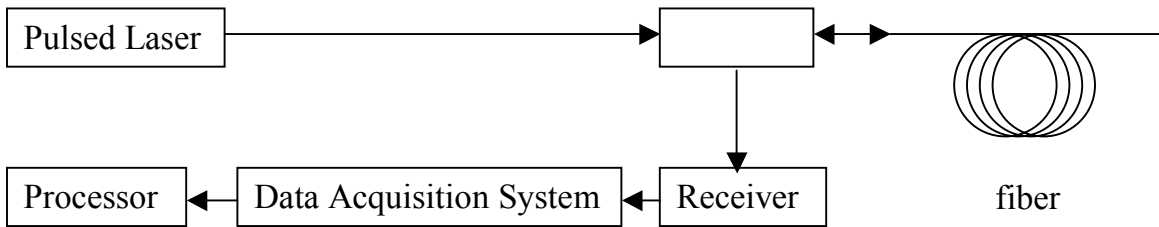


Figure 1.1. Diagram of the OTDR system

1.2.1.1. Rayleigh Scattering Based Distributed Fiber Sensor

Rayleigh scattering is elastic scattering of the optical radiation due to the displacement of the weakly bound electronic cloud surrounding the molecule which is perturbed by the incoming electro-magnetic field. This phenomenon is associated with optical scattering where the wavelength of light is much larger than the physical size of the scatterers [9].

In silica fiber, the basic unit of SiO_2 structure consists of a silicon atom surrounded by four oxygen atoms forming a tetrahedron. Each oxygen atom is shared by an adjacent tetrahedron. Structural irregularities occur during manufacturing when the glass is rapidly cooled, leading to the high-temperature structure being ‘frozen in’ to the final material. As a result, the material density exhibits random microscopic variations that correspond to those of the structure, which act as scattering centers. Additional structural fluctuations arise from dopant molecules that are introduced into the SiO_2 structure, leading to scattering losses that are dependent on dopant concentration [10].

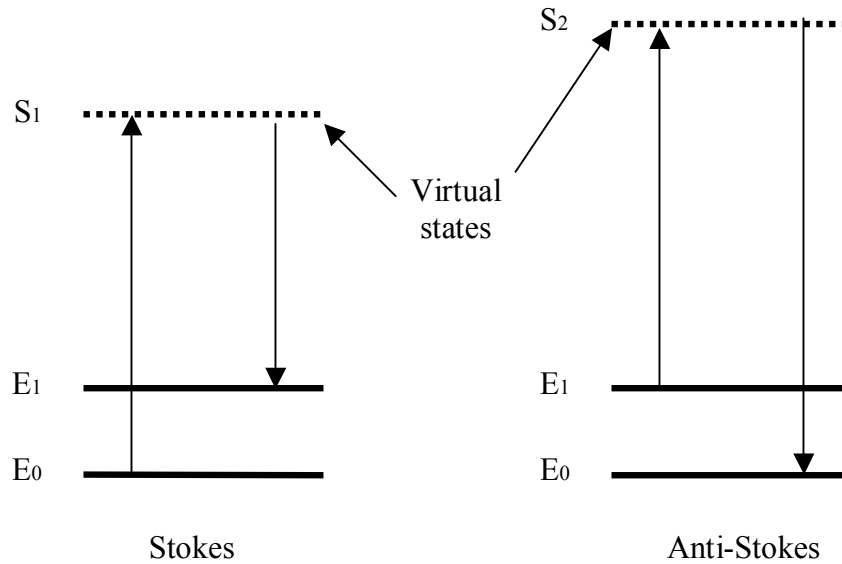
In a Rayleigh scattering based distributed fiber sensor system, the scattering coefficient α_s is a constant. If the loss α of the fiber is the only term that varies with the measurand of interest, this should be detectable by OTDR. The change of fiber loss will show up on the backscatter waveform as a change of slope on a logarithmic display according to Equation (1.1). This principle has been demonstrated by various approaches, such as inserting thin color-glass filters at selected positions in a fiber [11], using rare-earth ions doped fibers [12] and schemes employing a micro-bend structure [13]. Changes in the guidance of the fiber have also been used where glasses of dissimilar thermo-optic coefficient were used for the core and cladding of a single-mode fiber. The index-difference (and therefore the field penetration into the cladding) is thus modulated by the temperature of the fiber. The cladding material is, in addition, selected to have a far higher attenuation than the core material. The overall loss of the fiber is thus modulated by its temperature. The spatial resolution of 10cm along a fiber up to 100m has been demonstrated with $\pm 5^\circ\text{C}$ resolution within 0-150 $^\circ\text{C}$ range [14].

1.2.1.2. Raman Scattering Based Distributed Fiber Sensor

Raman scattering is an inelastic scattering process in which the wavelength of the scattered radiation is different from that of the incident light and a change in the internal energy of the scattering medium occurs. Raman scattering involves non-propagating collective modes in the material, for example thermally driven molecular vibrations in solids. Raman scattering can be viewed in the semi-classical model as shown in Figure 1.2. In a two-photon interaction, the material makes a real transition from an initial to a final state and an incident photon is destroyed while a Stokes or anti-Stokes photon is

created. The incident light, termed pump ω_L , is scattered into light at a longer and shorter wavelength, termed the Stokes wave ω_S and anti-Stokes wave ω_{AS} respectively, accompanied by the excitation of an internal mode of the medium at frequency ω_0 [15].

Unlike the narrow spectra demonstrated by free atoms and molecules, the Raman spectra of silica glass consists of very broad bands with a 200cm^{-1} wide band centered around 440cm^{-1} as shown in Figure 1.2. The intensity of these spectrum lines is temperature sensitive. By filtering out only one of these parts of the scattered light spectrum, the sensitivity of the measured signal to temperature can be greatly enhanced. This forms the basic principle of the Raman scattering based distributed fiber temperature sensor [16-17]. Illustrated in Figure 1.3 is a system diagram of a Raman distributed fiber temperature sensor [16], in which the anti-Stokes spectrum is filtered out to obtain the temperature information, and both the Stokes spectrum and the Rayleigh scattered pump light is filtered out and used to cancel the fiber attenuation effect. It is reported in 1995 that York DTS system achieved 2°C temperature resolution and 8m spatial resolution over 30km of single-mode fiber.



(a). Raman energy-level transitions

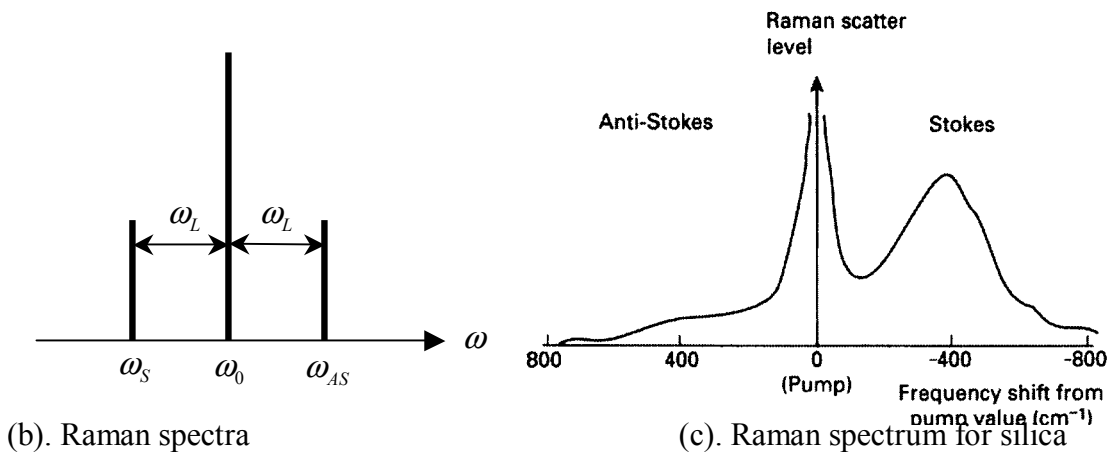


Figure 1.2. Raman spectrum

1.2.1.3. Brillouin Scattering Based Distributed Fiber Sensor

Brillouin scattering involves low-frequency propagating waves such as acoustic waves in solids. The scattering can be to a longer wavelength being termed the Stokes wave or a shorter wavelength being termed the anti-Stokes wave. For Brillouin scattering, the energies of the modes are much lower than for Raman scattering, resulting in a 0.1 to 100GHz frequency shift, and depend on the excitation wavelength and interaction geometry as well as on material properties.

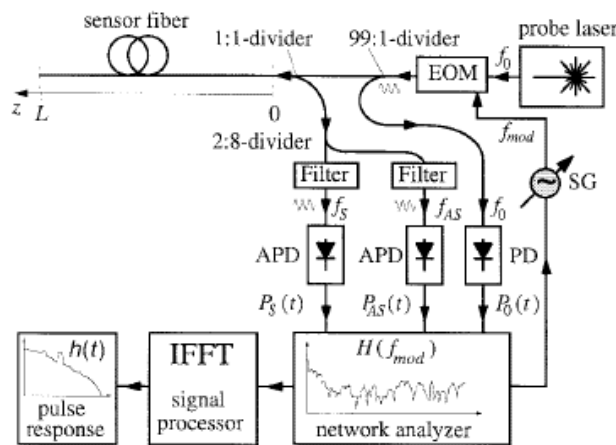


Figure 1.3. Raman distributed fiber temperature sensor

Measurement of temperature distribution has been demonstrated by using spontaneous Brillouin scattering, where the ratio of the Brillouin backscatter intensity to that of the

Rayleigh backscatter, the so-called Landau-Placzek ratio is used [18-20]. A temperature resolution of 1.4°C and a spatial resolution of 10m have been reported. Stimulated Brillouin scattering has also been proposed for distributed sensing. It is found that the frequency shift of the Brillouin gain spectrum is sensitive to temperature and strain. This has led to the demonstration of axial strain for installed cables [22-23]. Other distributed sensing schemes based on Brillouin scattering can also be found in literature [24-27].

1.2.1.4. Problems With Fully Distributed Fiber Sensors

Fully distributed sensors have been under research for over two decades, with some of the sensors finding their niche in industrial applications. But problems, as listed in this section, with this type of sensors still remain, some of which are inherited, some of which can be solved by further research.

- Poor measurand and spatial resolutions

The scattering signal is usually weak, resulting in a poor signal to noise ratio (S/N). For example, an Rayleigh scattering based system powered by a semiconductor laser operating at 850nm on 50/125 graded-index fiber, with launched power of 200mW, the near-end collected scattering signal is only $2\mu\text{W}$. For a Raman scattering based system powered by a Q-switched diode-pumped Nd:YAG laser at 1064nm, with 20W power and 7ns pulse duration, the near-end signal is of order 1nW and the signal after propagation through 10km of fiber in both directions is only a few pW. In addition, since the fully distributed sensors are intensity modulation based, the source power fluctuation and the fiber bending attenuation will affect the measurement significantly. Temperature resolution of $2\text{-}3^{\circ}\text{C}$, and spatial resolution of 8m for a 30km system is typical for this type of sensors. And the time the York DTS system takes to demodulate the signal is around 10mins. To address these problems, higher source power, and more complicated electronics and detection schemes have to be employed.

- Near and far problem

Since this type of sensor is intensity based, the far-end sensor has a worse S/N than the near-end sensor, which results in a worse resolution and spatial resolution. This is particularly severe in Rayleigh scattering systems. Because of the total loss modulation scheme, the S/N of each sensor is largely affected by all the sensors between it and the

terminal electronics. Another problem with a Rayleigh scattering system is that the performance and output of each sensor is dependent on the sensors before it, which results in a complicated demodulation algorithm and accumulation of errors.

1.2.2. Quasi-Distributed Fiber Sensor

Quasi-distributed fiber sensors have advantages over fully distributed fiber sensors in applications where a fully distributed fiber sensor is incapable of sensing the measurand with high spatial and measurand measuring resolutions are required, or lower terminal electronics cost is desired.

The applications where the quasi-distributed fiber sensors find their niche are undersea microphone array, oil well pressure monitoring, aircraft structure monitoring, large civil structure health monitoring, etc. And the available principles include the microbend [28-29], rare-earth doped fiber [30], GRIN lens coupling [31], Sagnac fiber loop [32], fiber Bragg gratings [33-34], to name just a few. The principle outline of the microbend and fiber Bragg grating based quasi-distributed fiber sensors is given in the following sections.

1.2.2.1. Microbend Based Distributed Fiber Sensor

Fiber sensors based on microbend principle were first proposed and demonstrated in 1980 [35-36]. The early interest in this type of sensors was for hydrophone arrays [37-38], but later expanded to pressure [39], temperature [40], acceleration [41], flow [42] and speed [43] detection.

Microbending sensor is an intensity sensor. The mechanical perturbation of a multimode fiber causes a redistribution of light power among the modes in the fiber. The more severe the mechanical perturbation or bending, the more light is coupled to radiation modes and is lost. A microbender, for example a set of corrugated plates or tooth blocks as shown in Figure 1.4, is used together with the fiber as a sensing element. The amount of displacement of the microbender affects the attenuation of the light power. The sensing scheme of a microbending type quasi-distributed fiber sensor is to associate with the measurand field the displacement of the cascading microbenders on a fiber. Research also indicates that the spatial pitch of the microbender has a significant impact on the sensitivity of the sensor.

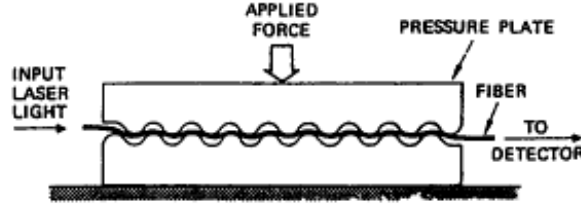


Figure 1.4. Micro-bend fiber sensor

A commercial product was supplied by Ericsson AB, in which a standard OTDR was used to interrogate a fiber, along which a section of spiral-wound plastic thread is attached and put in close proximity with wax. Upon heating above its melting point, the wax expands rapidly and forces the fiber against the plastic thread thus inducing localized microbending losses. A distributed temperature switch was thus provided, primarily for fire-detection applications. By changing the composition of the wax, a variety of switching temperatures could be selected.

1.2.2.2. Fiber Bragg Grating Based Distributed Fiber Sensor

Fiber Bragg grating consists of a periodic refractive index modulation of the core of a single-mode fiber. The light propagating in the fiber will be reflected by each of the grating plane. Only the wavelength which satisfies the Bragg condition will experience constructive interference, and close to 100% reflectivity is possible. The Bragg condition is given by

$$\lambda_B = 2n_{eff}\Lambda \quad (0.2)$$

where λ_B is the free space center wavelength of the light being constructively reflected. n_{eff} is the effective refractive index of the fiber core at the free space center wavelength, and Λ is the grating spacing.

n_{eff} and Λ are affected by strain and temperature. The Bragg grating center wavelength shift due to strain and temperature effects is given by

$$\Delta\lambda_B = \lambda_B \left\{ 1 - \frac{n}{2} [p_{12} - \nu(p_{11} + p_{12})] \right\} \epsilon_z \quad (0.3)$$

and

$$\Delta\lambda_B = \lambda_B(\alpha_\Lambda + \alpha_n)\Delta T \quad (0.4)$$

where p_{11} and p_{12} are the components of the strain optic tensor, ν is the Poisson's ratio and $\epsilon_z = \frac{\delta l}{l}$. $\alpha_\Lambda = \frac{\partial \Lambda}{\Lambda \partial T}$ is the thermal expansion coefficient for the fiber and is approximately 0.55×10^{-6} for silica. $\alpha_n = \frac{\partial n}{n \partial T}$ represents the thermo-optic coefficient and is approximately 8.6×10^{-6} for germania-doped silica-core fiber. The calculated strain and temperature sensitivities of a fiber Bragg grating at $1550 \mu\text{m}$ are $1.2 \text{ pm}/\mu\text{m}$ and $13.7 \text{ pm}/^\circ\text{C}$.

Fiber Bragg gratings are excellent fiber optic sensing elements. They can be conveniently multiplexed due to their narrow reflection bandwidth. Besides strain and temperature, other physical parameters such as pressure, flow, acoustics, acceleration, electric, magnetic fields and certain chemical effects can also be measured with modifications to the fiber Bragg grating structure.

The most straightforward means for interrogating a Bragg grating sensor array is based on a passive broadband illumination of the device. Light with a broadband spectrum which covers that of the Bragg grating sensors is input to the system, and the narrowband components reflected by the gratings are directed to a high spectrum resolution spectrometer, and the wavelength shift of each sensor is recorded [2].

1.2.2.3. Problems With Quasi-Distributed Fiber Sensor

For loss modulation based quasi-distributed fiber sensors, the near-and-far problems also exist as to that of the fully distributed Rayleigh scattering sensor. For fiber Bragg grating sensors, the problems are: use of an expensive high spectrum resolution (pm scale) signal interrogator is required; expensive fabrication stage, mask, laser and fiber; limited temperature working range due to the degradation of the grating.

1.3. Need for Novel Distributed Fiber Sensors

There are applications in which high spatial resolution, high measurand resolution, attenuation insensitivity, real-time or fast signal demodulation, large temperature working range are requested, and low cost fabrication process and terminal equipment is desired. Such applications include aircraft temperature and strain monitoring, civil structure strain

monitoring, building fire alarm, chemical engineering process control; temperature measurement in boilers, to name just a few.

Due to the problems discussed in the previous sections on the existing distributed fiber sensors, the current available technologies are insufficient to fulfill all the above application requirements and large room of improvement exists.

1.4. Scope of Research

In this research program, a novel quasi-distributed fiber sensor system based on intrinsic Fabry-Perot interferometers (IFPIs) is proposed, analyzed, implemented, characterized and field tested.

The novel sensor addresses the aforementioned application requirements in the following aspects: The sensing unit of the quasi-distributed fiber sensor is a Fabry-Perot interferometer, which is on the scale of tens of microns to hundreds of microns, thus bringing the system a high spatial resolution; Its high measurand resolution is achieved by adopting the interferometer structure, which is well-known for its high resolution measurement capability in the field of optics; The spectrum-coded signal renders the system the advantage of attenuation insensitivity, which brings the system robustness and high-resolution capability; Since the sensor system processes the signal in a parallel way, and the signal demodulation speed is only limited by the computer processor speed, the system is capable of real-time monitoring of the measurand; The sensor working temperature range is the same as that of the fiber used, thus enabling the sensor in high-temperature applications; Only a fiber splicer, a cleaver, commercially available communication grade fibers, a signal interrogator and a PC are needed in the sensor fabrication and interrogation, thus reducing the system overall cost.

The effort devoted to the research of this innovative sensing technique focuses mainly on the following issues.

- The study and modeling of sensing principles and schemes
- Signal processing algorithm study and implementation
- Sensor fabrication, characterization and optimization
- Sensor system implementation and sensor performance evaluation
- Sensor system field test

- Sensor system noise analysis

The principle of the Fabry-Perot interferometer based quasi-distributed fiber sensor is presented in Chapter 2, including signal interrogator principle, sensing principles and physics modeling of sensing unit performance. Different sensor signal processing schemes are illustrated and compared in Chapter 3. Sensors fabricated using different fibers and fabrication parameters are presented and compared in Chapter 4, including sensor characterization, discussions on practical considerations and sensor optimization. Chapter 5 is dedicated to sensor system implementation, performance evaluation, field test and system noise analysis. Chapter 6 summarizes the research work and proposes future research directions and improvements.

Chapter 2. Principles of Operation of Designed Quasi-Distributed Fiber Sensor

An optical wave is fully characterized by four variables: intensity, spectrum, phase and polarization state. These variables are sensitive, or can be made sensitive to a collection of measurands, thus forming the sensing principles of various types of fiber sensors. In the designed quasi-distributed fiber sensor, signal is encoded in both spectrum and phase, thus ensuring absolute measurement with high accuracy, high resolution, large dynamic measurement range and long-term measurement stability.

The proposed quasi-distributed fiber sensor system has two building blocks—the sensing unit and the signal processing unit. The sensing unit, also called the transducer, is the element that converts measurand into measurable physical signals through certain sensing schemes. The signal processing unit, which in this case, includes the signal interrogator and the signal demodulation algorithm, processes the signal and presents the measuring results. This chapter is devoted to the working principles of the sensing unit.

An introduction to optical fiber, modes in fiber and Gaussian approximation of modal distribution in fiber is illustrated in section 2.1. Section 2.2 is focused on the joining of different waveguides and its related issues such as modeling and performance simulation. A brief introduction to the Fabry-Perot theory is followed by discussion on fused silica properties and fiber Fabry-Perot interferometers in section 2.3. The proposed intrinsic Fabry-Perot interferometer based quasi-distributed fiber sensor system is presented in section 2.4.

2.1. Modes in Fiber

In 1966, Kao and Hockham [44] published their concept for signal transmission medium—optical fiber. In 1970, Corning Glass Works reported its development of fiber with 20dB/km loss [45-46]. The Corning announcement gave impetus to the study of the semiconductor laser, which in turn accelerated research on optical fibers. Further progress resulted by 1979 in a loss of only 0.2dB/km near the 1.55 μ m spectral region

[47]. The availability of low-loss optical fiber led to a revolution in the field of lightwave technology and started the era of optical fiber communications [48].

2.1.1. Basics of Fiber Optics

The simplest form of an optical fiber consists of a cylindrical core of silica glass surrounded by a cladding whose refractive index is lower than that of the core, which confines the light in the core through total internal reflection.

High purity silica glass SiO_2 is used as the principal material of the optical fiber. It has refractive index n of about 1.458. Dopant is mixed into the silica glass to change its refractive index to a proper level. GeO_2 , P_2O_5 , TiO_2 and Al_2O_3 are normally used to increase the refractive index, while B_2O_3 and F are used to reduce the refractive index. Table 2.1 shows the maximum relative refractive index difference $\Delta = (n_1 - n_2)/n_1$ (n_1 and n_2 are refractive indices of core and cladding) that could be given to SiO_2 containing a dopant. Attempt to obtain a larger Δ would result in cracks in the fiber owing to the difference in the thermal expansion coefficient of the two materials [49].

Material	Maximum value of Δ (%)
GeO_2 - SiO_2	3.5
P_2O_5 - SiO_2	1.2
B_2O_3 - SiO_2	-0.5
F - SiO_2	-0.7

Table 2.1. Δ of material with dopant

Optical fiber fabrication is a two-step process that includes preform fabrication and fiber drawing. A preform is a silica glass rod with material layers inside that build up the basic fiber structure. Preform fabrication achieves the desired refractive index profile by introducing dopant materials into the silica host medium. The difference in refractive index profiles leads to various types of fibers, for example step or graded index single-mode and multimode fibers, and dispersion-shifted fiber as shown in Figure 2.1.

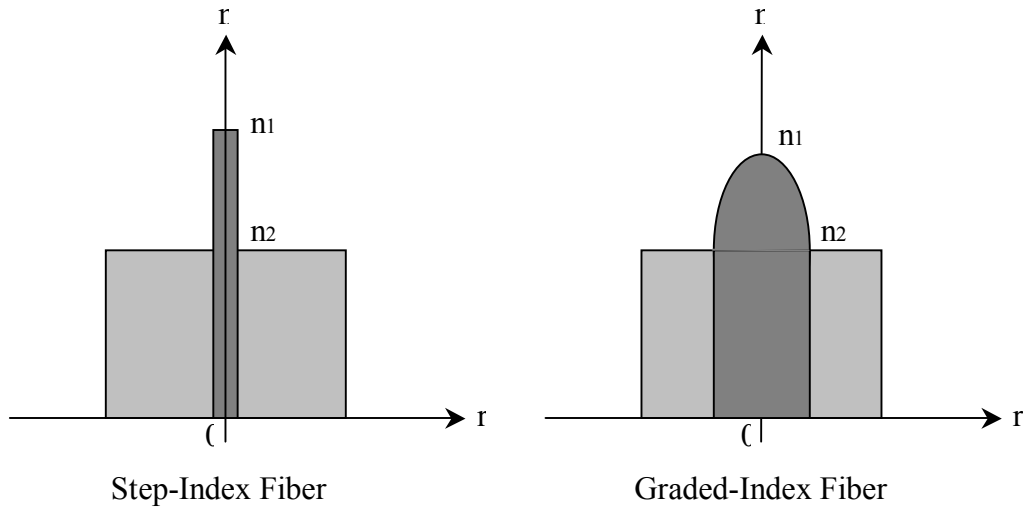
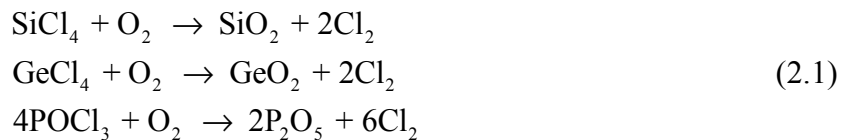


Figure 2.1. Different refractive-index profile fibers

The fiber dimensions are established by stretching the molten preform into the completed fiber in the fiber drawing process. Vapor phase manufacturing techniques are used in preform fabrication, which involves the oxidation of precursor gas mixtures to form different refractive index layers. Modified chemical vapor deposition (MCVD) is illustrated here to describe the basic chemistry; although other technologies such as outside vapor deposition (OVD), vapor axial deposition (VAD) and plasma-activated chemical vapor deposition (PCVD) are also used in preform fabrication. An MCVD system diagram is shown in Figure 2.2. Successive layers of higher purity silica glass SiO_2 are first deposited on the inner wall of the fused silica tube to form the cladding of the fiber. This is done by mixing SiCl_4 and O_2 at a temperature around 1800°C . A multi-burner torch is moved back and forth across the tube length to ensure uniformity of the doping. The core is formed by adding the vapors of GeCl_4 and POCl_3 . The chemical reactions are listed in Equation 2.1.



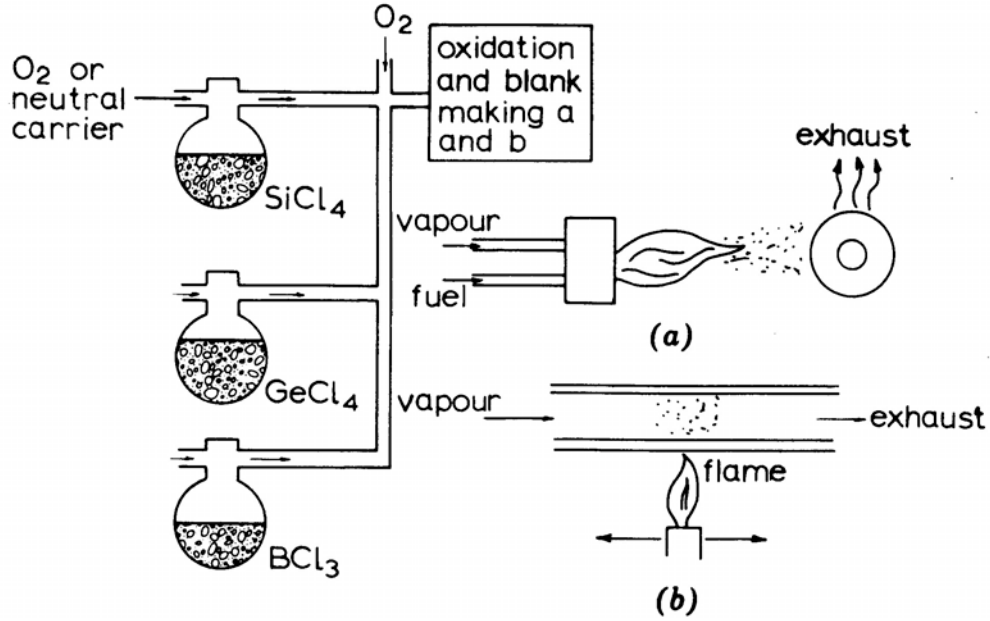


Figure 2.2. Diagram of the MCVD system [10]

P₂O₅ is used as a softening agent to reduce the viscosity of the silica-germania layers, which would improve the uniformity of the dopant concentration in each deposited layer. The flow rate of GeCl₄ and POCl₃ determines the amount of dopant and the corresponding increase in the refractive index of the core. A graded-index fiber is fabricated simply by varying the flow rate from layer to layer. When the deposition is done, the torch temperature is raised to collapse the tube into a solid rod of perform [50].

2.1.2. Step-Index Fiber Mode Theory

The refractive index profile of the optical fiber is generally divided into two categories: the step-index (SI) fiber, for example, single-step index fiber, and the special purpose index fiber, for example, parabolic graded-index (GI) fiber. The refractive index profiles of the two fibers are shown in Figure 2.1.

For the SI fiber, the analytical field solution exists. In the cylindrical coordinate system, the wave Equation has the form of

$$\frac{\partial^2 \Psi}{\partial r^2} + \frac{1}{r} \frac{\partial \Psi}{\partial r} + \frac{1}{r^2} \frac{\partial^2 \Psi}{\partial \phi^2} + (k_0^2 n^2 - \beta^2) \Psi = 0 \quad (2.2)$$

Accordingly, we write

$$\Psi(r, \varphi) = R(r)\Phi(\varphi) \quad (2.3)$$

By substituting Equation (2.3) into Equation (2.2), the electric field distribution has the form shown in Equation (2.4), where $V = \sqrt{u^2 + w^2} = k_0 a \sqrt{n_1^2 - n_2^2} = k_0 n_1 a \sqrt{2\Delta}$, $u = a \sqrt{n_1^2 k_0^2 - \beta^2}$, $w = a \sqrt{\beta^2 - n_2^2 k_0^2}$, $\Delta = \frac{n_1^2 - n_2^2}{2n_1^2} \approx 1 - \frac{n_2}{n_1}$, $NA = \sqrt{n_1^2 - n_2^2} = n_1 \sqrt{2\Delta}$.

$$\begin{cases} E_z = AJ_q \left(\frac{ur}{a} \right) \sin(q\Phi) \\ E_r = \left[-A \frac{j\beta}{(u/a)} J_q' \left(\frac{ur}{a} \right) + B \frac{j\omega\mu}{(u/a)^2} \frac{q}{r} J_q \left(\frac{ur}{a} \right) \right] \sin(q\Phi) \\ E_\Phi = \left[B \frac{j\omega\mu}{(u/a)} J_q' \left(\frac{ur}{a} \right) - A \frac{j\beta}{(u/a)^2} \frac{q}{r} J_q \left(\frac{ur}{a} \right) \right] \cos(q\Phi) \end{cases}, \quad r < a \quad (2.4)$$

$$\begin{cases} E_z = CK_q \left(\frac{wr}{a} \right) \sin(q\Phi) \\ E_r = \left[C \frac{j\beta}{(w/a)} K_q' \left(\frac{wr}{a} \right) - D \frac{j\omega\mu}{(w/a)^2} \frac{q}{r} K_q \left(\frac{wr}{a} \right) \right] \sin(q\Phi) \\ E_\Phi = \left[-D \frac{j\omega\mu}{(w/a)} K_q' \left(\frac{wr}{a} \right) + C \frac{j\beta}{(w/a)^2} \frac{q}{r} K_q \left(\frac{wr}{a} \right) \right] \cos(q\Phi) \end{cases}, \quad r > a$$

Using the boundary conditions, the characteristic Equation is obtained. Based on the weakly guiding approximation $n_1 \approx n_2$, the propagation constant β can be derived from the characteristic Equation, in which $q=0$ applies to TE_{0m} and TM_{0m} modes, and $q>0$ corresponds to hybrid modes EH_{qm} and HE_{qm} . Thus EH , HE , TE or TM modes that has the same characteristic Equation will have the same propagation constant β , and therefore degenerate.

$$u \frac{J_{l-1}(u)}{J_l(u)} = -w \frac{K_{l-1}(w)}{K_l(w)} \quad l = \begin{cases} 1 & TE_{0m}, TM_{0m} \\ q+1 & EH_{qm} \\ q-1 & HE_{qm} \end{cases} \quad (2.5)$$

The transverse electric field of each mode is given in Equation (2.6) through (2.7). The electric field superposition of these degenerate modes will form a linearly polarized pseudo mode LP_{lm} . The LP system is a simplified way of describing modes in weakly

guiding fibers. Furthermore, the *LP* modes are almost always observed in practice and are readily identified by their transverse intensity profiles.

$$\text{TE}_{0m}, \text{TM}_{0m}: \begin{cases} E_t(r \leq a) = E_0 J_1\left(\frac{ur}{a}\right) \\ E_t(r \geq a) = -E_0 \frac{u}{w} \frac{J_0(u)}{K_0(w)} K_1\left(\frac{wr}{a}\right) \end{cases} \quad (2.6)$$

$$\begin{aligned} \text{EH}_{qm}: & \begin{cases} E_r(r \leq a) = E_0 J_{q+1}\left(\frac{ur}{a}\right) \sin(q\phi) \\ E_r(r \geq a) = -E_0 \frac{u}{w} \frac{J_q(u)}{K_q(w)} K_{q+1}\left(\frac{wr}{a}\right) \sin(q\phi) \\ E_\phi(r \leq a) = -E_0 J_{q+1}\left(\frac{ur}{a}\right) \cos(q\phi) \\ E_\phi(r \geq a) = -E_0 \frac{u}{w} \frac{J_q(u)}{K_q(w)} K_{q+1}\left(\frac{wr}{a}\right) \cos(q\phi) \end{cases} \\ \text{HE}_{qm}: & \begin{cases} E_r(r \leq a) = -E_0 J_{q-1}\left(\frac{ur}{a}\right) \sin(q\phi) \\ E_r(r \geq a) = -E_0 \frac{u}{w} \frac{J_q(u)}{K_q(w)} K_{q-1}\left(\frac{wr}{a}\right) \sin(q\phi) \\ E_\phi(r \leq a) = -E_0 J_{q-1}\left(\frac{ur}{a}\right) \cos(q\phi) \\ E_\phi(r \geq a) = -E_0 \frac{u}{w} \frac{J_q(u)}{K_q(w)} K_{q-1}\left(\frac{wr}{a}\right) \cos(q\phi) \end{cases} \end{aligned} \quad (2.7)$$

Listed in Table 2.2 is the designation of the first 12 LP modes in a step index fiber [51].

Normalized propagation constant b is defined as

$$b = 1 - \frac{u^2}{V^2} = \frac{\beta^2 - n_2^2 k_0^2}{n_1^2 k_0^2 - n_2^2 k_0^2} = \frac{n_{\text{eff}} - n_2}{n_1 - n_2} \quad (2.8)$$

where effective guide index is defined as $n_{\text{eff}} \equiv \beta/k_0$. The normalized propagation constant b versus V for a SI fiber is shown in Figure 2.3.

Cutoff conditions are solutions of the characteristic Equation for V at $w=b=0$. When $w=0$, the exponential decay of fields in the cladding region is lifted and the energy is no longer bound to the core. Cutoff wavelength is the wavelength beyond which the energy begins

to radiate into the cladding region causing loss in the axial direction. For SI fibers, the ones with $V < 2.405$ are single-mode fibers, and the ones with $V > 2.405$ are multimode fibers. Modes in the waveguide are orthogonal.

$$\int_0^{2\pi} \int_0^\infty \text{Re}[\hat{E}_{\alpha\beta} \times \hat{H}_{\gamma\delta}] \cdot \hat{a}_z r dr d\phi = \delta_{\alpha\gamma} \delta_{\beta\delta} \quad (2.9)$$

Suppose an SI multimode fiber has 50 μm core diameter and 125 μm outer diameter. Its $\Delta = 1\%$. Its refractive indices of the core and cladding are $n_{\text{core}} = 1.4726$ and $n_{\text{cladding}} = 1.4580$. For this fiber, the calculated $V = 20.9625$, and the number of modes in this fiber is $N \approx 220$ using Equation (2.10)

$$N \approx \frac{1}{2} V^2 \quad (2.10)$$

The electric field and power distribution of the lowest six LP modes at 1.55 μm are shown in Figure 2.4.

LP Designation	Degenerate Modes	l	Bessel Function	V_c
LP_{01}	HE_{11}	0	-	0
LP_{11}	$TE_{01}, TM_{01}, HE_{21}$	1	J_0	2.405
LP_{21}	EH_{11}, HE_{31}	2	J_1	3.832
LP_{02}	HE_{12}	0	J_{-1}	3.832
LP_{31}	EH_{21}, HE_{41}	3	J_2	5.136
LP_{12}	$TE_{02}, TM_{02}, HE_{22}$	1	J_0	5.520
LP_{41}	EH_{31}, HE_{51}	4	J_3	6.380
LP_{22}	EH_{12}, HE_{32}	2	J_1	7.016
LP_{03}	HE_{13}	0	J_{-1}	7.016
LP_{51}	EH_{41}, HE_{61}	5	J_4	7.588
LP_{32}	EH_{22}, HE_{42}	3	J_2	8.417
LP_{13}	$TE_{03}, TM_{03}, HE_{23}$	1	J_0	8.654

Table 2.2. Designations of the First 12 LP Modes in a Step Index Fiber

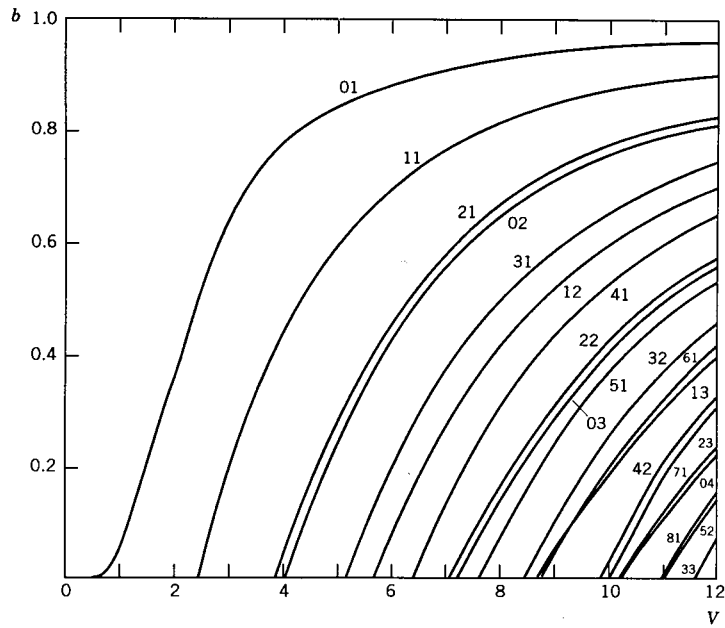
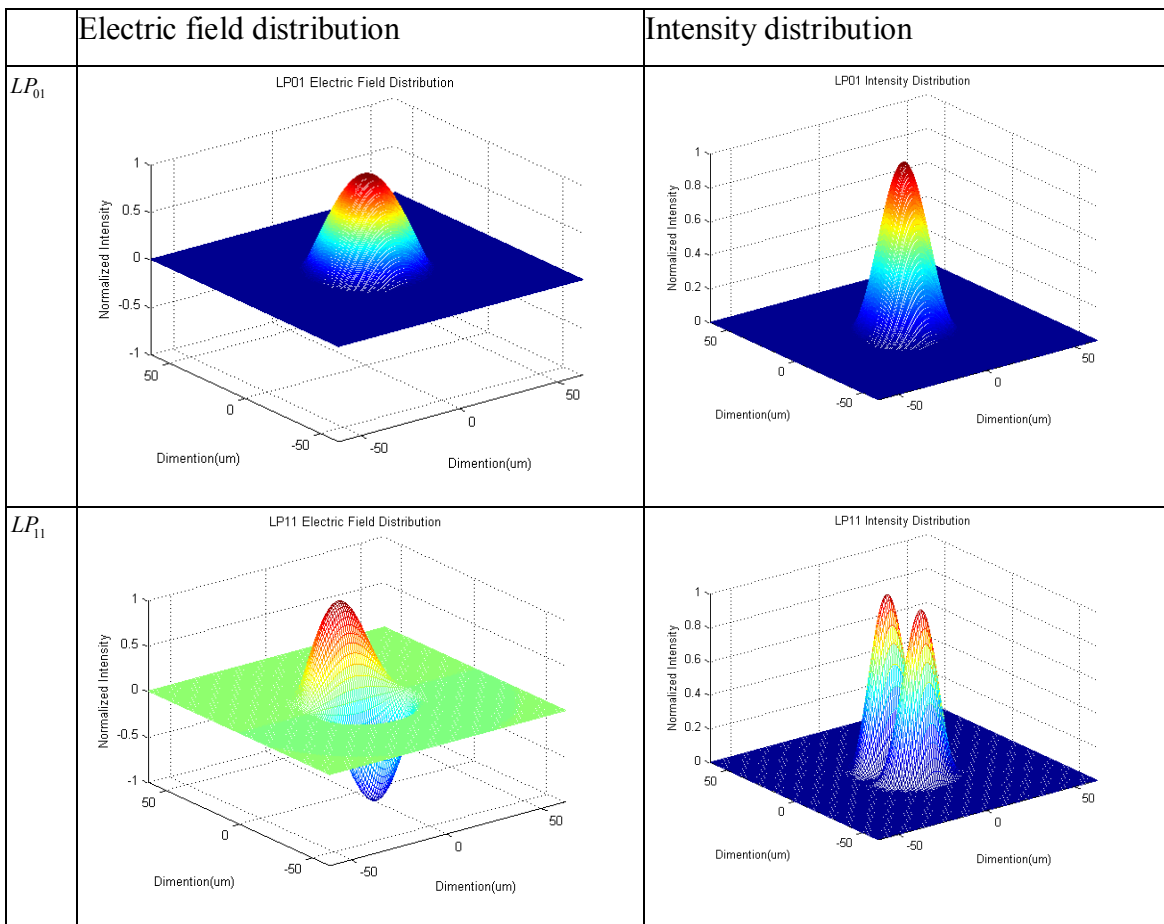


Figure 2.3. Normalized propagation constant, b , for designated LP mode



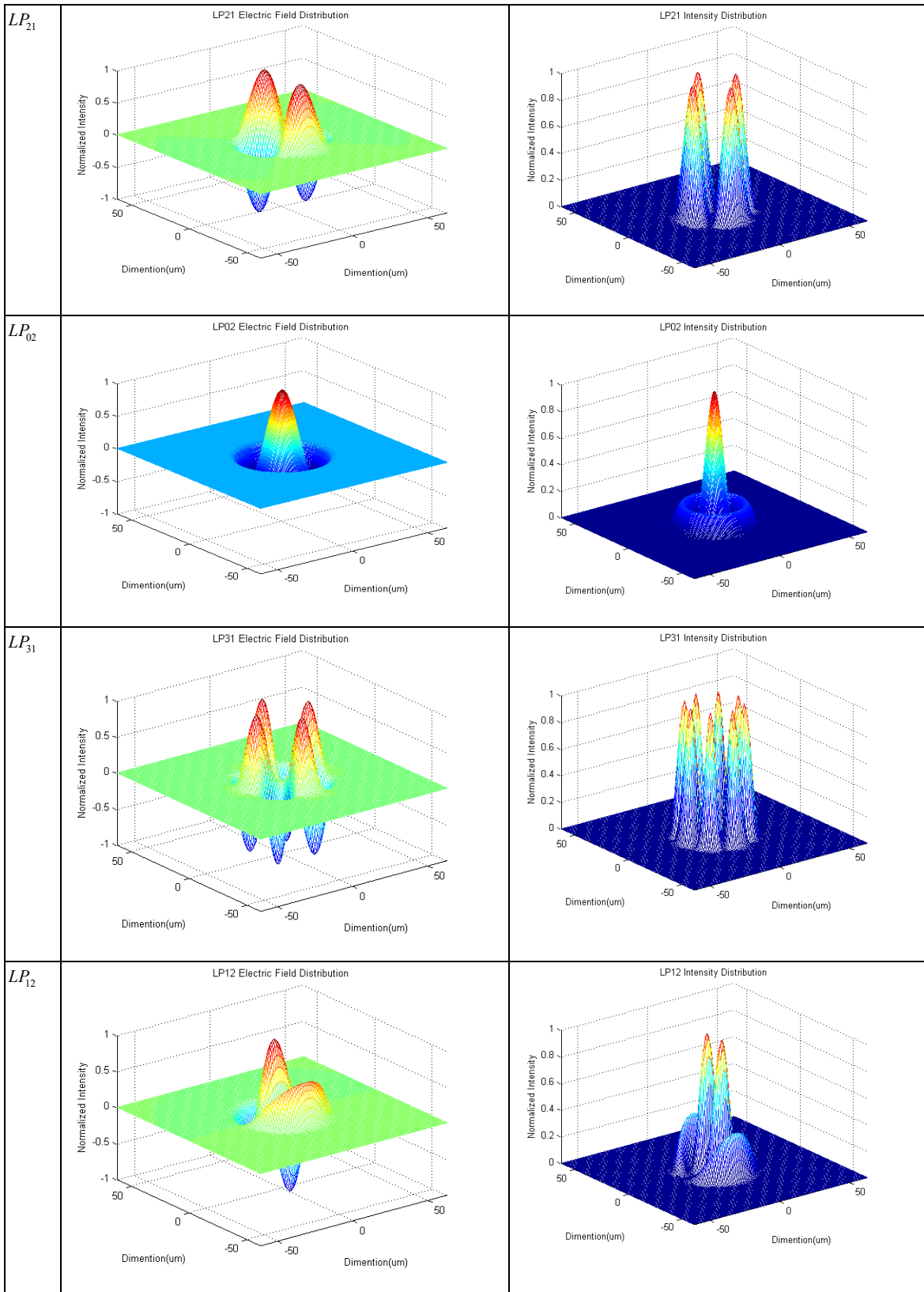


Figure 2.4. LP modes in the SI fiber

2.1.3. Graded-Index Fiber Mode Theory

The accurate analytical mode solution for the GI fiber is important. It can be used in multimode and single-mode GI fibers design to minimize dispersion and transmission loss. It can also be used to accurately analyze the transmission loss of the proposed quasi-distributed fiber sensor.

Since in GI fiber, the assumption of constant permittivity is no longer valid, the RHS term in the wave Equation (2.11) is a non-zero term. Thus Equation (2.2) is no longer valid. As far as the analytical solutions based on Maxwell's Equations are concerned, the exact analytical solutions are extremely difficult to obtain.

$$\nabla^2 E + k^2 E = -\nabla(E \cdot \frac{\nabla \epsilon}{\epsilon}) \quad (2.11)$$

Several methods are used in obtaining the mode field distribution of GI fibers. They are: the finite element method, geometrical optics method, ray method, and approximate methods such as the WKB method. These methods involve a number of approximations which limit the accuracy of its results and restrict their applications to modes of high radial order. It also yields no detailed information on the distribution and polarization of its modal fields.

In the proposed quasi-distributed fiber sensor fabrication, multimode SI fiber or GI fiber with parabolic refractive index is used. Fortunately, for the parabolic refractive index GI fiber, the modal fields in terms of known functions exist, and their propagation characteristics can be derived in a closed form.

The refractive index of a parabolic index profile GI fiber is shown in Equation (2.12)

$$n(r) = \begin{cases} n_{core} [1 - 2\Delta (\frac{r}{a})^2]^{\frac{1}{2}} & r < a \\ n_{core} [1 - 2\Delta (\frac{r}{a})] & r \geq a \end{cases} \quad (2.12)$$

By assuming the refractive index change only gradually in the radial direction, the RHS term in Equation (2.11) remains small enough and can be neglected. Thus the vector equation can be separated into three scalar wave equations. Suppose the solution takes the form of Equation (2.3), then the radial field distribution is

$$\frac{\partial^2 \Psi}{\partial r^2} + \frac{1}{r} \frac{\partial \Psi}{\partial r} + k_r^2 \Psi = 0 \quad (2.13)$$

$$k_r^2 = n^2(r)k_0^2 - \beta^2 - \frac{l^2}{r^2} \quad (2.14)$$

By substituting Equation (2.12) and (2.15) into (2.14), the solution is

$$\Psi(r, \varphi) = (\sqrt{2} \frac{r}{w})^l L_q^l (2 \frac{r^2}{w^2}) e^{-r^2/w^2} \quad (2.15)$$

where $L_q^l(\square)$ in this expression represents the generalized Laguerre polynomial of order l and degree q , and it takes the following form

$$L_q^l(x) = \frac{1}{q!} \sum_{i=0}^q \frac{q!}{i!} \binom{l+q}{q-i} (-x)^i \quad (2.16)$$

and

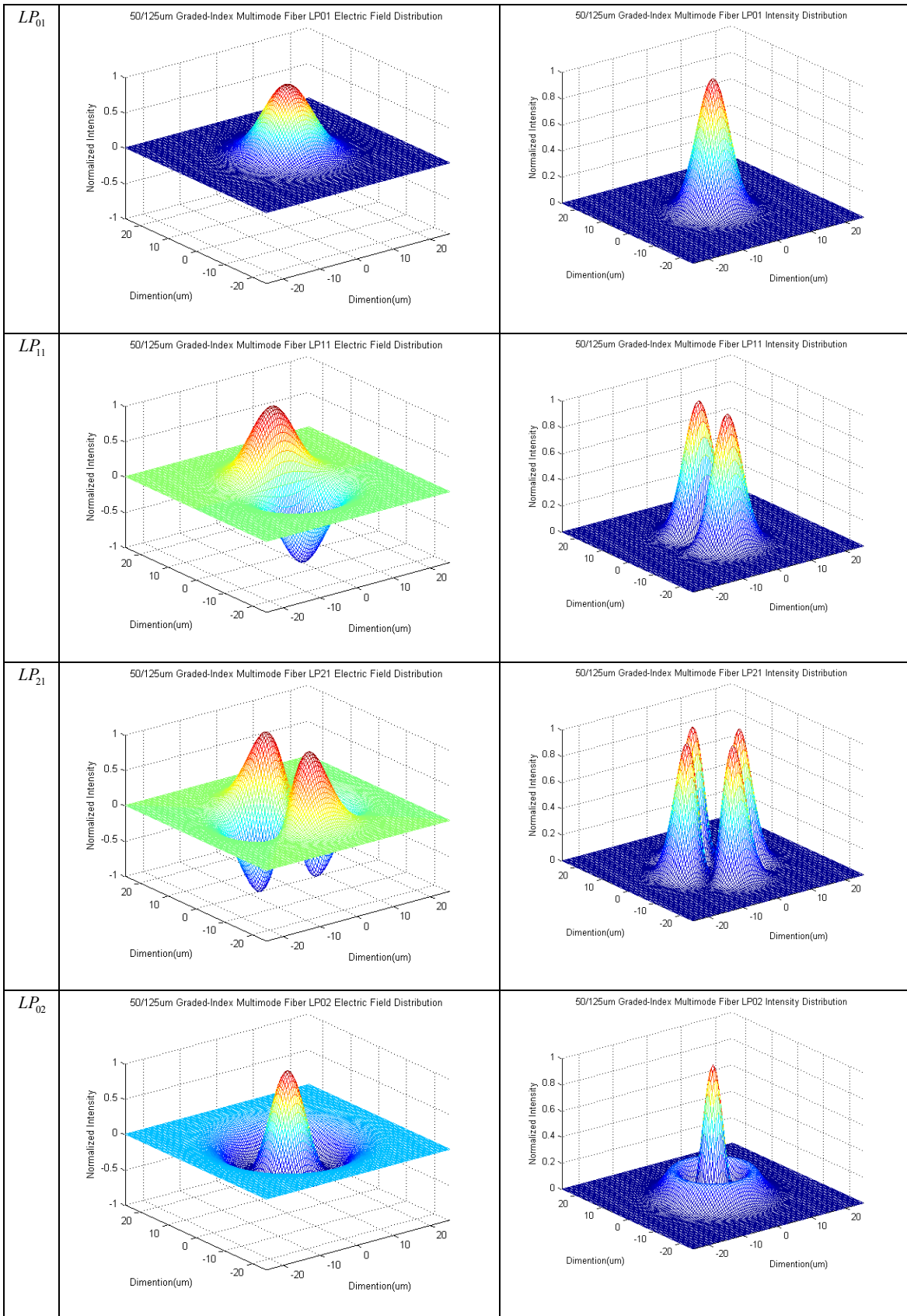
$$w = \left(\frac{2a}{n_{core} k_0 \sqrt{2\Delta}} \right)^{1/2} \quad (2.17)$$

The small index difference of the GI fiber yield small longitudinal field when compared with the transverse field. Thus the total field under these conditions is nearly transverse. The polarization of this field is nearly linear and uniform over any fiber cross-section, which leads to the designation of LP_{lp} modes. The two index values l and p of this nomenclature designate the circumferential and transverse orders of modes. l appears in $\cos l\varphi$ for the circumferential field distribution and also gives the order of the Laguerre polynomial for the radial field dependence. The radial order p is related to the degree q of the Laguerre polynomial of the radial field distribution by $p = q + 1$, and q counts the number of field nodes along any radius. The propagation constant is given by

$$\beta = n_{core} k_0 \left[1 - \frac{\sqrt{2\Delta}}{n_{core} k_0 a} (4q + 2l + 2) \right]^{1/2} \quad (2.18)$$

The LP_{01} mode is the lowest order and hence the fundamental mode for parabolic index GI fibers. The electric field and power distribution of the lowest six LP modes at 1.55um are shown in Figure 2.5.

	Electric field distribution		Intensity distribution
--	-----------------------------	--	------------------------



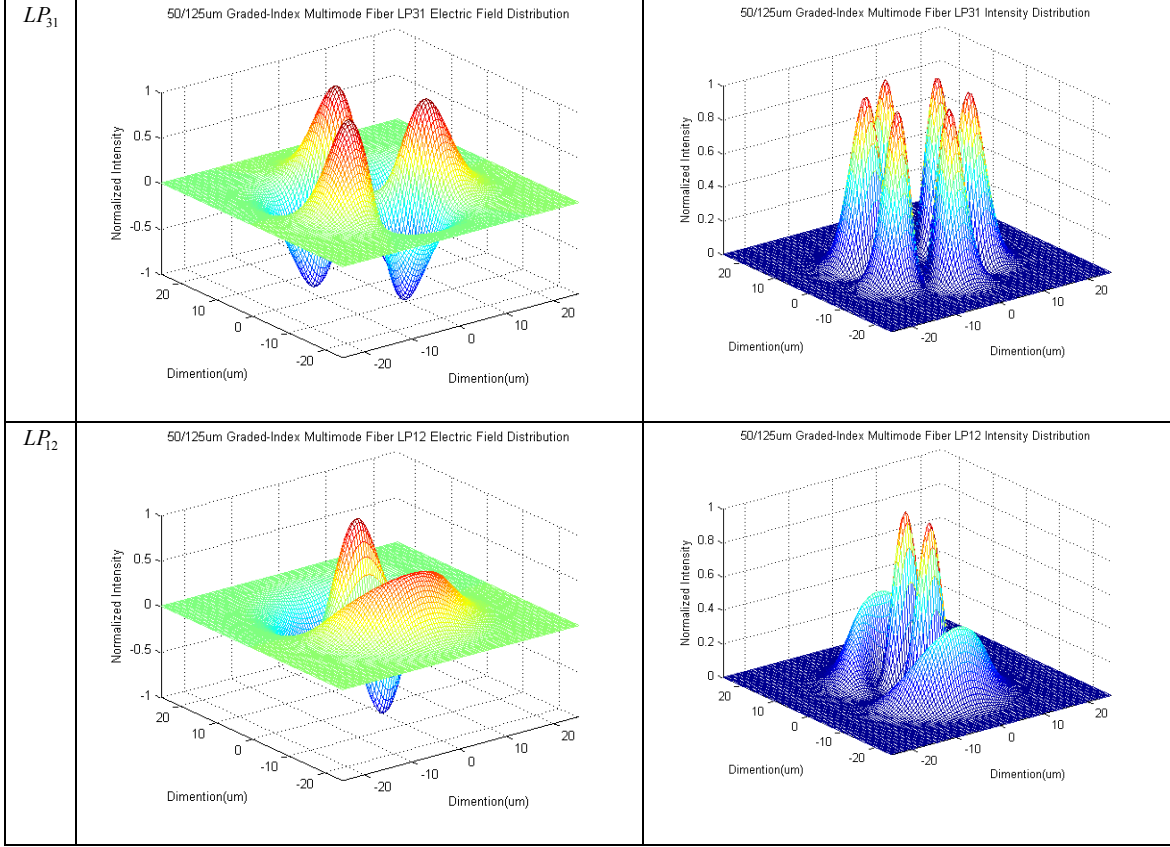


Figure 2.5. LP modes in the GI fiber

2.1.4. Gaussian beam approximation

As D. Marcuse pointed out [52], Gaussian function having width r_0 can be used to approximate LP_{01} mode given by Equation (2.7). The width r_0 is known as the mode field radius. It is defined as the radial distance from the core center to the $1/e$ point of the Gaussian electric field profile. The relation of r_0 with V is obtained using the following method.

Suppose the Gaussian field is expressed as

$$E_{gx} = E_{g0} e^{-\frac{r^2}{r_0^2}} \quad (2.19)$$

And the LP_{01} field having the same polarization is denoted as E_{1x} . C_{01} is used to evaluate the resemblance of the two fields. It is defined in the following Equation

$$\int_0^{2\pi} \int_0^{\infty} \frac{1}{2} \text{Re}\{E_{gx} H_{1y}^*\} r dr d\phi = \int_0^{2\pi} \int_0^{\infty} \frac{1}{2} \text{Re}\{C_{01} E_{1x} H_{1y}^*\} r dr d\phi = C_{01} P \quad (2.20)$$

By expressing both E_{gx} and H_{1y} in terms of P , C_{01} is obtained using Equation (2.21).

$$C_{01} = \frac{2\sqrt{2}}{r_0 a V} \left\{ \frac{w}{J_1(u)} \int_0^a J_0\left(\frac{ur}{a}\right) e^{-\frac{r^2}{r_0^2}} r dr + \frac{u}{K_1(w)} \int_a^\infty K_0\left(\frac{wr}{a}\right) e^{-\frac{r^2}{r_0^2}} r dr \right\} \quad (2.21)$$

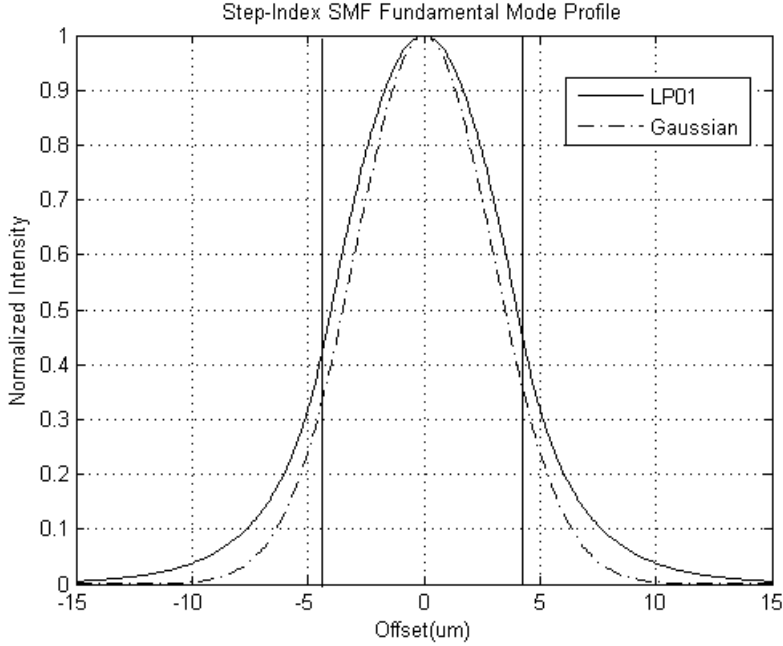


Figure 2.6. SI SMF fundamental mode profile and Gaussian approximation

For each choice of V , r_0 is varied until the Equation yields maximum C_{01} . The results of the above process are closely approximated by the empirical formula

$$\frac{r_0}{a} \approx 0.65 + \frac{1.619}{V^{3/2}} + \frac{2.879}{V^6} \quad (2.22)$$

This formula approximates the exact result to better than 1% accuracy. The electric field profile of the LP_{01} mode and its Gaussian approximation at $1.55\mu m$ is shown in Figure 2.6, where the vertical solid line is the core-cladding boundary. A larger fiber core diameter and operation wavelength, and a smaller doping concentration all lead to a larger mode field radius.

2.2. Joining of Different Fibers

2.2.1. Fiber mode excitation

A fiber junction comprises of two optical fibers as shown in Figure 2.7. The light is launched from Fiber A to Fiber B. Let E_i denote the electric field distribution at the end face of Fiber A, and E_0 denotes the electric field distribution on the surface of Fiber B. The two surfaces of the fibers are longitudinally separated by a distance z . If z is non-zero, then E_0 constitutes of the near-field radiation from the end face of the Fiber A. Kirchoff's diffraction theory leads to the following approximation for this radiation field. r is the distance between a source point on the end face of the Fiber A and the field point on the front face S_f of the Fiber B.

$$E_0 = \frac{1}{4\pi} \iint_{S_i} E_i \exp(-jk_0 r) \left[-jk_0 + \left(-jk_0 + \frac{1}{r}\right) \frac{z}{r} \right] d \frac{S}{r} \quad (2.23)$$

If both waveguides join directly together without any gap, then E_0 equals the electric field E_i of the incident wave of unit power in Fiber A.

$$E_0 = E_i \quad (2.24)$$

E_0 excites guided and radiation modes of Fiber B, the electric fields of which superimpose on its surface to give the total field

$$E_0 = \sum_{\mu} E_{\mu} \quad (2.25)$$

The summation extends over all the guided core and cladding modes of the fiber, but is meant to also include integration over the continuous spectrum of radiation modes. The orthogonality between all the guided modes can be expressed as

$$\left| \iint_{S_f} E_{\mu} E_{\nu} dS \right| = \frac{\sqrt{\mu_0 / \epsilon_0}}{n_1} |P_{\nu}| \delta_{\mu\nu} \quad (2.26)$$

where P_{ν} designates the power which the mode ν with the electric field E_{ν} transmits. Practical interest concentrates on the power with which the incident field excites core modes. If we form the inner product of Equation (2.25) with E_{ν} , integrate over the full fiber cross-section and apply the orthogonality condition, the only terms non-zero on the RHS are those for which $\mu = \nu$ and whose E_{ν} has the same uniform polarization as E_{μ} .

With these terms, the power with which a mode ν in its particular polarization is excited takes the following form

$$P_\nu = \left| n_1 (\epsilon_0 / \mu_0)^{1/2} \iint_{S_f} E_0 E_\nu dS \right| \quad (2.27)$$

Because E_0 is assumed to represent the incident field for unit incident power. Thus the obtained P_ν is the efficiency with which E_0 launches its power into the mode ν of the fiber.

Presented in Figure 2.8 is the electric field coupling coefficient and power coupling coefficient of the LP_{01} mode in an SI single-mode fiber to LP_p mode in a GI multimode fiber. The single-mode fiber is 0.32% doped, and the core radius is $a = 4.2\mu m$. The multimode fiber is 1% doped, and has $a = 25\mu m$. The wavelength considered here is $\lambda = 1.55\mu m$. The electric field coupling coefficient is the highest for the fundamental mode LP_{01} , which is 94.01%. The power coupling coefficient for LP_{01} to LP_{01} coupling is $\eta_p = 88.31\%$, which is one order higher than that of the LP_{01} to LP_{11} coupling. The coupling coefficient for higher order mode can be neglected.

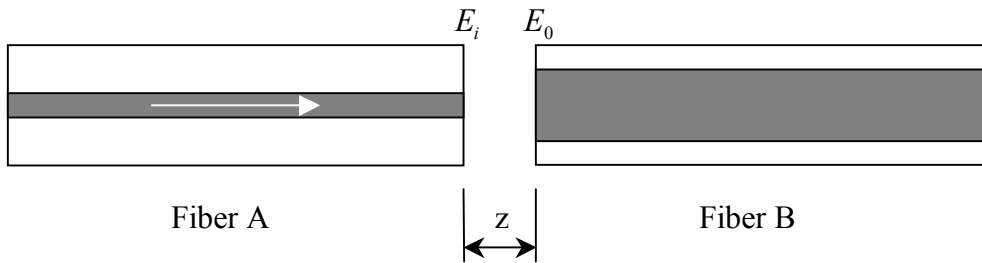
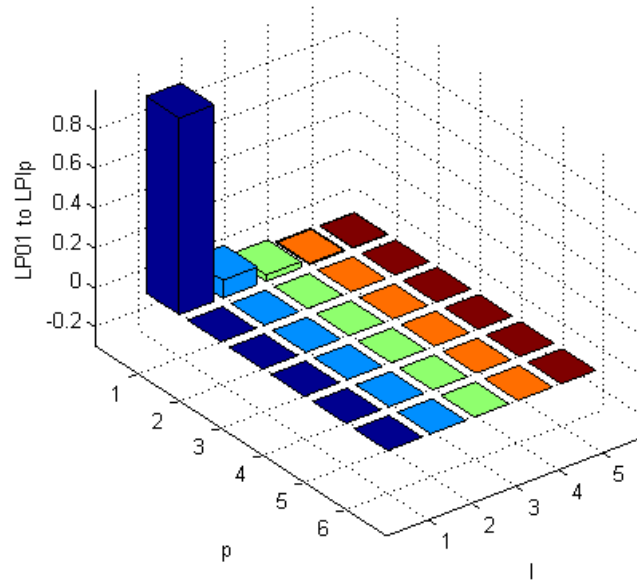


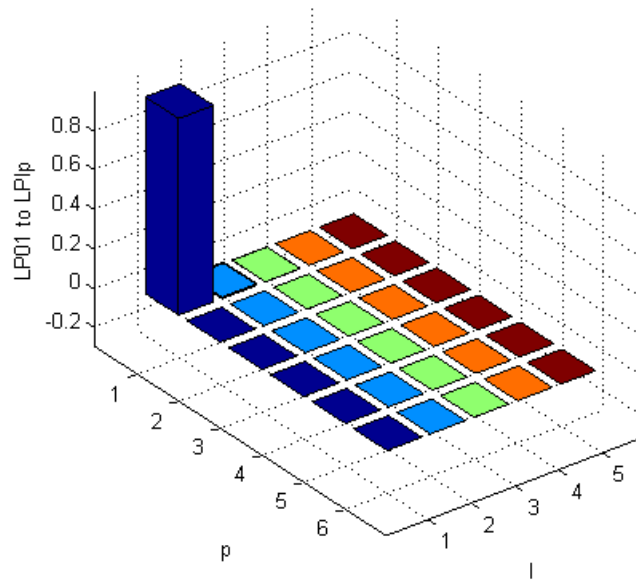
Figure 2.7. Fiber mode excitation

Single-mode fiber to multimode fiber electric field coupling coefficient



(a) Electric field coupling coefficients

Single-mode fiber to multimode fiber power coupling coefficient



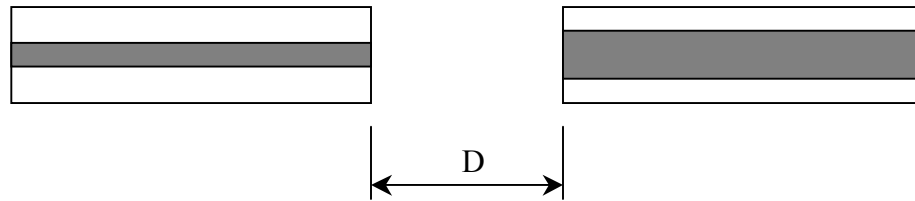
(b) Power coupling coefficients

Figure 2.8. SMF LP01 mode to GI MMF LPp mode coupling coefficients

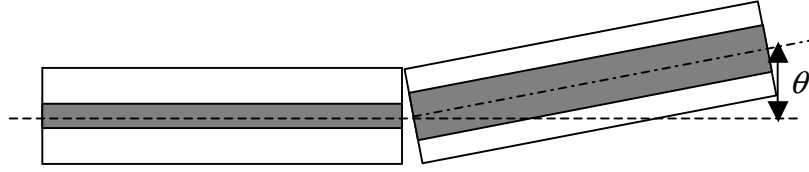
Using the mode-field-radius for GI fiber derived from the previous section, the power coupling coefficient for LP_{01} to LP_{01} coupling is $\eta_p = 87.31\%$. The difference in the power coupling coefficients obtained using rigorous mode coupling theory and Gaussian approximation is only 1%. Thus in the following modeling of the proposed quasi-distributed fiber sensor analysis, the Gaussian field model is used.

2.2.2. Fiber splicing

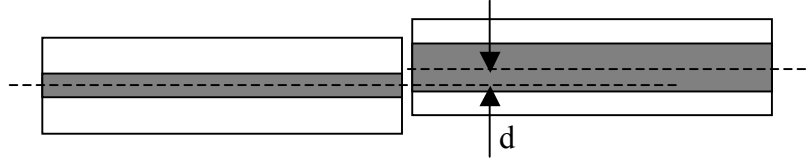
Arc fusion splicing is most commonly used for fiber splicing. The arc fusion splicing machine now available is sufficiently practical because of the following reasons: the arc fusion process and the machine as a whole can be made automatic; it is easy to design the machine in a small size and light weight; the machine can be so designed as to be easy to use and to make a highly reproducible and stable splice. The arc fusion splicing machines now in practical use have the following mechanisms: accurate axial alignment of the cores and claddings of the fibers; fine movement of the fibers; stable arc discharge and its control. During the splicing process, the fibers are inserted between electrodes (spacing of the electrodes is 1-2mm). The two fibers are aligned and their end surfaces are melted by the arc and then brought into contact with each other to form a splice. In the arc fusion process, AC voltage is applied to the electrodes. AC discharge causes a spark discharge at a 2000-4000V, which in turn generates ions between the electrodes. The ions reduce the spark voltage to about 300-600V. The alternating current is about 15-20mA, and the required power for splicing is about 5-10W. The fiber is cleaved by placing a fiber into a horizontal groove of an insulating board and then scoring it vertically by a diamond tip or edge placed into the other groove perpendicular to the previous one. The fiber is then pulled straight with slight bending until it snaps. This method reduces the end angle of the fiber and hence reduces angular tilt loss [53].



(a). Separation



(b). Tilt



(c). Offset

Figure 2.9. Several types of splice imperfections

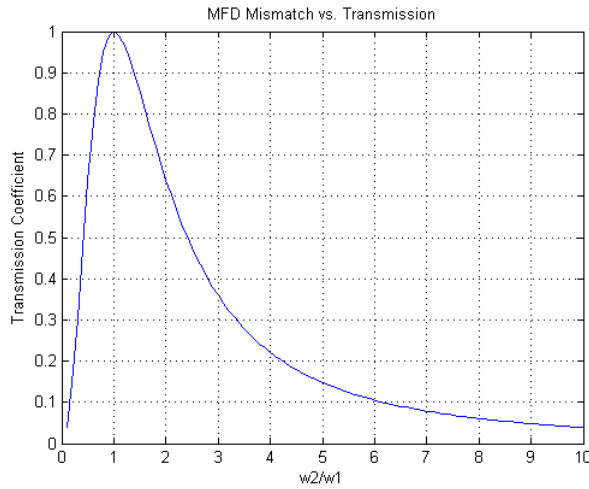
Fiber separation, tilt and offset are the major causes of loss in fiber splicing. These three problems are shown in Figure 2.9. According to D. Marcuse, the power transmission coefficient of the splice for these three situations are given in the following Equations

$$T = \frac{4[4Z^2 + \frac{w_1^2}{w_2^2}]}{[4Z^2 + \frac{w_1^2 + w_2^2}{w_2^2}]^2 + 4Z^2 \frac{w_2^2}{w_1^2}}, \quad Z = \frac{D}{n_2 k_0 w_1 w_2} \quad (2.28)$$

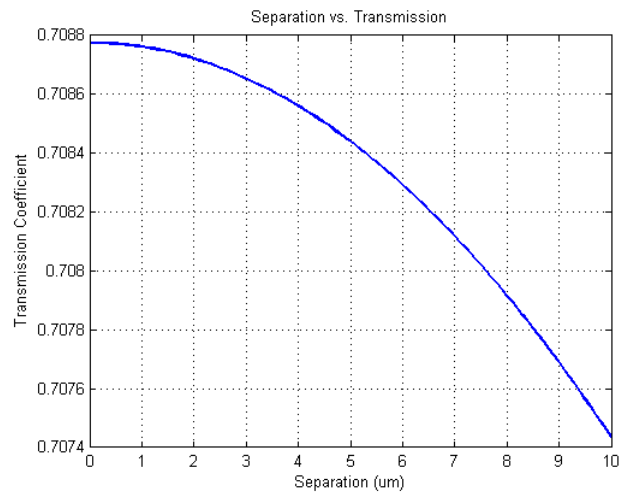
$$T = \left(\frac{2w_1 w_2}{w_1^2 + w_2^2}\right)^2 \exp\left[-\frac{2(\pi n_2 w_1 w_2 \theta)}{(w_1^2 + w_2^2)\lambda^2}\right] \quad (2.29)$$

$$T = \left(\frac{2w_1 w_2}{w_1^2 + w_2^2}\right)^2 \exp\left[-\frac{2d^2}{w_1^2 + w_2^2}\right] \quad (2.30)$$

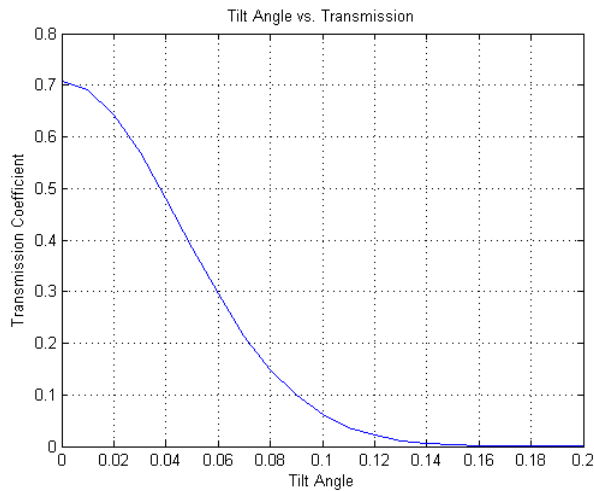
The simulation results are shown in Figure 2.10. More splice loss modeling can be found in literature [54-57].



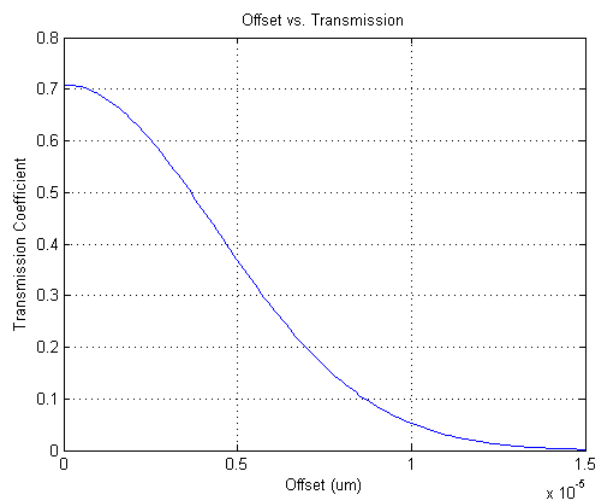
(a) MFD mismatch



(b) Separation



(c) Tilt



(d) Offset

Figure 2.10. Single-mode fiber to GI multimode fiber splice loss simulations

2.3. Fiber Fabry-Perot Interferometer for Distributed Sensing

Fabry-Perot interferometer, named after Charles Fabry and Alfred Pérot, is typically made of a transparent plate with two reflecting surfaces, or two parallel highly-reflecting mirrors. The varying transmission function of a Fabry-Perot interferometer is caused by interference between the multiple reflections of light between the two reflecting surfaces. Constructive interference occurs if the transmitted beams are in phase, and this corresponds to a high-transmission peak of the Fabry-Perot interferometer. If the

transmitted beams are out-of-phase, destructive interference occurs and this corresponds to a transmission minimum. Suppose a plane wave of monochromatic light is incident upon a Fabry-Perot cavity at angle θ as shown in Figure 2.11, where r and t are the reflection coefficient and transmission coefficient for wave traveling from the surrounding medium into the cavity, r' and t' is the reflection and transmission coefficients for the wave traveling from the cavity to the surrounding medium. The complex amplitude of the reflected electric field $E^{(r)}$ can be written as:

$$E^{(r)}(\omega) = \sum_{p=0}^{\infty} a_p \exp[-j(p+1)\delta] \quad (2.31)$$

where $a_p = tt' r'^{2p+1} E^{(i)}$ is the complex magnitude of p th beam, $E^{(i)}$ is the complex magnitude of the incident light, $\delta = 4\pi n' h \cos\theta' / \lambda$ is the phase delay between two adjacent transmission or reflection beams. From Fresnel Equations, we have

$$r' = r, \quad tt' + r^2 = 1 \quad (2.32)$$

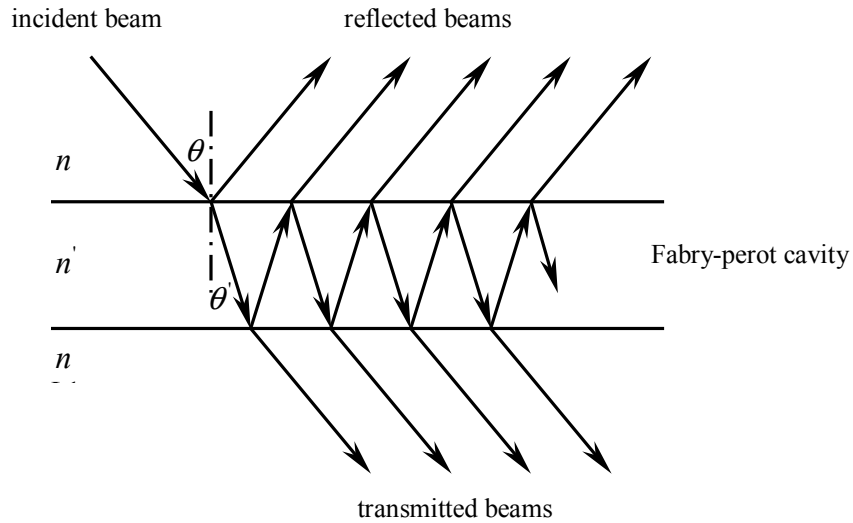


Figure 2.11. Fabry-Perot cavity interference model

Since $I \propto E^* E$, the reflection spectrum takes the following form

$$I^{(r)} = \frac{4R \sin^2 \frac{1}{2} \delta}{(1-R)^2 + 4R \sin^2 \frac{1}{2} \delta} I^{(i)} \quad (2.33)$$

where $I^{(i)}$ is the incident light power, and $R=r'r'$ is the reflectance. The transmission spectrum of a Fabry-Perot interferometer is shown in Figure 2.12. Higher R results in sharper interference fringe contrast. Interference fringe visibility is defined as

$$V = \frac{I_{\max} - I_{\min}}{I_{\max} + I_{\min}} \quad (2.34)$$

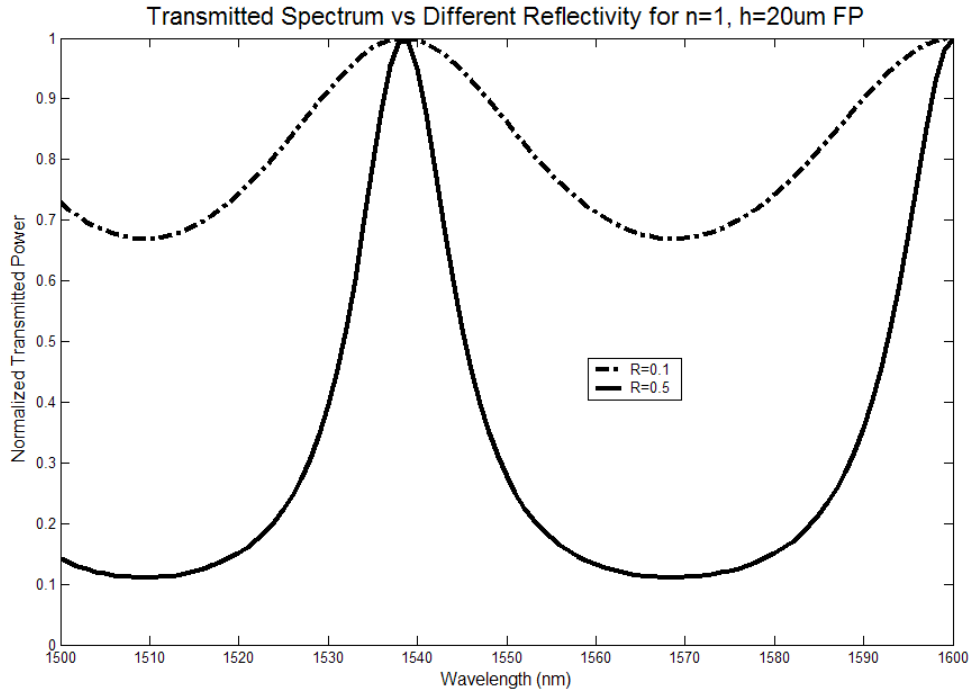


Figure 2.12. Transmission spectrum for a Fabry-Perot cavity with different reflectivity

Hence, the basic function of the Fabry-Perot interferometer is to encode Fabry-Perot cavity optical length information into wavelength domain. By associating different measurands with the Fabry-Perot cavity optical length through various packaging plans, Fabry-Perot interferometers can be turned into optical sensors. Since the measurement of extremely small phase shifts in the microradian range is possible in these sensors, extremely high sensitivities have been achieved. However, due to the strict requirement of the alignment between the two optical surfaces in a Fabry-Perot interferometer, most Fabry-Perot interferometers based on bulk optics can only maintain their stability in laboratory environments.

The convergence of optical fiber greatly eases the requirement of alignment in constructing Fabry-Perot interferometers, making fiber Fabry-Perot interferometers much more stable. The other advantages this technology offers are lightness and compactness, versatility, high reliability, low cost, and ease in fabrication. Early research work on fiber optic Fabry-Perot interferometric sensors can be traced back to the mid 70s when Christensen at the Washington University successfully demonstrated multimode fiber based Fabry-Perot temperature sensors. Thereafter, fiber optic Fabry-Perot sensors were developed into various structures and applied to the measurement of a wide variety of physical and chemical parameters. Many fiber optic interferometers in general depend on the interference between two light beams. Secondary reflections do exist but are generally negligible. Based on the construction of the Fabry-Perot cavities, fiber optic Fabry-Perot sensors can be categorized into two types: the extrinsic Fabry-Perot interferometer (EFPI) and intrinsic Fabry-Perot interferometer (IFPI).

2.3.1. EFPI Sensors

As shown in Figure 2.13 and 2.14, the EFPIs have an interferometric cavity outside the fiber, and the fiber is only acting as a medium to transmit light into and out of the Fabry-Perot cavity. Although the two reflectors of forming the Fabry-Perot cavity can be the surfaces of any optical components, a very simple way of forming an EFPI will be directly using the cleaved endfaces of two fibers. The light from an optical source propagates along the input optical fiber to the Fabry-Perot cavity that is formed by the input optical fiber and the reflecting optical fiber. A fraction of this incident light R_1 , approximately 4%, is reflected at the endface of the input optical fiber. The light transmitting out of the input optical fiber projects onto the fiber end face of the reflecting optical fiber. The reflected light R_2 from the reflecting optical fiber is partially re-coupled into the input optical fiber. EFPI fiber optic sensors can be found in a wide variety of sensing applications to measure various physical or chemical parameters such as displacement, temperature, strain, pressure, acoustic waves, and flow.

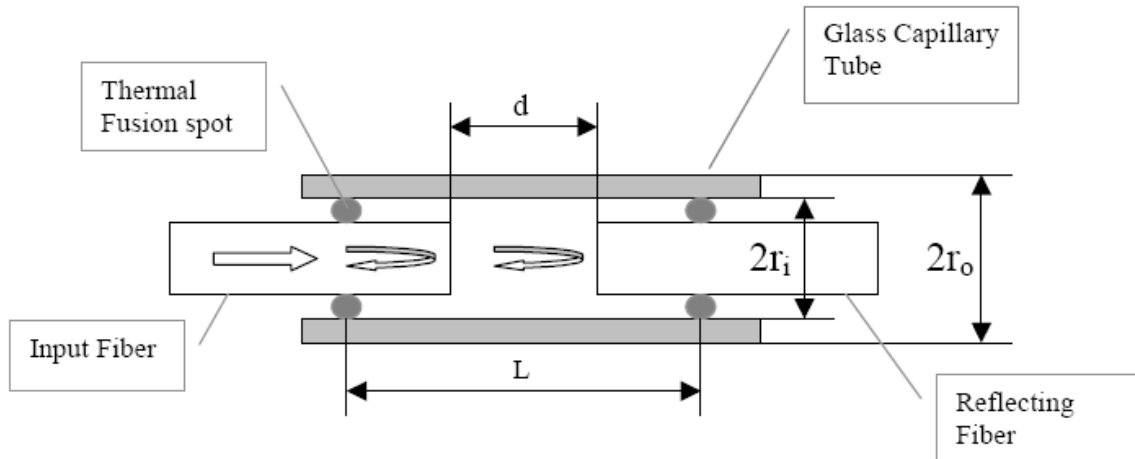


Figure 2.13. Illustration of an EFPI fiber optic sensor

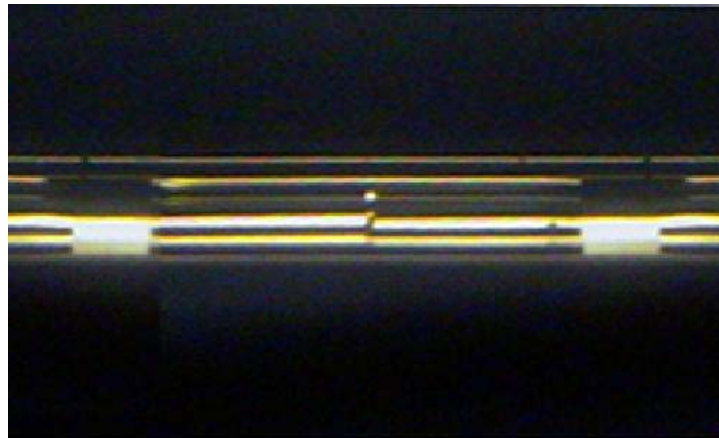


Figure 2.14. Picture of the EFPI sensor

2.3.2. IFPI Sensors

As shown in Figure 2.15, IFPIs have an interferometric cavity inside the fiber. For example, an IFPI sensor is fabricated by splicing a section of fiber with its two endfaces coated with reflective films to a regular fiber [add reference]. TiO_2 films with typical thickness of 40-80 nm are the common choice to form reflective coatings at the fiber endfaces with different reflectivity. The interferometric superposition of multiple reflections at the two fiber end-faces forms the output signal, which is a function of the fiber cavity length, the reflectance of the coating, and the refractive index of the fiber. The change of the cavity length or the refractive index of an IFPI sensor can be detected

by monitoring the interference output (either through the reflection or the transmission), thus, various physical or chemical parameters can be measured with a high resolution. Temperature measurement is the most successful application of the IFPI sensors. Because a long section of fiber can be used to make the Fabry-Perot cavity, the sensitivity of temperature measurement can be very high, smaller than 0.01°C as reported in the literature [add reference]. In principle, the IFPI sensor can also be used to measure parameters other than temperature such as pressure and strain. It is worth to point out that intrinsic Fabry-Perot interferometers have successfully found their position in the world of fiber optic communications [46-49]. Intrinsic Fabry-Perot interferometers with a very high finesse can be used as in-line tunable filters in WDM systems to select a wavelength channel. Those tunable filters have the advantages of a low insertion loss, a larger tunable spectrum range, and a high spectrum resolution.

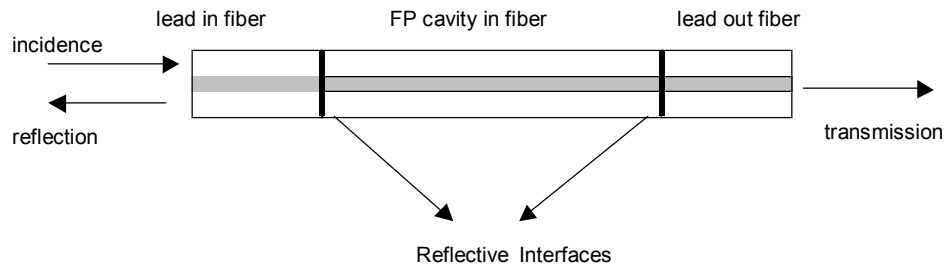


Figure 2.15. Illustration of the IFPI sensor

2.3.3. Fused Silica Properties and FPI Sensing Mechanism

Fused silica is an amorphous material made of almost pure silica, and is the major material of optical fibers and capillary tubing used to make Fabry-Perot interferometers. Therefore the optical and mechanical properties have to be explored to fully understand the sensing mechanism of such FPI sensors.

The thermal expansion of the fused silica can be characterized by linear thermal expansion coefficient (CTE) α_T , which is defined as

$$\alpha_T(T) = \frac{1}{L} \left. \frac{dL}{dT} \right|_T \quad (2.35)$$

The mean value of the linear CTE is found to be within the range of $0.5\text{-}0.6 \times 10^{-6} [\text{K}^{-1}]$.

More elaborate experiments reveal that CTE is not a constant under all temperatures.

The elastic properties of the fused silica can be described using elastic moduli that derived from the tensors of the material. Usually, the elastic properties of materials are expressed in terms of engineering moduli: Young's modulus E, shear modulus G, bulk modulus B and Poisson's ratio ν . The Young's modulus and Poisson's ratio are defined as

$$E = \frac{\text{Stress}}{\text{Strain}} = \frac{F/A}{\Delta L/L} \quad (2.36)$$

$$\nu = \frac{\text{Lateral Strain}}{\text{Longitudinal Strain}} = \frac{\epsilon_x}{\epsilon_z} \quad (2.37)$$

where F is the force applied, A is the area over which the force is applied, and ϵ is strain. The Young's modulus and Poisson's ratio are 95GPa and 0.08 respectively for fused silica.

The effect of temperature on refractive index depends upon two counteracting effects: the growth in specific volume caused by the increase in temperature, which decreases the refractive index; the increase in polarizability caused by the rising temperature, which increases the refractive index. The competition of these two effects determines the actual behavior of the refractive index with temperature [55]. If we define the change in polarizability with temperature as

$$\Phi = \frac{1}{P} \left(\frac{dP}{dT} \right) \quad (2.38)$$

and the CTE through the molar volume, M_v , as

$$CTE = \frac{1}{M_v} \left(\frac{dM_v}{dT} \right) \quad (2.39)$$

then

$$\frac{dn}{dT} = \frac{(n^2 - 1)(n^2 + 2)}{6n} (\Phi - CTE) \quad (2.40)$$

For fused silica, $\Phi > CTE$, and the refractive index increases with increasing temperature. The experimental value for commercial fused silica Corning 7940 [56] at $1.53\mu\text{m}$ is $dn/dT = 11.1 \times 10^{-6} [\text{K}^{-1}]$. However, more elaborate experiments reveal that refractive index CTE is not a constant under all temperatures.

A formalism similar to the preceding for the thermo-optic coefficient can be used to estimate the photoelastic constants of a material. The photoelastic constants are tensors whose components define the effect of individual strain or stress tensor terms. In the simplest case where longitudinal strain is applied, and the incident lightwave polarization direction is perpendicular to the strain, the refractive index can be expressed in the following term

$$\frac{dn}{d\sigma} = -\frac{n^3}{2E}[-\nu p_{11} + (1-\nu)p_{12}] \quad (2.41)$$

where σ is applied stress, p_{11} and p_{12} are elasto-optic coefficients. The calculated $dn/d\sigma = 3.8 \times 10^{-12} [\text{Pa}^{-1}]$.

The EFPI sensor pressure response is analyzed as follows: when a hydrostatic pressure is applied, the capillary tube will deform. As a consequence the cavity length will change, thus the applied pressure is measured. In actual application conditions, often the sensor is immersed in the pressurized environment. Thus both the longitudinal and the transverse directions should be considered in pressure response modeling. Assume the capillary tube has an outer radius of r_o and an inner radius of r_i . The sensor cavity length change ΔL resulted from the applied pressure p can be expressed as

$$\Delta L = \frac{L}{E}[\sigma_z - \nu(\sigma_r - \sigma_t)] \quad (2.42)$$

where L is the effective sensor gauge length defined as the distance between the two thermal bonding points. Three stresses are considered in the analysis: σ_r is the radial stress, σ_t is the tangential stress, and σ_z is the longitudinal stress generated by the applied pressure. These three stresses can be calculated by the following Equations

$$\sigma_r = \frac{r_o^2}{r_o^2 - r_i^2} \left(1 - \frac{r_i^2}{r_o^2}\right) p \quad (2.43)$$

$$\sigma_t = \frac{r_o^2}{r_o^2 - r_i^2} \left(1 + \frac{r_i^2}{r_o^2}\right) p \quad (2.44)$$

$$\sigma_z = \frac{r_o^2}{r_o^2 - r_i^2} p \quad (2.45)$$

Combining the above three Equations, the cavity length change of the sensor caused by the applied pressure can be calculated by

$$\Delta OPD(P) = \frac{Lr_0^2}{E(r_0^2 - r_i^2)}(1 - 2\nu)\Delta P \quad (2.46)$$

The EFPI sensor temperature response is analyzed as follows: assume that the effective sensor gauge length is L and the air-gap length is s , the CTE of the capillary tube and the fiber are α_h and α_f respectively. The temperature introduced cavity length change Δs can be calculated by

$$\Delta OPD(T) = [L\alpha_h - (L - s)\alpha_f]\Delta T = [\alpha_f s - (\alpha_f - \alpha_h)L]\Delta T \quad (2.47)$$

where ΔT is the temperature change.

The IFPI sensor pressure response and temperature response is the combination of the refractive index change and the fiber length change. The analytical solution is given in the following Equations

$$\begin{aligned} \Delta OPD(P) &= n(P)L(P) - n(P_0)L(P_0) \\ &= \int_{P_0}^P \frac{\partial n(P)}{\partial P} dP \times \int_{P_0}^P \frac{\partial L(P)}{\partial P} dP - n(P_0)L(P_0) \\ &\approx [L(P_0) \frac{\partial n(P)}{\partial P} + n(P_0) \frac{\partial L(P)}{\partial P}] \Delta P \end{aligned} \quad (2.48)$$

$$\begin{aligned} \Delta OPD(T) &= n(T)L(T) - n(T_0)L(T_0) \\ &= \int_{T_0}^T \frac{\partial n(T)}{\partial T} dT \times \int_{T_0}^T \frac{\partial L(T)}{\partial T} dT - n(T_0)L(T_0) \\ &\approx [L(T_0) \frac{\partial n(T)}{\partial T} + n(T_0) \frac{\partial L(T)}{\partial T}] \Delta T \end{aligned} \quad (2.49)$$

2.4. Study of Proposed Quasi-Distributed Fiber Sensor

The requirements for the proposed quasi-distributed fiber sensor are: high spatial resolution; high measurement resolution; large number of sensor multiplexed; high fringe visibility; easy, repeatable and low-cost fabrication.

2.4.1. Drawback of the EFPI sensor as quasi-distributed sensor

For the fiber optic interferometric sensor, both EFPI and IFPI sensors, the first and second requirements are intrinsically satisfied. The high spatial resolution is obtained by the small size of the Fabry-Perot sensing unit, which is usually on the scale of tens of

microns. The high measurement resolution of the fiber optic interferometric sensor is widely recognized by the research community. The reported high measurement resolution can be found easily in literature. But for the following three requirements, IFPI structure has a series of advantages over the EFPI structure.

Lets first study the EFPI based quasi-distributed fiber sensor. To maximize the number of sensor multiplexed on a single fiber, the insertion loss of the individual sensor has to be minimized. The insertion loss can be modeled using Figure 2.16. Light is transmitted from fiber A to fiber B. The gap in between A and B is the EFPI. The insertion loss α has two components. The first is the reflection loss caused by the two glass-air interfaces, which is denoted as α_R . α_R is derived using Fresnel Equations at normal incident situation

$$R = \left(\frac{n_{glass} - n_{air}}{n_{glass} + n_{air}} \right)^2 \quad (2.50)$$

Taking $n_{glass} = 1.458$ and $n_{air} = 1$, the calculated $R = 0.0347$. Since $R_1 = R_2$, $\alpha_R = 2R = 0.0694$.

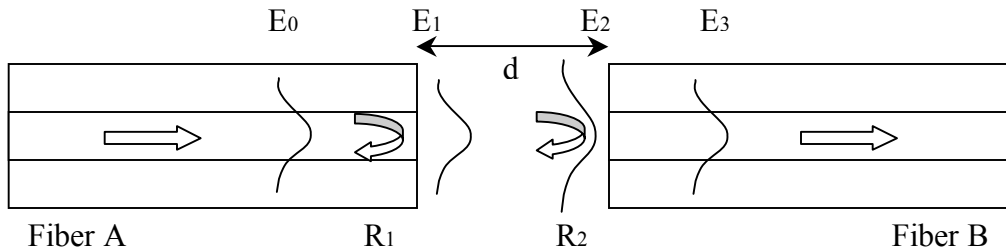


Figure 2.16. Transmission model of the EFPI sensor

The second term in the insertion loss is the coupling loss caused by the MFD mismatch, which is denoted as α_C . E_0 is the incident wave which has the unit power and MFD r_0 . When it is launched into the air, it is denoted as E_1 , which has decreased magnitude due to the reflection but the same MFD $r_1 = r_0$. The electric field E_1 will propagate in free-space for a distance d . According to Gaussian optics property, the MFD at the fiber B, $r_2(d)$ is given by the following Equation

$$r_2^2(d) = r_1^2 \left(1 + \frac{d^2}{z_0^2}\right) \quad (2.51)$$

where the distance z_0 , known as the Rayleigh range, defines the positions at which the beam size increases to $\sqrt{2}r_1$, and is given by

$$z_0 = \frac{\pi r_0^2 n_{air}}{\lambda} \quad (2.52)$$

The electric field E_2 with Gaussian beam radius r_2 will be coupled into fiber B. Single-mode fiber B only supports fundamental mode E_3 with the same radius as E_1 , $r_3 = r_1$. Thus the coupling loss α_c is given by

$$\alpha_c = 1 - \left(\frac{2r_1 r_2}{r_1^2 + r_2^2}\right)^2 \quad (2.53)$$

The insertion loss of a single-mode fiber based EFPI sensor versus Fabry-Perot air cavity length d is shown in Figure 2.18. The insertion loss increases sharply beyond $d = 20\mu m$. In the proposed spectrum multiplexing scheme, the cavity length is usually separated by tens of microns. Cavity length of $100\mu m$ is typical, which corresponds to over 5dB insertion loss. Insertion loss on this scale is often unbearable in a system.

The visibility of the interference spectrum is an important figure to judge the quality of the interferometer. For both single-mode fiber and multimode fiber based EFPIs, they all have decreased visibility when the Fabry-Perot cavity length increases. Figure 2.17 is used to explain this effect. When Fabry-Perot cavity length increases, the distance of the second reflection R_2 free-space Gaussian beam propagation is increased. Using Equation (2.51), but replace d with $2d$, the second reflection electric field profile before entering the launching fiber is obtained. Equation (2.53) is used to calculate the coupling coefficient, and the visibility is obtained using Equation (2.34). The visibility versus cavity length is shown in Figure 2.18. Large cavity corresponds to very poor interferometer performance.

In addition to high insertion loss and low visibility, the EFPI sensor fabrication cannot be made very repeatable and often costly. In the EFPI fabrication reported by Hai Xiao et al from Center for Photonics Technology, Virginia Tech, the multimode fiber based EFPI is always hard to fabricate. The requirement for parallels of the end-faces of the two

multimode fibers are very stringent. This would require long time tuning of one section of the fiber to achieve good visibility. The CO₂ laser welding also has the chance of damaging the core of the multimode fiber and the alignment of the fiber. In addition, the CO₂ laser, fabrication stage and the fusion splicer make the fabrication process costly. Due to these drawbacks, EFPI is not favored in the quasi-distributed fiber sensor.

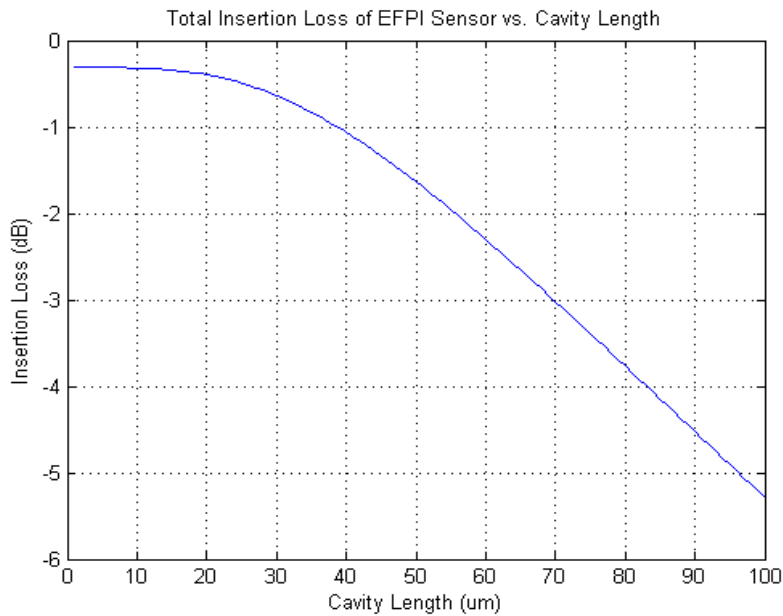


Figure 2.17. Insertion loss of an EFPI sensor

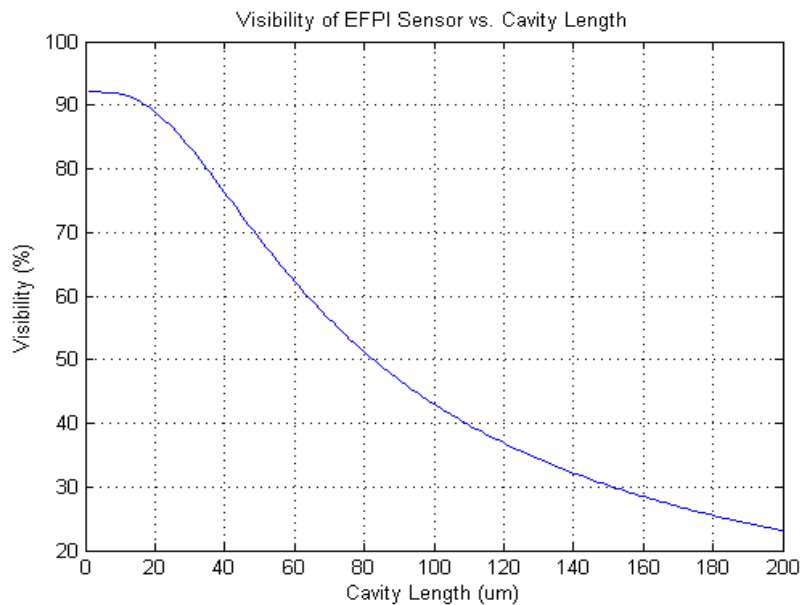


Figure 2.18. EFPI visibility versus cavity length

2.4.2. Proposed SxS IFPI sensor

The drawbacks from the EFPI sensor can be avoided by the proposed SxS IFPI sensor. The structure of the SxS IFPI sensor is shown in Figure 2.19 and Figure 2.20. A section of fiber is sandwiched in between two single-mode fibers to form a Fabry-Perot cavity. The fiber used as the Fabry-Perot cavity can be single-mode fibers, multimode fiber or fused silica rod. The section of the fiber is fusion spliced to the single-mode fiber. The selected fiber should have a core refractive index different from that of the single-mode fiber core. The reflections R_1 and R_2 of the Fabry-Perot cavity are generated by the Fresnel reflection on both fiber-fiber interfaces.

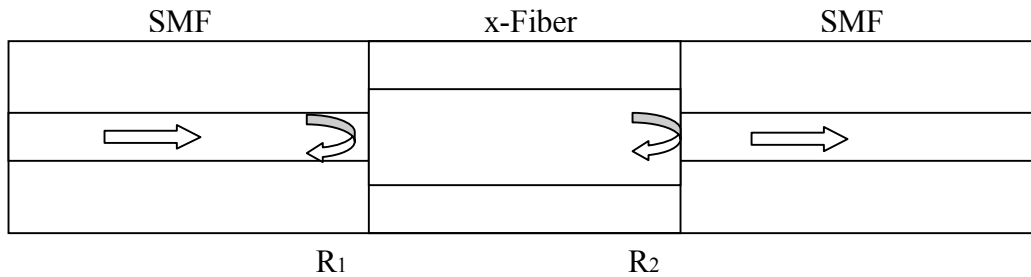


Figure 2.19. Model of SxS IFPI sensor

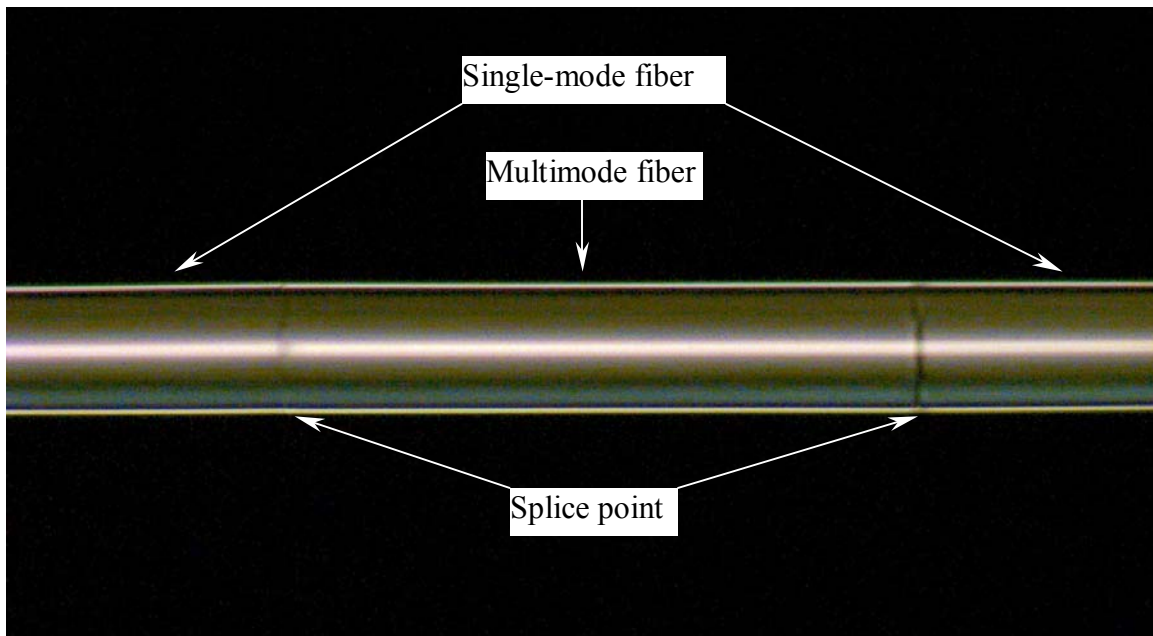


Figure 2.20. Photo of single-mode multimode single-mode fiber IFPI sensor

2.4.2.1.SMS IFPI sensor

When a section of GI or SI multimode fiber is used as the Fabry-Perot cavity, the IFPI sensor is denoted as SMS IFPI. The physics model of the sensor is shown in Figure 2.21.

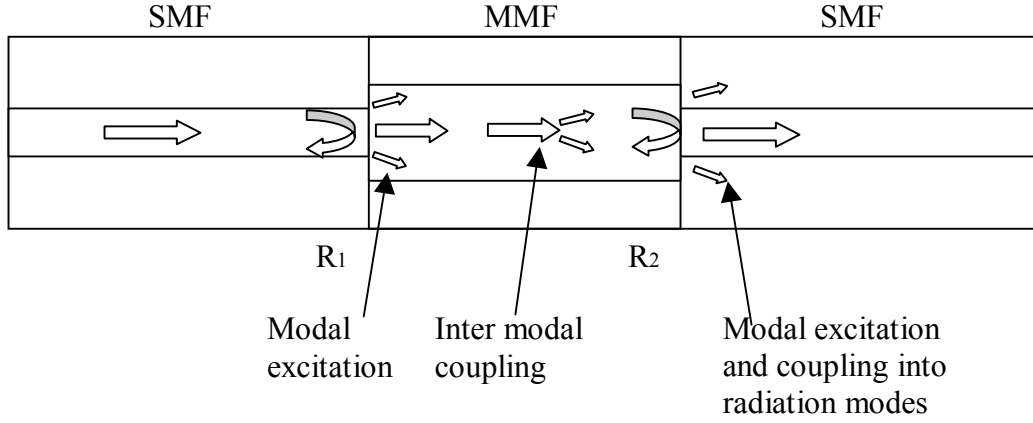


Figure 2.21. SMS IFPI insertion loss model

The insertion loss of the sensor is analyzed as follows. The light in the lead-in single-mode fiber is in LP_{01} mode. When it is launched into the Fabry-Perot cavity, it will excite multiple modes in the multimode fiber. Shown in Figure 2.8 is the simulation result at $1.55\mu m$ for single-mode fiber (Corning SMF28, $\Delta = 0.32\%$, $MFD = 4.2\mu m$) to GI multimode fiber (Corning Infinicor, $\Delta = 1\%$, $a = 25\mu m$) coupling. The largest coupling coefficient occurs at the single-mode fiber LP_{01} mode to multimode fiber LP_{01} mode coupling. The excited modes in the multimode fiber will propagate along the multimode fiber. During the propagation, the environmental disturbance and fiber manufacturing irregularities might facilitate the energy coupling from an excited mode into other modes, which mostly are the next higher mode and the next lower mode. When the light reaches the second boundary of the Fabry-Perot cavity, all the excited modes in the multimode fiber will couple into the fundamental mode in the single-mode fiber. The maximum coupling coefficient is between the multimode LP_{01} mode to single-mode LP_{01} mode coupling. The power that has not been transformed into single-mode fiber supported LP_{01} mode will couple into radiation modes in the single-mode fiber, and is therefore lost. Because the modal excitation of the fundamental mode to higher order modes or radiation modes is much less significant than the fundamental mode to fundamental mode

coupling, therefore only LP_{01} to LP_{01} coupling coefficient is used in the sensor insertion loss calculation. The insertion loss is shown in the following form

$$\alpha_i = \alpha_{SM} + \alpha_{MS} \quad (2.54)$$

where α_{SM} and α_{MS} are the losses induced by single-mode fiber to multimode fiber coupling and multimode fiber to single-mode fiber coupling respectively.

$$\alpha = 10 \lg(T) \quad (2.55)$$

where T is the power transmission coefficient, and is defined as

$$T = \left(\frac{2w_S w_M}{w_S^2 + w_M^2} \right)^2 \quad (2.56)$$

where w_S and w_M are the mode field radii of the SI single-mode fiber and GI multimode fiber respectively.

For a SMS IFPI sensor using single-mode fiber (Corning SMF28, $\Delta = 0.32\%$, MFD= $4.2\mu m$) and GI multimode fiber (Corning Infinicor, $\Delta = 1\%$, $a = 25\mu m$) operationed at $1.55\mu m$, the calculated power insertion loss for a SMS IFPI sensor is $\alpha_i = 1.1790dB$. If the GI multimode fiber (Spectran, $\Delta = 2\%$, $a = 31.25\mu m$) is used, the $\alpha_i = 0.8263dB$.

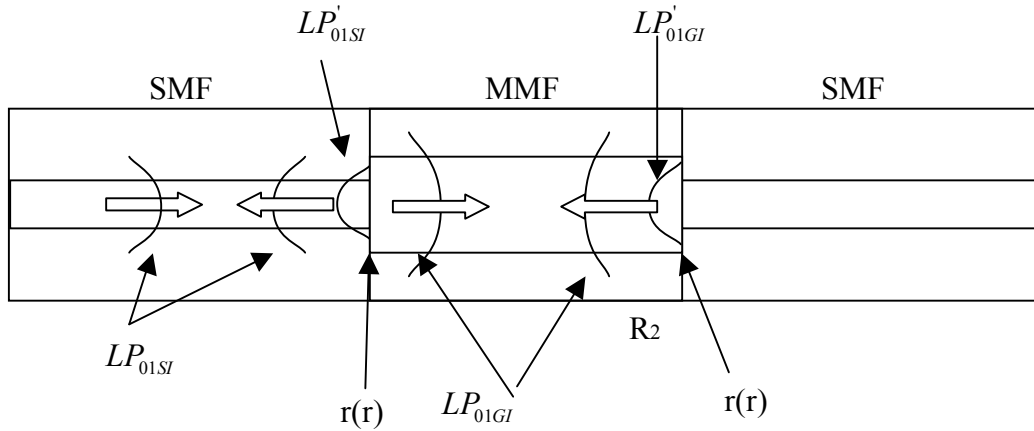


Figure 2.22. SMS IFPI reflection model

The signal is the consequences of the interference of the two reflections generated by the difference of the single-mode fiber core refractive index and the multimode fiber core refractive index. The reflection model is shown in Figure 2.23. The Fresnel reflection at

normal incidence is considered here. The expression is shown in Equation (2.50). Since in the core region of the GI multimode fiber, the refractive index is different with reference to position, the Fresnel reflection equation is adapted to the following form

$$r(r) = \frac{n_{GI}(r) - n_{SI}(r)}{n_{GI}(r) + n_{SI}(r)} \quad (2.57)$$

Thus in the rigorous analytical model, the electric field reflectivity is a function of the position. Considering the first reflection at the single-mode fiber to multimode fiber interface, the LP_{01SI} mode is reflected at the boundary. The reflected electric field LP'_{01SI} resembles the LP_{01SI} mode but has distortions introduced by the position varied $r(r)$

$$LP'_{01SI}(r, \varphi) = r(r)LP_{01SI}(r, \varphi) \quad (2.58)$$

Because of the distortion, some of the energy will be lost during the LP'_{01SI} to LP_{01SI} mode coupling. The coupling loss α_C is calculated using the Gaussian approximation. The loss term for the first reflection is shown in Equation (2.59)

$$\alpha_1 = \alpha_C \quad (2.59)$$

Now let's consider the second reflection at the multimode fiber to single-mode fiber interface. The reflected electric field LP'_{01GI} resembles the LP_{01GI} mode but has distortions introduced by the position varied $r(r)$. The loss term α_2 comprises of single-mode to multimode coupling loss α_{SM} , LP'_{01GI} to LP_{01GI} coupling loss α_C and multimode to single-mode coupling loss α_{MS}

$$\alpha_2 = \alpha_{SM} + \alpha_C + \alpha_{MS} \quad (2.60)$$

The LP'_{01SI} and LP'_{01GI} electric field distribution for a SMS IFPI using GI multimode fiber (Corning Infinicor, $\Delta = 1\%$, $a = 25\mu m$) is shown in Figure 2.23.

The simulated results is shown in Table 2.2. The simulation is based on the single-mode fiber (Corning SMF28, $\Delta = 0.32\%$, $MFD = 4.2\mu m$) system. The GI multimode fibers used are Corning Infinicor ($\Delta = 1\%$, $a = 25\mu m$) and Spectran 625 ($\Delta = 2\%$, $a = 31.25\mu m$). The operation wavelength is $1.55\mu m$. The calculated power reflectivity for both boundaries and the sensor visibility are listed in Table 2.2.

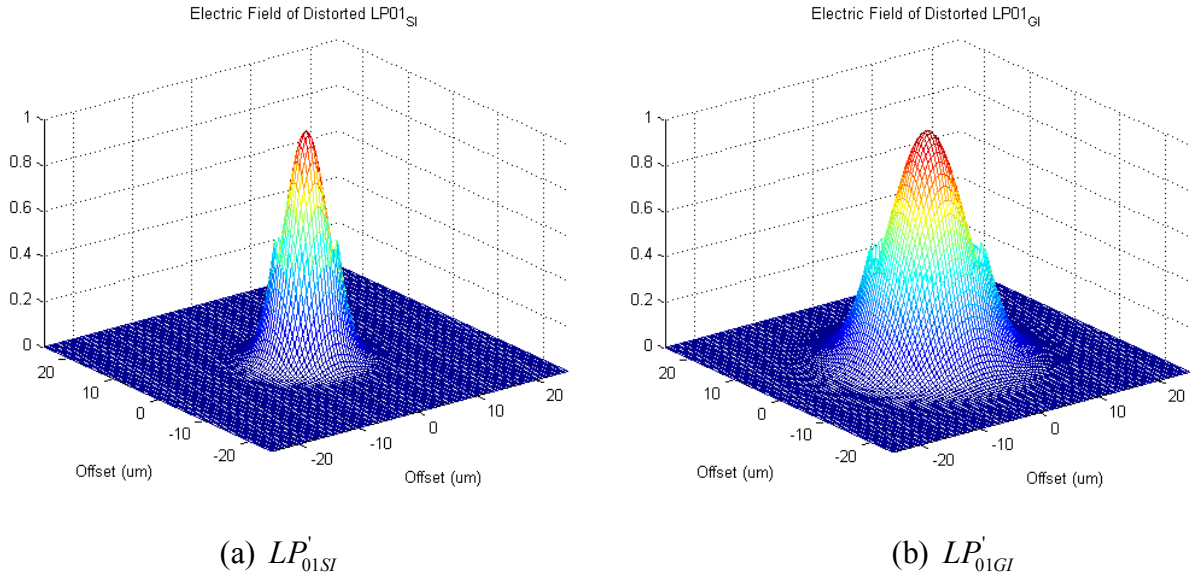


Figure 2.23. Electric field of distorted reflection of fundamental mode in SI single-mode fiber and GI multimode fiber

	Corning Infinicor (50/125)	Spectran GIF625 (52.5/125)
α_1	-0.1657dB	-0.0305dB
α_2	-1.2900dB	-0.9373dB
r1	-49.3704dB	-41.4116dB
r2	-50.4947dB	-42.3184dB
Visibility	97.2%	98.3%

Table 2.3. Reflection simulation for different GI multimode fibers

Compared with the EFPI sensor structure, the main difference in the SMS IFPI is that the light is bounded in the multimode fiber, which is a waveguide structure. This waveguide structure in the Fabry-Perot cavity would prevent the beam size from diverging, minimizing the coupling loss on the multimode fiber to single-mode fiber boundary, and therefore largely minimizes the insertion loss of the sensor.

Because of the small coupling loss, the power of the first and second reflection are comparable, resulting in a high interference fringe visibility. In the quasi-distributed SMS

IFPI sensor system, the transmitted power is scattered by each sensor cascaded on the fiber line. The sensor far from the signal interrogator will receive less power than the sensor near to the interrogator. The power received by the n th sensor is

$$P_n = P_0 \left(1 - \sum_{i=1}^{n-1} \alpha_i\right) \quad (2.61)$$

where P_0 is the initial power launched into the sensor system, α_i is the insertion loss of the i th sensor, P_n is the power launched into the n th sensor.

Suppose the reflectivities of the SM and MS interface are R_{SM} and R_{MS} respectively.

Then the power reflected by the SM and MS interfaces for the n th sensor are $P_n R_{SM}$ and $P_n R_{MS}$. The interference peak and valley would have the power

$$\begin{cases} I_{\max} = P_n R_{SM} + P_n R_{MS} \\ I_{\min} = P_n R_{SM} - P_n R_{MS} \end{cases} \quad (2.62)$$

Thus the visibility is

$$V = \frac{I_{\max} - I_{\min}}{I_{\max} + I_{\min}} = \frac{R_{MS}}{R_{SM}} = \frac{R_{SM} - \alpha_{SM}}{R_{SM}} = 1 - \frac{\alpha_{SM}}{R_{SM}} \quad (2.63)$$

Since α_{SM} is normally less than 0.5dB, the visibility of the SMS IFPI sensor is larger than 0.9.

The fabrication requires only a fiber fusion splicer, therefore it is low-cost. The fabrication process requires only splicing of single-mode fibers to multimode fiber, and this is done automatically by the fusion splicer. A sensor could be made in 5 minutes, so the process is very simple. Because the fiber splicing process is automated, the splicing condition is very repeatable, thus the sensor characteristics are very repeatable too. The detailed sensor fabrication process is outlined in Chapter 4.

2.4.2.2.SSS IFPI sensor

The insertion loss of SMS IFPI is caused by the difference between the fundamental mode mode field radius of the SI single-mode fiber and the GI multimode fiber. If the fiber used as the Fabry-Perot cavity has the same mode field radius as the SI single-mode fiber, then the insertion loss of such sensor can be largely minimized. And therefore increasing the visibility of the sensor as well. The ideal single-mode fiber for SSS IFPI would have the same mode field radius at the operation wavelength with the rest of the

single-mode fiber, which means that the two fibers should have the same V , although their core radius and Δ are not necessarily the same. However, in order to generate reflection at the two interfaces, the single-mode fiber should have a core reflective index slightly different from the light carrying single-mode fiber. The refractive index profile of the ideal single-mode fiber for the SSS IFPI application with reference to the light carrying single-mode fiber is shown in Figure 2.24. Thus the only insertion loss term is caused by the reflection on both interfaces. The reflection on both interfaces will couple into the transmitting single-mode fiber with no loss. No power is lost in the sensor system. SSS IFPI potentially can have maximum number of sensors multiplexed and highest interference signal visibility. The sensor fabrication process is the same as the SMS IFPI, except the strict mode field diameter requirement of the single-mode fiber might not be met in the commercially available product.

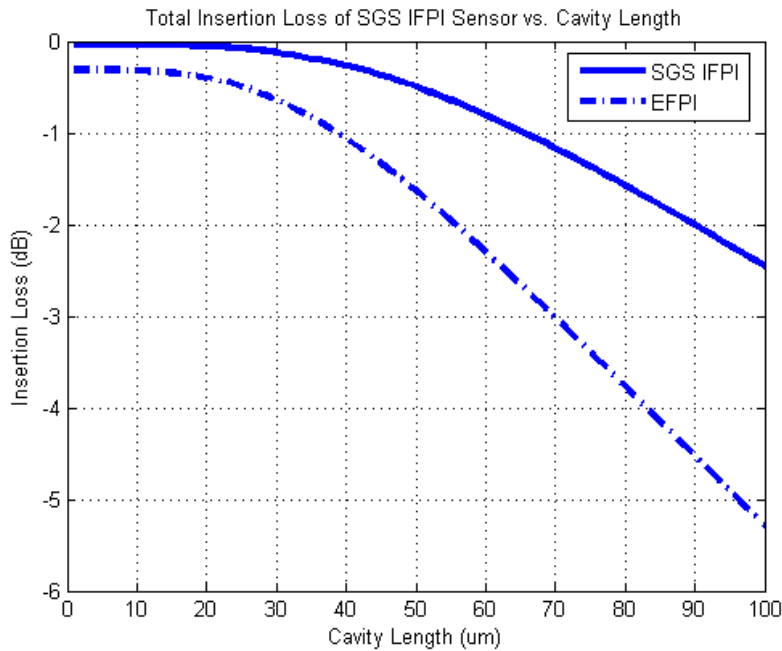


Figure 2.24. SGS IFPI insertion loss

The case considered here is the two single-mode fibers have the same $\Delta = 0.32\%$, $MFD = 4.2\mu m$, but $\Delta n = 0.68\%$. The calculated insertion loss is 0.0001dB, and the reflection generated from a single interface is -49.3704dB. Such insertion loss would enable large number of SSS IFPI sensors being multiplexed on a single fiber.

2.4.2.3.SGS IFPI sensor

For comparison purpose, we study here the SGS IFPI. In this type of IFPI, a section of glass rod is used as the Fabry-Perot cavity. The glass rod is not a waveguide structure, thus the insertion loss of SGS IFPI is expected to be larger than SMS or SSS IFPIs. But compared with EFPI, there are two major differences that makes the insertion loss significantly smaller: the reflection of each interface in the SGS is one order smaller than the EFPI, resulting in smaller reflection induced insertion loss; the divergence angle of the Gaussian beam in the glass rod is much smaller than it is in the air, resulting in smaller Gaussian beam waist, therefore less coupling loss. The insertion loss versus Fabry-Perot cavity length for the SGS IFPI and EFPI is shown in Figure 2.25. The advantage of SGS IFPI over EFPI is apparent.

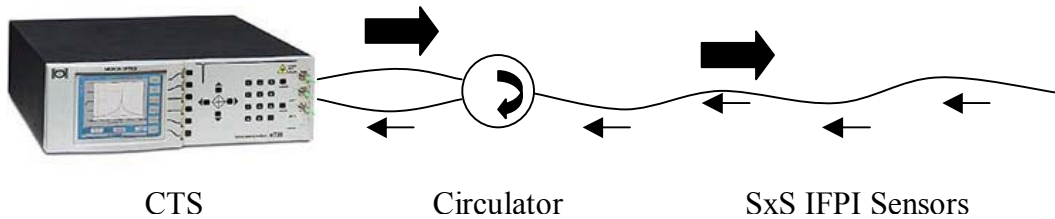


Figure 2.25. System diagram of the quasi-distributed SxS IFPI sensor system

Chapter 3. Principles of Quasi-Distributed Fiber Sensor Signal Processing

In the quasi-distributed fiber sensing applications, the locations where the measurands are of interest are separated by certain distances. The SxS IFPI sensors with different cavity lengths are arranged on a single-mode fiber so that they can be mounted at these locations with cabling. Thus the location information is encoded in the SxS IFPI sensor cavity length. The function of the sensor signal processing unit is to obtain the SxS IFPI sensors' cavity lengths in real-time, and relate them to the measurand reading at different locations.

The Micron Optics si720 system is used as the sensor interrogator. The specification of the si720 system is given in Table 3.1. It provides a large dynamic range, high wavelength accuracy and fine wavelength resolution over the entire C-band. Spectrum data at 20,000 wavelength points can be obtained in one sweep. The si720 has GPIB and T1 Ethernet ports to connect to the computer. The scheme of the sensor system is shown in Figure 3.1. The sensor line can be connected to the si720 system via a 3-dB coupler or a circulator. For the 3-dB coupler interrogation method, the reflection from the unused port should be frustrated. The 3-dB coupler method will reduce the dynamic range by 6dB due to its additional loss to the circulator method.

The whitelight algorithm [56] is improved by Bing Qi et al to precisely calculate the sensor cavity length given a single sensor's optical spectrum. The detailed discussion on the whitelight algorithm is included in section 3.1. For multiplexed sensors, the optical spectrum is contributed by all sensors. The whitelight algorithm cannot be implemented directly. Band-pass filters centered at each sensor's initial cavity length are used to filter out the Fourier spectrum of the individual sensor on the Fourier transformed spectrum of the overall optical spectrum. The Fourier spectrum of each sensor is then inverse Fourier transformed to obtain the single sensor optical spectrum. The whitelight algorithm is then used for each sensor's optical spectrum to calculate the precise cavity length of the sensor. The flowchart of the multiplexed sensor demodulation algorithm is shown in

Figure 3.2. The detailed discussion on the multiplexed sensor signal demodulation is given in section 3.2.

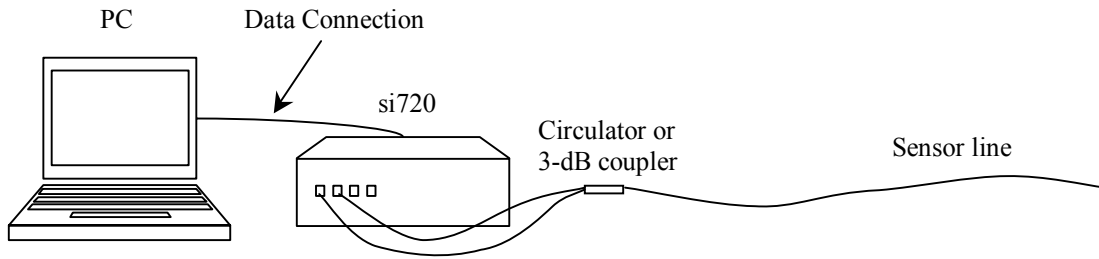


Figure 3.1. Sensor interrogation system scheme

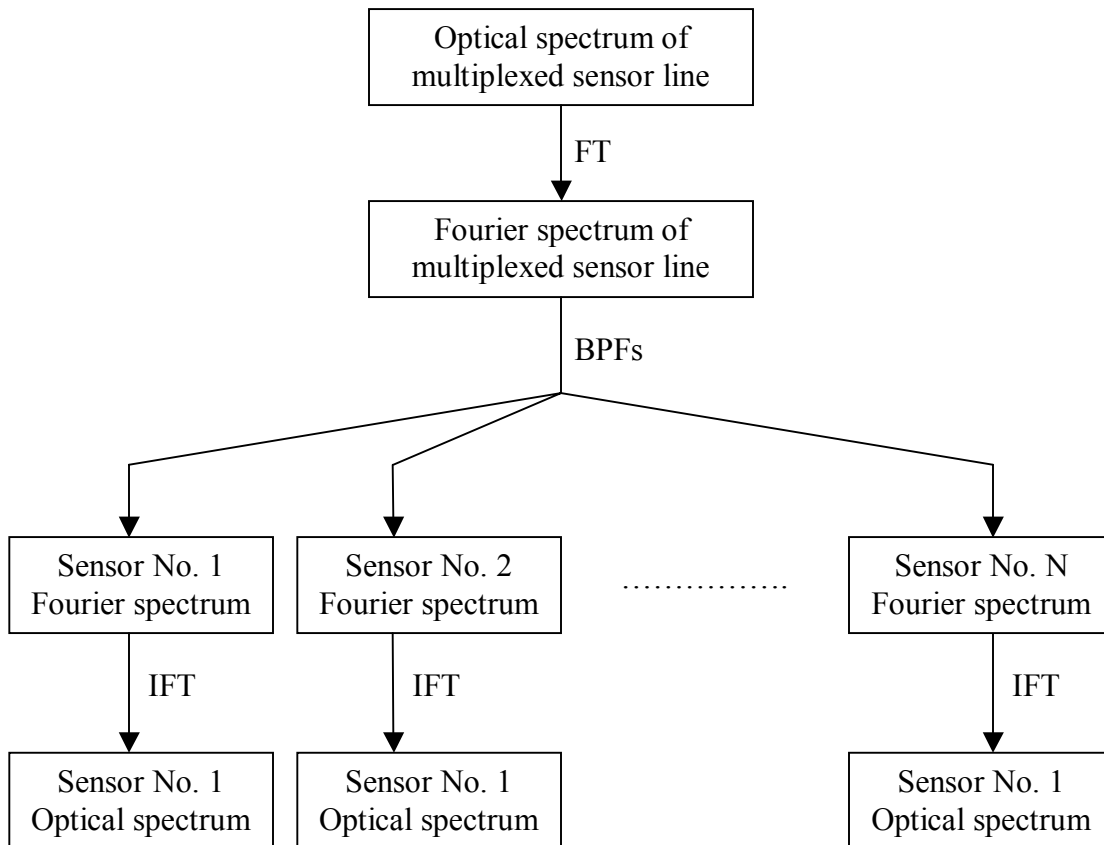


Figure 3.2. Flowchart of multiplexed sensor demodulation algorithm

3.1. Whitelight Algorithm

Whitelight or low coherence interferometry is a technique, which dates back to 1913 and was reapplied to optical fiber sensing in 1983. Instead of using a highly coherent light source, a broadband light source is used. Although the power-detection approach can be

used, to fully exploit the advantages of the whitelight system, spectrometer-based detection systems are more popular.

Laser Type	Fiber Laser
Laser Class	1
Laser Output Power (CW)	min>0.25mW, max<2mW
Laser Wavelength	1510-1580nm
Laser Line Width	4pm
Num of Optical Channels	2
Wavelength Range	1520-1570nm
Wavelength Accuracy	1pm
Wavelength Resolution	0.25pm
Dynamic Range	>60dB
Scan Frequency	0.5 or 5Hz
Optical Connector	FC/APC
Operation Temperature	0-50°C

Table 3.1. si720 system specification

The whitelight interferometric fiber optic sensor system inherits most of the advantages from the conventional interferometer, such as immunity to the light source power drift and changing of transmission losses, high resolution, large dynamic range, etc. On the other hand, by using the spectral detection technology, an absolute measurement of the distance between the interfering interfaces can be realized. Numerous applications of whitelight interferometric sensor systems have been reported, covering a wide range from single point measurement to distributed sensor systems [57-61].

Assume the broadband light source has a spectral intensity distribution $I_s(\lambda)$, the two-beam interference signal is then given by:

$$I(\lambda) = I_s(\lambda)[1 + \gamma \cos(\frac{2\pi L}{\lambda})] \quad (3.1)$$

where the factor γ is the visibility of the interference fringes, and L represents the optical length of the cavity. The ideal value of γ will be $\gamma=1$, and it may decrease because of the polarization mismatch and amplitude difference between the two reflections. The normalized interference output is expressed as

$$I_n(\lambda) = 1 + \gamma \cos(\frac{2\pi L}{\lambda}) \quad (3.2)$$

Based on the normalized interference spectrum, the sensor cavity length can be obtained. The existing algorithms for the cavity length calculation either possess high resolution with limited measurement range (such as peak-tracing method), or large dynamic measurement range with limited resolution (such as the two-point method). The improved whitelight algorithm reported by Bing Qi et al could achieve both high resolution and large dynamic range simultaneously, and therefore it is adopted in this work.

3.1.1. Peak-Tracing Method

Based on the measured spectrum fringes patterns, the value of the sensor cavity length can be obtained through tracing a special point in the interference fringes (such as one peak point). In this method, the wavelength λ_m of a peak point in the interference spectrum satisfies the relationship:

$$\frac{2\pi L}{\lambda_m} = m2\pi \quad (3.3)$$

where the spectral order m is a non-negative integer. Equation (3.3) can be rewritten into the following form

$$L = m\lambda_m \quad (3.4)$$

To calculate the sensor cavity length L from a special peak wavelength λ_m , the interference order m must be known first. For the selected peak, the identification of the interference order m is difficult so that the unambiguous operating range of the sensor cavity length is limited in only half of the wavelength range. The resolution of this peak tracing method is mainly dependent on the resolution of the spectrometer as shown in Equation (3.3). The relative uncertainty of the measurement can be described as

$$\left| \frac{\Delta L}{L} \right| \cong \left| \frac{\Delta \lambda}{\lambda} \right| \quad (3.5)$$

where $\Delta \lambda$ is the measurement resolution of the wavelength, determined by the measurement resolution of the spectrometer.

3.1.2. Two-Point Method

To increase the measurement range of the sensor cavity length values, two special points instead of one point in the interference spectrum need to be used for the absolute measurement. Suppose λ_1 and λ_2 ($\lambda_1 > \lambda_2$) are the wavelengths of the two adjacent peak

points in the interference spectrum. Their interference orders are m and $m+1$. From Equation (3.3),

$$\begin{cases} \frac{2\pi L}{\lambda_1} = m2\pi \\ \frac{2\pi L}{\lambda_2} = (m+1)2\pi \end{cases} \quad (3.6)$$

The sensor cavity length can be determined,

$$L = \frac{\lambda_1 \lambda_2}{\lambda_2 - \lambda_1} \quad (3.7)$$

The wide dynamic measurement range can then be obtained by using two special wavelengths, as long as the two such special wavelengths exist (two peaks or two valleys) in the spectrum pattern. The sensor cavity length can be calculated using Equation (3.7). In this case, the relative uncertainty induced by the spectrometer is

$$\left| \frac{\Delta L}{L} \right| \cong \left| \frac{\lambda_2}{\lambda_2 - \lambda_1} \right| \left| \frac{\Delta \lambda}{\lambda} \right| \quad (3.8)$$

With the central wavelength of the light source at 1550nm, for the operating range of sensor cavity length (500-1000 μ m), this factor is about 388—646. Thus, this method has lower resolution in a large dynamic measurement range compared to the peak tracing method.

Combining the advantages of the two methods described above, the novel data processing algorithm has been developed can achieve both high resolution and large dynamic range. The basic idea of this method is to use two peak points in the interference spectrum to get a coarse sensor cavity length value first (Large dynamic range is then achieved); this length is then used to determine the order number m_c of a special peak point in the interference fringes. Then, an accurate m_a value will be recovered from the coarse m_c . From Equation (3.4), the accurate cavity length can be calculated based on the accurate m_a and the peak wavelength location in the spectrum (High resolution is thus achieved).

The algorithm used to recover the accurate m_a is discussed as follows:

In Equation (3.4), for a given peak the m is a constant value. For adjacent peaks, the difference between the interference orders is 1. For example, if m for one peak is 12, then

for the adjacent peaks the interference order will be 13, 14, 15...and 11, 10, 9....By calibration, the value of m for a special peak m_0 can be acquired accurately and stored in computer. When the coarse m_c value for any peak has been acquired, the accurate m_a will be obtained from m_0 by adding the integer part in the difference between the coarse m_c and m_0 . The whole process of demodulating sensor cavity length from the interference spectrum can then be separated into two sub-processes: the calibrating sub-process and the measuring sub-process.

With the whitelight interferometer system in a stable condition, the sensor cavity length is set to a known value L_0 . The m_0 of a peak in the interference spectrum can be calculated accurately from the L_0 and the wavelength λ_0 . This is the calibrating sub-process.

With known m_0 , the measuring sub-process can be carried out as follows: first, use the two peak points in the interference spectrum to acquire a coarse value of L_c using Equation (3.7); second, select a peak point near the center of the interference spectrum, then use the wavelength of this peak and the coarse L_c from previous step to calculate a coarse m_c ; third, the accurate m_a can be calculated from m_c and the stored m_0 using Equation (3.9); fourth, the accurate sensor cavity length can be calculated from the accurate m_a and the wavelength of the peak with Equation (3.4).

$$m_a = m_0 + INT(m_c - m_0 + 0.5) \quad (3.9)$$

where the function $INT(\dots)$ means to take the integral part.

Advanced computer software has been developed to demodulate the sensor cavity length values from the interference spectral patterns, based on the novel data processing algorithm presented previously. The software program is implemented in the Matlab environment. The program first starts with the si720 system initialization, and then the computer acquires the optical spectrum from the si720 system via a GPIB interface. The optical spectrum is a 1×20000 array covering 1520 to 1570nm with 2.5pm wavelength spacing. The desired peak positions in the interference spectrum are selected to demodulate the sensor cavity length. The valley positions in the interference spectrum can also be located with a similar method. The technique for locating peaks is described as follows. The first step is to find the coarse locations of the peaks by a smart

comparison algorithm. The basic idea of this algorithm is to find all the local maximum points in a special range in the interference spectrum. The size of the searching range, which is defined as the window size of the peak searching, must be large enough to eliminate the influence of the noise. To avoid missing some peaks, the window size must be smaller than the space between adjacent peaks. After the coarse positions of the peaks are found, a mass-centroid algorithm is applied to find the accurate positions of the peaks. The basic idea of the mass-centroid algorithm is shown in Figure 3.3. If the function $Y(X)$ is symmetric around its peak position, then the peak position coincides with the X coordinate of the centroid of $Y(X)$. The peak position X_0 can be calculated from

$$X_0 = \frac{\int_{-\infty}^{+\infty} xf(x)dx}{\int_{-\infty}^{+\infty} f(x)dx} \quad (3.10)$$

Since around the peak point, the spectrum is a symmetrical function of the wave number $k = 2\pi/\lambda$, the spectrum $Y(\lambda)$ needs to be expressed in terms of the wave number $Y(k)$ first. With $Y(k)$, the accurate peak positions can be calculated from the coarse peak positions with

$$\left\{ \begin{array}{l} k_i = \frac{1}{\lambda_i} \\ k_m^p = \frac{\sum_{i=-\infty}^{i=+\infty} y_i k_i (k_i - k_{i-1})}{\sum_{i=-\infty}^{i=+\infty} y_i (k_i - k_{i-1})} \\ \lambda_m^p = \frac{1}{k_m^p} \end{array} \right. \quad (3.11)$$

Once the coarse sensor cavity length is calculated using two peak positions, and then the coarse m_c value for a selected peak near the center wavelength is determined. Using the calibrated m_0 value stored in the computer, the accurate m_a value is obtained and then is used to calculate the accurate sensor cavity length value. Finally, using the calibration curve, the temperature is extracted from the accurate sensor cavity value. The flowchart of the whitelight software is given in Figure 3.4.

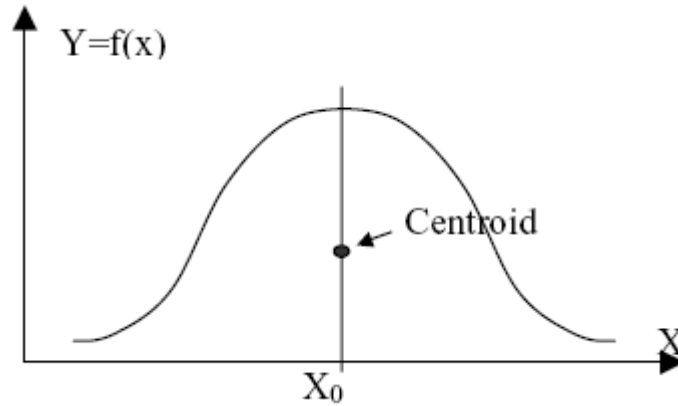


Figure 3.3. Mass-centroid method for peaks locating in the spectrum

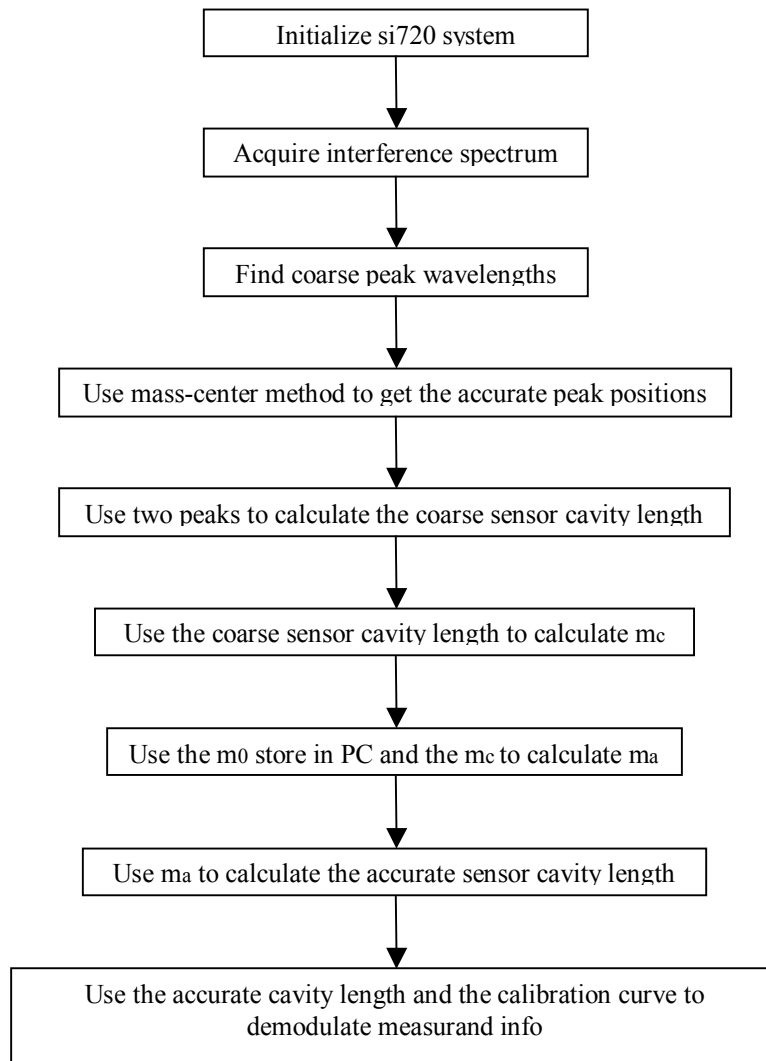


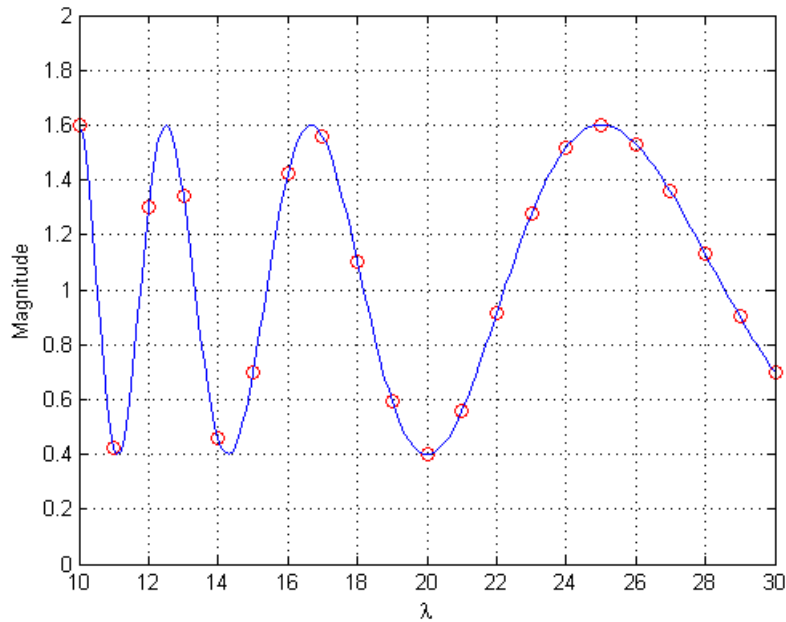
Figure 3.4. Flowchart of the whitelight algorithm

3.2. Multiplexed Sensor Demodulation

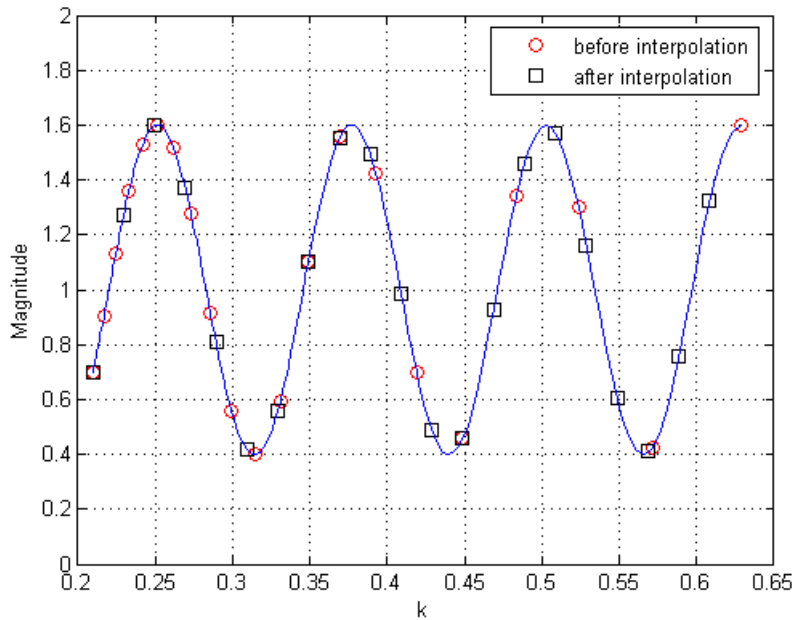
For the SxS IFPI quasi-distributed sensing applications, the sensors with different cavity lengths are multiplexed on a single-mode fiber. The optical spectrum is the sum of the optical spectrum of the individual sensors. The band-pass filters centered at each sensor's cavity length are used to obtain the individual sensor's optical spectrum. And whitelight algorithm is used on each sensor's optical spectrum to precisely calculate the cavity length. The flowchart of the process is illustrated in Figure 3.2.

The spectrum data obtained from si720 system is with reference to wavelength λ with even wavelength separation $\Delta\lambda = 2.5 \text{ pm}$. Such spectrum cannot be directly used in Fourier transform because the Fourier transformed frequency is inverse proportional to λ . In order to do that, the spectrum should be expressed in terms of wave number $k = 2\pi / \lambda$. Equation (3.1) can be rewritten as

$$I(k) = I_s(k)[1 + \gamma \cos kL] \quad (3.12)$$



(a) Original spectrum data in wavelength representation



(b) Spectrum in wave number representation and interpolation

Figure 3.5. Spectrum mapping and interpolation

The $I(k)$ transformed directly from $I(\lambda)$ is not evenly spaced in k domain, and has to be linearly interpolated. The interpolated optical spectrum $I_{ipl}(k)$ has even k spacing and could be used in Fourier transform. The $I(\lambda)$ to $I(k)$ mapping and $I(k)$ interpolation $I_{ipl}(k)$ process is illustrated in Figure 3.5. The optical spectrum of 8 multiplexed SMS IFPI sensors and its Fourier transform spectrum is shown in Figure 3.6. The band-pass filters (BPF) are used to obtain each sensor's optical spectrum, and there are several requirements. First, the pass-band bandwidth should be very narrow and the distinction ratio of the BPF should be large. In the Fourier transformed domain, for the sensor of interest, the other sensors' Fourier transform spectrum is considered noise and will introduce cross-talk. The system noise within the pass-band will also be picked up. Thus the narrow bandwidth and high distinct ratio BPF would reduce the noise caused by neighboring sensors and system noise. Second, during measurement the cavity length of the sensor will change. Its Fourier transform peak position will also change as a result. The BPF should have wide enough bandwidth to accommodate the whole measurement range. Third, the BPF should induce no distortion to the pass-band signal. The output

spectrum $I_{out}(k)$ of the BPF $H(e^{jk})$ exhibits some wave number shift relative to the input optical spectrum $I_{in}(k)$ caused by the nonzero phase response $\theta(k) = \arg\{H(e^{jk})\}$ of the BPF. If the input Fabry-Perot interference spectrum is a sinusoidal of length L_0 , the output is also a sinusoidal optical spectrum with the same length but lagging in phase by $\theta(L_0)$ radians. It is shown in the following equation

$$I_{out}(k) = A \left| H(e^{jL_0}) \right| \cos \left[L_0 \left(k + \frac{\theta(L_0)}{L_0} \right) + \phi \right] \quad (3.13)$$

indicating a wave number shift, more commonly known as phase shift at $L = L_0$ given by

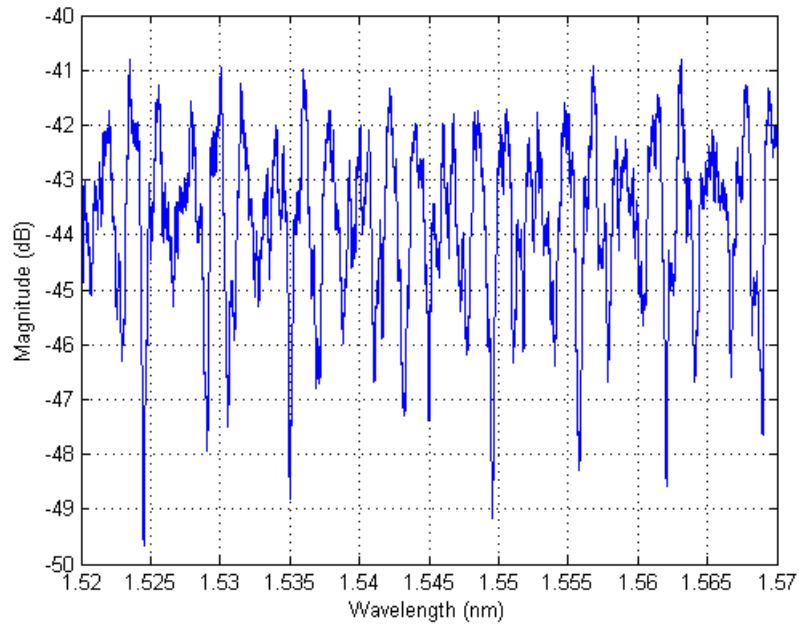
$$k_p(L_0) = -\frac{\theta(L_0)}{L_0} \quad (3.14)$$

When the input signal contains many sinusoidal components that are not harmonically related, each component will go through different phase delays when processed by the BPF, and the output signal, in general, will not look like the input signal. The group shift is defined by

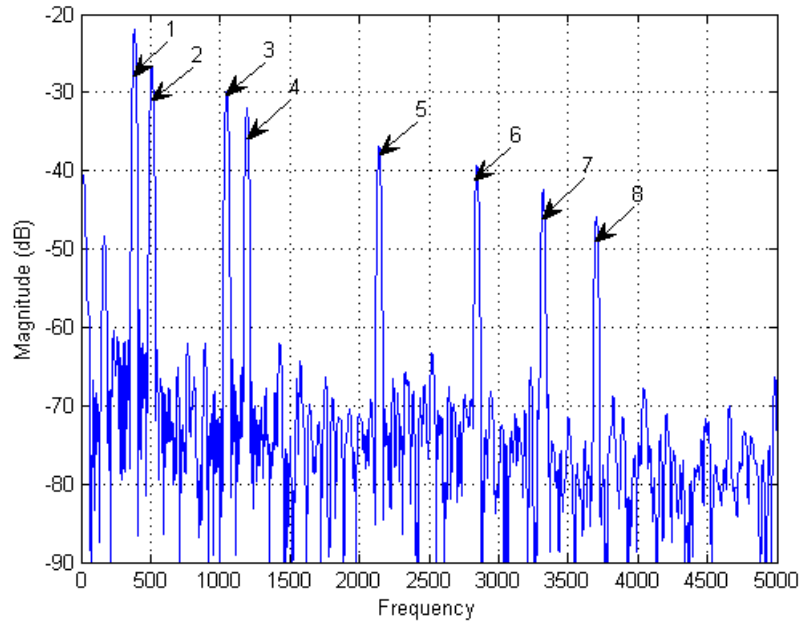
$$\tau_g(L) = -\frac{d\theta(L)}{dL} \quad (3.15)$$

The group shift is a measure of the linearity of the phase function as a function of the length and is the wave number shift between the input optical spectrum and the filtered optical spectrum. The waveform of the output shows distortion when the group shift of the BPF is not constant over the bandwidth of the input optical spectrum. The digital filters can be divided into two categories depending on their impulse response. If it has finite impulse response, it is FIR filter. It is IIR filter if it has infinite impulse response. In order to cancel the phase distortion caused by the filter, the filter should have linear-phase transfer function. It is always possible to design an FIR filter with an exact linear-phase response, while it is nearly impossible to design a linear-phase response IIR filter. Thus in the sensor signal demultiplexing, FIR BPF is preferred.

An FIR filter of order M takes the following general form



(a) Optical spectrum of 8 multiplexed SMS IFPI sensors



(b) Fourier transformed spectrum of the 8 multiplexed SMS IFPI sensors

Figure 3.6. Optical spectrum and Fourier spectrum of the multiplexed SMS IFPI sensors

$$H(z) = b_0 + b_1 z^{-1} + \dots + b_M z^{-M} = \sum_{n=0}^M b_n z^{-n} \quad (3.16)$$

The FIR filters can be designed based on fixed window functions. The window functions are used to improve the filtering quality. Three commonly used tapered windows of length $2M+1$ are listed below

$$\text{Hann : } w[n] = \frac{1}{2} \left[1 + \cos\left(\frac{2\pi n}{2M+1}\right) \right], \quad -M \leq n \leq M \quad (3.17)$$

$$\text{Hamming : } w[n] = 0.54 + 0.46 \cos\left(\frac{2\pi n}{2M+1}\right), \quad -M \leq n \leq M \quad (3.18)$$

$$\begin{aligned} \text{Blackman: } w[n] = & 0.42 + 0.5 \cos\left(\frac{2\pi n}{2M+1}\right) \\ & + 0.08 \cos\left(\frac{4\pi n}{2M+1}\right), \quad -M \leq n \leq M \end{aligned} \quad (3.19)$$

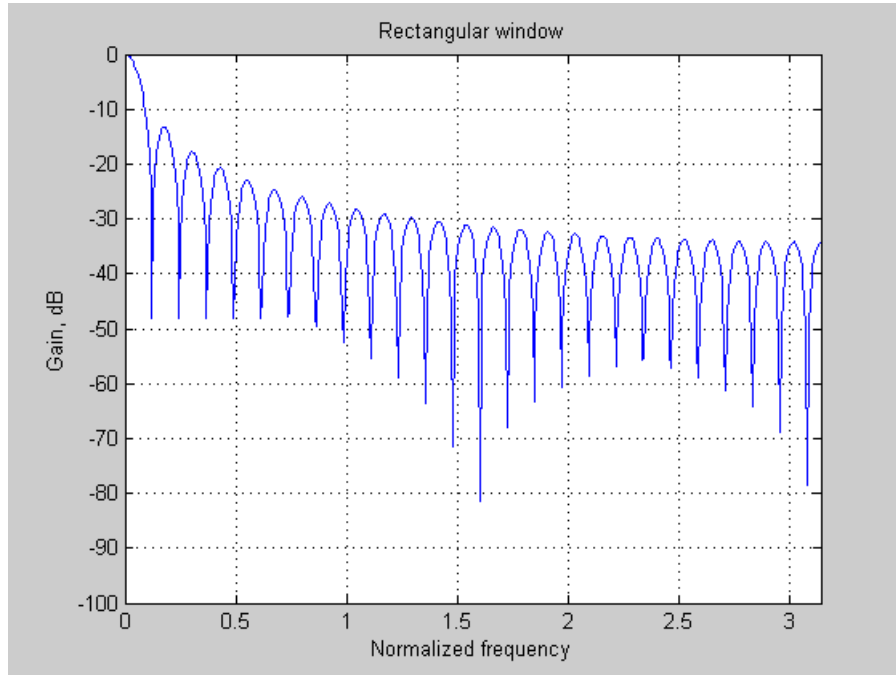
A plot of the magnitude of the Fourier transform of each of the above windows in the dB scale is shown in Figure 3.7. As can be seen from these plots, the magnitude spectrum of each window is characterized by a large main lobe centered at $\omega = 0$ followed by a series of sidelobes with decreasing amplitudes. Two parameters that somewhat predict the performance of a window in FIR filter design are its main lobe width and the relative sidelobe level. The main lobe width Δ_{ML} is the distance between the nearest zero crossings on both sides of the main lobe, and the relative sidelobe level A_{sl} is the difference in dB between the amplitudes of the largest sidelobe and the main lobe. Table 3.2 summarizes the essential properties of the above window functions. The Hamming window has large stopband attenuation and small transition bandwidth and is used in the sensor demultiplexing.

Type of window	Main lobe width	Relative sidelobe level	Minimum stopband attenuation	Transition bandwidth $\Delta\omega$
Rectangular	$4\pi/(2M+1)$	13.3dB	20.9dB	$0.92\pi/M$
Hann	$8\pi/(2M+1)$	31.5dB	43.9dB	$3.11\pi/M$
Hamming	$8\pi/(2M+1)$	42.7dB	54.5dB	$3.32\pi/M$
Blackman	$12\pi/(2M+1)$	58.1dB	75.3dB	$5.56\pi/M$

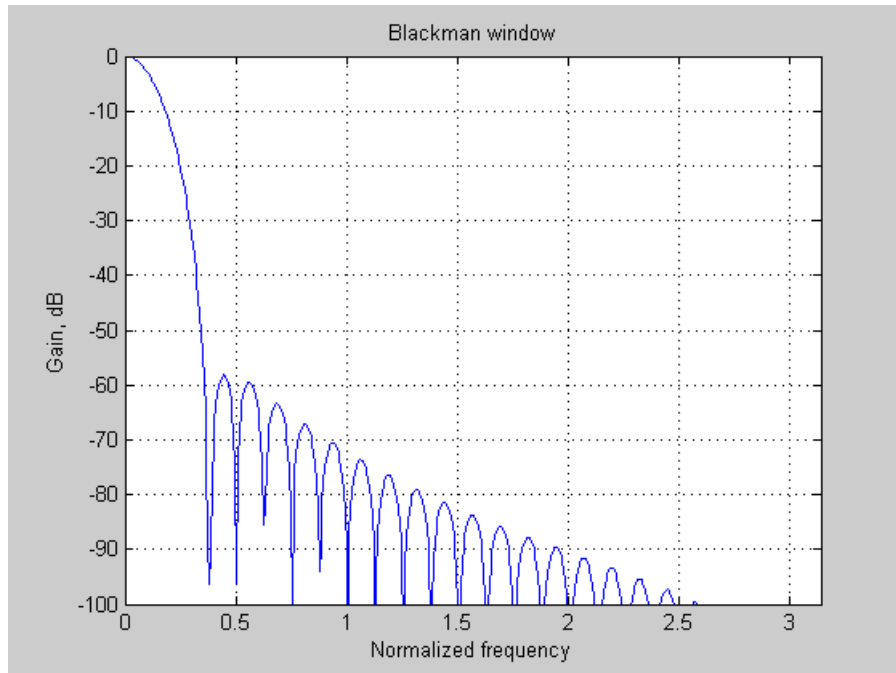
Table 3.2. Properties of some fixed window functions

The BPF is designed using the Filter Design and Analysis Toolbox (FDAtool) in Matlab. The toolbox interface is shown in Figure 3.8. For a given window function, the FIR BPF

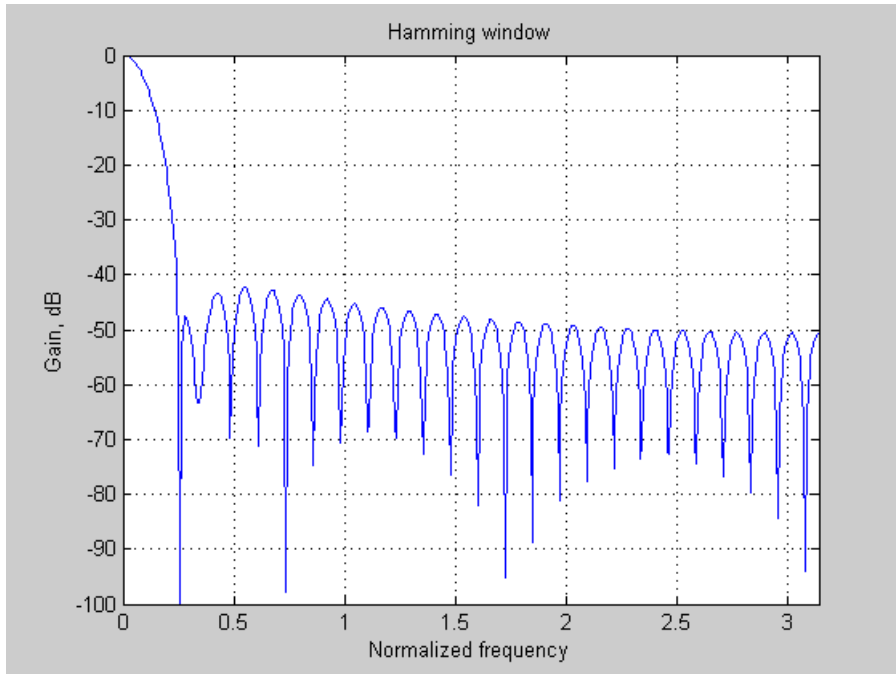
bandwidth is related to the order of the FIR. Larger FIR order leads to narrower bandwidth. The FIR order against Hamming window based BPF magnitude spectrum is shown in Figure 3.9.



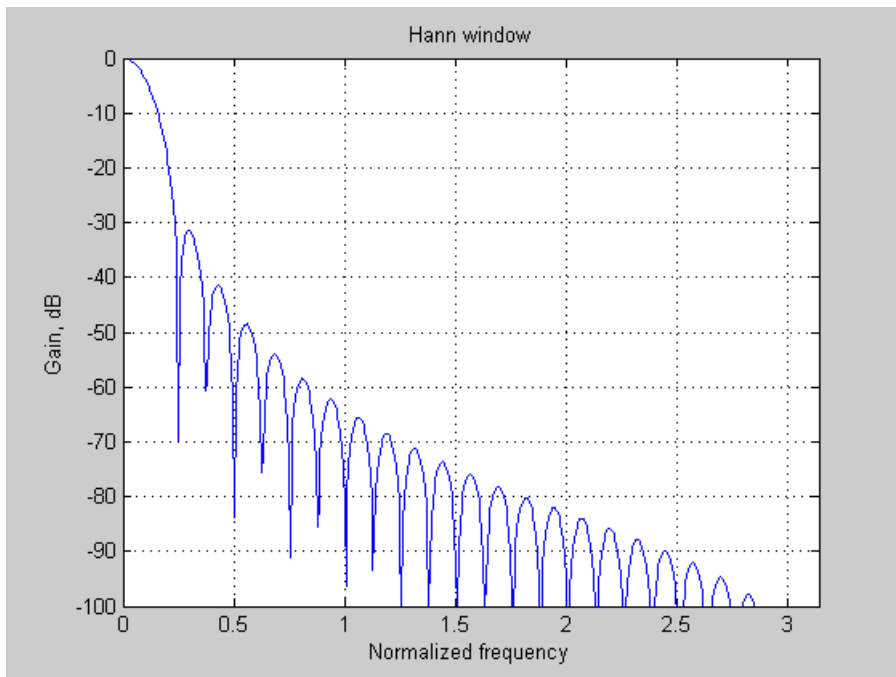
(a) Rectangular window



(b) Blackman window



(c) Hamming window



(d) Hann window

Figure 3.7. Fourier spectrum of different window functions

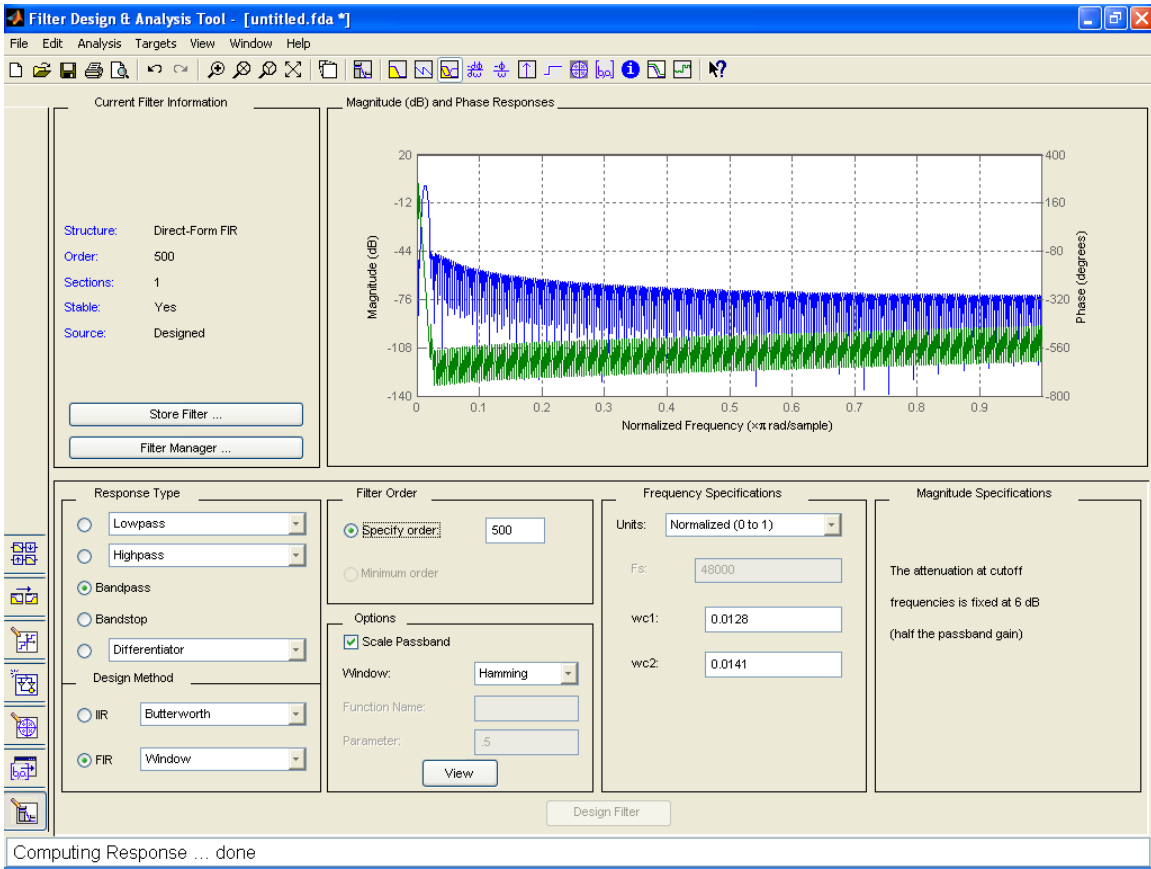
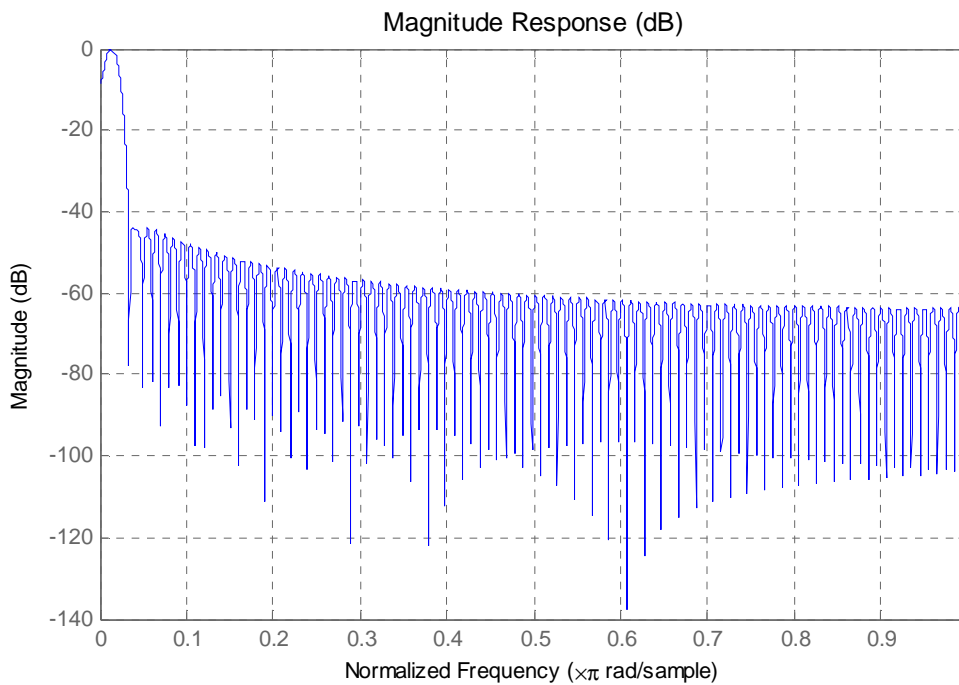
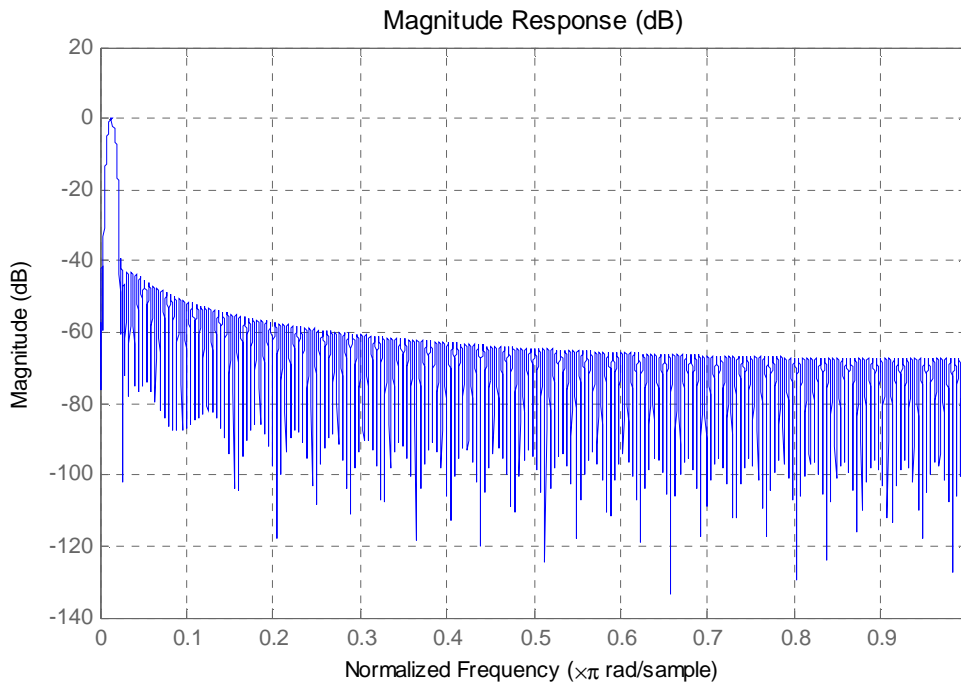


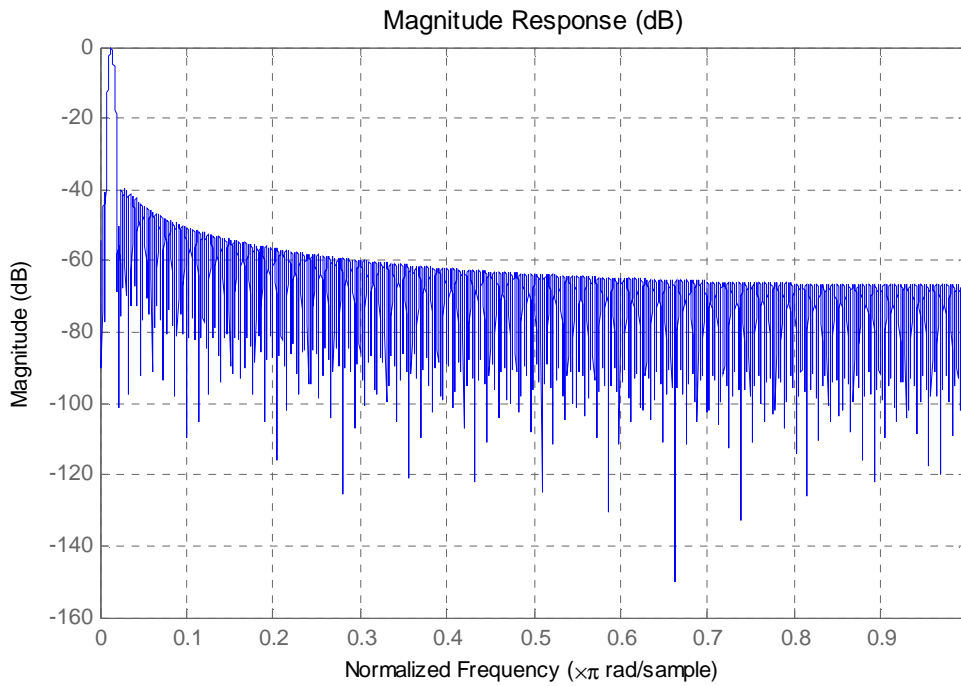
Figure 3.8. FDA tool in Matlab



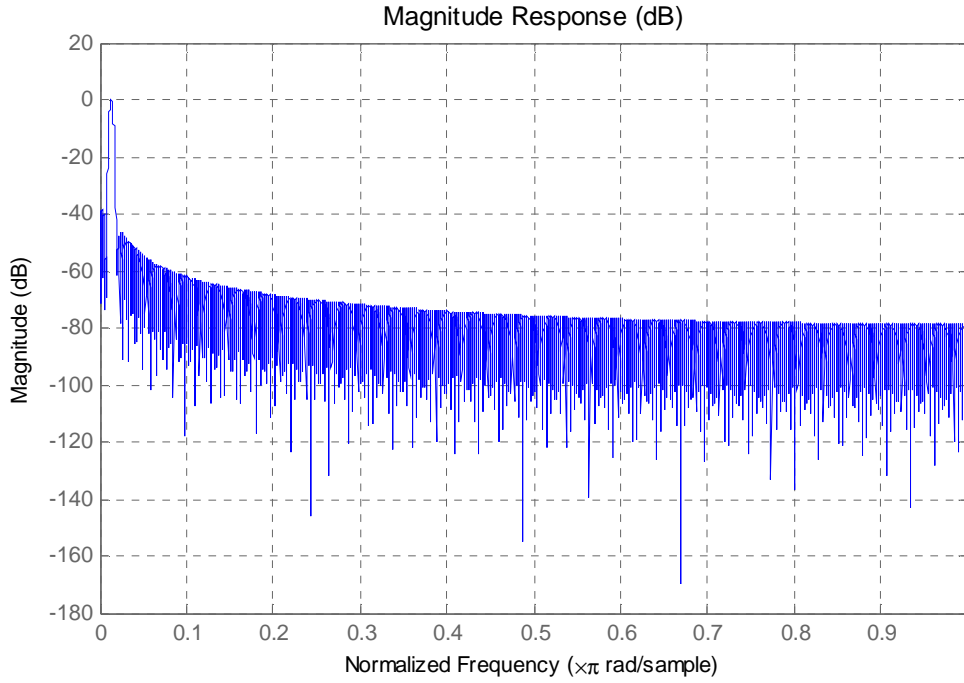
(a) FIR based on Hamming window with order 200



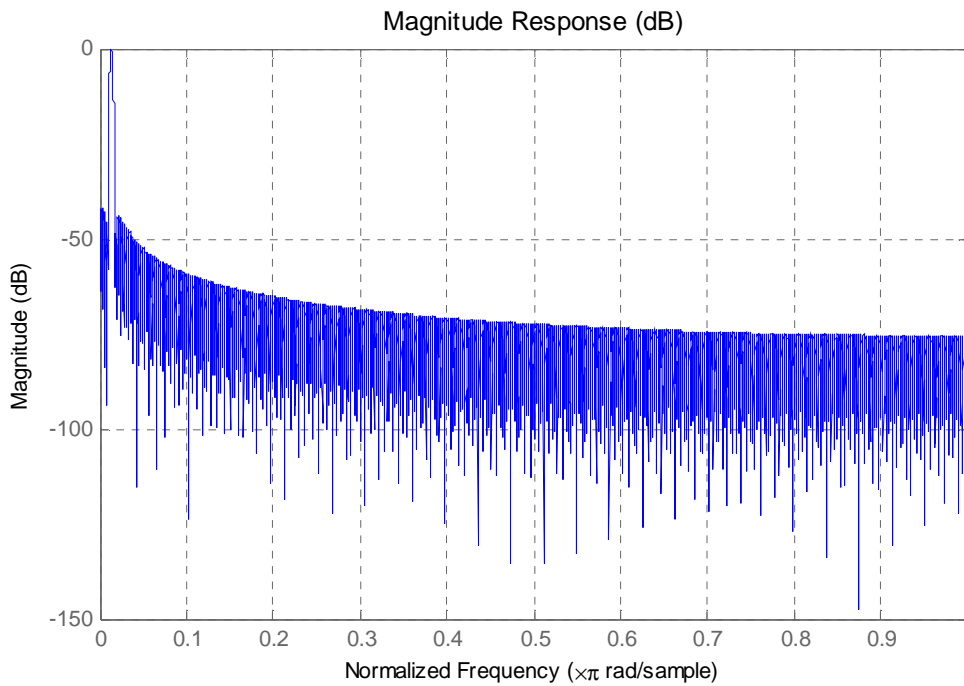
(b) FIR based on Hamming window with order 400



(c) FIR based on Hamming window with order 600



(d) FIR based on Hamming window with order 800



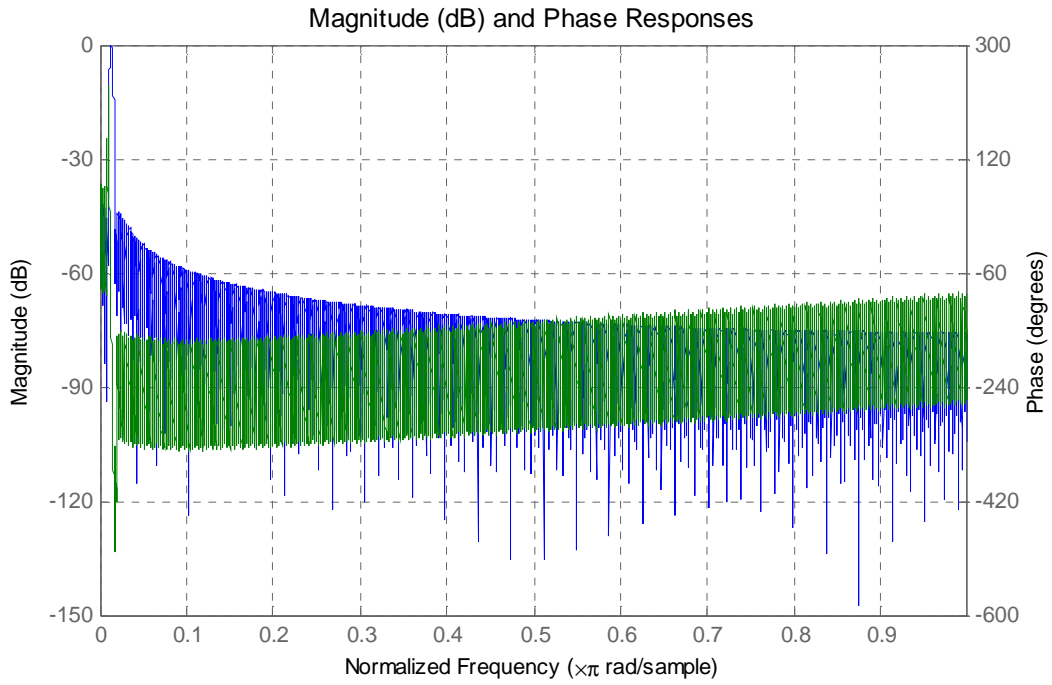
(e) FIR based on Hamming window with order 1000

Figure 3.9. FIR filter magnitude spectrum

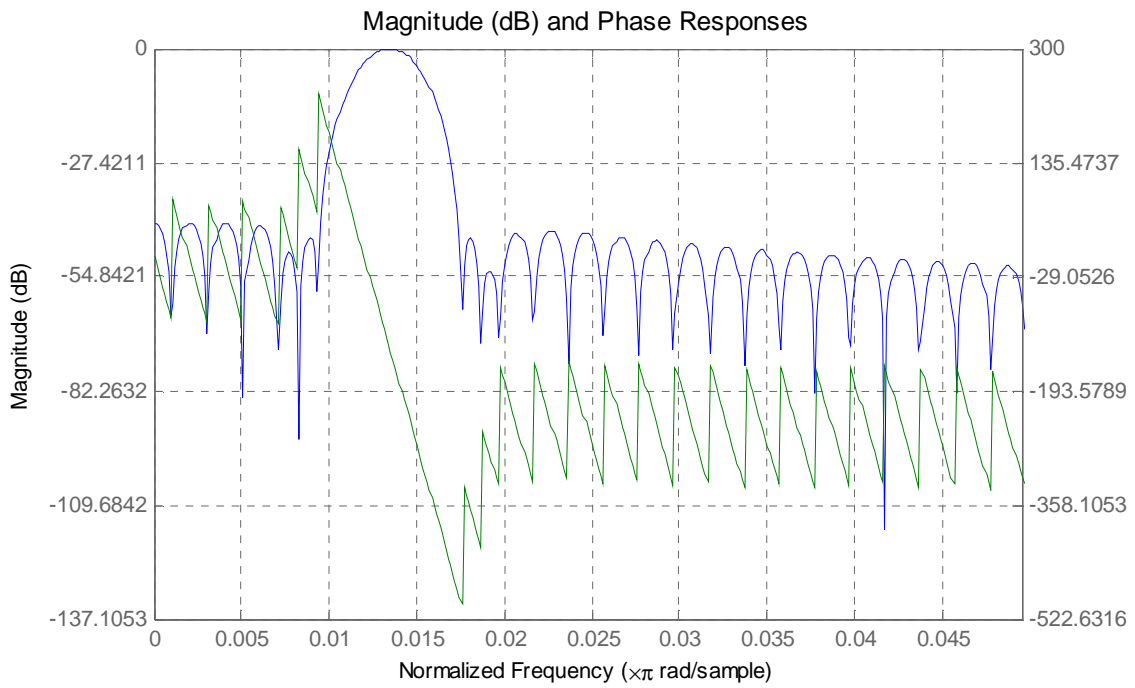
An example showing how to design a BPF to extract an individual sensor optical spectrum is given as follows. The multiplexed sensor optical spectrum is given in Figure

3.6(a), and we want to obtain the sensor with its Fourier transform peak labeled No. 5 in Figure 3.6(b). The BPF's 6dB pass-band boundary in terms of normalized frequency is first calculated using Figure 3.6(b) and found to be 0.0131 to 0.0135. The normalized frequency is obtained by dividing the absolute frequency of the boundary point by the maximum frequency of the Fourier transform. From the SMS IFPI temperature and strain measurement we know that the dynamic range is within $\pm 1\%$ of the IFPI's initial cavity length. Thus the BPF's pass-band boundary is chosen to be 0.0129 and 0.0137 respectively. The FIR BPF based on Hamming window is first designed using the FDA toolbox. In order to achieve best filtering result, the order of the BPF is chosen to be 1000. The magnitude and phase spectrum of the BPF are shown in Figure 3.10. The designed BPF is then exported to Matlab as an object, and can be called in the Matlab program. The interpolated optical spectrum $I_{ipl}(k)$ is then filtered by the designed BPF. The filtering of the original sensor Fourier spectrum is shown in Figure 3.11. The filtered optical spectrum has a k-shift in k domain. This is induced by the non-zero linear phase spectrum of the FIR BPF filter. This shift has to be corrected because otherwise it would induce an error in the cavity length calculation. The amount of k-shift induced by the filter is $k = N/2$, where N is the order of the BPF. To compensate that, the filtered spectrum has to be shifted $k = -N/2$, which is -500 in this case. The filtered optical spectrum and the shift compensated optical spectrum is compared with the original No. 5 SMS IFPI optical spectrum in Figure 3.12. The filtered spectrum has same periodicity and same peak positions but improved signal-to-noise ratio with the original spectrum. By applying whitelight algorithm to this optical spectrum, the sensor cavity length can be calculated.

In the multiplexing applications, a series of BPFs are designed corresponding to the SxS IFPI sensors cascaded on an SMF. During each si720 scan, the multiplexed optical spectrum is filtered by each BPF to obtain individual sensor's optical spectrum. The whitelight algorithm is then used to calculate the sensors' cavity lengths based on the obtained optical spectrum of the sensors.

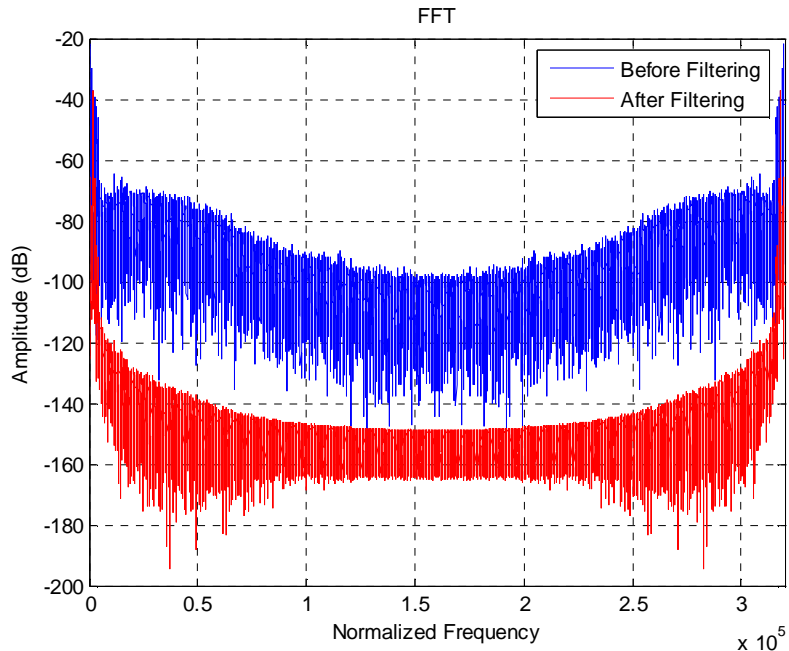


(a) 1000 order FIR BPF

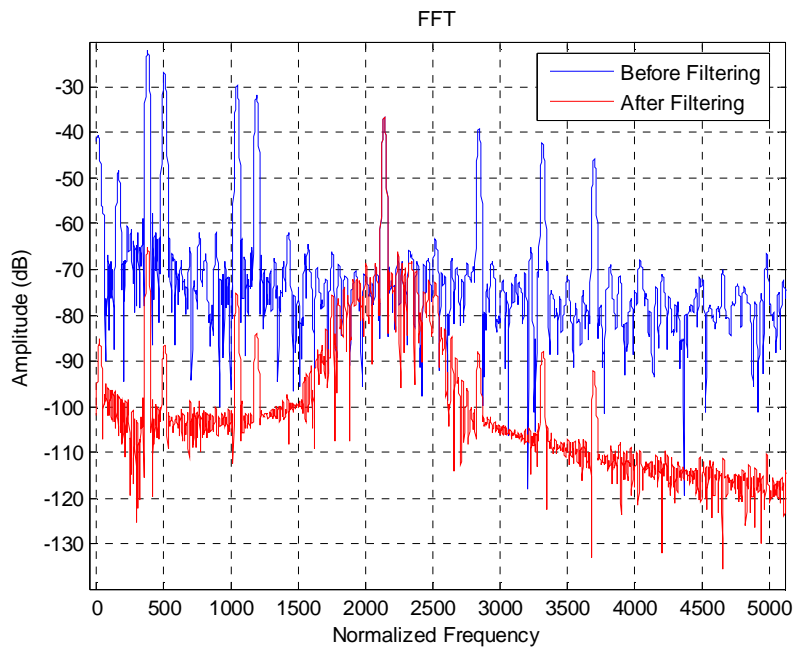


(b) close up of this filter

Figure 3.10. The designed FIR BPF filter

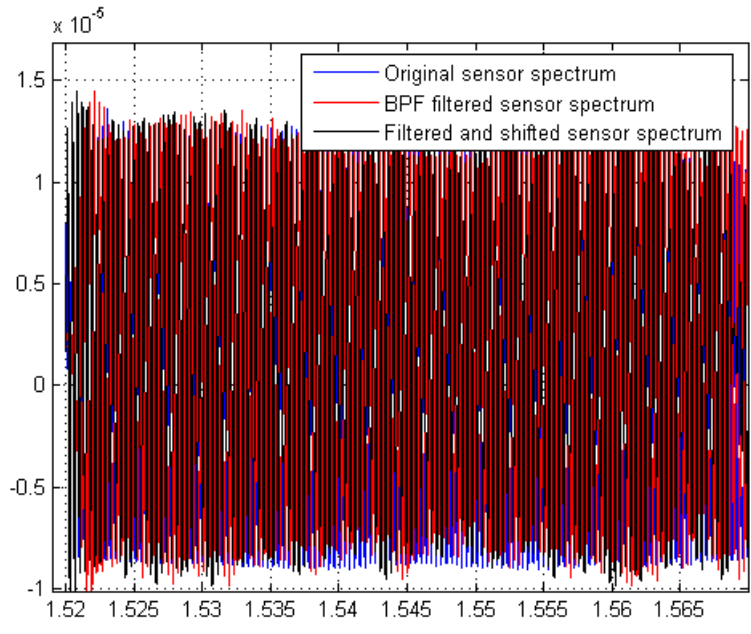


(a) after filtering

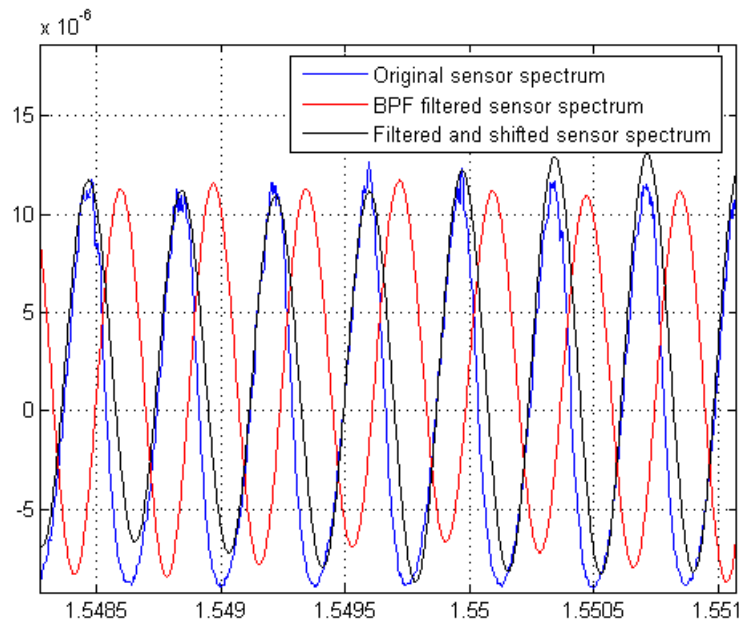


(b) close up

Figure 3.11. The filtering process



(a) After filtering



(b) Close-up

Figure 3.12. The filtering process

Chapter 4. SxS IFPI Sensor Fabrication and Optimization

The objective of the SxS IFPI based quasi-distributed fiber sensor fabrication and process optimization research is to find a low-cost, simple, high yield rate, highly repeatable and robust unit sensor fabrication process, which yield optimized sensor parameters. It is explained in detail as follows:

- Low-cost

Fiber optic sensor fabrication usually requires a set of expensive tools, resulting in the high cost of fiber optic sensors. For example, in the fabrication of the EFPI sensor reported by Anbo et al, expensive CO₂ laser, 5-D precision stage, monitor are required. In Fiber Bragg Grating fabrication, the expensive UV source, special fiber and mask, and optical beam conditioning are required. When adding the equipment maintenance cost into the final sensor cost, the high price will prevent the sensor from being popular. We want to develop a sensor fabrication process that requires minimum investment of manufacturing tools.

- Simple with high yield-rate

Fiber optic sensor fabrication processes are usually complicated, time-consuming and labor intensive. For example, the diaphragm-based EFPI acoustic sensor fabrication process can break-down into more than twenty steps, and normally takes a whole day's effort. The complicated process will introduce many uncertainties to the final sensor, and some parameters can not be well controlled, which would make the repeatability of sensor characteristics poor. The extensive manual fabrication process will require well trained personnel. These human interactions will reduce the repeatability of the sensor characteristics, and increase the cost of the sensor. We want to develop a simplified and largely automated process that minimizes human interaction. This will largely increase the sensor characteristics repeatability and the sensor yield rate.

- Highly repeatable sensor characteristics

Sensor calibration is normally required for each fiber optic sensor. The reason why the calibration is necessary is because the sensor characteristics are not well controlled in the fabrication process, which would result in very different sensor performance. For

example, the visibility of the multimode fiber based EFPI sensor is prone to the parallelism of the two cleaved fiber end-faces, and thus has large variations; the magnitude of the signal is sensitive to the CO_2 bonding process—Too large power would damage the core of the multimode fiber resulting in reduced signal power. It can also degrade the alignment and parallelism of the two Fabry-Perot surfaces, resulting in a poor interference visibility. Too small laser power would result in poor sealing of the sensor. If the sensor characteristics are highly repeatable and the sensor performances are predictable, then the calibration process is no longer required. To ensure high sensor fabrication repeatability, fabrication automation is required.

- Optimized sensor characteristics

For a given type of optical fiber used in the SxS IFPI sensor fabrication, to maximize the number of sensor multiplexed on a single fiber, it is important to minimize the insertion loss while obtain high signal-to-noise ratio. It is also important to study the factors that lead to sensor characteristic fluctuations, and therefore minimize them during the fabrication process.

- Robustness

Fiber optic sensor mechanical strength is often under-emphasized, but important when dealing with real-world applications. The fiber sensor should have good mechanical properties to survive the field installation and function in harsh environments. Often the mechanical strength of the sensor is degraded in the fabrication process. For example, in the diaphragm-based EFPI acoustic sensor fabrication, the sensor is required to be heated up to $800^\circ C$ to bond the diaphragm to the fused silica ferrule. This process will facilitate the water migration into the fiber therefore degrading the fiber. Thus the fabrication process of SxS IFPI sensors should be designed that no mechanically harmful steps are used in the process. The sensor packaging is another factor that would lead to strengthening of the sensor, and should be well designed.

An introduction to the devices used in the SxS IFPI sensor fabrication is illustrated in section 4.1. Section 4.2 is focused on the generalized fabrication process of SxS IFPI sensors. SSS IFPI sensors fabrication is discussed in section 4.3, and fabrication of SMS IFPI sensors is discussed in section 4.4.

4.1. Fabrication and Characterization Tools

The tools used in the SxS IFPI sensor fabrication are: fiber cleaver, fiber fusion splicer and microscope. The devices used in the SxS IFPI sensor characterization are: optical time-domain reflectometer (OTDR) and Micron Optics si720 system. The picture of each device is shown in Figure 4.1.

The Fujikura fiber cleaver provides precise and highly repetitive optical fiber cleaving in a high quality, economical instrument. Each fiber is quickly scribed and broken without further requirements for additional processing before splicing or termination. The CT-04B cleaver features a flexible design which permits it to adapt to cleave 250 μ m to 900 μ m coated fiber and preset 16mm cleave lengths.

The Fujikura FSM-30P fusion splicer is an automatic core alignment type splicer. It utilizes the direct core monitoring Profile Alignment System (PAS) to achieve ultra low loss and very accurate splice loss estimation regardless of fiber quality or age. The FSM-30P optical system and a built-in microprocessor automatically align the fibers and inspect cleave quality. By using the Eccentricity Correction Function (ECF), the splicer determines the fiber core/cladding eccentricity and automatically compensates for in order to assure precise core alignment of the completed splice. The FSM-30P has the following specifications:

- splice loss: typical 0.02dB with single-mode fiber, 0.01dB with multimode fiber
- return loss: 60dB
- cleaved fiber end angle alarm: programmable up to 5°
- viewing method: CCD camera with high resolution 4" LCD monitor
- memory: 100-splice data sets with internal memory

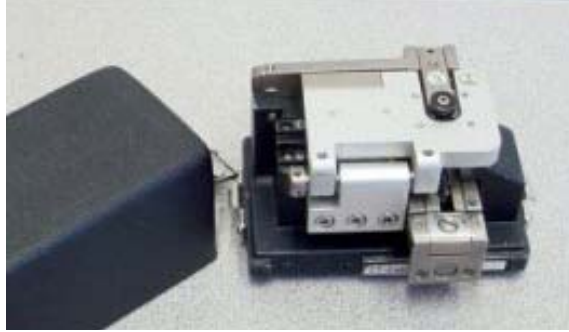
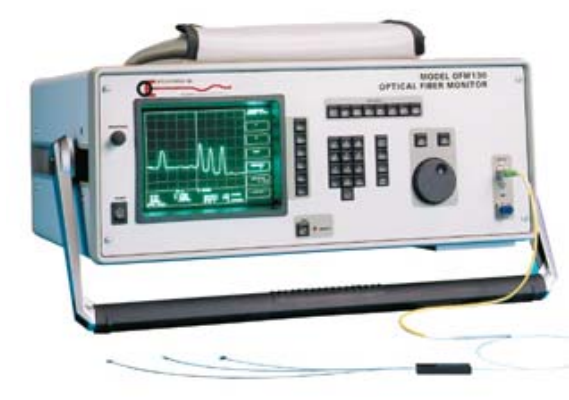
The optical time-domain reflectometry (OTDR) is a well-known method for investigating the attenuation characteristics of an optical fiber. In a basic OTDR measurement, a laser transmitter emits a short optical pulse into the fiber at a time determined by an internal delay generator. The OTDR detects the backscattered light after a time delay associated with the time that the pulse was launched into the fiber. The relative time delay between emission and detection is determined by an internal delay generator. The time-delay is unique addressing information related to a specific location along the fiber, and the

temporal profile of the light intensity returned from the fiber each time delay is also measured and analyzed. This technique was demonstrated for the first time by Barnoski and Jensen [67]. An avalanche photodiode (APD) can be used to count photons if biased slightly above its break down voltage. Healey [68-70] developed this technique and it has become an important application in high-resolution fiber measurements. The OTDR used in the SxS IFPI characterization is OFM130 (Opto-Electronics, Inc). It is a fixed wavelength, high resolution OTDR designed to operate in the long wavelength region (1200 nm to 1635 nm) in real-time. When operated in the Fresnel mode, return loss as low as 80 dB can be measured from individual concatenated components, separated by as little as 50 cm. Rayleigh-mode operation allows for splice-loss measurements (even between unlike fibers) in confined lengths such as experienced in erbium amplifiers. The OFM130 real-time operational capability makes it unmatched for fault-finding applications. The high resolution also makes the OFM130 suitable for beat-length measurements in PM fiber in addition to more normal length and delay-line applications. The specifications for OFM130 are listed in Table 4.1.

Deadzone: Rayleigh Operation Fresnel Operation	<30 Zero
Distance Range: Singlemode Multimode	10 cm to 20 km 10 cm to 5km
Distance Accuracy:	The greatest of: $\pm 0.01\%$ or ± 1.5 cm
Distance Resolution: One Point Two Point	5.0 mm 10 cm
Dynamic Range:	>90dB Minimum Return Value (RV)
Return Loss: Dynamic Range Accuracy	>*80dB ± 0.5 dB for RL<75dB ± 1 dB for RL>75dB
Insertion Loss – Fresnel: Dynamic Range Accuracy: SNR>50	>30dB ± 0.3 dB
Insertion Loss – Rayleigh: Dynamic Range Accuracy: SNR>50	>10dB ± 0.02 dB

Table 4.1. OFM130 specifications

The si720 is a high power, high accuracy, high-resolution sensor interrogator that can be used for a wide variety of fiber optic sensors. The system is composed of an extremely low-noise fiber ring laser, a NIST-traceable absolute optical reference, fast analog-to-digital conversion, two detectors enabling the measurement of sensors in transmission and reflection, two sensor channels allow simultaneous interrogation of multiple sensors on two fibers. The wavelength is automatically calibrated with each scan in less than 200 ms. The laser is continuously swept across a 80 nm spectrum at a rate of 5.0 or 0.5 Hz. The wavelength repeatability is 0.05 pm and wavelength accuracy is 1 pm.

<p>Fiber cleaver (Fujikura CT-04B)</p>	
<p>Fiber fusion splicer (Fujikura FSM-30P)</p>	
<p>OTDR</p>	

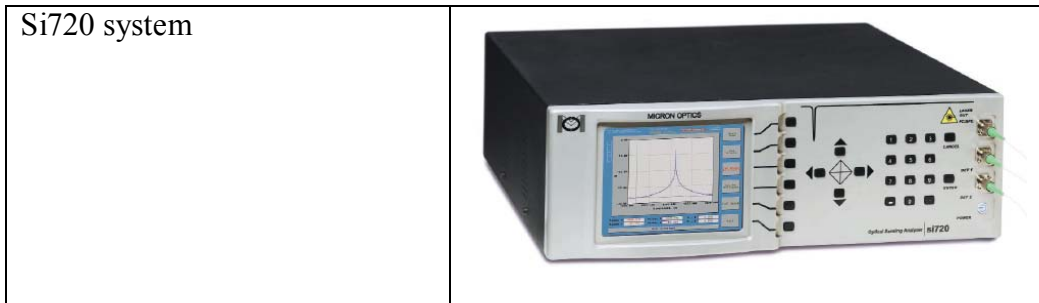
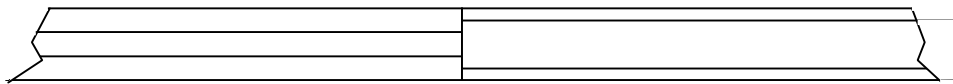


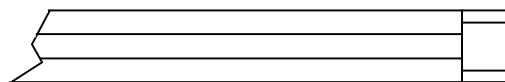
Figure 4.1. SxS IFPI sensor fabrication and characterization tools

4.2. SxS IFPI Sensor Fabrication

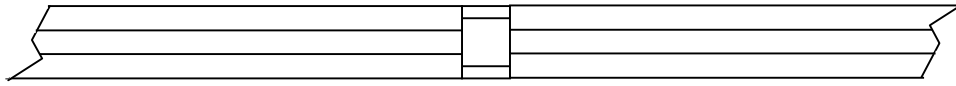
The SxS IFPI sensor fabrication starts with splicing a standard single-mode fiber to a fiber chosen as the Fabry-Perot cavity fiber, such as the GI multimode fiber. The splicing is done on a fiber fusion splicer with relative low arc power and short arc duration compared to standard single-mode fiber to single-mode fiber splicing. The reason this splicing condition is chosen is because in order to generate enough reflection, the boundary of the single-mode fiber to GI multimode fiber cannot be blurred. After these two fibers are joined together, the fiber is put onto the fiber cleaver. Under the microscope, the fiber position on the fiber cleaver is manually adjusted so that the diamond wheel scratches the multimode fiber at a desired length to the single-mode fiber to Fabry-Perot fiber splice point. After that, the multimode fiber is cleaved. The single-mode fiber with a section of multimode on tip of it is placed again onto the fiber fusion splicer to splice with another section of the single-mode fiber. Such an SMS IFPI is made. The diagrams that illustrate the process are shown in Figure 4.2. Although the fabrication process is explained using SMS IFPI, the same procedure also applies to SSS IFPI and SGS IFPI.



(a). Joining a single-mode fiber with a multimode fiber



(b). Cleaving the multimode fiber to form a Fabry-Perot cavity at the tip of the single-mode fiber

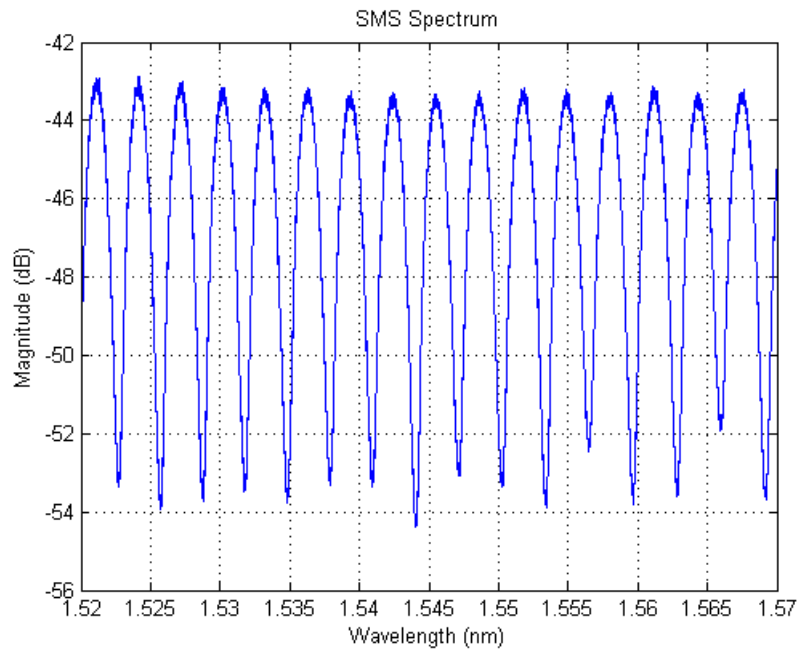


(c). Splice a single-mode fiber to the cleaved multimode fiber end to form the SMS IFPI sensor

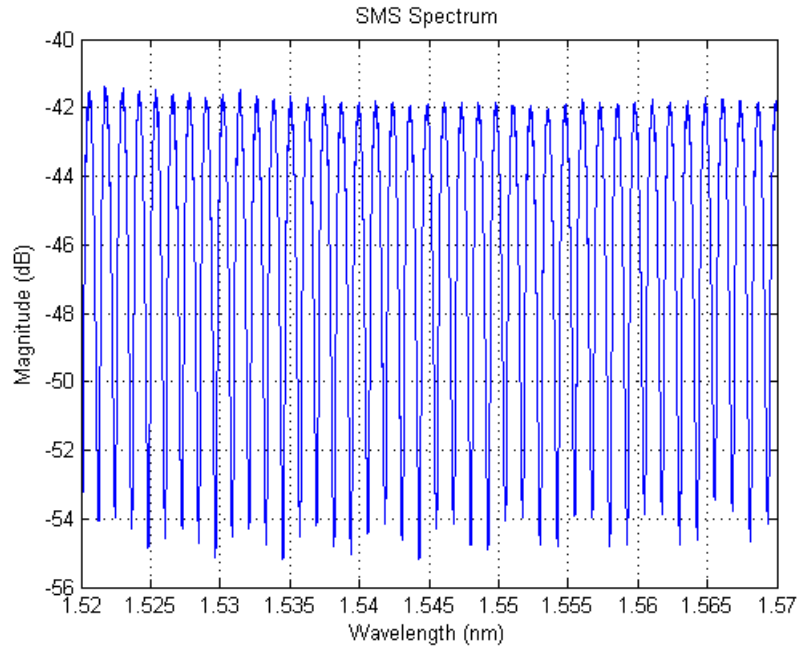
Figure 4.2. The process of SxS IFPI sensor fabrication

4.3. SMS IFPI Sensor Fabrication

In the SMS IFPI sensor fabrication process, a number of issues can affect the characteristics of the sensor, such as fusion splicing conditions, type of multimode fiber used, fiber cleaved angle effect, sensor visibility micro-adjustment, range of SMS IFPI cavity length, the inter-modal interference problem, the bandwidth and harmonics of the sensor, the mechanical strength of the sensor, etc. To deliver a sensor with optimized characteristics, these issues have to be studied thoroughly. The typical SMS IFPI sensor spectrum is shown in Figure 4.3.



(a). 0.5mm cavity length



(b). 1mm cavity length

Figure 4.3. Typical SMS IFPI sensor spectrum measured by si720 system

4.3.1. Fusion splice condition

The single-mode fiber and GI multimode fiber used in this study is Corning SMF-28 and Corning InfiniCor50 respectively. The specifications of each fiber is listed in Table 4.2 and 4.3.

Mode-Field Diameter	
Wavelength (nm)	MFD (μm)
1310	9.2 \pm 0.4
1550	10.4 \pm 0.5
Core Diameter	8.2 μm
Numerical Aperture	0.14
Refractive Index Difference	0.36%
Rayleigh Backscatter Coefficient (for 1ns Pulse Width)	
Wavelength (nm)	Rayleigh Backscatter Coefficient
1310	-77dB
1550	-82dB
Cladding Diameter	125.0 \pm 0.7 μm
Core-Clad Concentricity	<0.5 μm

Cladding Non-Circularity	<0.7%
Fiber Attenuation	
Wavelength (nm)	Maximum Value (dB/km)
1310	0.33-0.35
1550	0.19-0.20

Table 4.2. Corning SMF-28 specifications

Numerical Aperture	0.200±0.015
Refractive Index Difference	1%
Rayleigh Backscatter Coefficient (for 1ns Pulse Width)	
Wavelength (nm)	Rayleigh Backscatter Coefficient
850	-68dB
1300	-76dB
Core Diameter	50.0±3.0 μm
Cladding Diameter	125.0±2.0 μm
Core-Clad Concentricity	<1.5 μm
Cladding Non-Circularity	<1.0%
Fiber Attenuation	
Wavelength (nm)	Maximum Value (dB/km)
1310	0.8

Table 4.3. Corning InfiniCor50 specifications

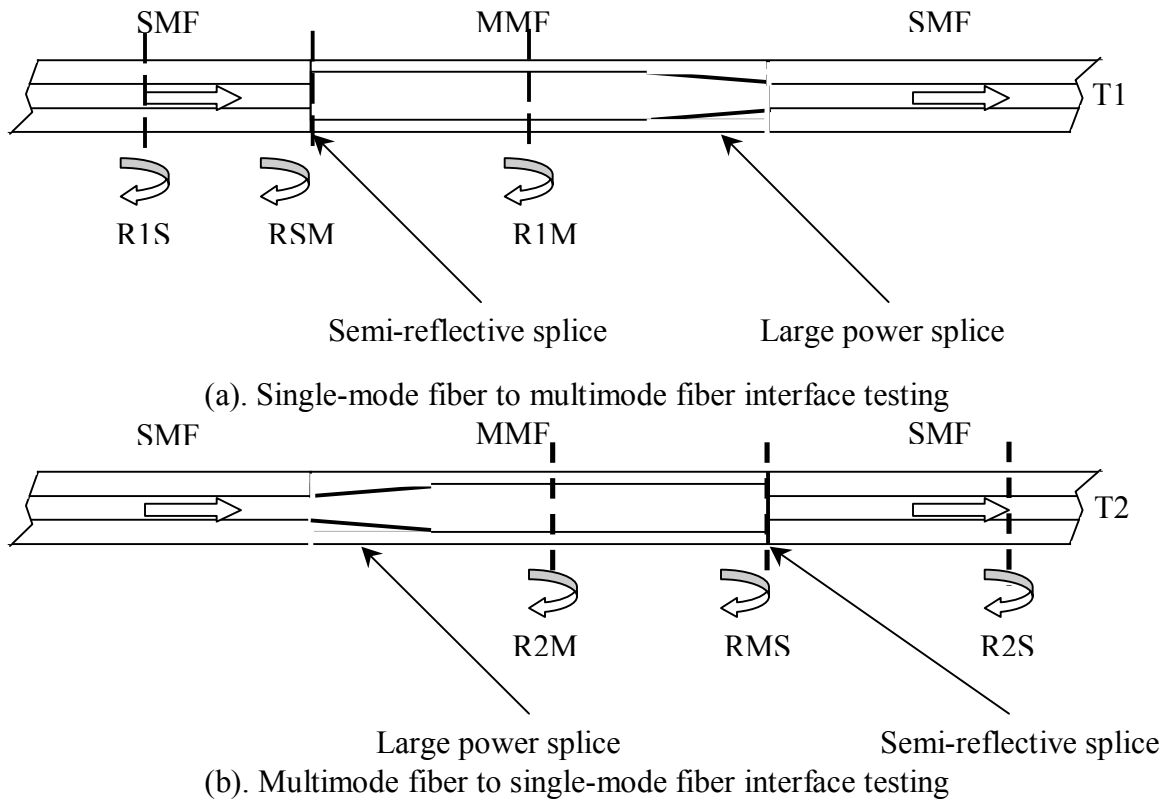


Figure 4.4. Experiment on fusion splice condition

The fiber fusion splice variables considered in this experiment are the arc power P , arc duration D , fiber overlap OLP and fiber offset. Arc power P is a dimensionless number (For FSM-30P splicer, the P ranges from 1 to 150). The arc temperature is proportional to the P value. The unit of arc duration is micro seconds (For FSM-30P splicer, the D ranges from 0 to 30,000). The overlap OLP measures the pressure applied on the fiber end-face (For FSM-30P splicer, the P ranges from 0 to 200 μm), and is directly proportional to the pressure applied. Fiber offset is the relative lateral offset of the two spliced fibers, and it is measured in micron. For reference, the standard single-mode fiber splice parameters for the Fujikura FSM-30P are: $P=15$, $D=2,000\text{ms}$, $OLP=30\mu\text{m}$ and offset is $0\mu\text{m}$.

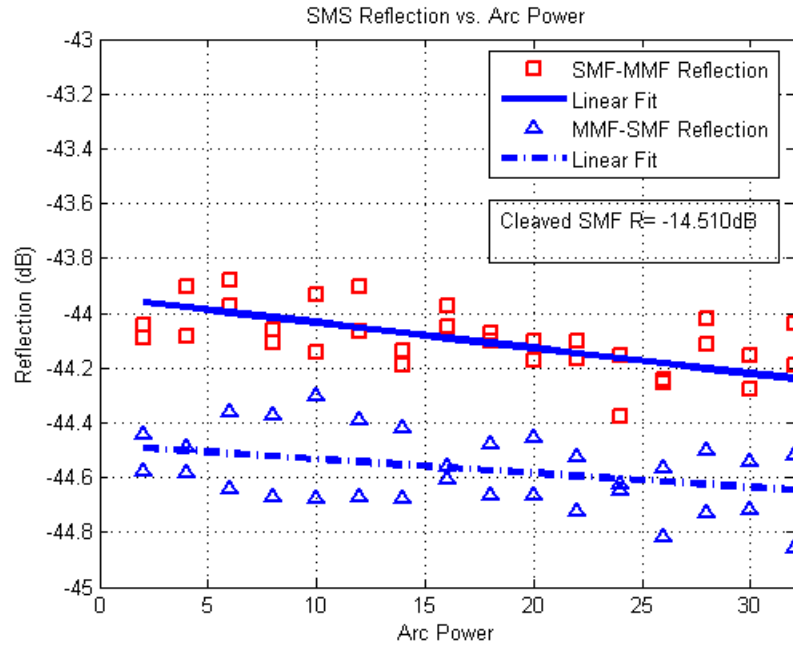
The experiment is conducted for two interfaces respectively: the single-mode fiber to multimode fiber interface and the multimode fiber to single-mode fiber interface. The experimental setup and the quantities measured is shown in Figure 4.4. In each case, one of the interfaces is spliced with large power and long duration to completely frustrate the reflection induced by this interface. Thus the only source of reflection is generated by the interface of concern. The transmission power is measured by the second channel on the si720 system, the fiber end of which is angle polished to eliminate the reflection. Three reflection values at three different positions are recorded. The reflection at the interface is recorded by leaving the SMS structure intact. The rest of the reflections are obtained by cleaving the fiber at the specified location. For reference purpose, the cleaved single-mode fiber end-face reflection and the single-mode fiber without the SMS structure transmission power is measured at the beginning of the experiment.

The SMS characteristics versus fusion splice arc power are shown in Figure 4.5. During the experiments, the other fusion splice parameters are kept the same for reference purposes (arc duration $D=2000\text{ms}$, fiber overlap is $11\mu\text{m}$, fiber offset is $0\mu\text{m}$). The cleaved single-mode fiber reflection is $R = -14.5\text{dB}$. The transmission power without the SMS structure is $T = 0.65\text{dB}$. Shown in Figure 4.5(a) is the SM and MS reflection. The SM reflection is around $R_{SM} = -44\text{dB}$, 30dB lower than cleaved single-mode fiber reflection. The Corning SMF28 single-mode fiber has $n_{cladding} = 1.458$, $n_{core} = 1.463$, $\Delta = 0.36\%$. Assuming the GI multimode fiber has the same cladding refractive index, then its core index should be $n_{core} = 1.481$ to achieve such SM reflection. This would

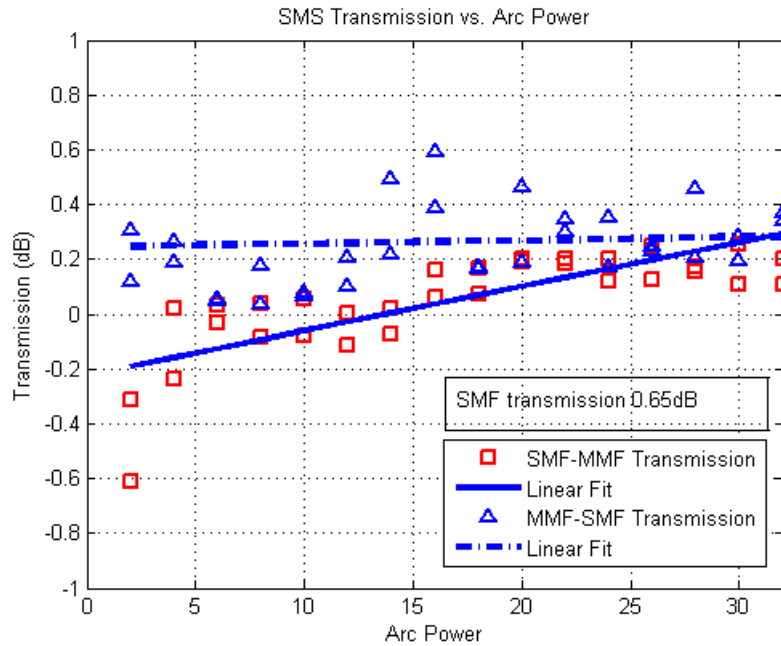
correspond to $\Delta = 1.58\%$, which is contradictory to the Corning InfiniCor50 specifications. Thus we assume the cladding index of the fiber used are different. Both the SM and MS reflections decline with increasing arc power. This is because the temperature at the splicing point is directly proportional to the arc power. Larger arc power would result in higher temperature, which would facilitate the diffusion of multimode fiber dopants into the single-mode fiber, blurring the interface and making it deviates from the ideal thin-boundary assumption, therefore result in reduced reflectivity. The MS reflection is $0.4 - 0.5dB$ down from the SM reflection. This is because the SM reflection is directly measured by si720 system, while MS reflection has to pass the SM boundary first to be measured. As calculated in Chapter 2, the MFD mismatch would induce a coupling loss of $0.57dB$ for the MS reflection. The transmission characteristics for SM and MS arc splice power is very similar. The insertion loss is $0.8dB$ for the SMS IFPI sensor, which agrees with the theoretical analysis. The reflection from different locations along SMS IFPI sensor is shown in Figure 4.5(c). The magnitude difference between R_{1S} and R_{1M} , R_{2M} and R_{2S} is caused by the MFD mismatch, and is around $0.5dB$. The difference between R_{1S} and R_{2S} is the return-loss of the SMS IFPI sensor, and it is approximately $1.5dB$ from the experiment. From the experiment, the measured return-loss is twice the insertion-loss, and agrees well with the theoretical value.

In arc duration experiment, the arc duration is varied from 400 to 2000ms. The result is shown in Figure 4.6. The other fusion splice parameters are kept unchanged, and they are: arc power is 25, fiber overlap is 11 μ m, fiber offset is 0 μ m. The cleaved single-mode fiber reflection is $R = -14.51dB$. The transmission power without the SMS structure is $T = 0.65dB$. Shown in Figure 4.6(a) is the SM and MS reflection. The SM reflection starts around $R_{SM} = -43.2dB$, and declines with increasing arc duration. This is because the amount of heat generated at the splicing point is directly proportional to the product of arc power and arc duration. Longer arc duration would facilitate the diffusion of multimode fiber dopants into the single-mode fiber, blurring the interface and making it deviates from the ideal thin-boundary assumption, therefore result in reduced reflectivity. The $0.4 - 0.5dB$ deviation of MS reflection with reference to the SM reflection is again due to the coupling loss occurred at the SM boundary. The transmission characteristics

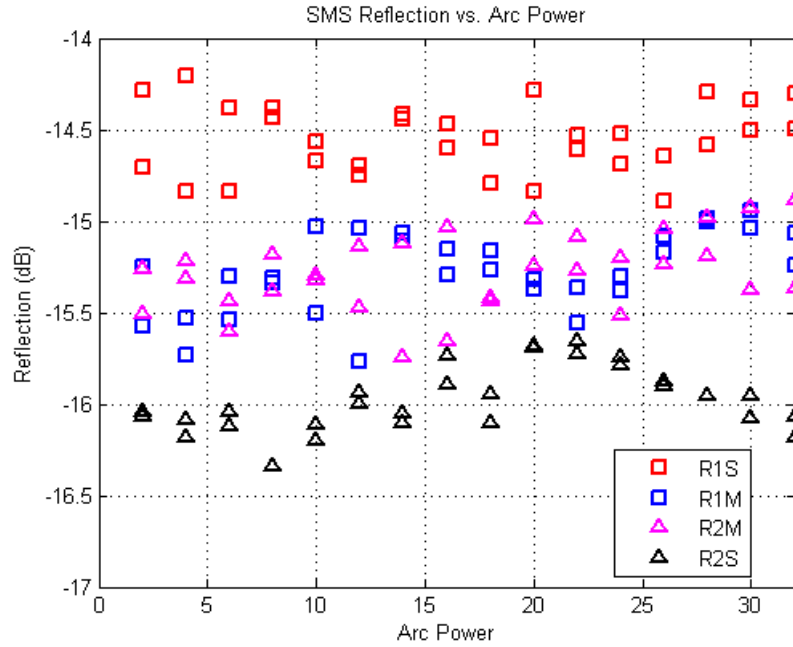
are shown in Figure 4.6(b), and similar for SM and MS cases. The insertion loss is 0.8dB for the SMS IFPI sensor. The reflection from different locations along SMS IFPI sensor is shown in Figure 4.6(c), and can be analyzed in the same way as for the previous experiment.



(a). SM and MS interface reflection vs. arc power

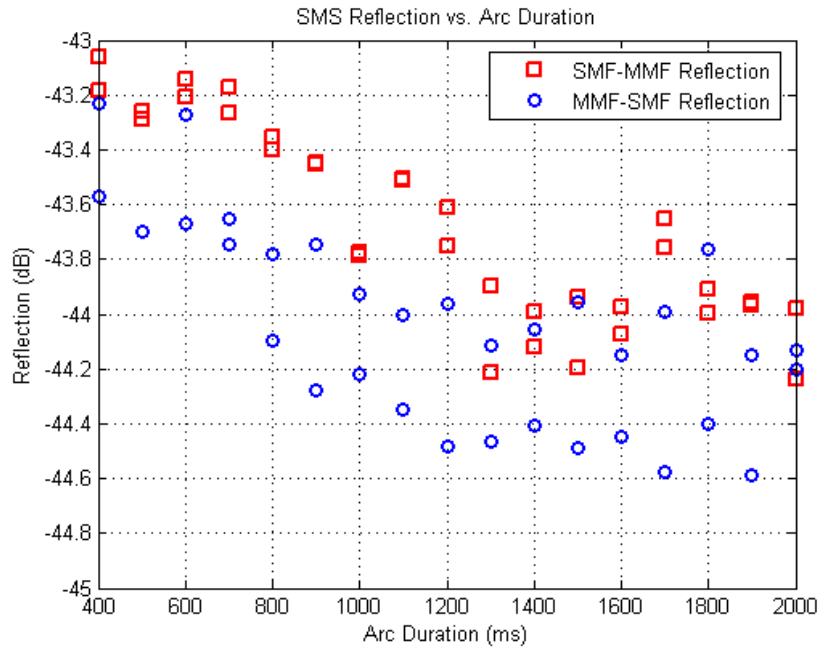


(b). SM and MS interface transmission vs. arc power

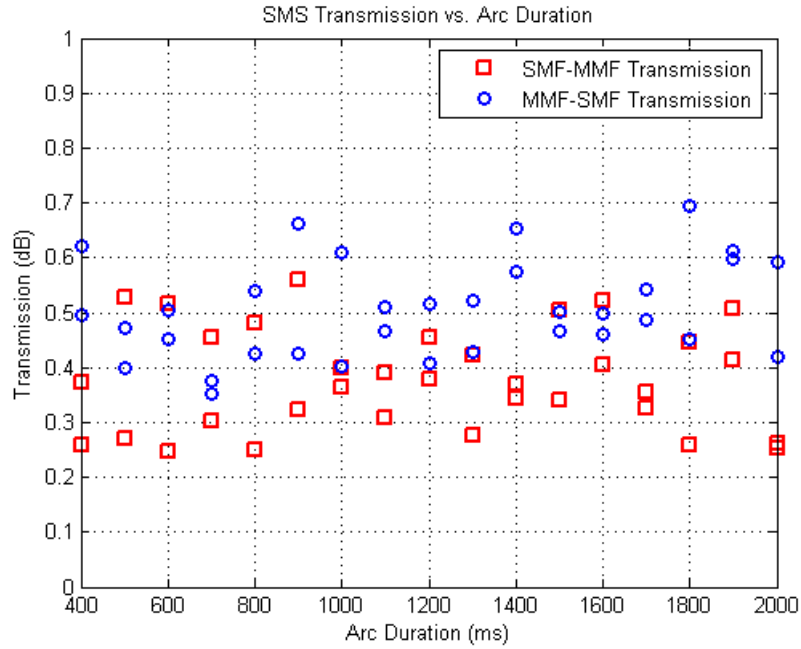


(c). SM and MS interface reflection vs. arc power

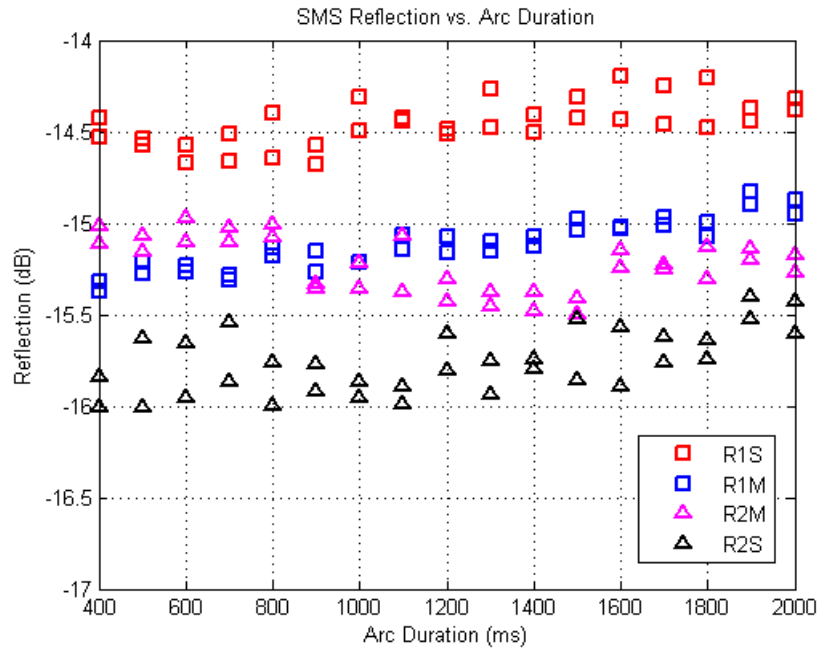
Figure 4.5. SMS characteristics vs. arc power (D=2000ms, Overlap=11um, Offset=0um)



(a). SM and MS interface reflection vs. arc duration



(b). SM and MS interface transmission vs. arc duration

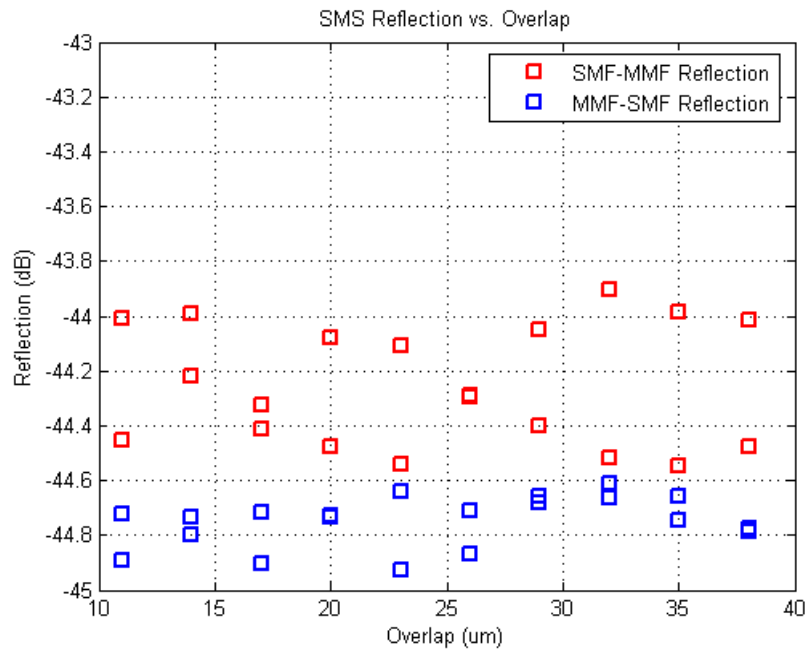


(c). SM and MS interface reflection vs. arc duration

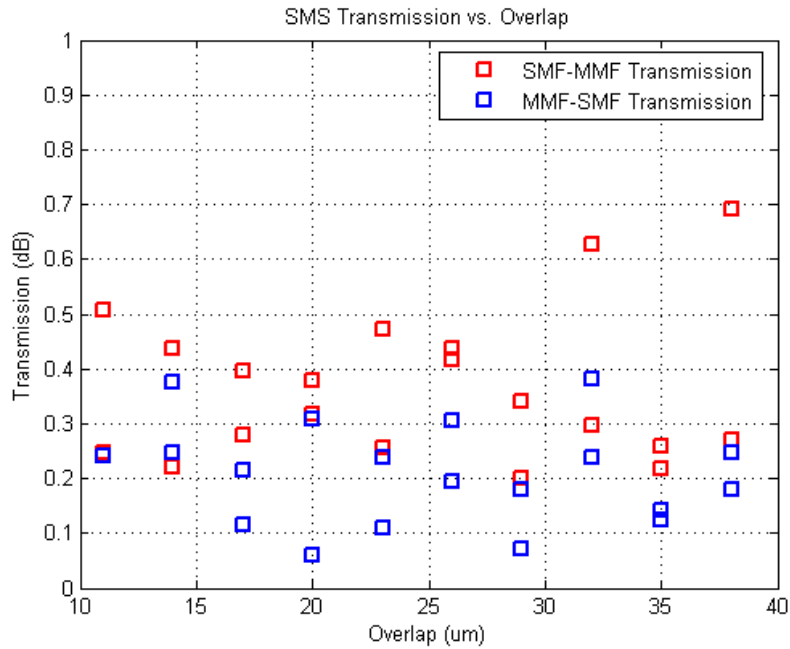
Figure 4.6. SMS characteristics vs. arc duration

In fiber overlap experiment, the overlap is varied from 11 to 40 μm . The result is shown in Figure 4.7. The other fusion splice parameters are kept unchanged, and they are: arc power is 1, arc duration is 1000ms, and fiber offset is 0 μm . The cleaved single-mode fiber reflection is $R = -14.51\text{dB}$. The transmission power without the SMS structure is $T = 0.65\text{dB}$. Different from the previous two experiments, all the SMS IFPI characteristics are insensitive to the fiber overlap value.

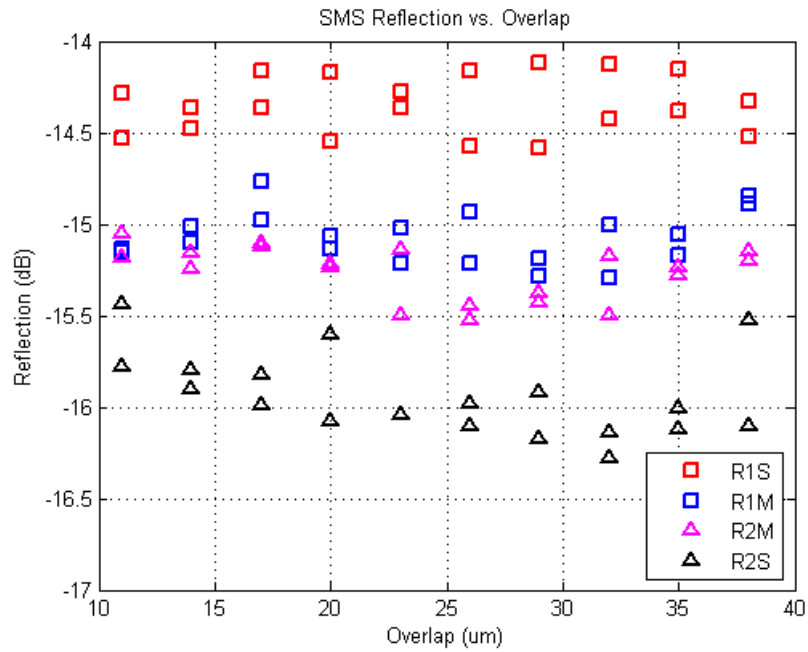
In fiber offset experiment, the offset is varied from 0 to 6 μm . The result is shown in Figure 4.8. The SMS reflection characteristics do not change with offset, but the transmitted power decreases sharply with increased offset. Thus the well alignment of the fibers are very important in SMS IFPI sensor fabrication. The transmission loss can be modeled using Equation (2.30). From Figure 4.8(b), the experiment data agrees well with the theoretical calculation.



(a). SM and MS interface reflection vs. overlap

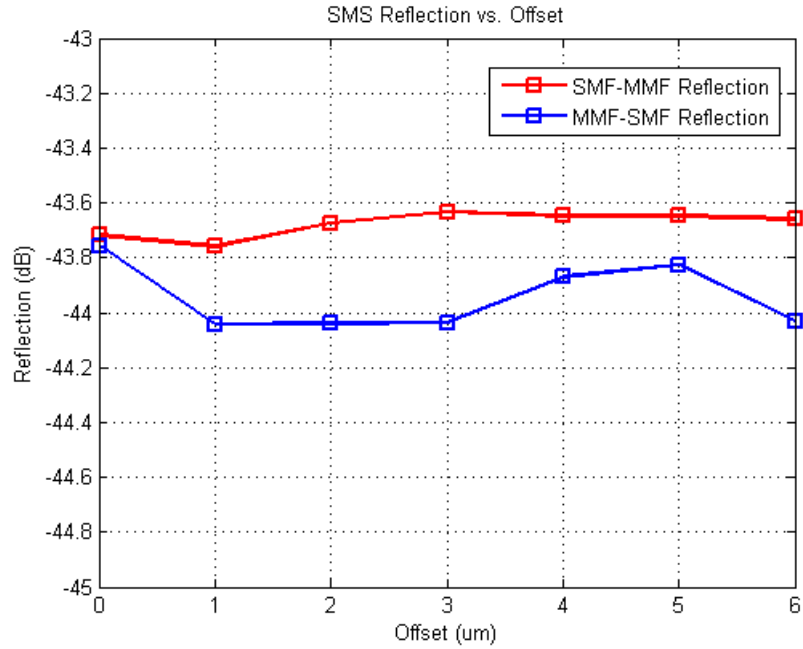


(b). SM and MS interface transmission vs. overlap

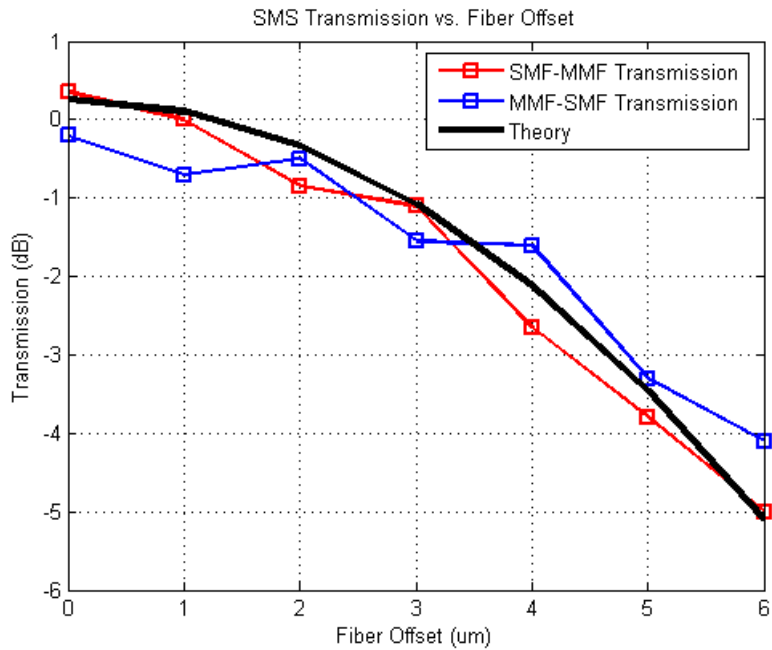


(c). SM and MS interface reflection vs. overlap

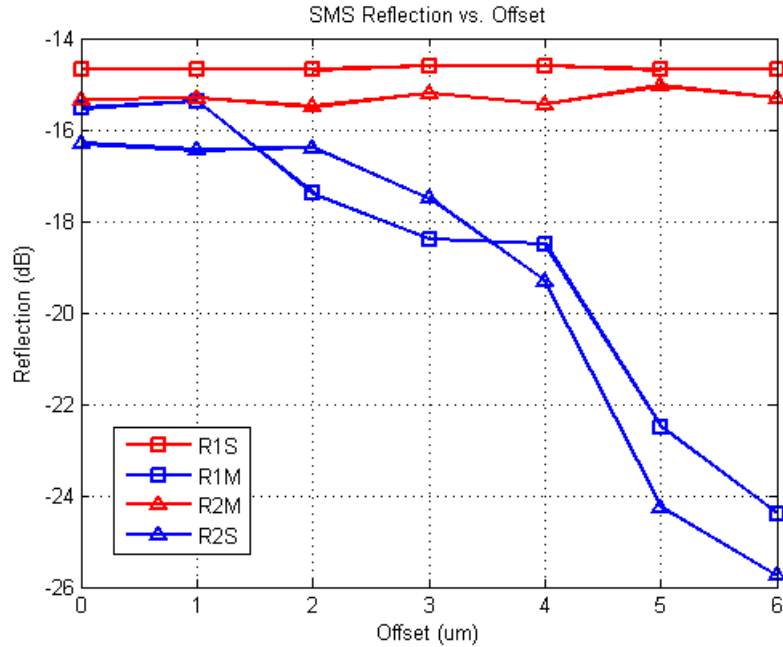
Figure 4.7. SMS characteristics vs. overlap



(a). SM and MS interface reflection vs. fiber offset



(b). SM and MS interface transmission vs. fiber offset



(c). SM and MS interface reflection vs. fiber offset

Figure 4.8. SMS characteristics vs. fiber offset

4.3.2. Fiber cleaved angle

Fiber cleaved angle is one of the main factors that contribute to the fiber splice loss. It will also affect the characteristics of the SMS IFPI sensor.

The fiber cleaver is designed that all the cleaved fiber will have an end angle within 0.3° . But in real applications, the fiber cleaved angle is affected by a number of factors such as aging of the cleaver, operator experience, etc. Shown in Figure 4.9 is the cleaved angle distribution of 170 cleaved fibers. The probability the cleaved angle is within 0.3° is 0.55. The angle is measured by the Fujikura fusion splicer.

In the first experiment, a bare single-mode fiber is cleaved, its reflection and cleaved angle is recorded. A well cleaved single-mode fiber and multimode fiber is spliced together, and the other end of the multimode fiber is cleaved, its cleaved angle and reflection is recorded. The reflection of the cleaved single-mode fiber and cleaved SM structure versus cleaved angle is compared in Figure 4.10. From the data we found that the single-mode fiber reflection is more susceptible to cleaved angle than the SM structure multimode fiber. Increased cleaving angle would result in decreased reflection

for both fibers. The SM reflection is smaller than single-mode fiber reflection due to the MFD mismatch.

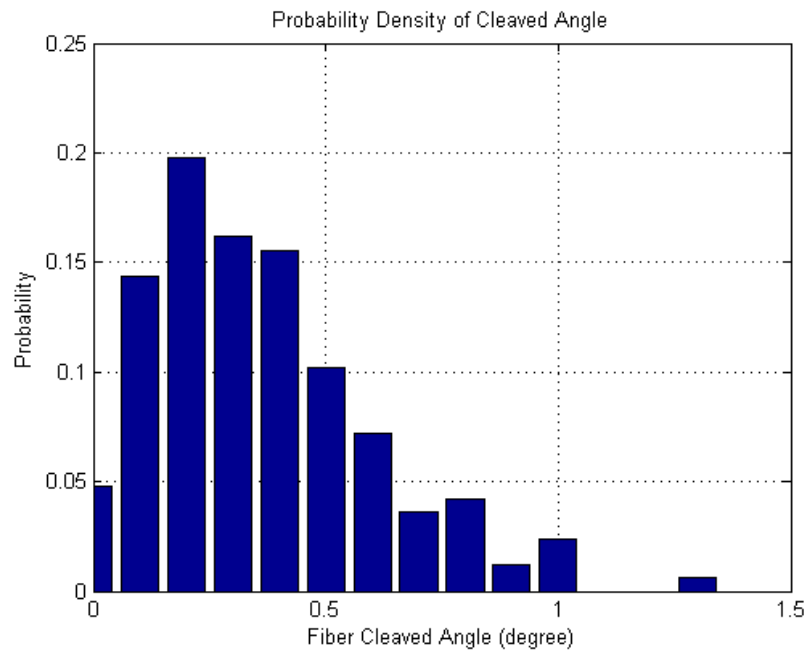


Figure 4.9. Probability density of fiber cleaved angle



Figure 4.10. Reflection vs. fiber cleaved angle for single-mode fiber and SM structure

For an SMS IFPI sensor, the SM and MS structure transmission and reflection characteristics versus total cleaved angle is shown in Figure 4.11 and 4.12 respectively. The total angle is defined as the sum of the cleaved angle of the two fibers in SM or MS structure. Increased total angle would reduce both transmission and reflection. It is because the large cleaved angle would facilitate coupling to higher order modes in the multimode fiber; therefore reduce the light power coupled to fundamental mode of the single-mode fiber. The theoretical value is compared with experimental data. Both agree well with each other.

4.3.3. Visibility tuning

From the analysis in Chapter 2, the transmitted power declines along the quasi-distributed sensor line. Assume all the sensors have the same visibility, and the interference fringe peak-to-peak is 20dB. Thus along the sensor line, the interference fringe of an individual sensor is down shifted. The down shift between the neighboring sensors equals the insertion loss of a sensor. The si720 sensor interrogator has a detection limit of -70dB. When the valley of the sensor interference fringe has the power lower than the interrogator detection limit, the spectrum cut-off occurs. Such is shown in Figure 4.13. The cut-off effect would introduce harmonics in the sensor spectrum's Fourier transform spectrum. This is shown in Figure 4.14. The cut-off effect generated harmonics are harmful in the system because it has the probability to fall onto other sensors' Fourier transform frequencies, and it will reduce the usable Fourier transform frequencies. Thus it is important to eliminate the harmonics. To achieve this, one can reduce the peak to peak value, in other words, the visibility of the sensor so that the valley power is still above the detection limit of the CTS system. This is done by fusion splicing one of the sensor's interfaces with slightly larger power or duration, or by repeating arc splicing the interface. In this experiment, a SMS IFPI sensor's MS interface is repeatedly arc spliced. The arc duration is varied from 500ms to 800ms. The sensor visibility change versus arc counts are shown in Figure 4.15. Thus increasing arc power or arc heat in the sensor fabrication is a reliable measure to eliminate the sensor harmonics in real applications. The visibility reduced sensor spectrum Fourier transform spectrum is shown in Figure 4.14 in black, it is apparent that the harmonics are eliminated.

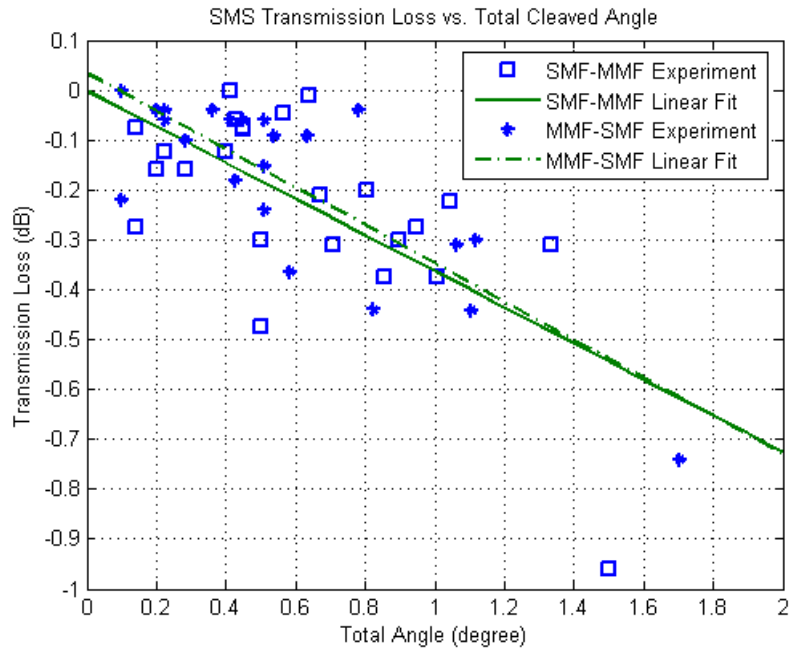


Figure 4.11. SM and MS transmission characteristics vs. total cleaved angle

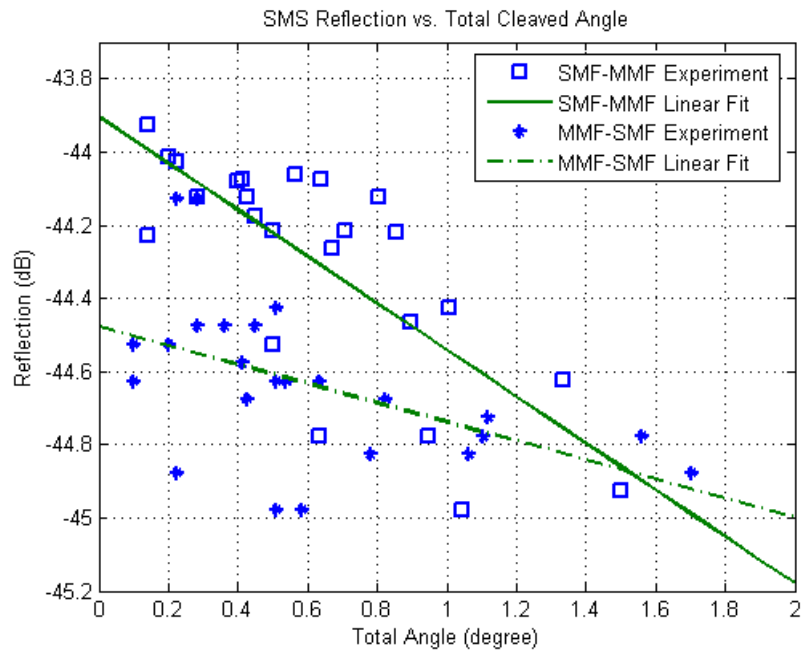


Figure 4.12. SM and MS reflection characteristics vs. total cleaved angle

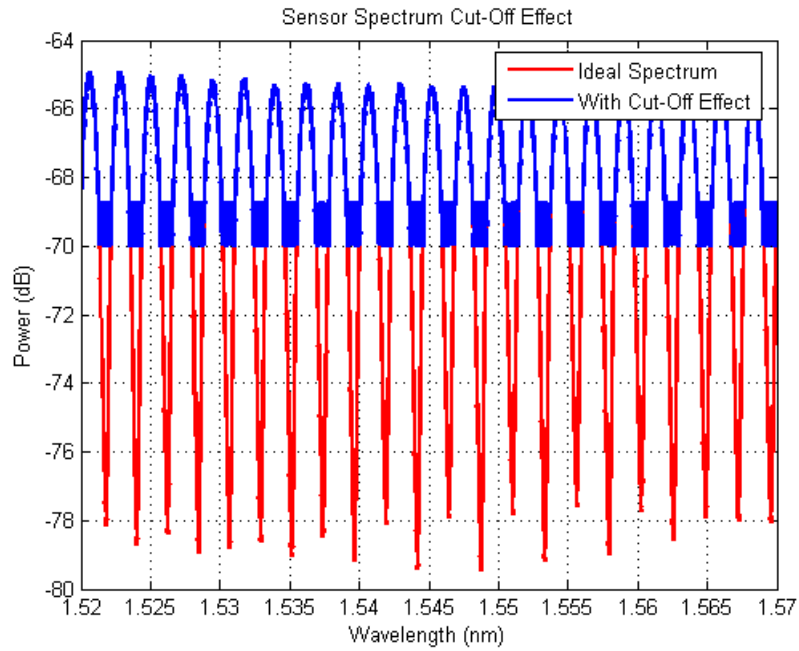


Figure 4.13 Sensor spectrum cut-off effect

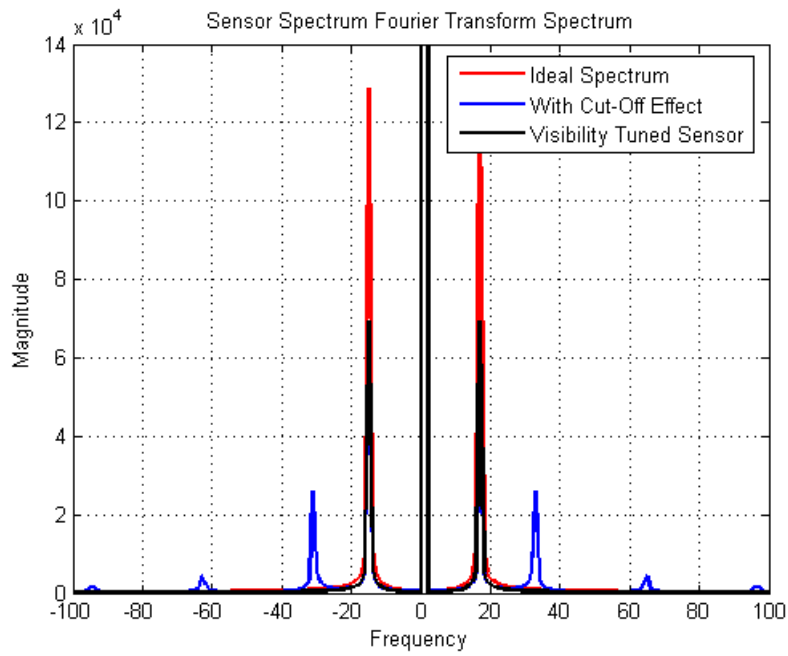


Figure 4.14 Cut-off effect induced Fourier transform harmonics

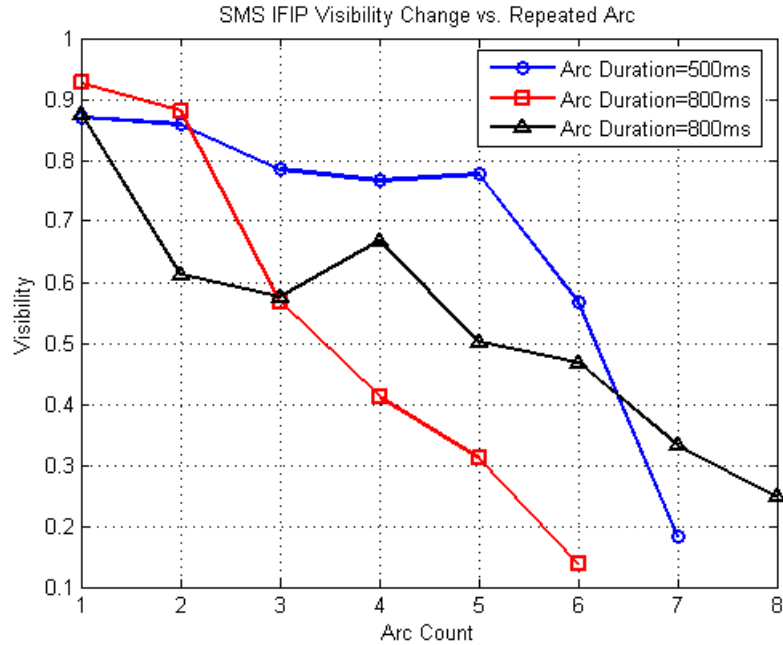


Figure 4.15 Sensor visibility tuning

4.3.4. Sensor cavity length problem

The major difference between the IFPI and EFPI is that IFPI confines light inside the cavity using a waveguide structure. In this way the IFPI is much more stable and much less lossy than the EFPI. Because the power from the second interface reflection is largely preserved in the IFPI, it has much higher visibility at large cavity length than that of the EFPI structure. An experiment comparing the IFPI and EFPI visibility versus cavity length is shown in Figure 4.16. When the cavity length is around 5mm, the visibility of the IFPI and EFPI is 0.786 and 0.024 respectively.

Although the IFPI has high visibility when compared with the EFPI, it also suffers from decreasing visibility when the cavity length is increased. The IFPI visibility decreased from 0.89 to 0.71 when the cavity length increased from 484 μ m to 9,504 μ m.

The experiment result shown in Figure 4.17 reveals the same phenomena in a different perspective. In this experiment, 22 SMS IFPI sensors with different cavity length are made, and their Fourier spectrum shown. The Fourier spectrum magnitude of the AC components decrease with increasing cavity length. When the cavity length is larger than 90mm, the interference signal is so poor that its Fourier transform spectrum has poor signal-to-noise ratio.

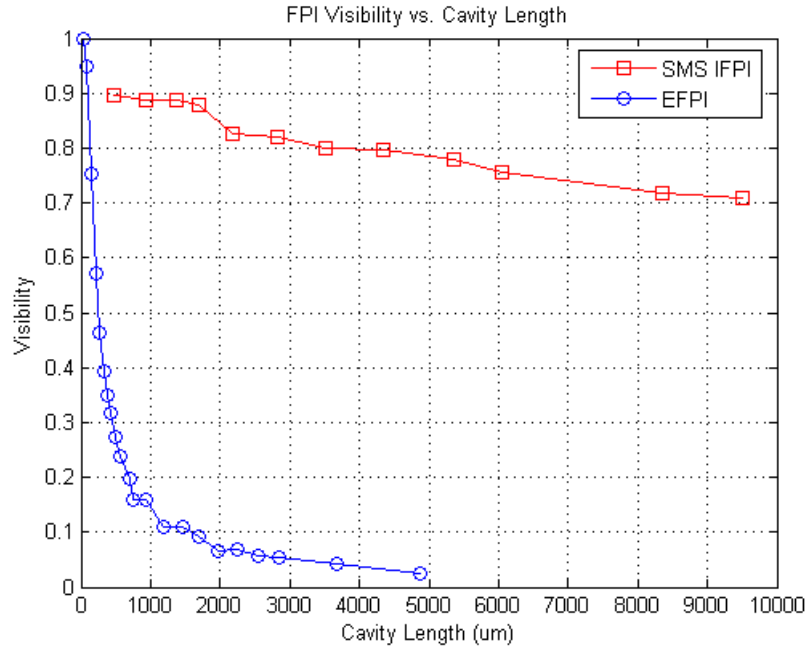


Figure 4.16. EFPI and IFPI visibility versus cavity length

There are two reasons for SMS IFPI's decreased visibility and Fourier spectrum magnitude with reference to increased cavity length. The first is the coherent length of the sweeping laser in the si720 system. According to Chapter 3, the fiber laser has a coherent length of 200mm. The coherence of the light decreases with the increasing OPD. With larger cavity length, the coherence is poorer, which results in lower visibility and smaller Fourier spectrum magnitude. The second reason is the change of the polarization in the multimode fiber. The EFPI does not have polarization problem because when the light propagates in the air cavity, the polarization does not change. But in IFPI, when the light passes the SM interface, the polarization of the light could change due to the irregularities of the fiber, the micro and macro bending, the reflection of the MS interface, etc. When this second arm of light is re-coupled into the single-mode fiber, it will interfere with the SM reflection. Because the state of polarization of the second arm is changed, only its component parallel to the SM reflection polarization will participate in the interference. The perpendicular polarizing component of the second arm of light will only function as a background noise in the interference. The longer the cavity length, the more the possibility of polarization change of the second light beam, which results in a decreased visibility and magnitude of the Fourier spectrum.

Based on these experiments, the SMS IFPI sensor cavity length should be kept short, and the suggested length is less than 90mm.

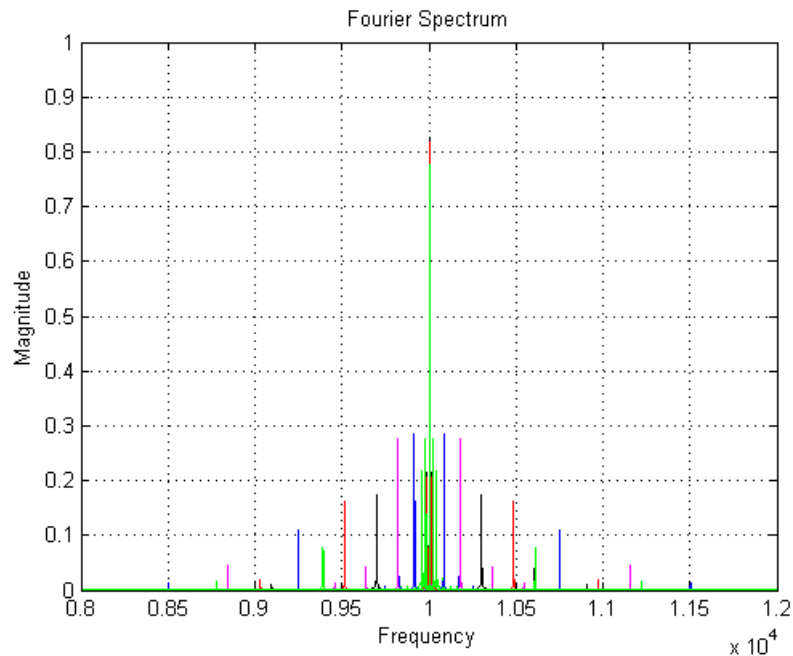


Figure 4.17. Fourier spectrum of 22 IFPI sensor with different cavity length

4.3.5. Sensor separation distance

In quasi-distributed fiber sensing line, the sensors are placed at locations where the measurand is interested. Sometimes people want to obtain measurand information at two adjacent locations. But what is the minimum allowed distance between two SMS IFPI sensors, and what are the limiting factors for this minimum distance?

In the previous section, the IFPI cavity length is limited by the coherent length of the fiber laser in the si720 system and the polarization state change of the second reflection arm. Those two imposed limitations would limit the cavity length to be less than 90mm. In the discussion of minimum sensor separation distance, the limiting factors are again the coherent length of the fiber laser and the polarization state of the second sensor's two reflections with reference to the polarization state of the first sensor's two reflections.

The experiment setup is shown in Figure 4.18. Two short cavity SMS IFPI sensors are made. They are spliced onto the same single-mode fiber with a separation of L . With varying L , the spectrum is recorded, and its Fourier transformed spectrum is shown in Figure 4.19.

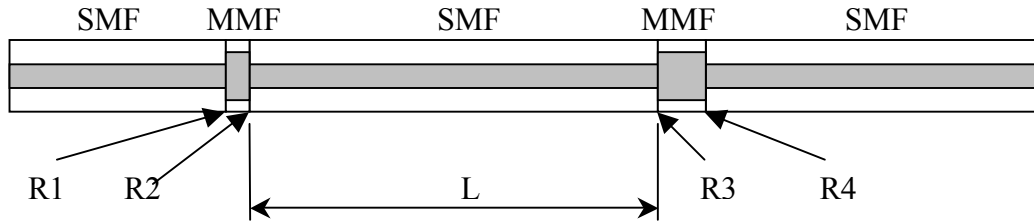


Figure 4.18. Experiment setup

When the two sensors are close to each other, the reflection from the second sensor will interfere with the reflections from the first sensor. Six set of interference fringe are present, they are labeled as R1-R2, R3-R4, R1-R3, R1-R4, R2-R3 and R2-R4. R1-R2 and R3-R4 are the two sensors' intrinsic fringe, and corresponds to the Fourier spectrum peaks close to DC. The rest of the fringes is generated from the interference between one of the reflection interfaces of each sensor, and therefore corresponds to the Fourier spectrum peaks shifted far away from the DC. The shift is in the amount of the length of the separation of the two sensors. The six interferences are presented in the Fourier spectrum domain as six discrete frequency components in Figure 4.20. With increasing L , the coupling between the two sensors are loosened because of the coherent length of the fiber laser and the polarization state change. From the experiment data, when the separation exceeds 60mm, the coupling between the two sensors can be omitted. Thus the spatial resolution of the sensor is roughly 60mm.

4.3.6. Inter-modal interference

In SMS IFPI sensor fabrication, a number of factors, such as fiber offset, fiber cleaved angle, would facilitate the coupling between fundamental mode and higher order modes in multimode fiber. The power can be coupled in both directions: from fundamental mode into higher order modes; from higher order modes into fundamental mode. With fiber offset or fiber cleaved angle, the light from the lead-in single-mode fiber will couple into fundamental mode in multimode fiber, but a part of it will also couple into higher order mode in the multimode fiber. The coupling on both directions will also happen on the multimode fiber to single-mode fiber boundary. When the modes reflected reach the single-mode fiber to multimode fiber boundary again, the modes in the multimode fiber will couple into the fundamental mode in single-mode fiber. Although the fundamental

mode in the multimode fiber has the highest coupling coefficient, higher order modes in the multimode fiber can also couple part of their power into the single-mode fiber. Thus the light with different OPD will interfere with each other and result in interference. The diagram is shown in Figure 4.21. This interference pattern can be used as a sensing mechanism, but in the SMS IFPI sensing system it is harmful. It could broaden the Fourier spectrum of a given SMS IFPI sensor, reducing the utilizable bandwidth, and it could be a noise factor to the Fourier spectrum neighboring sensor. The inter-modal interference can be eliminated by using only well cleaved fiber in the fabrication and ensure good fiber alignment. The latter is ensured by the auto alignment function of the fusion splicer.

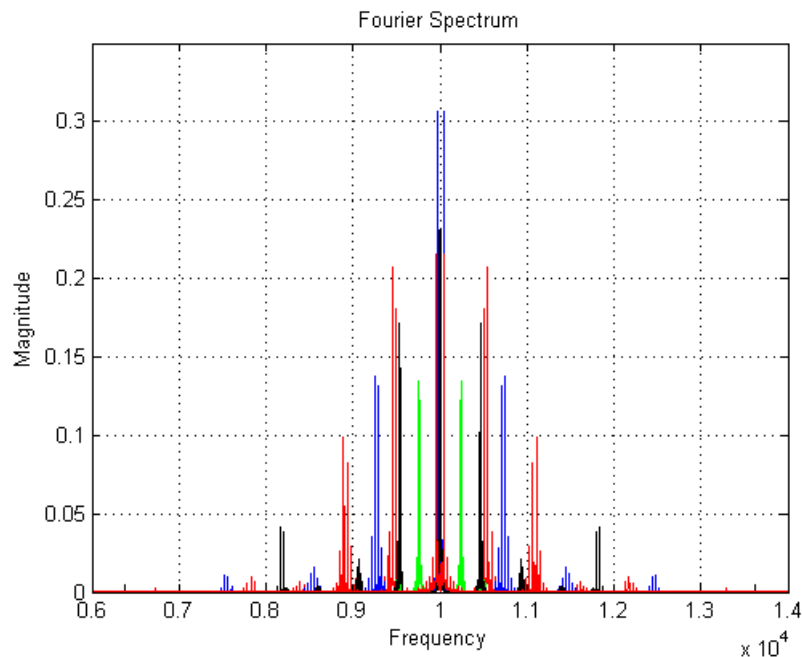


Figure 4.19. Sensor separation problem

The experiment is designed to demonstrate the inter-modal interference. A single-mode fiber is spliced to a section of the multimode fiber by a certain amount of offset. The far end of the multimode fiber is well cleaved. The length of the multimode fiber is kept around 1m to fully demonstrate the interference, although in real SMS IFPI sensor, the length of the multimode fiber is less than 10mm, resulting in much less severe inter-modal interference problem. From Figure 4.22 and Figure 4.23 it is observed that the larger the offset, the less power is in the DC component of the Fourier spectrum, and the

more power is distributed into the broadened bands. This is because larger offset result in more power coupled into the higher order modes in the multimode fiber, therefore more interference. The ideal cleaved multimode fiber reflection would have only the DC component in the Fourier spectrum, which is in yellow line in Figure 4.22.

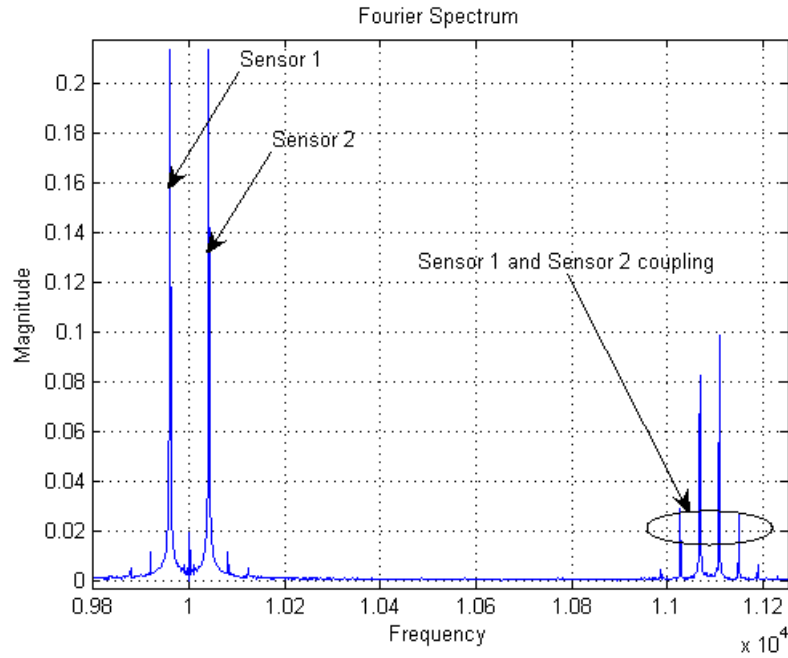


Figure 4.20. 6 Fourier transform spectrum peaks caused by adjacent sensor coupling

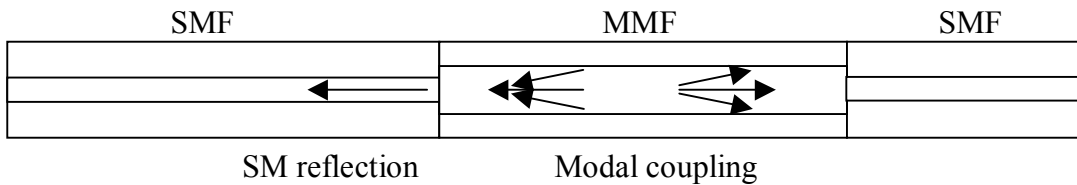


Figure 4.21. Experiment setup

4.3.7. Sensor mechanical strength

The semi-reflective fusion splicing condition used in SMS IFPI sensor fabrication would result in reduced mechanical strength of the sensor. In this experiment, the mechanical strength of a single-mode fiber to multimode fiber fusion splice is studied. Weight is added to the multimode fiber until the splice point breaks, and the according weight number is recorded. The tensile stress is obtained by dividing the weight number by the area of fiber cross-section. For comparison purpose, the standard single-mode fiber to

single-mode fiber splicing point is also tested. The data is shown in Figure 4.23. The tensile stress for Corning SMF28 single-mode fiber is $\geq 0.7\text{GPa}$. The standard single-mode fiber to single-mode fiber splice has tensile stress roughly at 0.4GPa , the SM tensile stress is roughly 0.18GPa . Thus the SMS IFPI sensor would have tensile stress half of the standard single-mode fiber splicing. The splicing condition used for the SM structure is $P=1$, $D=600\text{ms}$. If the mechanical strength of the sensor is in first priority, the arc power or arc duration can be increased to increase the mechanical strength of the sensor to 0.4GPa as that of the standard single-mode fiber splicing. In this situation, the reflection generated by the SMS IFPI would reduce.

4.3.8. SMS IFPI sensor fabrication repeatability

To study the repeatability of the SMS IFPI sensor fabrication, 50 sensors are made. The SM reflection, sensor transmission and sensor visibility is recorded and shown in Figure 4.25. The mean and standard deviation of the SM reflection, sensor transmission and sensor visibility is listed in Table 4.4. The fabrication process is very repeatable. The standard deviation of the sensor visibility is only 0.013 , and the standard deviation of the SM reflection and SMS IFPI sensor transmission loss is less than 0.5dB and around 0.2dB respectively.

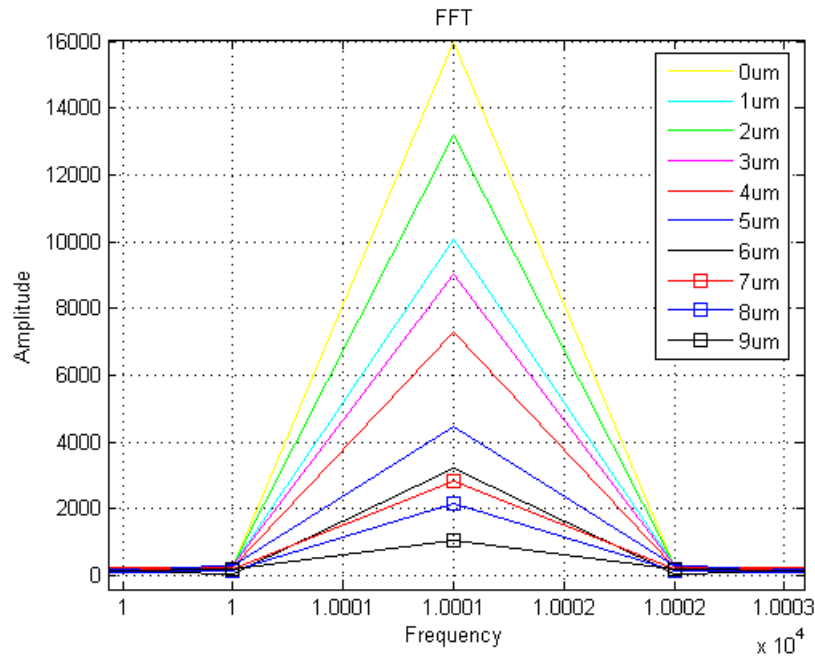


Figure 4.22. Fourier transform spectrum DC components of inter-modal interference

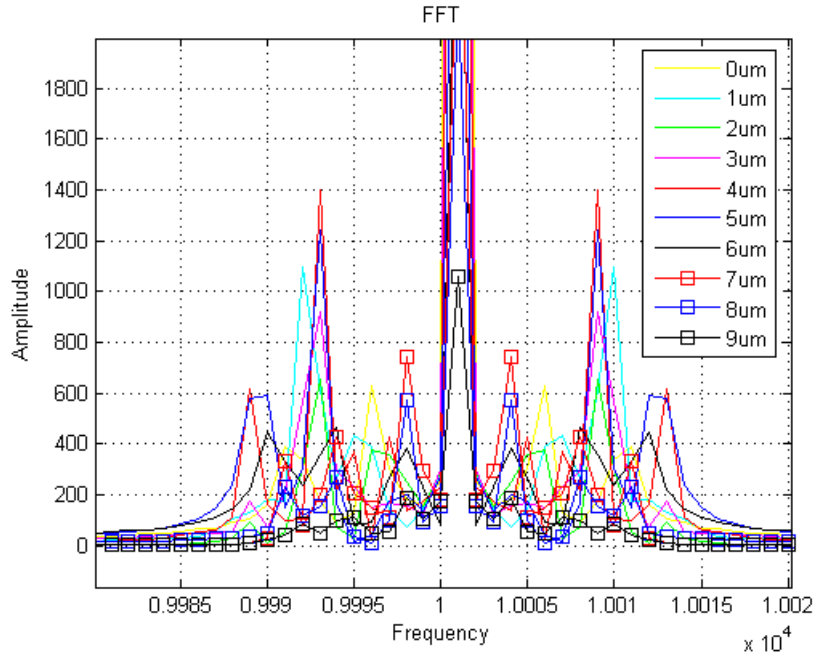


Figure 4.23. Fourier spectrum broadening from inter-modal interference

Thus with the simple fabrication process and the automated fiber fusion splicer, the uncertainty introduced by the operator is minimized, resulting in a very repeatable fabrication process.

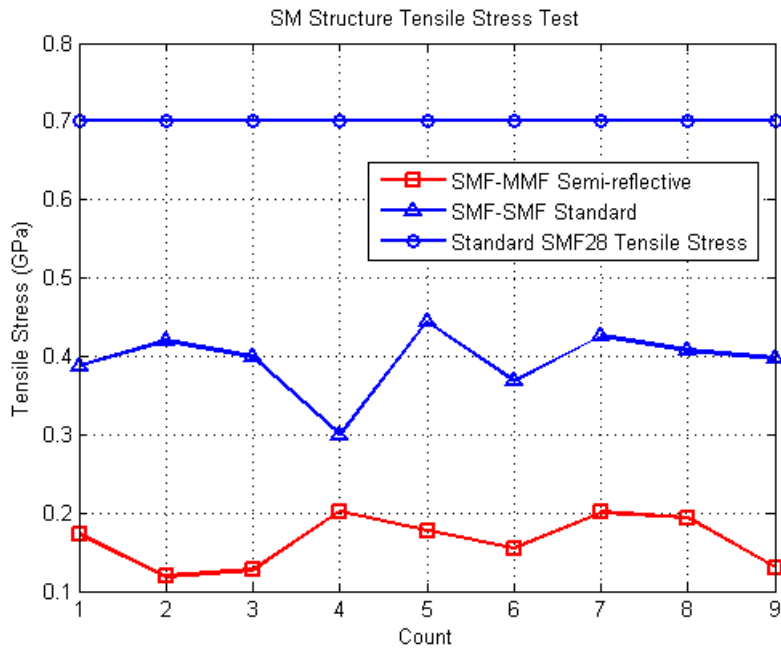


Figure 4.24. SM structure tensile stress test

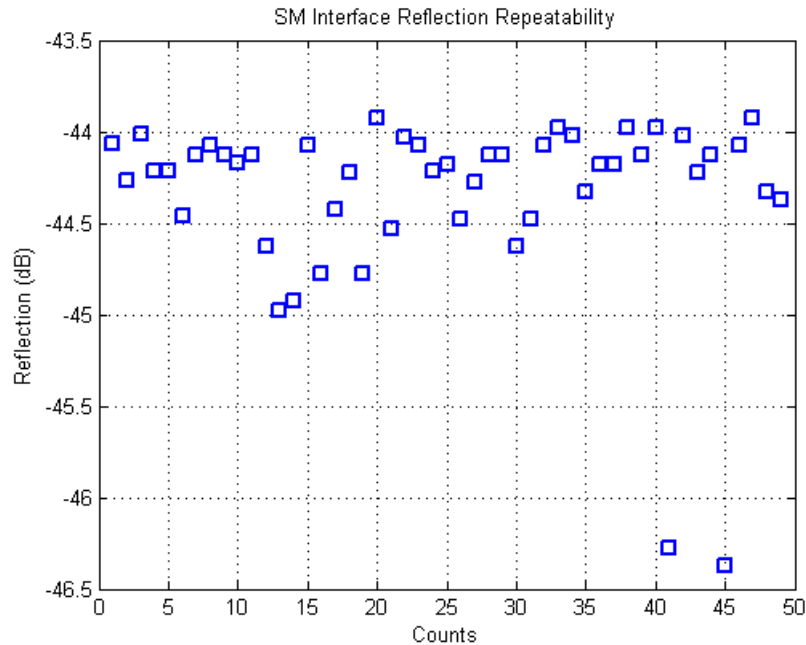
	Mean	STD
SM reflection (dB)	-44.33	0.49
SMS IFPI transmission (dB)	0.14	0.23
SMS IFPI visibility	0.87	0.01

Table. 4.4. SMS IFPI sensor characteristics fabrication repeatability

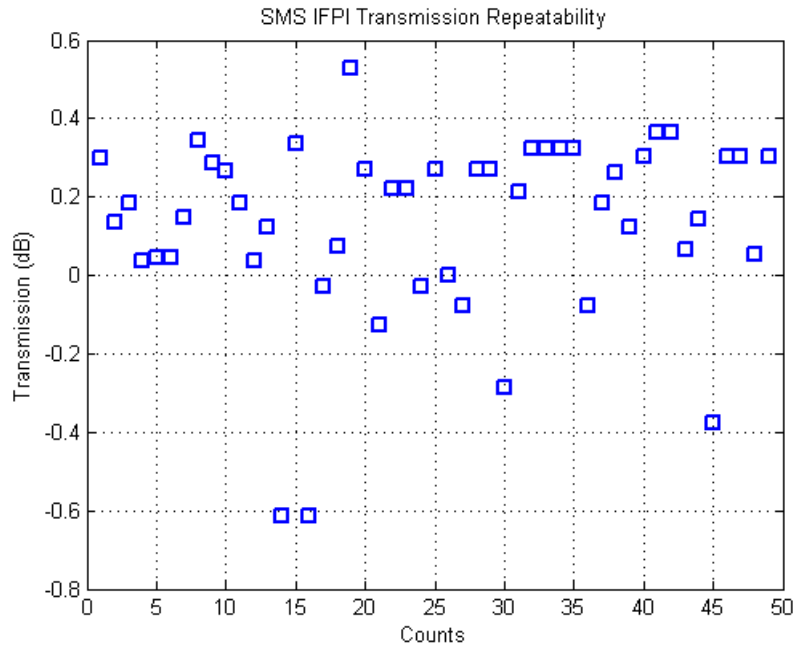
4.3.9. SMS IFPI using different multimode fibers

The guideline for SMS IFPI fabrication is to maximize reflection while minimize transmission loss. Therefore large doping concentration and small mode-field-diameter mismatch multimode fiber should be considered.

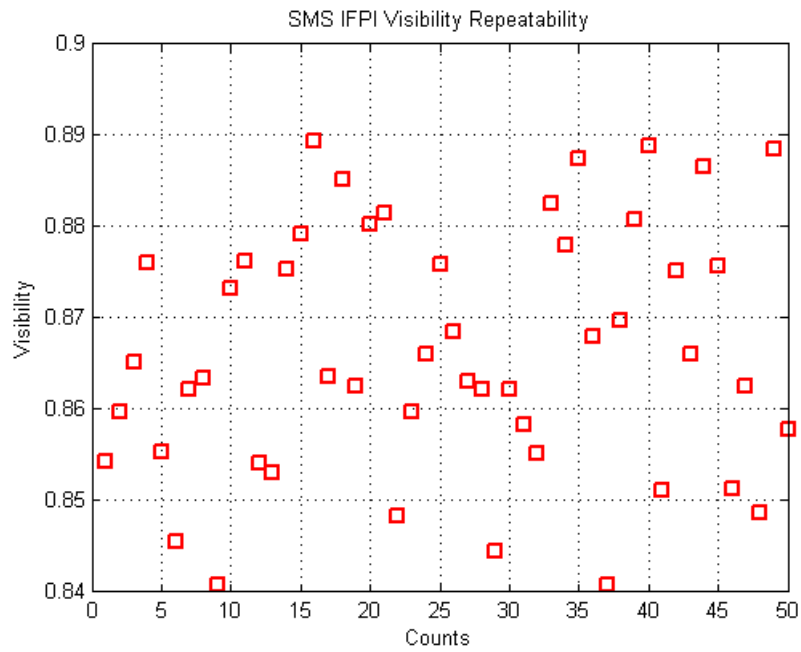
Listed in Table 4.5 is the SMS IFPI characteristics evaluated at 1550nm for different GI multimode fibers. From the data we know that larger doping concentration multimode fiber has larger reflection. Since such commercially available fibers usually has large core diameter, the MFD of the fundamental mode is larger than GI multimode fiber with small doping concentration, which would result in larger insertion loss. The simulation data is based on the analysis in Chapter 2. It agrees well with the data.



(a) SM interface reflection repeatability test



(b) SMS IFPI transmission repeatability test



(c) SMS IFPI sensor visibility repeatability test

Figure 4.25. SMS IFPI sensor fabrication repeatability test

Multimode Fiber	Core Diameter	Δ (%)	Predicted Reflection (dB)	Average Reflection (dB)	Predicted Insertion Loss (dB)	Average Insertion Loss (dB)
Corning SMF50	50 μ m	1	-45.20	-43.44	0.36	0.44
Corning InfiniCor600	50 μ m	1	-45.20	-43.50	0.36	0.40
Corning InfiniCor300	62.5 μ m	2	-37.21	-39.80	0.53	0.58
Spectran GIF625	62.5 μ m	2	-37.21	-38.70	0.53	0.50

Table 4.5. SMS IFPI characteristics using different multimode fiber

4.4. SSS IFPI Sensor Fabrication

Using single-mode fiber as the cavity material in SSS IFPI is attractive. First, the single-mode fiber could have the closest MFD if not the same to that of the single-mode fiber used in the transmission line. Thus the MFD mismatch induced insertion loss is minimized or even cancelled. Second, by using the specially designed single-mode fiber, the reflection can be largely increased, which would improve the signal-to-noise ratio. Third, by using the single-mode fiber as the cavity material, the fundamental mode to higher order mode coupling is avoided, because only the fundamental mode is allowed in the cavity. Thus the inter-modal interference problem is eliminated. Thus by using the SSS IFPI, the number of sensors can be significantly increased, and the signal-to-noise ratio as well.

4.4.1. Ideal single-mode fiber for SSS IFPI applications

The ideal single-mode fiber for the SSS IFPI applications would be the fiber that has the same MFD as the single-mode fiber used on the transmission line, while has large enough core refractive index difference to produce large enough reflection.

Unfortunately, such single-mode fiber does not exist. Because most of the commercially available single-mode fibers are targeted at the fiber communication market, the core index difference has to be minimized to cancel the splicing reflection. The splicing reflection is normally kept under -60dB. But in SSS IFPI applications, the large splicing reflection is desired. -60dB splicing loss is too low for the sensor interrogator to detect.

Thus for SSS IFPI applications, special single-mode fiber should be designed and fabricated.

Assume the single-mode fiber for the transmission line is Corning SMF28, which has $\Delta = 0.36\%$ and $MFD = 10.4\mu m$ at 1550nm. The cladding refractive index $n_{cladding} = 1.458$. Based on this fiber, the cavity fiber design is shown in Figure 4.26. The single-mode fiber has the same refractive index difference as the Corning SMF28, which is $\Delta = 0.36\%$. To have the same MFD, according to Equation (2.22) the core diameter of the designed single-mode fiber is $9.52\mu m$, which is larger than the $8.2\mu m$ of the Corning SMF28. The cladding and the core is highly doped to obtain the splicing reflection. The core is doped to $\Delta = 2\%$, and the cladding is $\Delta = 1.64\%$ with reference to Corning SMF28 cladding refractive index. The cladding has two layers: the inner layer with $\Delta = 1.64\%$ is a thin layer. The light will be bounded by this layer, and can not 'see' the outer layer. The outer layer has the same refractive index as the Corning SMF28 cladding, which is 1.458. This layer has no function in the waveguide structure. It saves the doping material in the fiber fabrication. In the single-mode fiber preform fabrication using MCVD method, the high purity quartz tube is first deposited with a thin layer of high purity silica to minimize the cladding induced attenuation, and this layer is the outer cladding layer. The tube is later deposited with the inner cladding layer, which is $\Delta = 1.64\%$. Finally the core is $\Delta = 2\%$ doped. The preform is then clasped, and brought to the fiber draw tower to pull the single-mode fiber.

For this idea single-mode fiber, the launched power is either reflected or transmitted. No power is being lost by radiation. The calculated interface reflection is -41.83dB, the insertion loss of a SSS IFPI sensor is less than 0.001dB.

4.4.2. Available single-mode fiber for SSS IFPI applications

Since the specially designed single-mode fiber is currently unavailable, some quick experiments are conducted using the commercially available single-mode fibers. Because these fibers are not designed for the IFPI applications, the splicing reflection is usually very small if can be detected. OTDR is used to evaluate the reflection because it has larger dynamic range than the si720 system, although its noise is larger too. si720 system is used to evaluate the transmission characteristics.

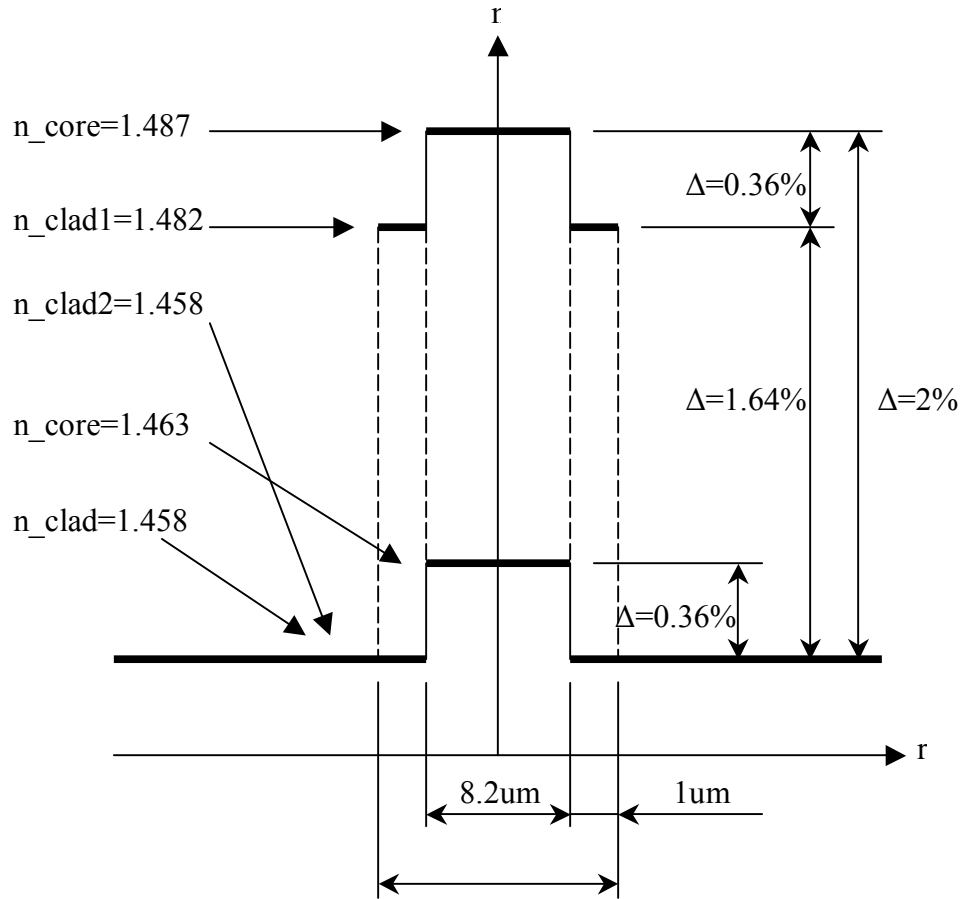


Figure 4.26. Special single-mode fiber design for SSS IFPI applications

In the first experiment, the SSS IFPI based on 11 different single-mode fibers from 6 vendors are evaluated. The single splice point reflection is characterized by OTDR at -45dB sensitivity/div. The insertion loss of the SSS IFPI sensor is characterized by the si720 system. The MFD, Δ and the characteristics are listed in Table 4.6. Fiber with small MFD mismatch demonstrates low insertion loss. The insertion loss for Corning HI1060Flex is only -0.01dB, and it also has considerable reflection. But this reflection is still small when compared with the single-mode fiber to multimode fiber interface reflection. The SSS IFPI sensor interference spectrum using Corning HI1060Flex fiber is shown in Figure 4.27. The SM reflection is 15dB higher than the SS reflection. The sensor interrogator should have dynamic range larger than the si720 system to use the SSS IFPI based on Corning HI1060Flex fiber; otherwise the signal-to-noise ratio is too high for such system.

SMF	Vendor	Δ (%)	MFD(μ m)	Splice reflection (OTDR sensitivity@-45dBm/div)	Insertion loss(dB)
HI1060Flex	Corning	1	6.3@1550nm	2.7	0.01
HI1060LH	Corning	0.45	6.2@1060nm	0.4	0.08
SCSM1060HPI	StockYale	NA	9.4-10.5@1550nm	0.2	0.23
BIF_1550_L2	StockYale	NA	6.3-7.5@1550nm	0.3	0.01
BF06160	OFS	NA	5.8@1550nm	3	1.39
BF06158	OFS	NA	7.5@1550nm	2.7	0.12
FS_SC_5924	3M	NA	3.0@1060nm	1.3	14.30
FS_SC_5624	3M	NA	6.6@1060nm	1.8	0.45
FS_SN_4224	3M	NA	5.5@820nm	3.5	10.70
980HP	Fibercore	NA	4.2 μ m@980nm	2.1	-0.26
CF04246_30	OFS	NA	NA	1.3	-0.09

Table 4.6. Different SMF based SSS IFPI

In the second experiment, the SS reflection and SSS IFPI transmission characteristics versus fusion splice arc power, duration and overlap is studied, and the result is presented in Figure 4.28. The fusion splice arc power and duration would not change the sensor insertion loss, but increasing arc power or arc duration will degrade the reflection sharply.

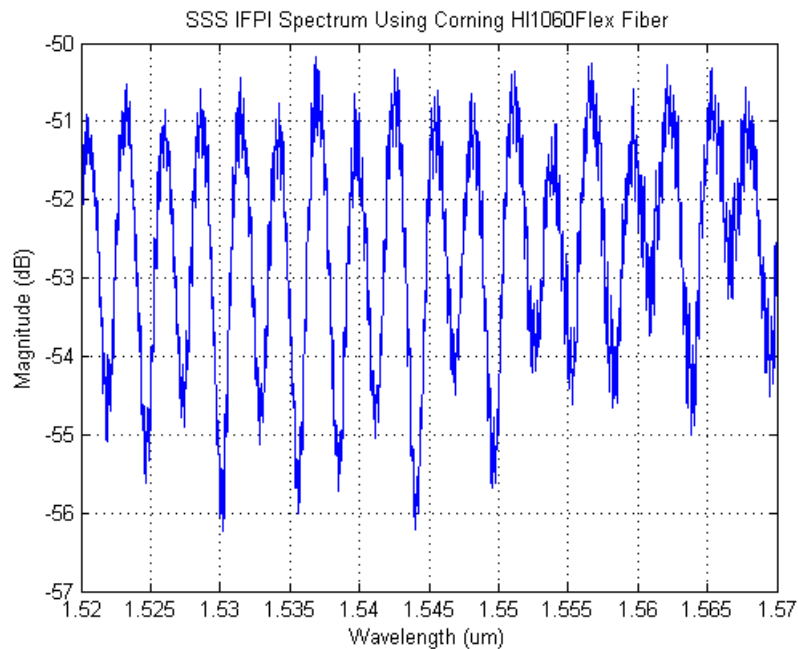
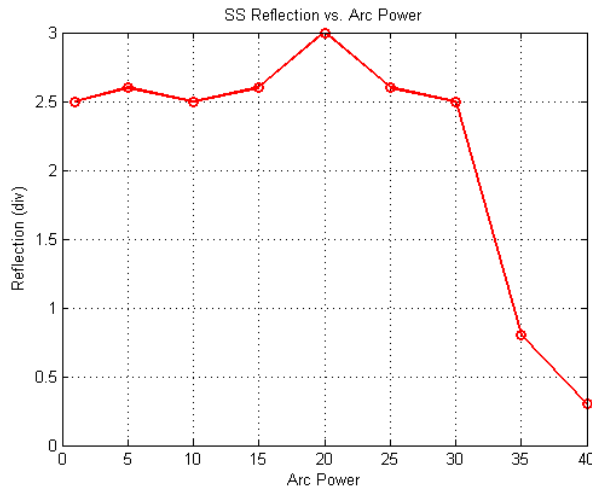
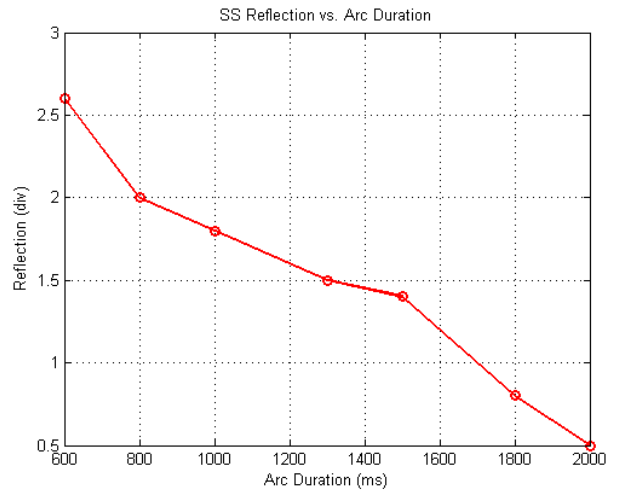


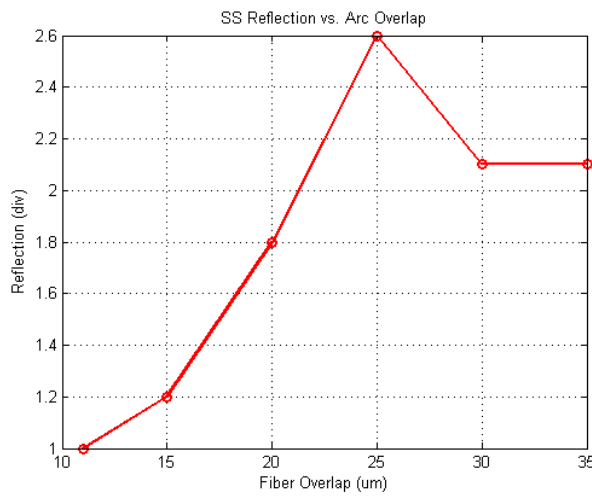
Figure 4.27. Corning HI1060Flex fiber based SSS IFPI spectrum



(a) SS reflection versus splice arc power



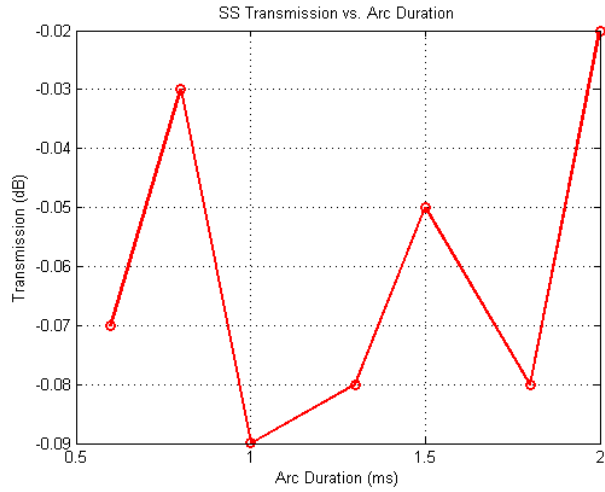
(b) SS reflection versus splice arc duration



(c) SS reflection versus splice overlap



(d) SSS transmission vs arc duration



(e) SSS transmission vs. arc duration

Figure 4.28. Fusion splicing parameter effect on SSS IFPI sensor characteristics

Chapter 5. SxS IFPI Sensor Performance Evaluation and Sensor System Analysis

With the SxS IFPI sensor and sensing system principles, sensor fabrication and characterization optimization discussed in detail in the previous chapters, this chapter will be focusing on the performance evaluation of SxS IFPI sensor and sensor system analysis. Some of the most commonly used terminology for optical sensing system specifications and performance characteristics are defined first, followed by the performance of the sensor system.

5.1 Definitions of Performance Characteristics

A wide range of terms has been used to describe the essential performance characteristics of measurement instruments and sensors. The most widely used terms include repeatability, precision, accuracy, resolution, sensitivity, stability, hysteresis, and frequency response [71]. There is always a trade-off among these specifications that can be achieved at a given cost. The intention of this section is to provide clear definitions for the terms used to describe the performance of the SxS IFPI sensing system.

Repeatability

The repeatability of an instrument is an indication of its ability to give the same measurement results on the same quantity with repeated measurements under the same conditions. An instrument with good measurement repeatability needs a good design and should be carefully manufactured, so it can provide the same readout. But an instrument with good measurement repeatability does not necessarily mean that it has a good accuracy, since it could give the same wrong answer all the time.

Accuracy

The accuracy of an instrument indicates the deviation of the measurement results from the true value of the measurand, so it is a measure of its ability to tell the truth. Accuracy can be expressed as a percentage of the full scale readings, or as an absolute value over all working ranges of the instrument. Accurate calibration on repeated measurement results against a standard is necessary for a good accuracy for the instrument.

Resolution

Resolution or sensitivity of an instrument is defined as the minimum resolvable change in the value of the measurand. The resolution of an instrument can be interpreted by the statistical standard deviation of a series of measurements under stable circumstances. It is common to use twice the standard deviation as the direct measurement of the resolution. The resolution for an instrument usually has different values for different measurement scales.

Stability

It is defined as the capability of an instrument to maintain the same output within a specific length of a time period. The stability of an instrument is usually measured by the quantity of drift compared to a standard, which is a well-calibrated measurement instrument.

Hysteresis

If there is a difference between outputs for a given value of the measured quality when the value is approached from above or below, an instrument is said to exhibit hysteresis. It can be significant when rapid level fluctuations are likely to occur, as the result of mechanical friction, magnetic effect, elastic deformation or thermal effects.

Frequency response

This is a measure of the sensor's capability to track dynamic changes of the measurand.

5.2. SxS IFPI Sensor Temperature Performance

In this set of experiments, the temperature characteristics of the SxS IFPI sensor are evaluated. The sensor used is SMS IFPI sensor employing Corning SMF2850 GI multimode fiber with 50 μ m core diameter. The experiments investigated the relation of the SM reflection, transmission and SMS IFPI sensor signal to the changing temperature; the unit SMS IFPI temperature sensor performance; the long-term stability of the SMS IFPI sensor under high temperature. The data and discussion is listed as follows.

5.2.1. SM interface reflection versus temperature

The purpose of this experiment is to understand if the SM interfaces reflection changes with temperature, or changes with time under elevating temperature. To explore this issue is crucial, because if the reflection degrades rapidly with the elevating temperature or

prolonged duration under high temperature, the sensor's signal-to-noise ratio will degrade resulting in degraded performance.

The single SMS IFPI sensor is packaged with a stainless steel pipe, and inserted into the furnace (ThermaLyne 48000). The fiber is taped down to the bench to cancel the fiber bending induced intensity fluctuation. The fiber end-face reflection is frustrated by both bending the fiber into small radius and using the index-matching gel. The reflection spectrum is recorded by the si720 system. The temperature is increased at 50°C per step to 800°C . The temperature is kept at each level for 1 hour. The reflection spectrum is recorded every 3 minutes to monitor possible change or fluctuation.

The obtained SM interface reflection spectrum versus temperature is shown in Figure 5.1. The maximum power fluctuation is within 1dB over the entire RT- 800°C temperature range. The increase of light power at high temperature is caused by the blackbody radiation. The random power fluctuation is caused by the si720 light source fluctuation and detection noise. The SM interface reflection is stable over large temperature range. The SM interface reflection spectrum under 100°C , 400°C and 800°C with each temperature level for 1 hour is shown in Figure 5.2. The power fluctuation is mainly caused by the interrogator noise and the light source.

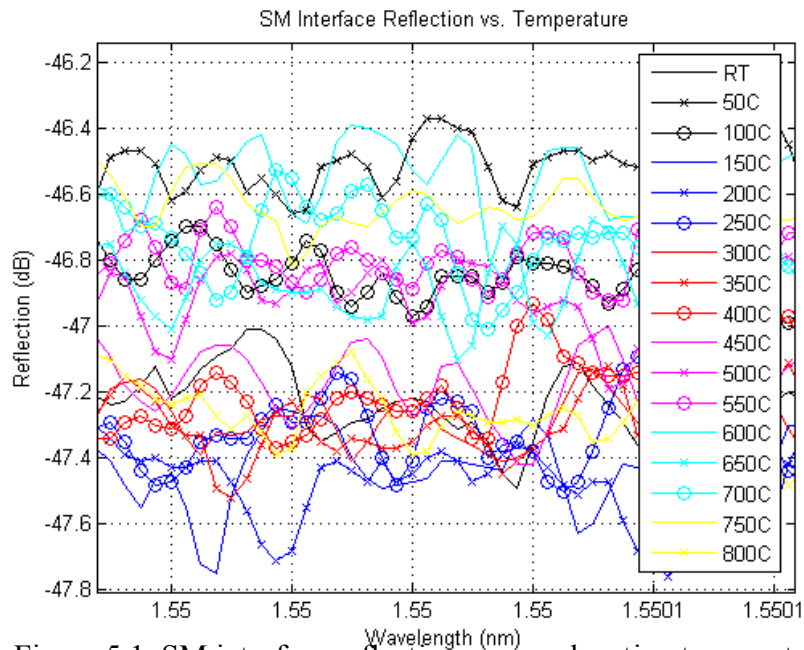
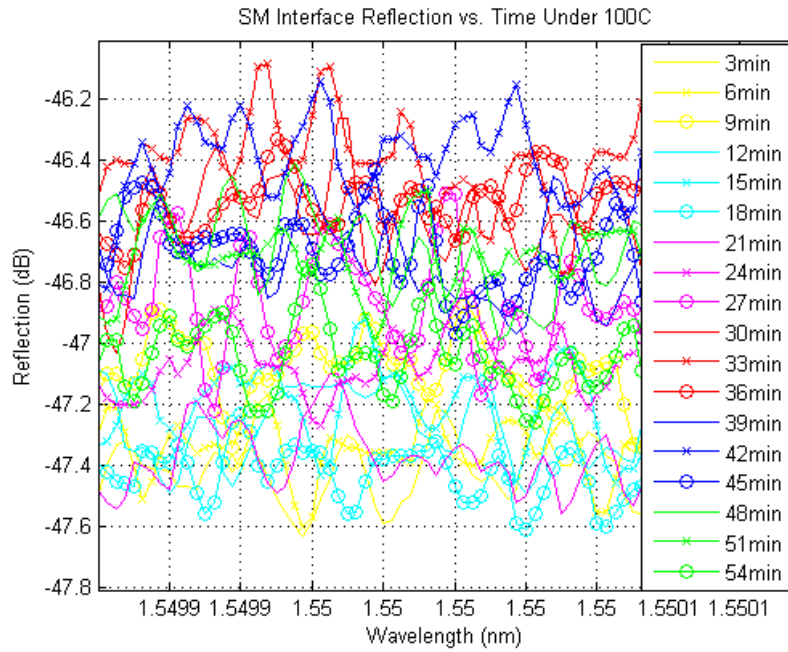
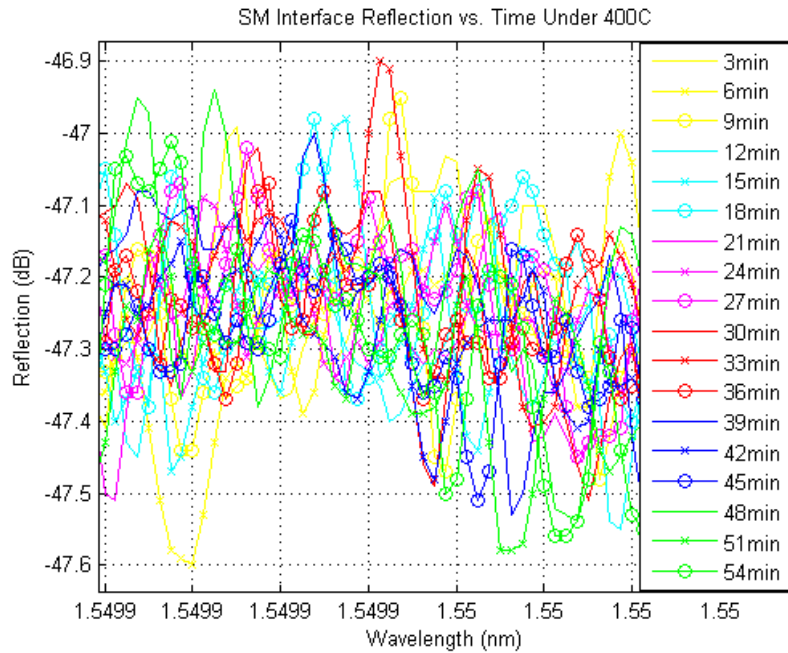


Figure 5.1. SM interface reflection versus elevating temperature

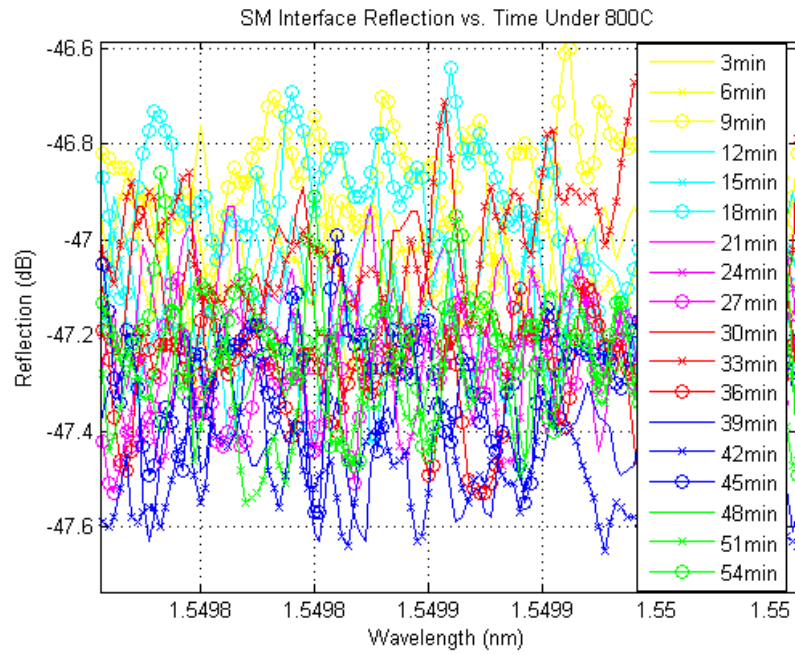
The SM interface reflection at 1520, 1550 and 1570nm at $50^{\circ}C$ a step to $800^{\circ}C$, each step for 1 hour is shown in Figure 5.3. The fluctuation is within 0.5dB. The increase is due to the blackbody radiation.



(a) 100C



(b) 400C



(c) 800C

Figure 5.2. SM reflection stability under different temperatures

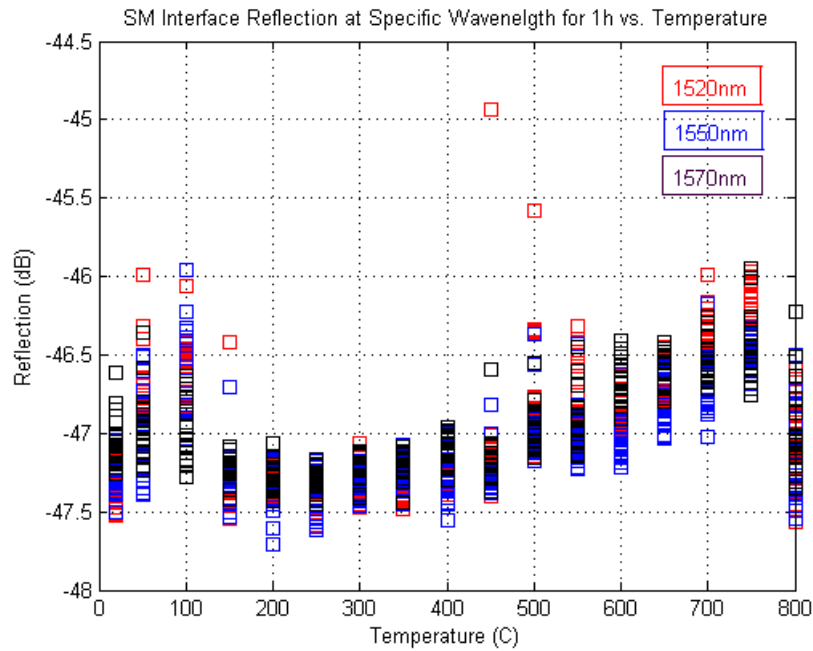


Figure 5.3. SM reflection at elevated temperatures

5.2.2. SMS IFPI transmission versus temperature

The transmission of SMS IFPI sensor under varying temperature is studied. The ideal sensor transmission would not change with temperature. If the sensor's insertion-loss varies with temperature, the signal-to-noise ratio of the each sensor will be subject to the sensors multiplexed between the terminal sensor interrogator and this sensor. This effect is considered harmful to the sensing system and needs to be investigated. In this experiment, the experimental setup is the same as the previous experiment, except the transmission spectrum is monitored by the si720 system. The temperature is increased with 50°C a step to 800°C , with temperature rested at each level for 1 hour. The transmission spectrum is recorded every 3 minutes.

The SMS IFPI transmission spectrum against temperature is shown in Figure 5.4. The power fluctuation is within 0.3dB over the entire temperature range. The increase of light power at high temperature is caused by the blackbody radiation. The random power fluctuation is caused by the si720 light source fluctuation and detection noise. The sensor transmission is stable over large temperature range.

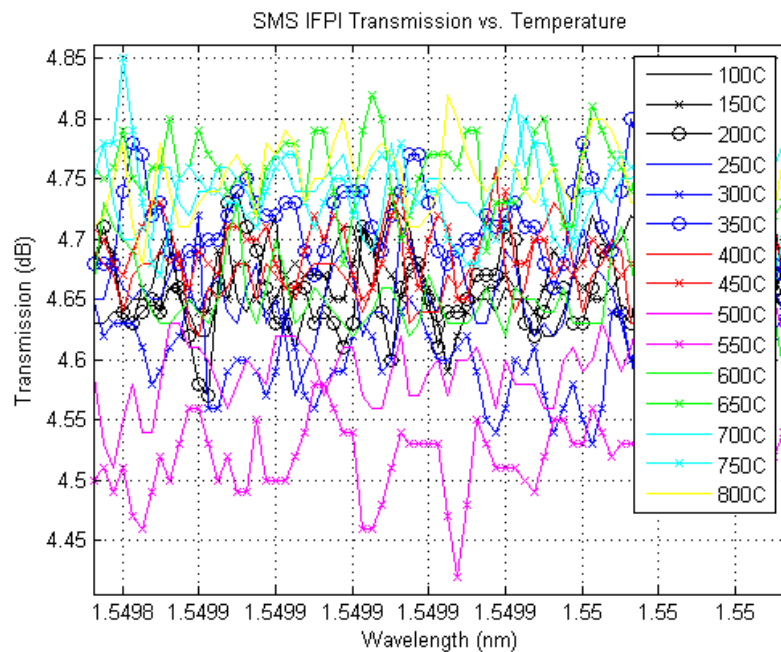


Figure 5.4. SMS IFPI transmission versus elevating temperature

The SMS IFPI transmission spectrum under 100°C , 400°C and 800°C each temperature level for 1 hour is recorded. No power fluctuation is observed.

The SMS IFPI transmission at 1520, 1550 and 1570nm at $50^{\circ}C$ a step to $800^{\circ}C$, each step for 1 hour is shown in Figure 5.5. The fluctuation on average is within 0.3dB. The loss is due to the thermal expansion induced MFD mismatch insertion loss.

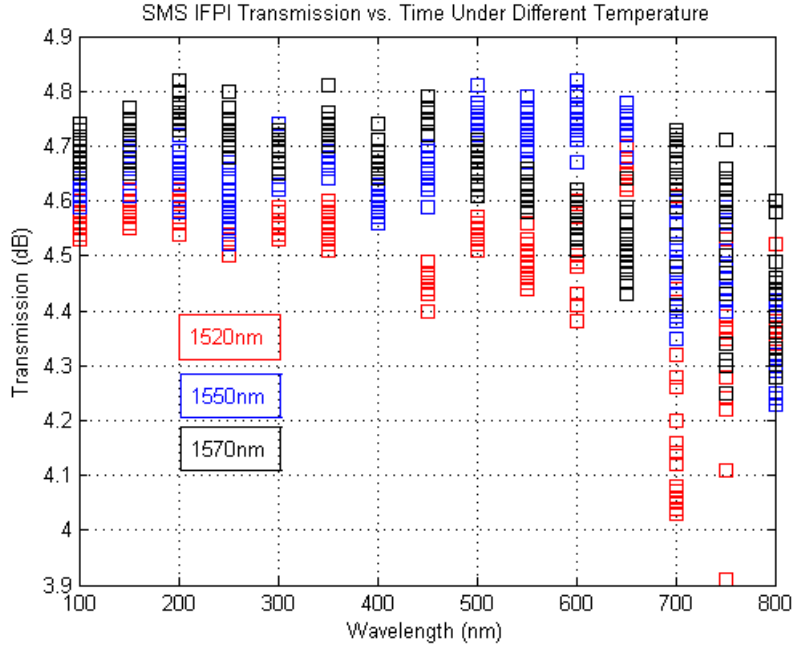


Figure 5.5. Power fluctuations at different wavelengths

5.2.3. SMS IFPI signal versus temperature

The spectrum of an SMS IFPI sensor under varying temperature is studied. If the sensor interference fringe visibility degrades with elevating temperature or prolonged duration under high temperature, its Fourier transform peak power will decrease and result in degraded signal-to-noise ratio and large measurement error. The experimental setup is the same as that of the previous experiment. The temperature is increased $50^{\circ}C$ a step to $800^{\circ}C$. The temperature is kept at each level for 1 hour. The sensor interference spectrum is recorded every 3 minutes.

The SMS IFPI signal against temperature is shown in Figure 5.6. The SMS IFPI signal under $100^{\circ}C$, $400^{\circ}C$ and $800^{\circ}C$ each for 1 hour is shown in Figure 5.7. The result shows that the sensor interference fringe visibility does not change with elevating temperature.

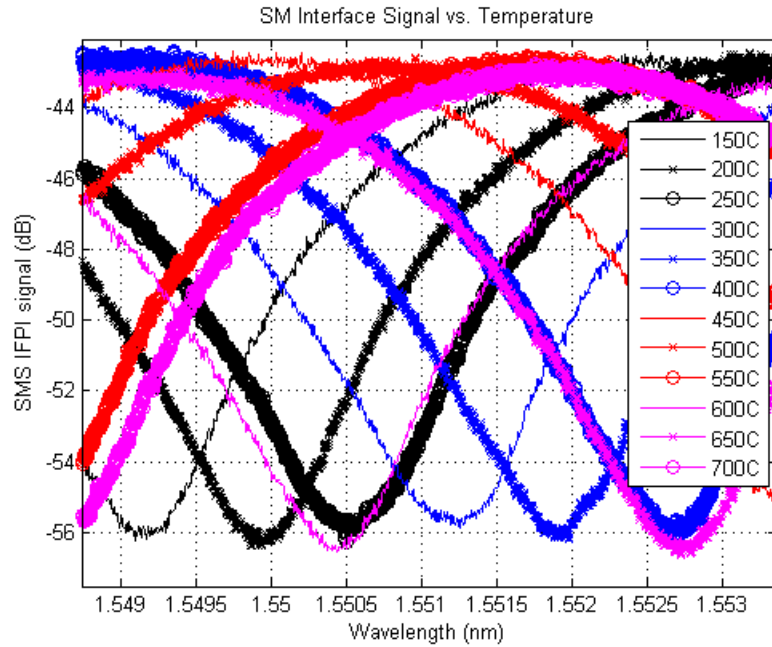
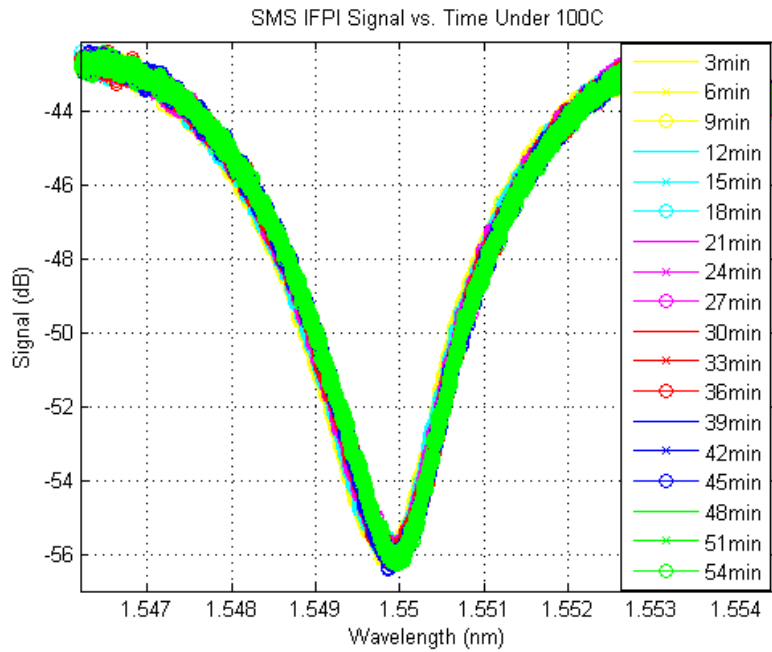
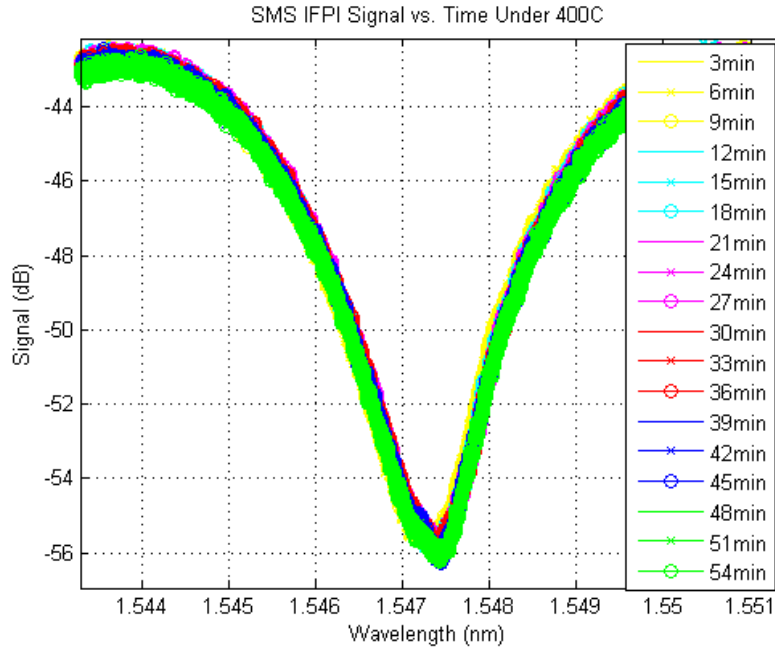


Figure 5.6 SMS IFPI sensor signal vs. temperature



(a) 100C



(b) 400C

Figure 5.7 SMS IFPI sensor under different temperature for 1 hour

5.2.4. SMS IFPI temperature performance

The SMS IFPI sensor’s temperature characteristics are evaluated through the following experiments. The sensor is co-positioned with a thermocouple (K-type, Omega) in a double-bore ceramic tube and placed in a furnace (Thermolyne 48000). The K-type thermocouple has 1.1°C accuracy and a working range of -200—1250°C. The Thermolyne furnace has an accuracy of 1°C and working temperature range of RT—1200°C. Because of the large volume of the furnace and its heating element spatial arrangement, the temperature is not even at different places within the furnace. The function of the ceramic tube is to damp the temperature fluctuation. The temperature is increased with 50°C a step and 1hrs at each step from room temperature (RT) to 600°C and back to RT for 5 cycles. The sensor cavity length is sampled at 1Hz frequency. Because of the temperature control mechanism of the furnace, the temperature would exceed the preset temperature level 10—20°C. It takes 10—20mins for the temperature to get back to the preset level. Thus in the experiment, only the second half of the 1hrs data is considered reliable. The 30mins time average of the sensor cavity length and thermocouple reading is used.

5.2.4.1. Sensor temperature calibration

During the calibration process, the sensor is heated from room temperature to 600°C. Each sensor cavity length value obtained and each of the real-time temperatures acquired from the thermocouple are related simultaneously and stored in the computer. By taking the average of the temperatures within the temperature-holding period, the measurement error is minimized. The one-to-one relation of the applied temperature and the OPD was then used to find the calibration equation through a polynomial curve-fitting. With the minimum root mean square error between the experimental results and the fitting-curve, experimental results revealed that the optimal order of the polynomial curve-fitting is 3:

$$T = 6.3676OPD^3 - 15.964OPD^2 + 182.55OPD + 316.61 \quad (5.1)$$

The 5-round OPD vs. temperature test result is shown in Figure 5.8. With the averaged OPD vs. temperature curve, the sensor calibration curve and the cubic fitting curve is shown in Figure 5.9. With the calibrated sensor, the performance of the sensing system, such as repeatability, accuracy compared to the thermocouple and temperature measurement resolution can then be evaluated in detail.

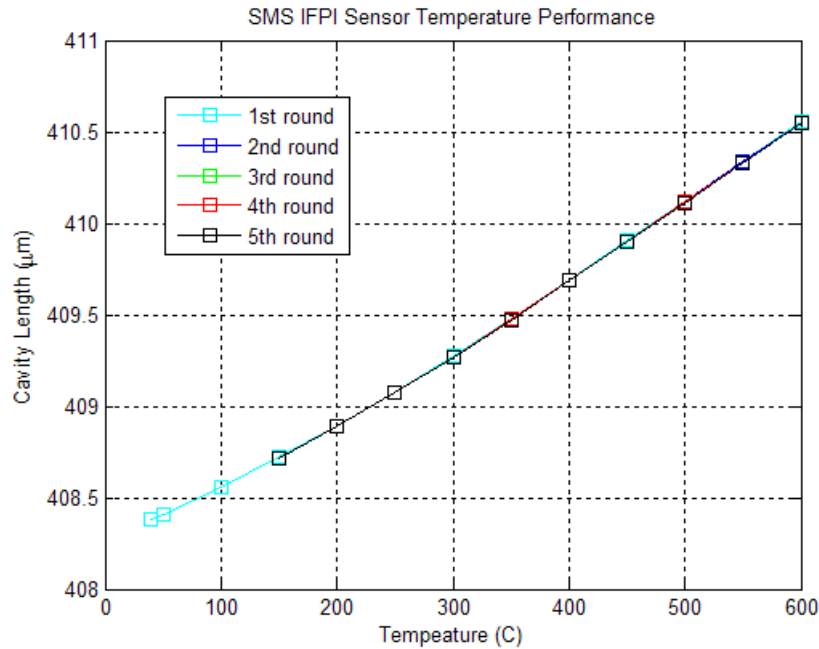


Figure 5.8. Temperature performance of the SMS IFPI sensor

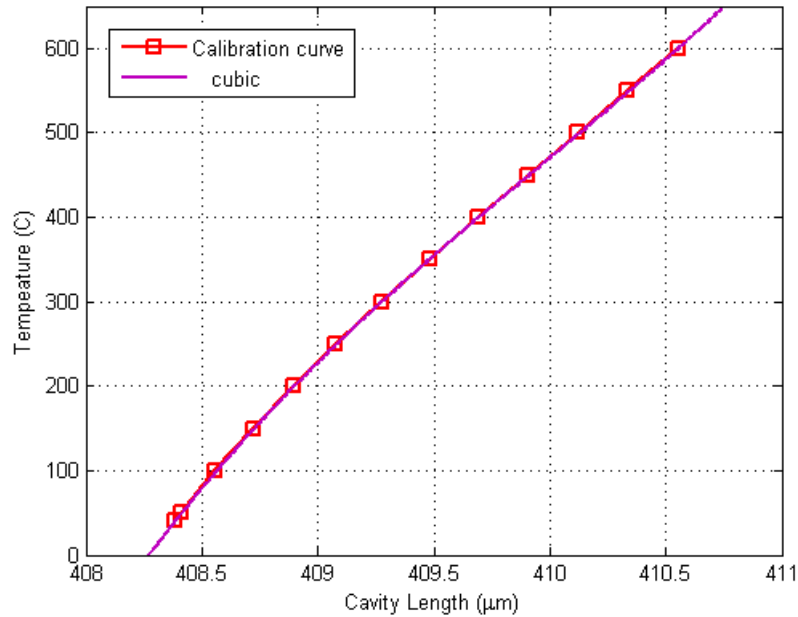


Figure 5.9. Calibration curve of the tested SMS IFPI sensor

5.2.4.2. Sensor repeatability

Repeatability of the sensor can be evaluated by applying temperature to a certain preset point repeatedly from one direction (increasing or decreasing). The largest difference of the sensor output readings can be used to specify the repeatability of the sensor.

With an SMS IFPI sensor with 408μm initial cavity length at room temperature, 4 consecutive measurements were performed from 150 to 600°C. The results are shown in Figure 5.10. The temperature values on the x-axis are the four-time averaged temperature readouts of the SMS IFPI sensor, and the temperature values on the y-axis are the SMS IFPI sensor readouts. As shown in Figure 5.11, the maximum deviation between the measured temperature and the averaged temperature is within the range of ±0.5°C. The normalized repeatability of the sensor system with respect to its dynamic range is therefore ±0.1% of the full measurement scale. This is the measurement precision that this system can achieve.

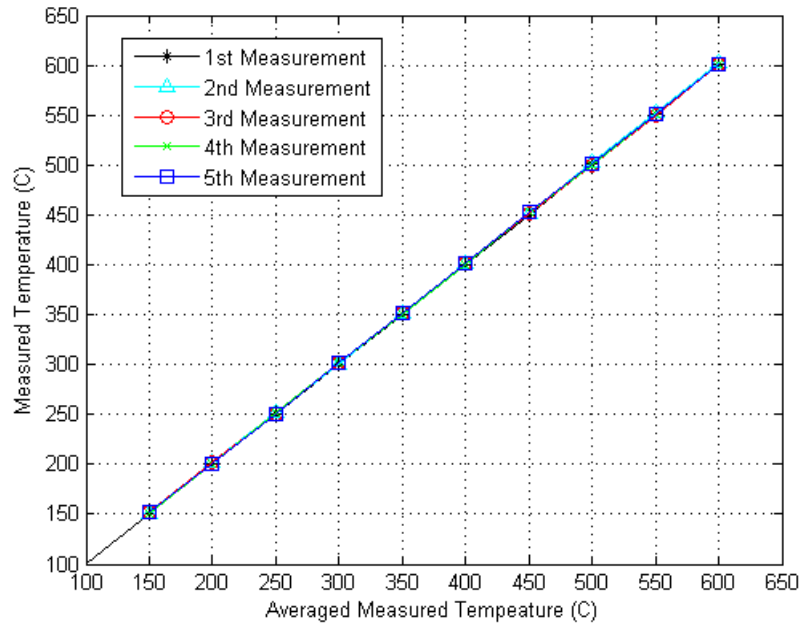


Figure 5.10. SMS IFPI temperature sensor repeatability test

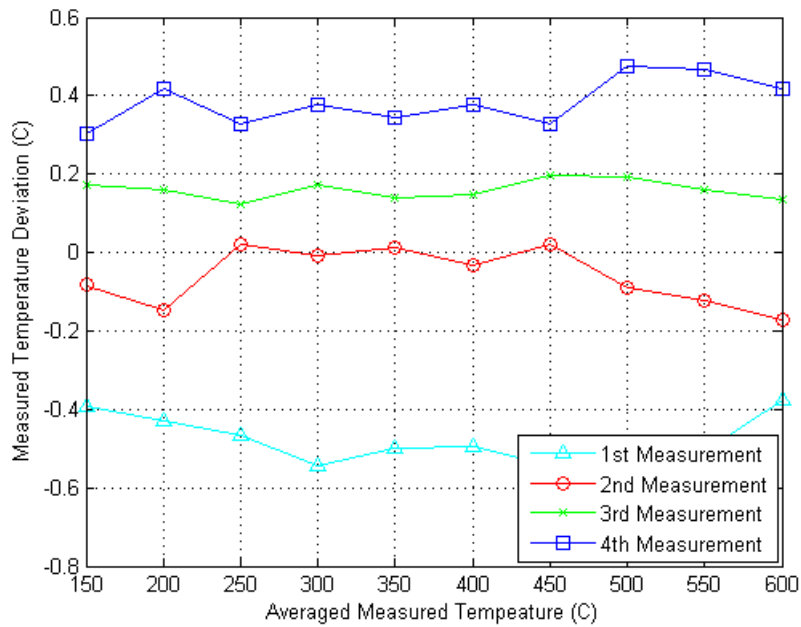


Figure 5.11. SMS IFPI temperature sensor maximum temperature deviation

5.2.4.3. Sensor accuracy

The K-type thermocouple is used for the sensor system calibration from 150 to 600°C. The K-type thermocouple has a resolution of 0.05°C and an accuracy of ±1.5°C. Figure 5.12 shows the SMS IFPI temperature sensor readout deviations from the thermocouple reference for each of the measurements, which gives accuracy in the range of ±1.5°C. The accuracy of the SMS IFPI sensor is the same with the K-type thermocouple, which is ±1.5°C and ±0.33% of the measurement range. This implies that the SMS IFPI sensor has at least equal if not better accuracy with the K-type thermocouple.

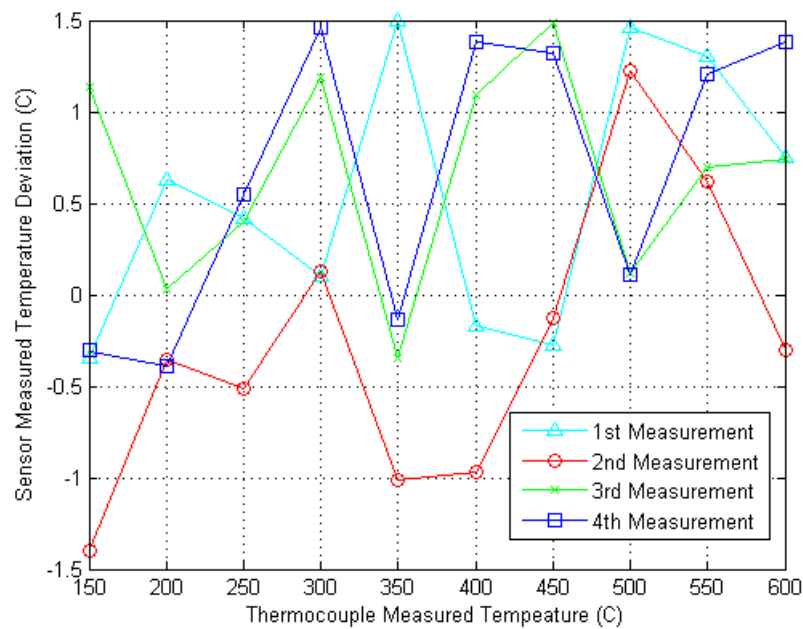


Figure 5.12. SMS IFPI temperature sensor accuracy test

5.2.4.4. Sensor resolution

Fiber optic sensor has high resolution by detecting differential phase changes. The resolution of the sensor system can be interpreted by its standard deviation of a series of temperature measurements at one constant temperature value. It is common to use twice the standard deviation as the direct measurement of the resolution. The evaluation of the sensor resolution was performed using a calibrated sensor at room temperature and also at 600°C for 20mins respectively. The temperature readout of the SMS IFPI sensor is sampled at 1Hz. The standard deviation of the temperature data was calculated to be $\sigma=0.0408^{\circ}\text{C}$ and $\sigma=0.0562^{\circ}\text{C}$. Therefore the resolution of the sensor system is estimated

to be $2\sigma=0.0816^{\circ}\text{C}$ and $2\sigma=0.1124^{\circ}\text{C}$. The normalized resolution with respect to the dynamic range of the system is 0.019%.

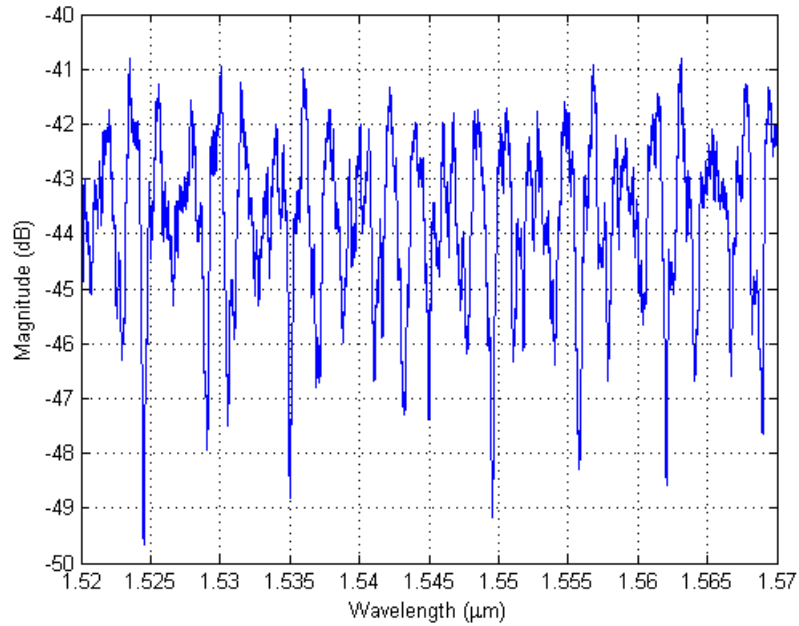
5.3. SxS IFPI Quasi-Distributed Temperature Sensor Field Test

A field test was conducted for the SxS IFPI quasi-distributed temperature sensor at Tennessee Valley Authority (TVA) in April 2005. The sensors were installed in the boiler facility in the power plant. The function of the boiler is to transfer the heat of the combusted gas to the embedded water pipe. The heat absorbed by the water pipe is used to turn water into steam and therefore to power the turbine engine to generate electricity. The hot exhaust gas at the same time is cooled by the water pipes and then delivered to the next processing unit to get rid of the hazardous gas components, such as NO, CO and SO_x before draining into the air. If the temperature gets too high, the vicious chemical components will start to corrode the boiler and the water pipes. If the temperature gets too low, the heat exchange will be inefficient. Thus the temperature in the boiler has to be carefully controlled in a narrow range. In this field test, the developed SxS IFPI quasi-distributed temperature sensor is used to real-time monitor the temperature profile across the transection of the boiler. In the future, the temperature readouts can be used for dynamic combustion control.

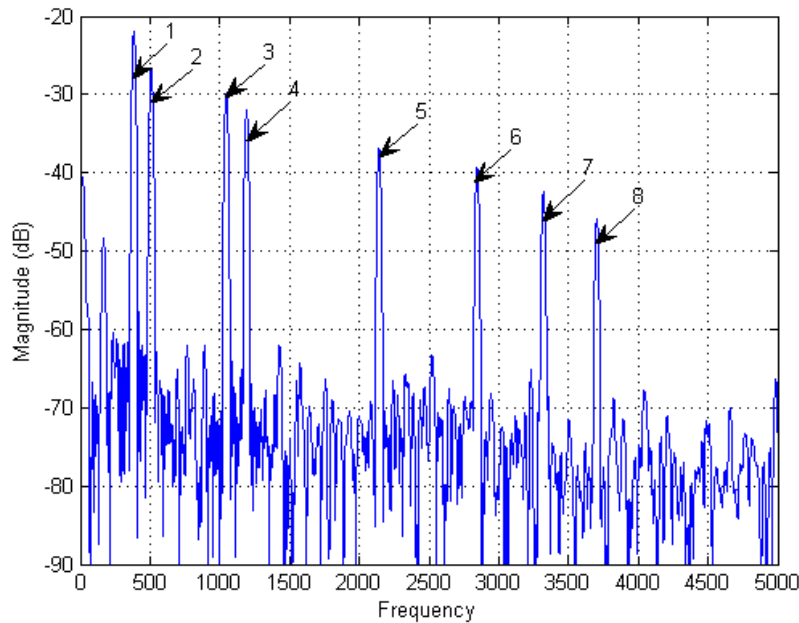
The transaction of the boiler is a 12×5m area. The operation temperature is 400°C, the operation pressure is slightly above atmosphere pressure to keep the hot gas circulating. The gas is rich in NO_x, CO_x and SO_x components. 2 set of quasi-distributed sensor lines are made, each with 8 SMS IFPI sensors. The spacing of the SMS IFPI sensors is 1m. The sensors are coated with fiber recoater to give extra protection at the sensing area. The normalized calibration curve from previous test is used for each sensor. The optical spectrum and its Fourier spectrum of the sensors are shown in Figure 5.13. One end of the single-mode fiber is reflection frustrated and sealed in silica tubing. The other end is terminated with FC connector.

During field installation, a stainless steel tube is first fixed into the boiler with the two terminals fixed on the two ports of the boiler at each side. The sensors are then deployed into the stainless steel tube. The FC connector is fixed to the stainless steel tube. The Micron Optics si720 system and the laptop is located in the control room one deck above.

The laptop is connected to the internet via a telephone line. The sensor readout is real-time monitored at Virginia Tech through the internet. The photos of sensor installation is shown in Figure 5.14.



(a) Optical spectrum of 8 SMS IFPI sensors multiplexed

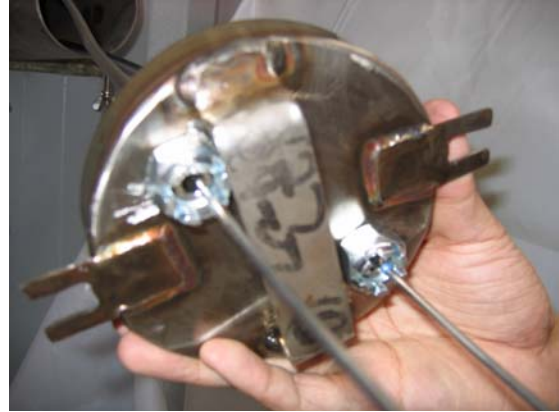


(b) Fourier spectrum of 8 SMS IFPI sensors multiplexed

Figure 5.13. Spectrum of the SMS IFPI sensors



(a) inside the boiler



(b) sensor terminal cover



(c) cable tray



(d) interrogator and laptop

Figure 5.14. Field test pictures

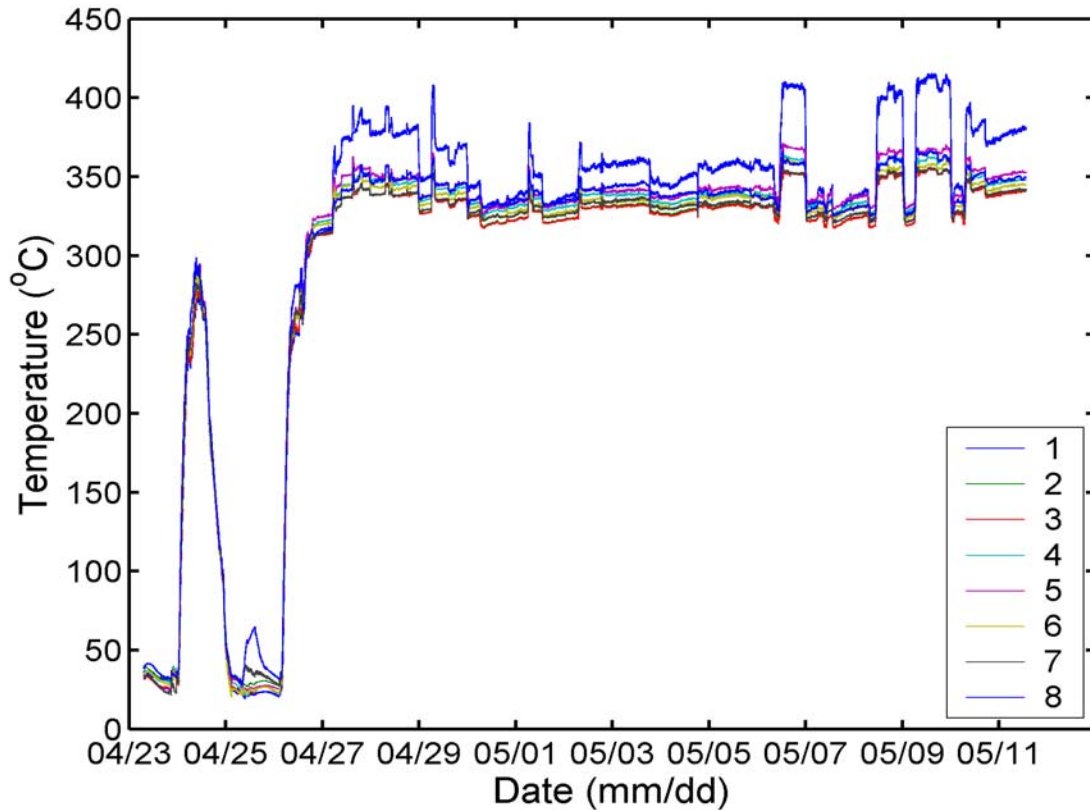
The test runs from April 4th to May 15th. The si720 system was taken back because the test goal is achieved. The sensor is still in good condition when the system is retrieved. The temperature profile for a 20-day period is shown in Figure 5.15.

5.4. SxS IFPI Sensor Strain Performance

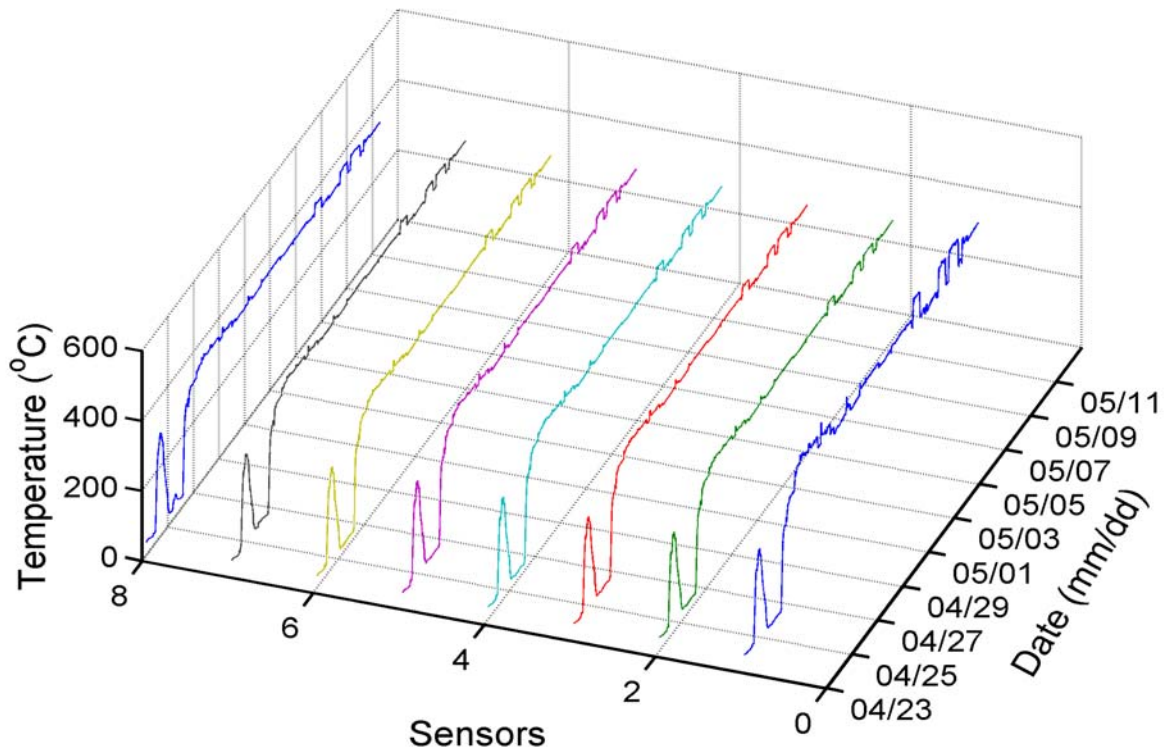
In this set of experiments, the SxS IFPI sensor strain characteristics are evaluated. The sensor used is SMS IFPI sensor employing Corning SMF2850 GI multimode fiber with 50 μ m core diameter. Although the evaluation is based on the SMS IFPI, other SxS IFPI strain sensor is expected to demonstrate the similar behavior. The experiments investigated the SMS IFPI sensor signal and transmission under elevated strain level; the

unit SMS IFPI strain sensor performance evaluation and the frequency response of the strain sensor.

The general experimental setup is shown in Figure 5.16. A rectangle is cut from an aluminum sheet to form the cantilever beam. The cantilever beam is first polished on one side and then cleaned with alcohol. The SMS IFPI sensor and the foil strain gauge (Measurements Group, Inc, CEA-09-125UW-350) are co-located on the beam using cement (Measurements Group, Inc, M-Bond 610) as shown in Figure 5.16. The foil strain gauge is connected to a signal conditioning amplifier. The amplified signal from the foil strain gauge is viewed from a multimeter. The cantilever beam is clamped at one end and left free on the other end. An optical positioner is used as the beam bender. The fiber is taped down to the bench to cancel the fiber bending induced intensity fluctuation. The SMS IFPI strain sensor is characterized using this setup.



(a)



(b)

Figure 5.15. Temperature profile of the boiler in a 20 day period

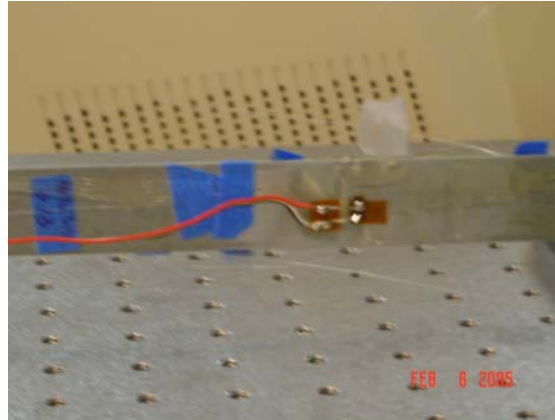
5.4.1. SMS IFPI transmission versus strain

The purpose of this experiment is to understand if the SMS IFPI sensor insertion-loss varies with elevating strain level, or changes with time under fixed strain level. If the sensor insertion-loss increases with elevating strain level, it would degrade the sensor signal-to-noise ratio cascaded after it, resulting in enlarged measurement error. The ideal SMS IFPI strain sensor insertion-loss should not change with strain or time.

The transmission spectrum is recorded by the si720 system. The strain is added by an increment of 50μ from 0 to 520μ . The sensor is resided at each strain level for 15 minutes. The SMS IFPI sensor transmission versus strain is shown in Figure 5.17. No insertion-loss change is observed over the entire measured strain range. The SMS IFPI sensor transmission spectrum under 165μ , 418μ and 519μ each for 10 minutes. No transmission spectrum change is observed.



(a) Strain testing setup



(b) close up

Figure 5.16. Strain testing setup

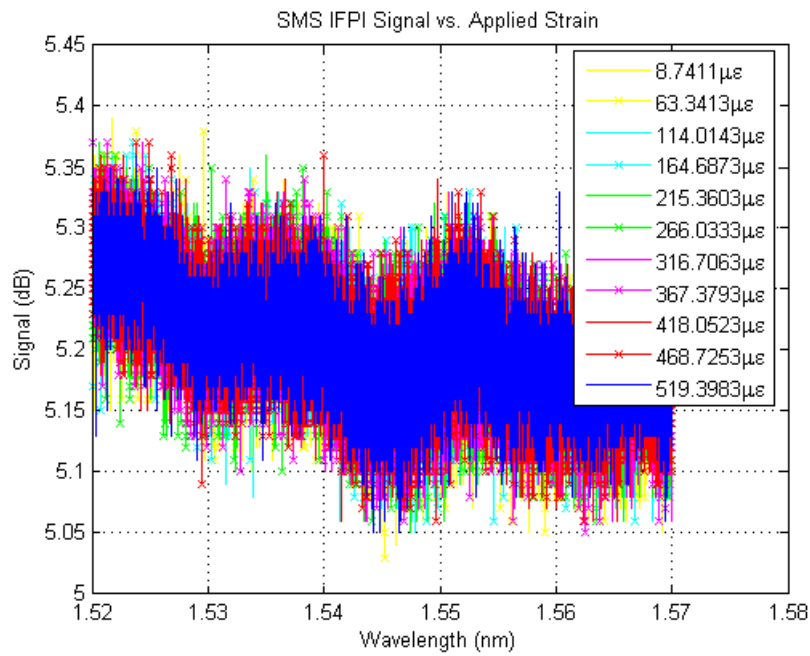


Figure 5.17. SMS IFPI transmission spectrum versus applied strain

5.4.2. SMS IFPI signal versus strain

The purpose of this experiment is to understand if the SMS IFPI sensor signal degrades with elevating strain level, or changes with time under fixed strain level. The ideal SMS IFPI strain sensor signal would be time independent, and the SM, MS reflection, the sensor visibility should not change with strain or time.

The strain is added by an increment of 50μ from 0 to 520μ . The sensor is resided at each strain level for 15 minutes. The SMS IFPI sensor signal versus strain is shown in Figure 5.18. The SMS IFPI sensor signal spectrum under 519μ for 10 minutes is shown in Figure 5.19. The SM, MS reflection and the interference signal visibility is not changed over time and strain. The sensor is stable in the measuring environment.

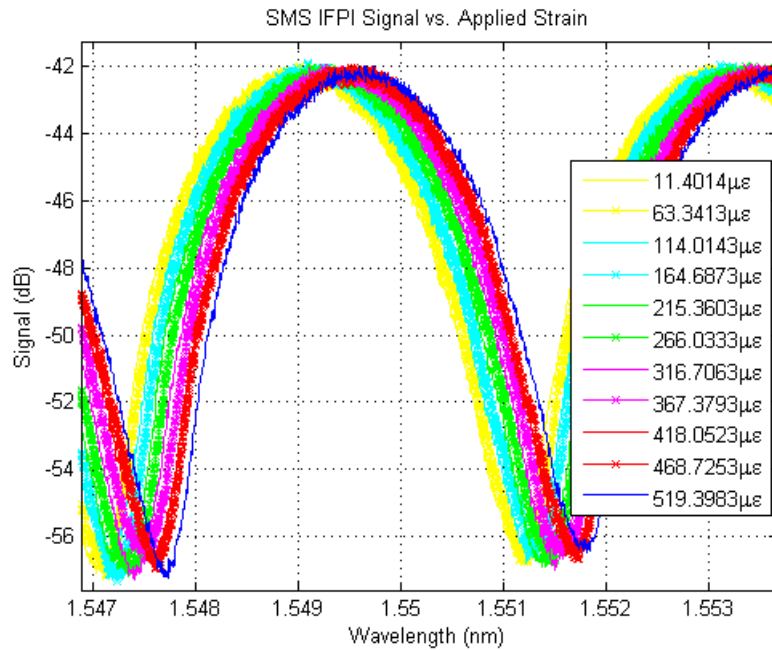


Figure 5.18. SMS IFPI signal versus applied strain

5.4.3. SMS IFPI strain performance

The SMS IFPI sensor's strain characteristics are evaluated through the following experiments. The sensor is co-positioned with a foil strain gauge (Measurements Group, Inc, CEA-09-125UW-350) on a polished aluminum cantilever beam. They are glued down to the beam using special cement developed for this type of application (Measurements Group, Inc, M-Bond 610). The work range of the foil strain gauge is within 5% strain.

5.4.3.1. SMS IFPI strain calibration

During the calibration process, the strain is added by tuning the optical positioner to bend the cantilever beam. The amount of strain added is monitored on the multimeter. The strain is increased at a step of $26\mu\epsilon$ from -520 to $520\mu\epsilon$. At each strain level, the sensor is kept for 3mins let reach stable state. The sensor cavity length is sampled at 1Hz. By

taking the average of the strains within the strain-holding period, the measurement error is minimized. The one-to-one relation of the applied strain and the sensor cavity length was then used to find the calibration equation through a polynomial curve-fitting. Linear fitting is found to have satisfactory result:

$$\varepsilon = 4550OPD - 1.3373 \times 10^6 \quad (5.2)$$

The sensor calibration curve and the linear fitting curve is shown in Figure 5.20. With the calibrated sensor, the performance of the sensing system, such as repeatability, accuracy, stability and hysteresis compared to the foil strain gauge can then be evaluated in detail.

5.4.3.2 SMS IFPI strain repeatability

Repeatability of the sensor can be evaluated by applying strain to a certain preset point repeatedly from one direction (increasing or decreasing). The largest difference of the sensor output readings can be used to specify the repeatability of the sensor.

With an SMS IFPI sensor with 293.92 μm initial cavity length at room temperature, three consecutive measurements were performed from 0 to 520 μe . The results are shown in Figure 5.21. The strain values on the x-axis are the three-time averaged strain readouts of the SMS IFPI sensor, and the strain values on the y-axis are the SMS IFPI sensor readouts. As shown in Figure 5.22, the maximum deviation between the measured temperature and the averaged temperature is within the range of $\pm 3\mu\text{e}$. The normalized repeatability of the sensor system with respect to its dynamic range is therefore $\pm 0.58\%$ of the full measurement scale. This is the measurement precision that this system can achieve. The repeatability test is done in 3hrs. Since the sensor is very temperature sensitive, a small change in temperature would result in false signal in strain measurement. If the temperature of the strain measurement is held very stable, the sensor's strain repeatability can be significantly improved.

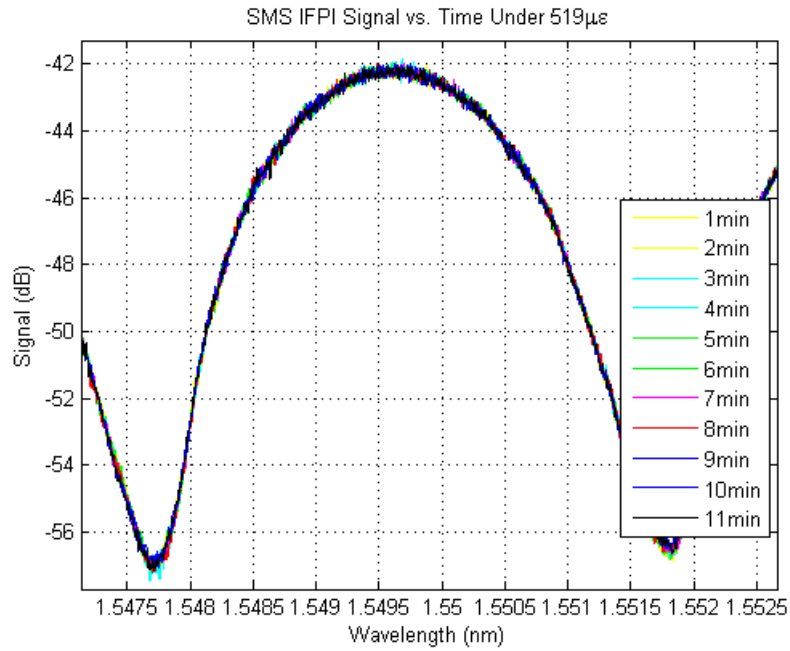


Figure 5.19. SMS IFPI signal versus time under large strain

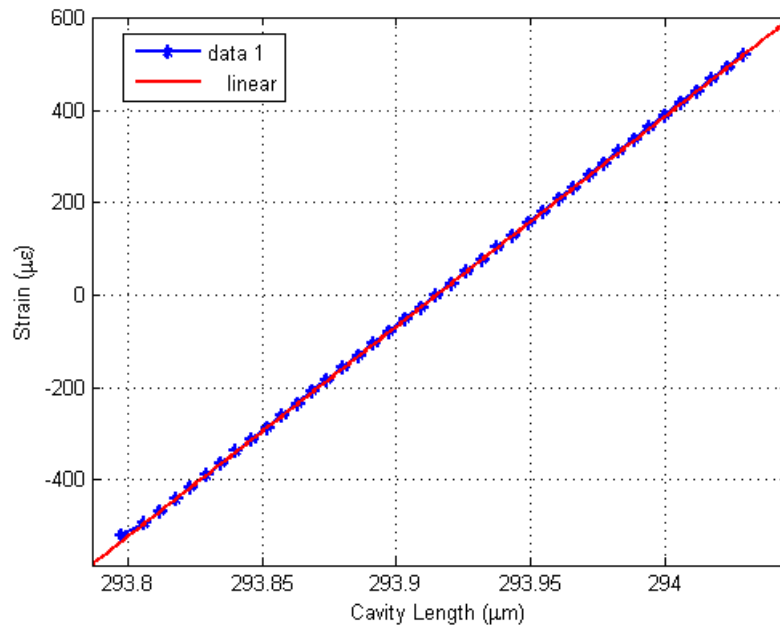


Figure 5.20. SMS IFPI strain sensor calibration curve

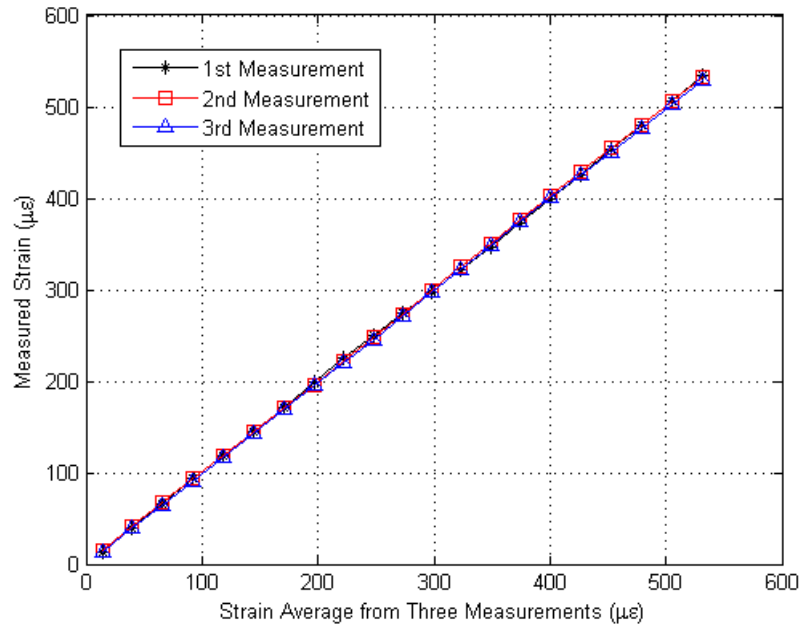


Figure 5.21. Strain repeatability test

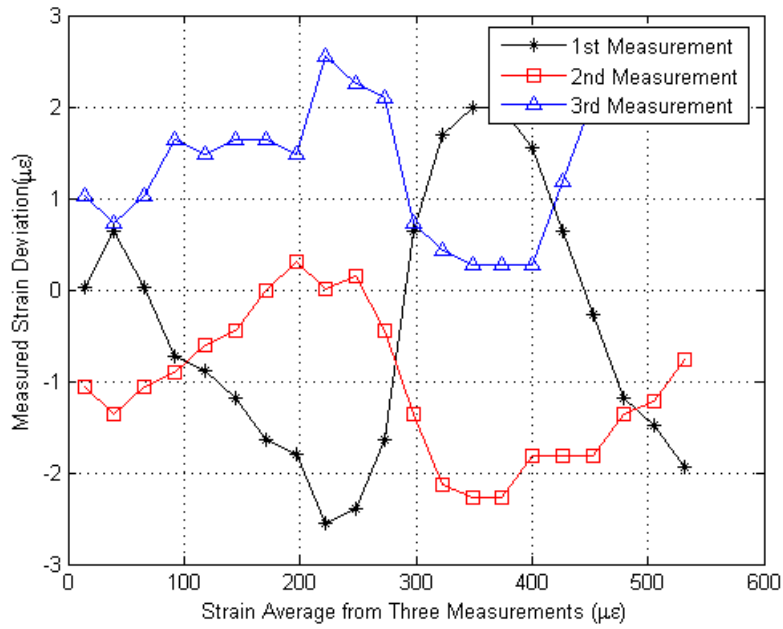


Figure 5.22. Strain repeatability close up

5.4.3.3 SMS IFPI strain accuracy

The aforementioned foil strain gauge is used for the sensor system calibration from 0 to $520\mu\epsilon$. Figure 5.23 shows four measurement results, and Figure 5.24 shows their deviations from the foil strain gauge reference for each of the measurements, which gives accuracy in the range of $\pm 5\mu\epsilon$ and 1% of the measurement range. The test took 3hrs and the temperature variation is not compensated in the test. If the test is conducted in a temperature stable environment, the accuracy of the sensor is expected to be significantly improved.

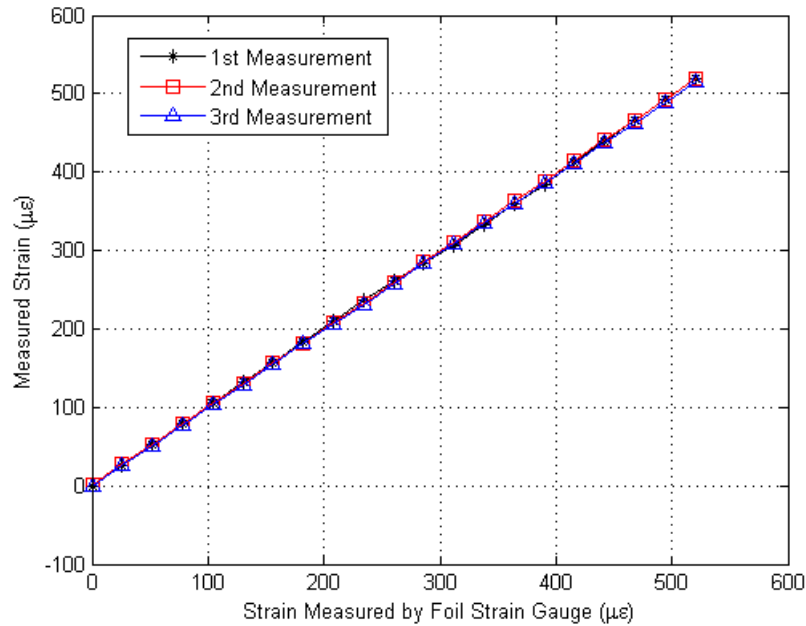


Figure 5.23. Strain sensor accuracy test

5.4.3.4 SMS IFPI strain resolution

The evaluation of the sensor resolution was performed using a calibrated sensor at $52\mu\epsilon$, $260\mu\epsilon$ and $520\mu\epsilon$ for 10mins respectively. The strain readout of the SMS IFPI sensor is sampled at 1Hz. The standard deviation of the temperature data was calculated to be $\sigma=0.267\mu\epsilon$, $\sigma=0.272\mu\epsilon$ and $\sigma=0.278\mu\epsilon$. Therefore the resolution of the sensor system is estimated to be $2\sigma=0.534\mu\epsilon$, $2\sigma=0.544\mu\epsilon$ and $2\sigma=0.556\mu\epsilon$. The normalized resolution with respect to the dynamic range of the system is 0.1%.

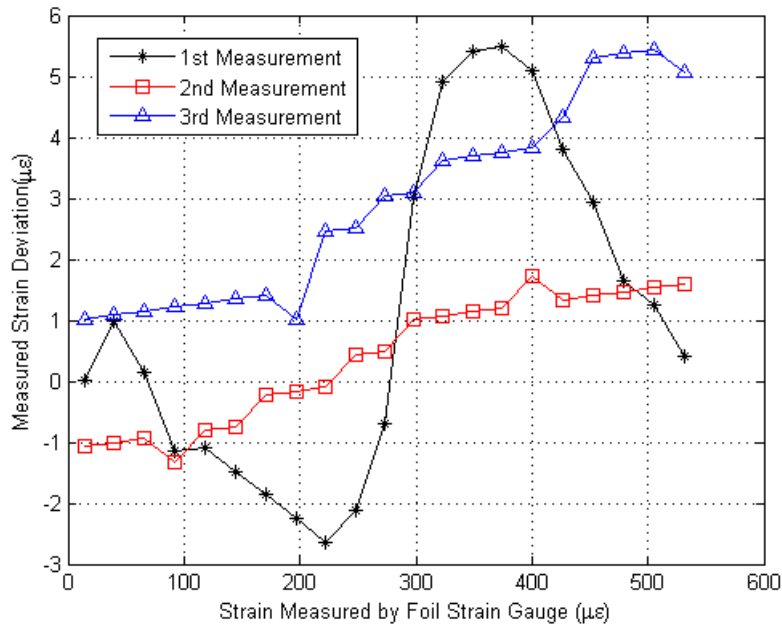


Figure 5.24. Strain sensor accuracy test close up

5.4.3.5 SMS IFPI strain hysteresis

Hysteresis of the strain sensor can be measured by cycling the applied temperature between the minimum and the maximum of the operating range in both increasing and decreasing directions. The hysteresis can be calculated as the largest difference among the output readings of the temperature cycles.

In the experiment, the applied strain is increased and decreased from 0 to 520 to 0 µε for 3 rounds. The result is shown in Figure 5.25 shows four measurement results. The largest difference of each round occurs at 0 µε. The maximum difference recorded is 6.15 µε. Thus the hysteresis is 6.15 µε and 1.2% of the full measurement range. The test took 6hrs and the temperature variation is not compensated in the test. If the test is conducted in a temperature stable environment, the hysteresis of the sensor is expected to be significantly decreased.

5.4.3.6 SMS IFPI strain stability

The long-term stability testing results are shown in Figure 5.26. the experiment is carried out at 520 µε strain level for 20hrs. the strain readout differences between the foil strain gauge and the SMS IFPI sensor readout is in the range of ±1.5 µε over 20hrs, which

means the normalized maximum variation is $\pm 0.3\%$ of the full dynamic measurement range.

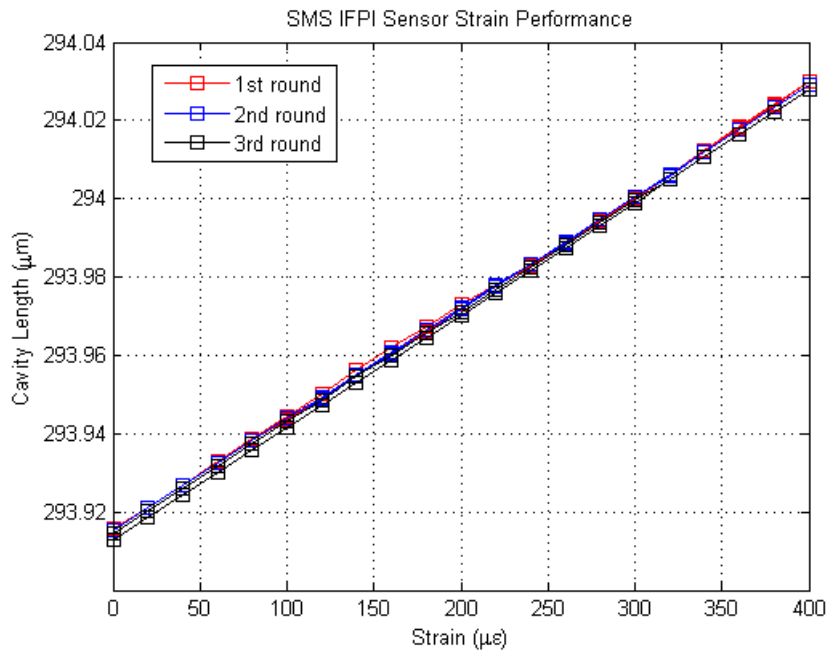


Figure 5.25. Strain sensor hysteresis test

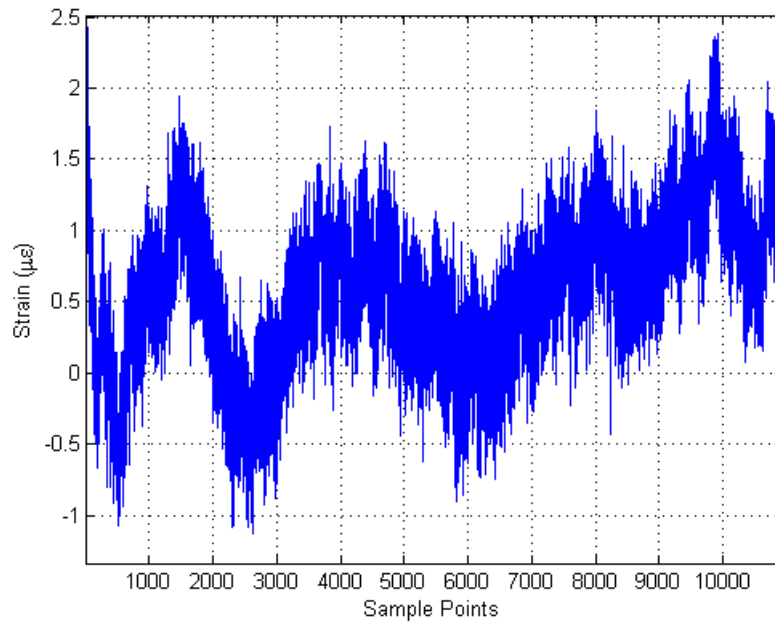


Figure 5.26. Strain sensor stability test

5.4.3.7 SMS IFPI strain frequency response

To characterize the frequency response of the SMS IFPI strain sensor, the si720 system cannot be used because its maximum laser sweeping frequency is 5Hz. Furthermore, because the data transfer rate is limited by the GPIB interface, the sensor cavity length sampling rate cannot exceed 1Hz. Thus using the si720 system to explore the sensor frequency response over 1Hz is not possible. However, the frequency response of the sensor could be measured based on the system shown in Figure 5.27. Instead of using a broadband light source, a tunable laser (1509—1583nm, Velocity 6300, New Focus, Inc) is used. The laser wavelength is first tuned to find the SMS IFPI sensor interference fringe neighboring peak and valley wavelengths. Once the wavelength is found, the work point wavelength is between the peak and valley. The laser wavelength is set to the work point wavelength. The work point is in the middle of the sensor linear range. The SMS IFPI sensor is co-located with the foil strain gauge on the cantilever beam. Since it is hard to generate clean step function or delta function in strain, the natural vibration of the beam is used to tentatively study the frequency response of the fiber sensor. The cantilever beam is bent, and suddenly released. The amplified strain oscillation signal from the fiber sensor and the foil strain gauge is compared on the oscilloscope. The 20Hz oscillation signal from both sensors are compared in Figure 5.27. The fiber sensor has the same output as that of the foil strain gauge. Higher frequency response can be obtained using specially developed setup. The fiber sensor is expected to have excellent high frequency response.

5.5. Sensor System Analysis

The performance of the SxS IFPI quasi-distributed sensor system is limited by the noise associated with individual electronic and optical components and their combined effects. A detailed analysis of the noise sources and their effects on the system performance is a very important design step since it provides a guideline to achieve an optimal system performance.

For the quasi-distributed SxS IFPI sensor system, the optical spectrum of the multiplexed sensors is the sum of the spectrum of all the SxS IFPI sensors. To obtain each sensor's cavity length, BPF is first used to filter out each sensor's optical spectrum, then

Whitelight algorithm is applied to the sensor's optical spectrum to precisely calculate the corresponding sensor cavity length. The goal of the Whitelight algorithm is to unambiguously determine the sensor cavity length which can be calculated by Equation (3.7) and (3.4) with known spectral positions of the peaks and valleys in the interference spectral curves. The noise in the detected optical spectrum affects the accurate determination of the peak and valley positions in the interference spectral curves. We now analyze the noise effects on peak positions. By differentiating Equation (3.2), the noise amplitude δI , or the signal uncertainty, is related to the uncertainty of the valley positions $\delta\lambda$

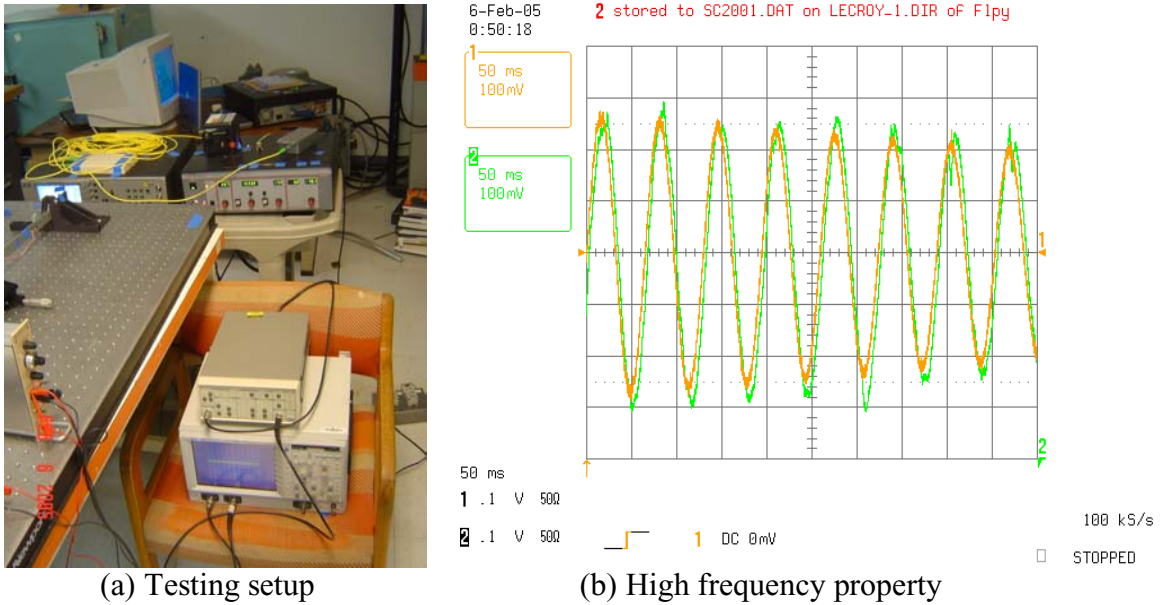


Figure 5.27. Strain sensor frequency response test

$$\delta I = I_s(\lambda)\gamma \frac{2\pi L\delta\lambda}{\lambda^2} \sin\left(\frac{2\pi L}{\lambda}\right) \quad (5.3)$$

where $\sin(2\pi L/\lambda)=1$ for peaks. The L is the OPD value, λ is the optical wavelength, $I_s(\lambda)$ is the optical signal, and γ is the visibility of the interference spectral curves. This equation can be transformed into

$$\delta\lambda = \frac{\lambda^2}{2\pi\gamma L\sqrt{SNR}} \quad (5.4)$$

where $SNR = [I_s(\lambda) / \delta I]^2$. For a band-limited signal, its signal-to-noise ratio SNR can be written as

$$SNR = \frac{S}{N} = \frac{\int_A^B P_s(f) df}{\int_A^B P_n(f) df} \quad (5.5)$$

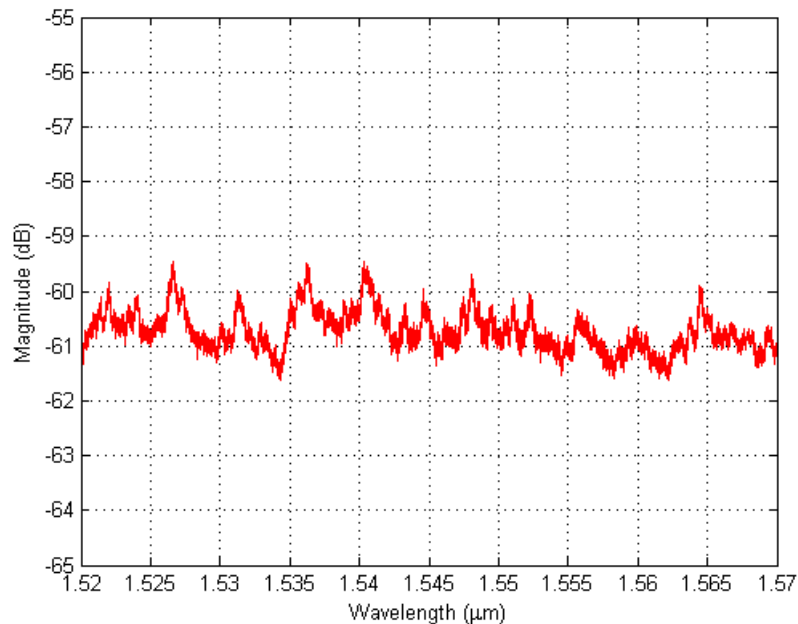
where S is the signal power, N is the noise power, $P_s(f)$ and $P_n(f)$ are the power spectral density (PSD) of the signal and the noise. But the noise analysis of the sensor system cannot simply be carried out using the PSD of the sensor optical spectrum because the peak and valley positions is not directly found by finding the maximum and minimum value in the neighboring wavelengths. In fact, mass-center algorithm, shown in Equation (3.10), is used in finding the peak and valley position. It is difficult to find the SNR transfer function of the mass-center algorithm. But empirically, larger SNR result in better testing results. Therefore, in the following discussion the SNR will still be used as a criteria in judging the performance of the sensor system. The noise sources and their effects on sensor system performance will be qualitatively analyzed.

5.5.1. si720 system noise

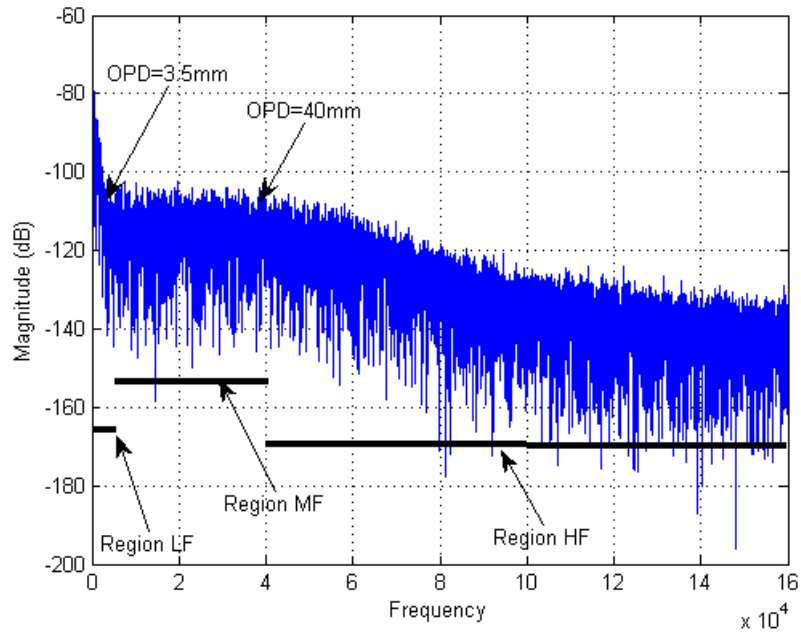
The si720 system integrates the light source with the spectrometer. Instead of detailed analysis of the contribution of all the noise factors in the system, experimental results are used to evaluate the system overall noise. The light reflected from the SMF end face is frustrated and the optical spectrum is recorded. Its Fourier spectrum is shown in Figure 5.28. The noise PSD is high in the lower frequency end of the transformed spectrum specified as Region LF. The noise PSD decreases sharply with frequency. In the middle region Region MF, the noise PSD is 30dB lower than that in the Region LF. The noise PSD is kept as a constant level at Region MF, and then decreases slowly in the Region HF. The Fourier transform peaks of the sensors with OPD not longer than 3.5mm falls in the LF region. The sensors with OPD between 3.5mm and 40mm falls in the MF region. MF region has better SNR than the LF region. Within the LF region, higher frequency end has better SNR. Thus in the SxS IFPI sensor multiplexing applications, sensor with longer cavity length is preferred.

5.5.2. Sensor induced noise

In the ideal situation, a sensor's Fourier transformed spectrum consists only one peak. But in real application, besides its primary peak there are a series of harmonics with decreasing power. Shown in Figure 5.29 is three sensors' Fourier transform spectrum. The three sensors all have harmonics. The second harmonica is generally 15dB less than the primary peak. As shown in Figure 5.30, for the same SMS IFPI sensor, the arc power is repeatedly applied to the MMF to SMF splicing point. The power in the harmonics reduces according to reduced visibility of the sensor, but the power difference between the first and second harmonica is still around 15dB. The harmonics are not generated by multiple reflections. The harmonics are intrinsic to the IFPI fabrication, and hard to eliminate during sensor fabrication. In the sensor multiplexing applications, the sensors should not have their primary Fourier transform peak fall on the harmonics of other sensors. Otherwise, the sensor will suffer from degraded SNR. Since the sensor primary transform peak is very narrow, and the primary peak shift during measurement is usually within 1% of its initial value. Thus it is not difficult to pick the sensors that their harmonics do not collide with each other.



(a) Optical spectrum of the noise



(b) PSD of the
Figure 5.28. PSD of the sensor interrogator

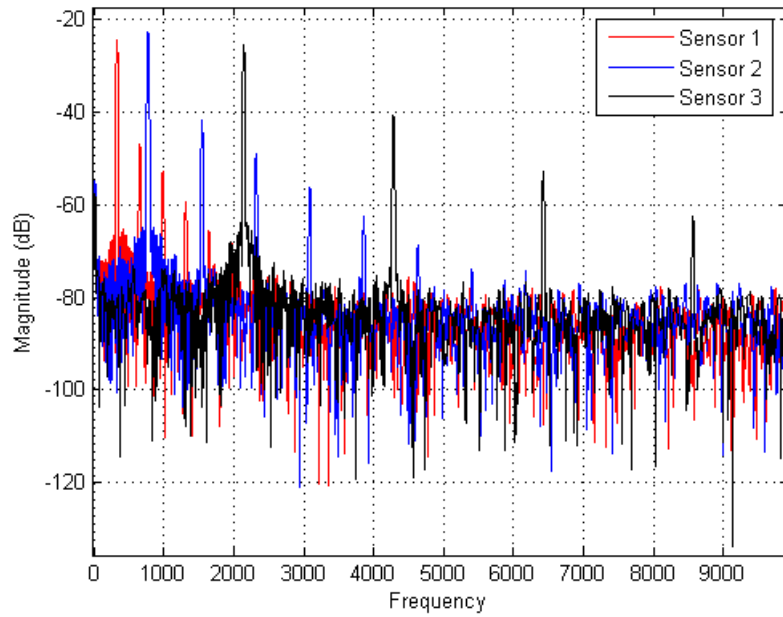


Figure 5.29. Sensor Fourier spectrum harmonics

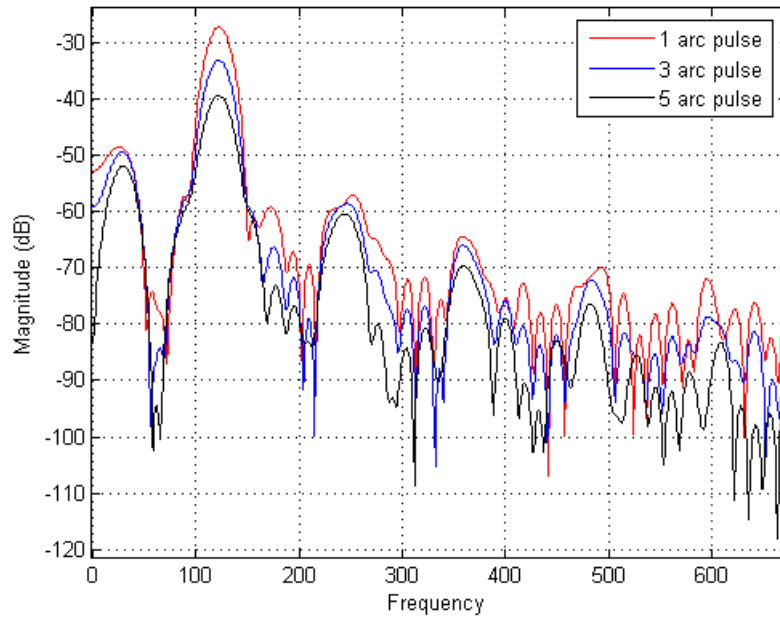


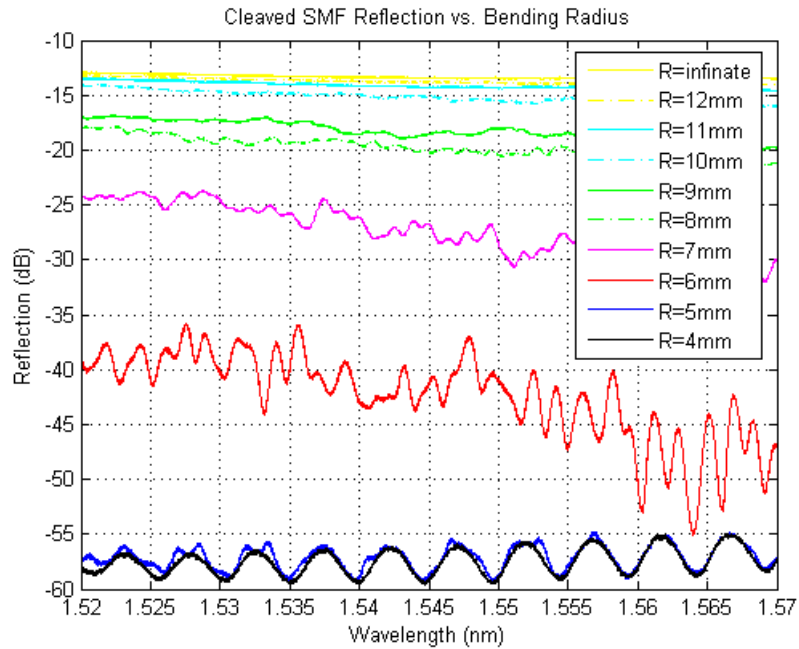
Figure 5.30. Sensor Fourier spectrum with repeated arc splice

Other than the sensor harmonica induced noise, the sensor temperature-strain cross-sensitivity should be considered. It is shown in the experimental results that the strain-temperature crosstalk is $13\mu / ^\circ\text{C}$, and the temperature-strain crosstalk is $0.08^\circ\text{C}/\mu$. When the SMS IFPI sensor is used as the strain sensor, the local temperature should be carefully monitored and compensated in the strain measurement.

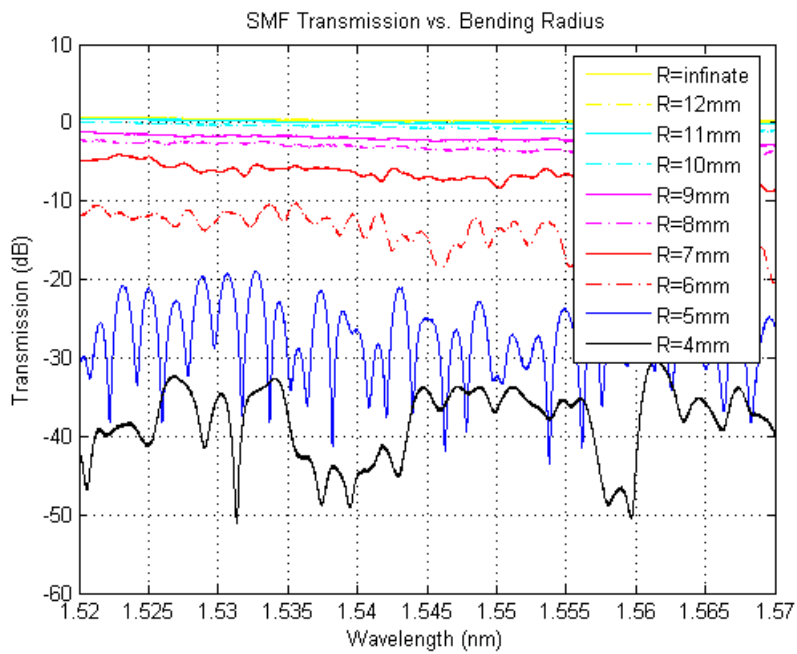
5.5.3. Fiber induced noise

The fiber induced noise includes fiber bending noise, Rayleigh scattering noise and fiber transmission loss induced noise.

The spectrum of the light waves transmitted in a fiber will change when the fiber is bent. The fiber bending induced spectrum change is a very complicated phenomenon. Although theoretical modeling of this process is possible, it will be easier and more direct to investigate this phenomenon experimentally.



(a) reflection versus bending radius



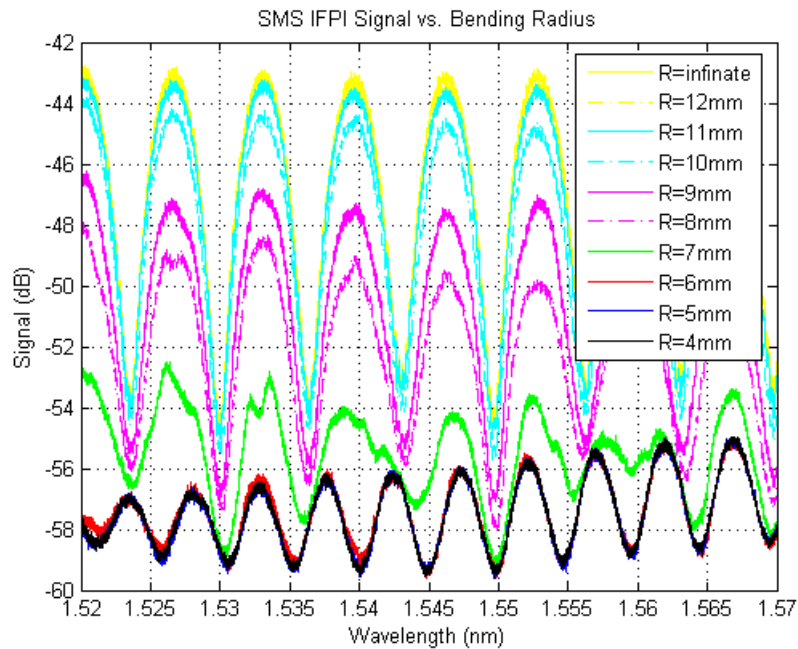
(b) transmission versus bending radius

Figure 5.31. Cleaved SMF characteristics versus fiber bending radius

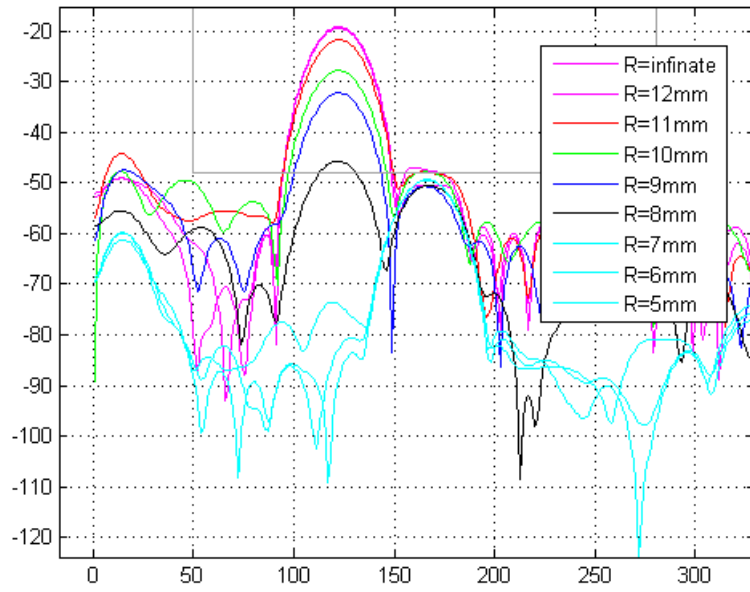
First, the fiber bending effect on cleaved SMF reflection and SMF transmission is studied. Figure 5.31 shows the SMF bending radius effect on reflection and transmission

spectrum, and its effect on specific wavelengths. An SMS IFPI sensor is then spliced in the loop with its reflection and reflection spectrum Fourier transform spectrum monitored against fiber bending radius. The result is shown in Figure 5.32. The sensor is held at each bending radius for 5mins, and its OPD recorded. The OPD at each bending radius is shown in Figure 5.33, and their corresponding STD values normalized to its initial OPD are shown too. The bending radius does not introduce distortion to the sensor signal since it only induces low-frequency noise to the Fourier transformed spectrum. But it will affect the OPD calculation by degrading the SNR. In real applications, tight fiber bending should be avoided.

Reighley scattering is an intrinsic effect to the fiber and cannot be avoided in the sensor interrogation. In the experiment, the Reighley scattering effect of 600m Corning SMF28 fiber is investigated. The spectrum and its Fourier transformed spectrum is shown in Figure 5.34. The data shows that although longer fiber gives more collected Reighley scattering, but the scattering only provides low-frequency noise. For the sensors with OPD larger then several microns, they won't be affected. Thus the Reighley effect does not affect the sensor performance.

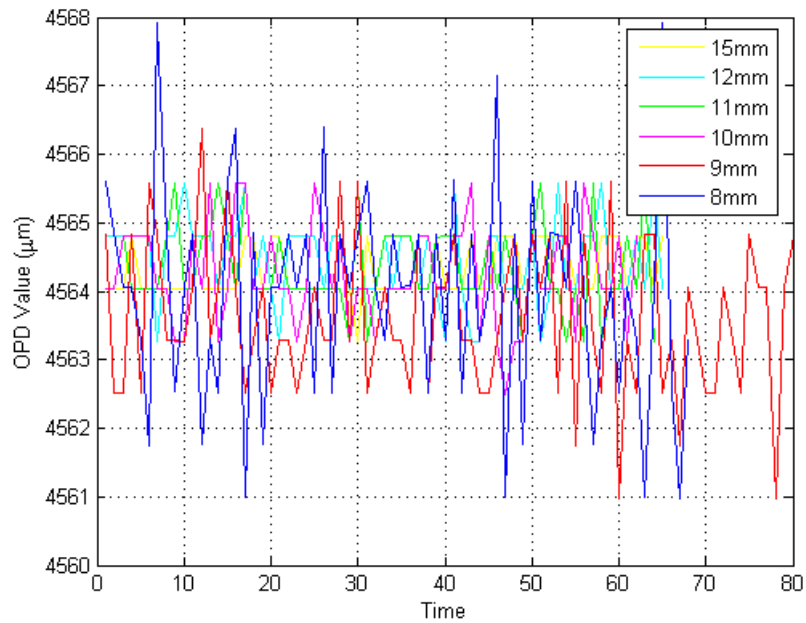


(a)

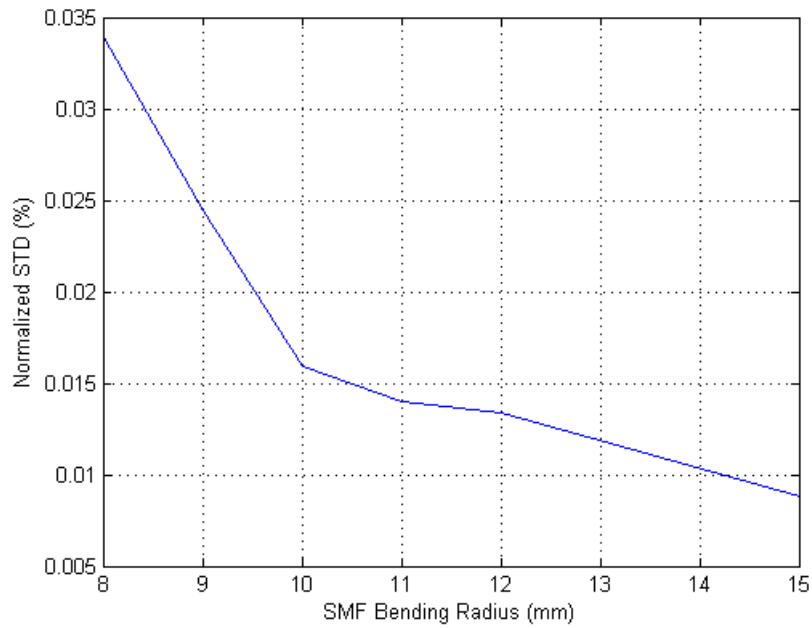


(b)

Figure 5.32. SMS IFPI spectrum and Fourier spectrum versus bending radius

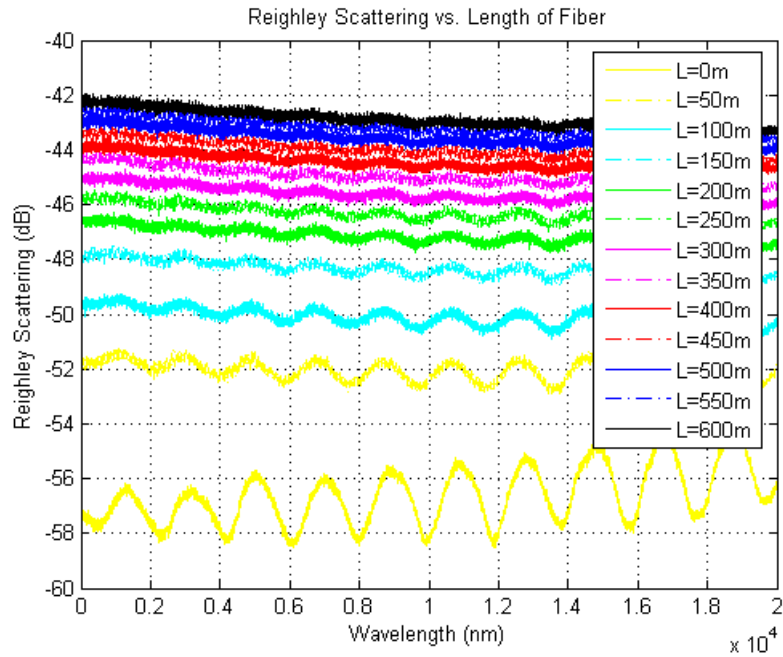


(a) SMS IFPI OPD versus bending radius

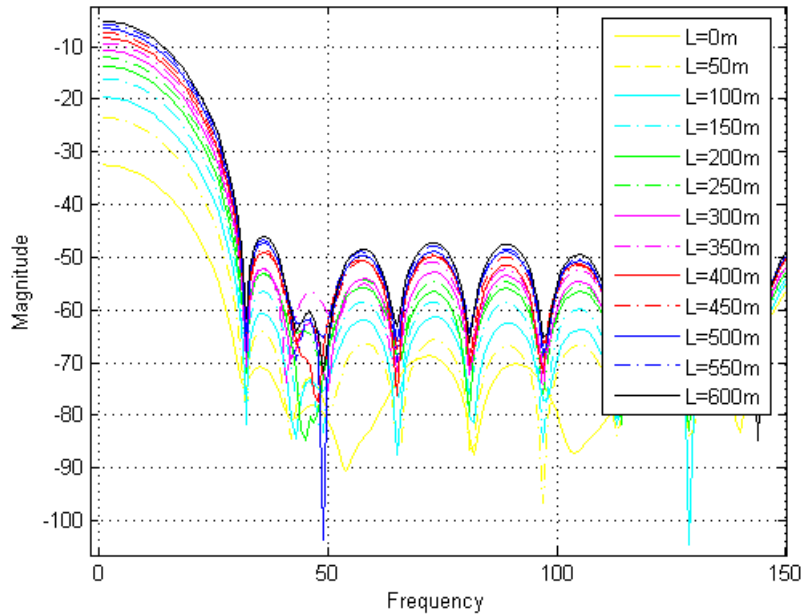


(b) SMS IFPI OPD STD versus bending radius

Figure 5.33. Bending radius effect on OPD measurement



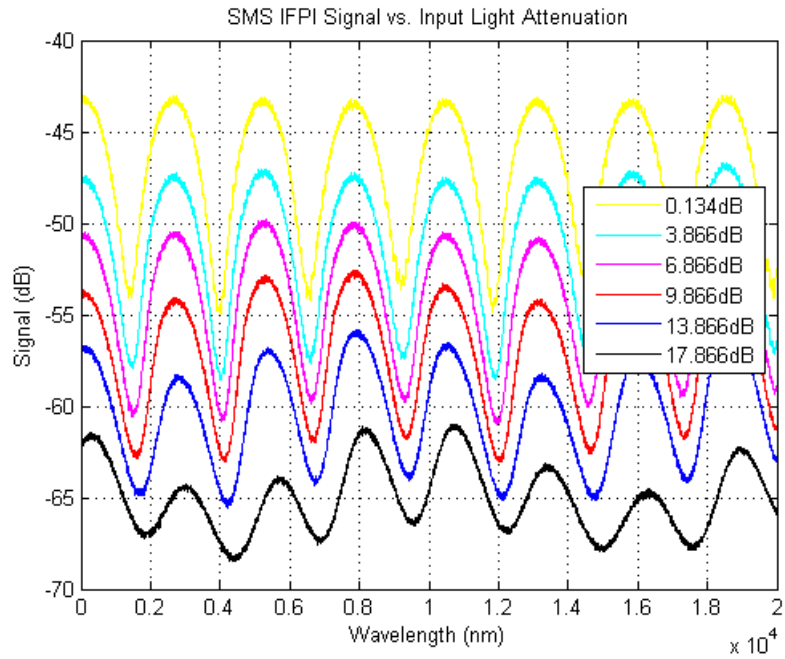
(a) Reighley scattering versus length of fiber



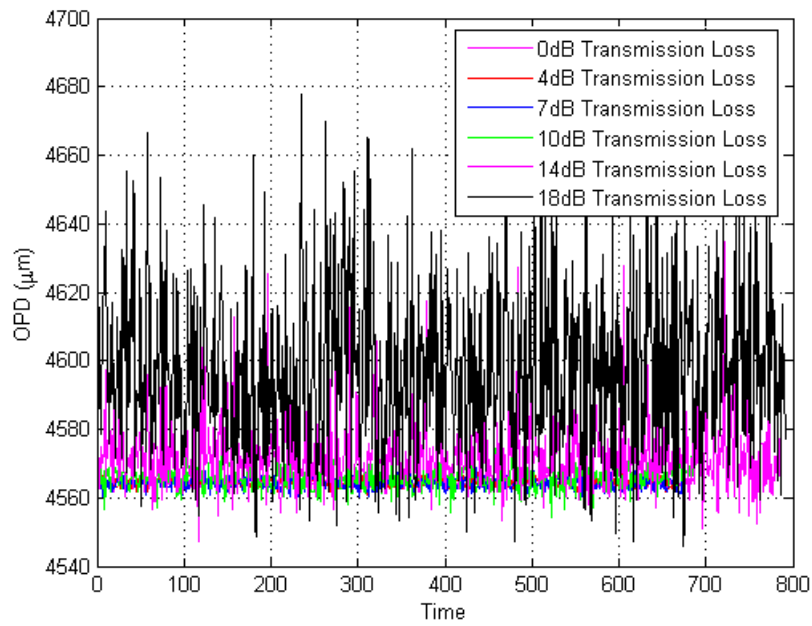
(b) Fourier transform of Reighley scattering spectrum

Figure 5.34. Fiber length effect

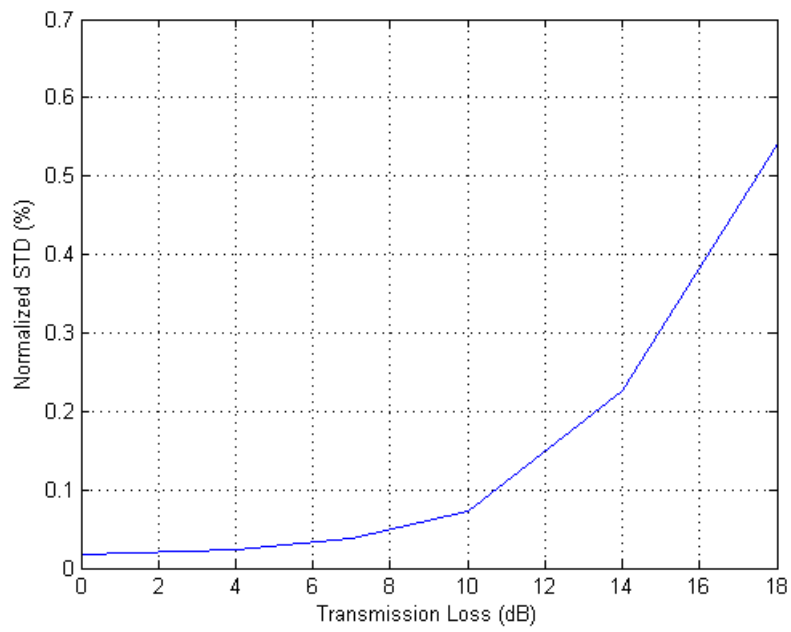
Fiber transmission loss and sensor insertion loss will have effect on the sensor performance. An experiment is conducted by varying attenuation at the input to the SMS IFPI sensor to simulate the transmission loss or sensor insertion loss effect. The calculated sensor OPD and normalized STD under increasing attenuation is shown in Figure 5.35. The deviation from the correct OPD increases with increasing attenuation. The transmission loss caused by the fiber and the cascaded sensor will degrade the SNR of the sensor multiplexed after them. In the real application, the number of sensors that can be multiplexed on a single fiber is governed by the tolerance of the SNR of the last sensor cascaded on the line.



(a) SMS IFPI spectrum versus insertion loss



(b) SMS IFPI OPD versus insertion loss



(c) SMS IFPI OPD STD versus insertion loss

Figure 5.35. Sensor insertion loss effect

Chapter 6. Conclusions and Future Work

6.1. Conclusions

In this research, it is demonstrated that an IFPI sensor can be made by splicing a section of different waveguide structure into the single-mode fiber transmission line. The waveguide structure could be a multimode fiber (SMS IFPI), single-mode fiber (SSS IFPI) or even a glass rod (SGS IFPI). The SMS IFPI has a high interference visibility. It demonstrated an interference fringe visibility of 0.8 at a Fabry-Perot cavity length of 5000 μm when compared to that of 0.02 for a standard EFPI interferometer. The insertion-loss of an SMS IFPI sensor using Corning Infinicor600 fiber is 0.8dB, and is 1.06dB for SMS IFPI sensor using Spectran GIF625 fiber. The experiment result converges well with the model prediction. Study also shows that by using the specially designed singlemode fiber having a large core refractive index difference and a matching MFD with the lead-in singlemode fiber, the SSS IFPI could have much lower insertion-loss, which would enable tens of sensors multiplexed on a single fiber. With specially designed cleaving tools that can control the FP cavity length at a fine resolution, the Fourier spectrum of the optical spectrum can be better utilized, which would allow more sensors cascaded on a single fiber without infringing each other. The tensile strength of the SMS IFPI sensor is on average 0.4 times of that of the standard singlemode fiber. This will render the sensor excellent mechanical strength during sensor handling and installation in the field. Since the sensor is made without modifying the refractive index of the fiber, the sensor does not require post-fabrication annealing and calibration. The sensor fabrication is simple, low-cost and high yield-rate.

Whitelight algorithm employing the combination of two-peak algorithm and peak-tracing algorithm is used in the sensor cavity length demodulation. FIR digital band-pass filter combined with Hamming window is used to filter out the Fourier transform spectrum component of the individual sensors out of their superimposed optical spectrum.

In the SMS IFPI sensor laboratory temperature measurement test, it demonstrated $\pm 0.15\%$ FS repeatability and 0.037%FS resolution from room temperature to 600°C. In

the SMS IFPI sensor laboratory strain measurement test, it demonstrated $\pm 0.20\%$ FS repeatability and 0.20% FS resolution from $-520\mu\epsilon$ to $520\mu\epsilon$.

6.2. Future Work

A complete and systematic performance evaluation of this sensor provides feedback information for further design improvement. Based on the work done so far, the suggested future works are: development of advance sensor demodulation software; detailed evaluation of unit sensor temperature and strain performance; evaluation of the multiplexed sensor system overall performance; study of system level issues; sensor system noise analysis; development of methods for largely increasing the number of sensor multiplexed on a single fiber; being able to precisely control the Fabry-Perot cavity length, and search for ways to achieve high repeatability on length control; robust sensor packaging for field installation harsh environment applications; improvements to sensor interrogation system so that it has larger dynamic range that enable more sensor being multiplexed on a single fiber; the Fourier transform phase spectrum based sensor demodulation scheme. These issues will be explained in detail as follows.

6.2.1. Development of sensor demultiplex software

The software now can only deal with a single SxS IFPI sensor spectrum. To demodulate the multiplexed sensors, a demultiplexing algorithm is needed to separate out the individual sensor spectrum.

The study on the demultiplexing algorithm also involves the study of band-pass filters. Different filters have different demultiplex effects. This has to be characterized and optimized.

6.2.2. Full characterization of sensor temperature and strain performances

The repeatability, accuracy, hysteresis, drift, stability and frequency response of the sensor should be more fully characterized.

6.2.3. Full characterization of multiplexed sensor system

The multiplexed sensor system should be more fully characterized, including the simultaneous demodulation of each sensor information, and the cross-talk between the sensors.

6.2.4. System level issues

Several system level issues have to be explored, such as: what is the bending effect on signal demodulation, how does the decreased input power affect the demodulation, how does the blackbody radiation affect the temperature measurement at high temperatures, how does the Rayleigh scattering affect the system, etc.

6.2.5. System noise analysis

A complete system noise analysis is needed to understand the performance limit of the sensor system.

6.2.6. Design and manufacture the special single-mode fiber

With current available multimode fibers, the insertion loss per unit sensor is relatively large due to the mode-field-diameter mismatch with that of the single-mode fiber, thus preventing the multiplexing of a large number of sensors. With the available single-mode fibers, the mode-field-diameter mismatch is small and the sensor insertion loss can be largely reduced. But the splice reflection is too small, it could not be detected. Both the multimode fiber and the single-mode fiber can not make good use of the dynamic range of the sensor interrogation system, resulting in a small number of sensors being multiplexed.

As shown in Chapter 4, the special index profile single-mode fiber for the quasi-distributed SSS IFPI sensor applications should be designed and fabricated. Such a sensor has a matching mode-field-diameter with the Corning SMF28 fiber, and a large core refractive index difference. Thus the reflection is large, and insertion loss is small. This would allow a maximum number of sensors being multiplexed on a single fiber.

6.2.7. Fabry-Perot cavity length control

By the experiment data in Chapter 4, the sensor insertion loss, splice reflectivity, and sensor visibility are highly repeatable in sensor fabrication. But the Fabry-Perot cavity length is not precisely controlled. The reason is two fold: first, the fiber used as the Fabry-Perot cavity is cleaved using a fiber cleaver under a microscope. It is a manual process. With an experienced operator, the accuracy of the length can be controlled within tens of microns, but can not be raised further; the fiber fusion splicer has an arc power fluctuation on the scale of 20% average. During the splicing, the melted fiber end-face

will be pressed against each other. The splice zone has thickness of 1-2 μm . Thus, the length accuracy of the Fabry-Perot cavity is hard to raise up to less than 1 μm scale.

On the other hand, the length control is important, because: the highly precise control of the Fabry-Perot cavity length would enable the sensor being calibration-free. With the rest of the sensor characteristics highly repeatable, the sensor response to the measurand is only a function of the measurand and the sensor cavity length. If the sensor cavity length is precisely fixed, the sensor behavior is highly predictable, and can be made calibration-free. This would significantly reduce the sensor cost and increase the sensor yield rate; without precise control of the sensor cavity length, the Fourier spectrum can not be used efficiently. The two sensors having too close cavity length will infringe each other. The sensors having widely separate cavity length will waste the available Fourier spectrum bandwidth.

The precise control of the sensor cavity length could involve integrating the micro-positioner onto the fiber cleaver. Another alternative method is to use high precision polisher to polish sections of fibers into micro-cavities, and have them spliced into the single-mode fiber as the SxS IFPI sensors.

6.2.8. Use Fourier spectrum efficiently

If the SxS IFPI sensor has a very low insertion loss and high reflectivity, a large number of sensor would be able to multiplex on a single fiber. Under this situation, the Fourier spectrum bandwidth would become a limiting factor for the sensors being able to multiplex on a fiber.

As discussed in Chapter 4, the maximum length of the cavity is 90mm due to the coherent length of the si720 system fiber laser and the polarization state change in the cavity. Thus the Fourier spectrum bandwidth is limited. The length of each sensors should be precisely controlled so that the dynamic range of the length of one sensor does not infringe with the other sensors' length dynamic range. The length of the sensor cavities should be arranged so that all the Fourier spectrum bandwidth is used. To achieve this goal, the sensor cavity length should be precisely controlled.

Another factor that reduces the Fourier spectrum usable bandwidth is the sensor's Fourier transform harmonica problem as demonstrated in Chapter 4. The harmonics would introduce noise to the neighboring sensors and therefore reduce accuracy of the sensor.

To avoid this, the sensors should be made to avoid such harmonics in the Fourier spectrum domain. This would reduce the efficiency of Fourier spectrum utilization, and result in decreased number of sensor being multiplexed. The sensor fabrication process should be explored to eliminate the harmonics of the sensor to expand the bandwidth that can be used for sensor multiplexing.

6.2.9. Sensor packaging

The major work on the SxS IFPI quasi-distributed sensor is done in the laboratory environment, but the targeted applications are harsh environments. The sensor system should be robust and reliable that can function properly during field installation and harsh environment operation. The sensor protection issues that have to be considered in sensor packaging include: installation packaging, mechanical robustness, corrosion resistance, temperature sensor thermal shock. The unit sensor packaging should be able to reduce the sensor crosstalk, avoid reducing the sensor sensitivity and resolution.

6.2.10. Sensor interrogation system

The si720 system has a 60dB dynamic range for sensor interrogation. Although the sensor insertion loss can be reduced to a small number, the problem with SxS IFPI is that the signal is very weak. The splice reflection is around -40dB. Thus the only part of the large dynamic range used is from -40 to -60dB. The range from 0- -40dB is not used. If we have a sensor interrogation system that its entire dynamic range can be used, more sensors could be multiplexed onto a single fiber.

The si720 system is composed of a sweeping fiber laser, a detector and synchronizing circuits. Since the 0- -40dB dynamic range is of no use in the SxS IFPI sensing application, we can use a customized detector that has much larger amplification factor than the one in the si720 system. The custom amplifier should be designed that the corresponding 0- -40dB on the si720 system is saturated for this amplifier, and the dynamic range of the amplifier starts at -40dB. By doing so, the whole dynamic range of the amplifier can be used for sensor interrogation. Thus the number of sensors can be largely increased.

The diagram and picture of the proposed system is shown in Figure 6.1 to 6.2. The system is composed of a si720 system (only its sweeping fiber laser is used in the proposed system), a GaAs detector, a Oriel amplifier and an oscilloscope. The light is

launched from the sweeping fiber laser into the sensor line through a 3-dB coupler. The reflected sensor signal reaches the GaAs detector, and is amplified by the amplifier. The signal is shown on the oscilloscope screen. The amplifier is set to an amplification factor of $\times 10^8$. The screen of the oscilloscope with the signal of an SSS IFPI sensor is shown in Figure 7.3. With this customized amplifier, the weak signal can be seen clearly on the screen. Because in each sweeping period, the sweeping fiber laser sweeps from 1570nm to 1520nm and then back to 1570nm, the signal shown is symmetrical to the center. The most important future work on improving the system interrogator is first to make a synchronizing system that can relate the timing to the wavelength information. Only by doing so, the signal from the oscilloscope can be used to retrieve sensor information.

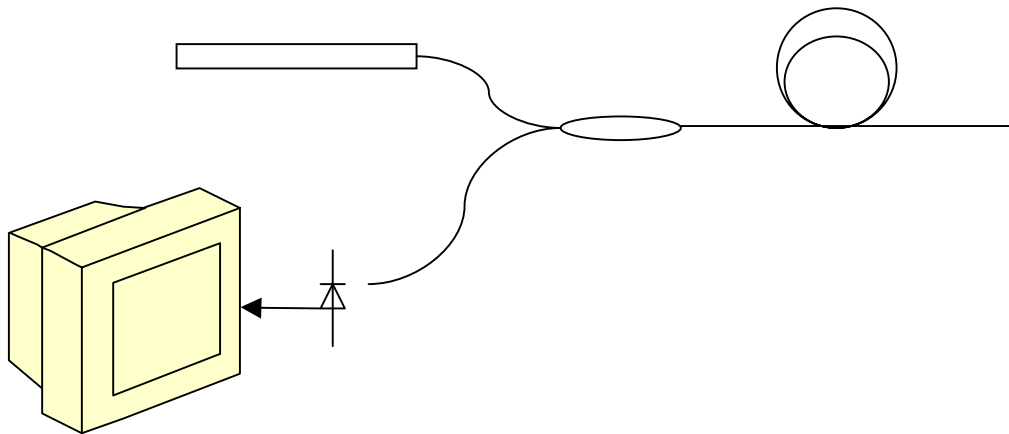


Figure 6.1. Alternative system interrogation method

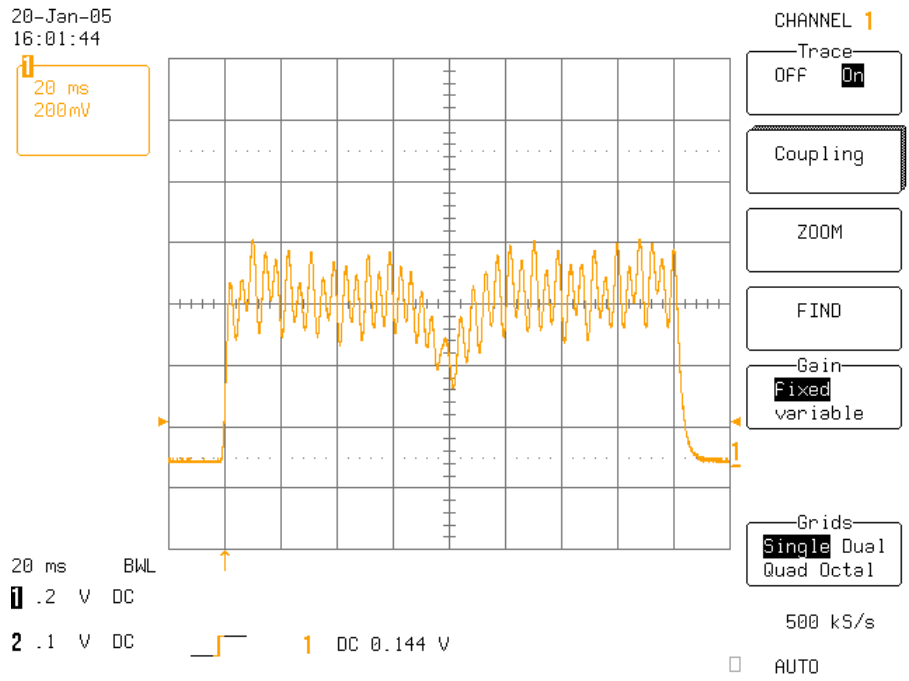


Figure 6.2. Oscilloscope screen

References

1. John Dakin and Brian Culshaw, *Optical Fiber Sensors: Principles and Components*, vol. 1, Artech House, Boston., 1988
2. K. T. V. Grattan and B. T. Meggitt, *Optical Fiber Sensor Technology*, Kluwer Academic Publishers, Boston, 2000
3. Stein, J. *EPRI survey*, Electrical Power Research Institute, Palo-Alto. Ca, June 1989
4. Rogers, A. J. "Distributed optical fibre sensors," *J. Phys. D., Appl. Phys.*, 1986, pp:2237-2255
5. Rogers, A. J. "Distributed optical-fibre sensors for measurement of pressure, strain and temperature," *Phys. Rep. (Phys. Lett.)*, 1988, vol 169, pp: 99-143
6. Barnoski, M. K. and Jensen, S. M, *Applied Optics*, 1976, vol 15, pp: 2112-2115
7. Hartog, A. H, *J. Lightwave Technol*, 1983, LT-1, 498-509
8. Farries, M. C. et al, *Electron. Lett.* 1986, vol 22, pp: 418-419
9. Michael Bass, Eric W. Van Stryland, David R. Williams, William L. Wolfe, *Handbook of Optics, Fundamentals, Techniques, and Design*, Second Edition, Volume I; McGraw-Hill, Inc, New York, 1995
10. John A. Buck, *Fundamentals of Optical Fibers*, John Wiley & Sons, Inc, New York, 1995
11. Theocharous, E. *IEE Colloquium on distributed optical fibre sensing*, London, May 1986 (Digest no 1986/74)
12. Farries, M. C. et al, *Electron. Lett.* Vol. 22, pp: 418-419, 1986
13. Bergqvist, E. A. "An optical fiber cable for detecting a change in temperature," European Patent Application 0-490-849-A1, Nov 26th, 1991
14. A. A. Boiarski, G. Pilate, T. Fink, N. Nilsson, "Temperature Measurements in Power Plant Equipment Using Distributed Fiber Optic Sensing," *IEEE Transactions on Power Delivery*, Vol. 10, No. 4. October 1995, pp: 1771-1778
15. Michael Bass, Eric W. Van Stryland, David R. Williams, William L. Wolfe, *Handbook of Optics—Fiber Optics & Nonlinear Optics*, Second edition, Vol IV, McGraw-Hill, Inc, New York, 1995

16. Mostafa Ahangrani Farahani and Torsten Gogolla, "Spontaneous Raman Scattering in Optical Fibers with Modulated Probe Light for Distributed Temperature Raman Remote Sensing," *Journal of Lightwave Technology*, vol. 17, no. 8, August 1999, pp: 1379-1391
17. Peng-Chun Peng, Hong -Yih Tseng, and Sien Chi, "Long-Distance FBG Sensor System Using a Linear-Cavity Fiber Raman Laser Scheme," *IEEE Photonics Technology Letters*, vol. 16, no. 2, February 2004, pp: 575-577
18. Lees, G. P. et al, "Recent Advances in Distributed Optical Fiber Temperature Sensing using the Landau-Placzek ratio," *SPIE Distributed and Multiplexed Fiber Optic Sensors VII*, 1998
19. Wait, P. C. and Newson, T. P. *Optics Commun.*, no. 122, 1996, pp: 141-146
20. Souza, K. De et al, *Electron. Lett*, no. 32, 1996, pp: 2174-2175
21. Lees, G. P. et al, *Photonics Technol. Lett.*, no. 10, 1998, pp: 126-128
22. Horiguchi, T. et al, *IEEE Photon. Technol. Lett*, no. 1, 1989, pp: 107-108
23. Tateda, M. et al, *J. Lightwave Technol.*, no. 8, 1990, pp: 1269-1272
24. P. C. Wait and A. H. Hartog, "Spontaneous Brillouin-Based Distributed Temperature Sensor Utilizing a Fiber Bragg Grating Notch Filter for the Separation of the Brillouin Signal," *IEEE Photonics Technology Letters*, VOL. 13, NO. 5, MAY 2001, pp: 508-510
25. Xiaoyi Bao, M. DeMerchant, A. Brown, and T. Bremner, "Tensile and Compressive Strain Measurement in the Lab and Field With the Distributed Brillouin Scattering Sensor," *Journal of Lightwave Technology*, VOL. 19, NO. 11, NOVEMBER 2001, pp: 1698-1704
26. V. Lecoche, M. W. Hathaway, D. J. Webb, C. N. Pannell, and D. A. Jackson, "20-km Distributed Temperature Sensor Based on Spontaneous Brillouin Scattering," *IEEE Photonics Technology Letters*, VOL. 12, NO. 10, OCTOBER 2000 pp: 1367-1369
27. Kazuo Hotate, *Senior Member, IEEE*, and Sean S. L. Ong, "Distributed Dynamic Strain Measurement Using a Correlation-Based Brillouin Sensing System," *IEEE Photonics Technology Letters*, vol. 15, no. 2, February 2003, pp: 272-274

28. John W. Berthold III, "Historical Review of Microbend Fiber-Optic Sensors," *Journal of Lightwave Technology*, vol 13, no. 7. July 1995, pp1193-1199
29. Denis Donlagi'c and Brian Culshaw, "Microbend Sensor Structure for Use in Distributed and Quasi-Distributed Sensor Systems Based on selective Launching and Filtering of the Modes in Graded Index Multimode Fiber," *Journal of Lightwave Technology*, vol. 17, no. 10, October 1999, pp1856—1868
30. Kathryn W. Quoi, Robert A. Lieberman, Leonard G. Cohen, D. Scott Shenk and Jay R. Simpson, "Rare-Earth Doped Optical Fibers for Temperature Sensing," *Journal of Lightwave Technology*, vol 10, no 6, June 1992, pp847—852
31. Culshaw, B.; Johnstone, W.; McLean, A.; Mauchline, I.; Moodie, D; Stewart, G, "Large scale multiplexing a point sensor for methane gas detection," *Optical Fiber Sensors Conference Technical Digest, 2002. OFS 2002, 15th , 6-10 May 2002*, Pages:261 - 264 vol.1
32. Benjamin J. Vakoc, Michel J. F. Digonnet, and Gordon S. Kino, "A Novel Fiber-Optic Sensor Array Based on the Sagnac Interferometer," *Journal of Lightwave Technology*, vol. 17, no. 11, November 1999, pp: 2316—2326
33. Yasukazu Sano and Toshihiko Yoshino, "Fast Optical Wavelength Interrogator Employing Arrayed Waveguide Grating for Distributed Fiber Bragg Grating Sensors," *Journal of Lightwave Technology*, vol. 21, no. 1, January 2003, pp: 132—139
34. José Azaña, Miguel A. Muriel, Lawrence R. Chen and Peter W. E. Smith; "Fiber Bragg Grating Period Reconstruction Using Time-Frequency Signal Analysis and Application to Distributed Sensing," *Journal of Lightwave Technology*, vol. 19, no. 5, May 2001, pp: 646—654
35. J. N. Fields et al., "Pressure sensor," *Journal of Acoustic. Soc. Am.*, vol. 67, pp: 816-818, 1980
36. J. N. Fields, "Attenuation of a parabolic-index fiber with periodic bends", *Applied Physics Letter*, vol. 36, pp. 799-801, 1980
37. J. N. Fields and J. H. Cole, "Fiber microbend acoustic sensor", *Applied Optics.*, vol. 19, pp 3265-3267

38. N. Lagakos et al., "Microbending sensor design optimization", *Proc. CLEO'81*, vol. 100, 1981
39. J. W. Berthold et al., "Design and characterization of a high temperature pressure transducer", *J. Lightwave Technol.*, vol. LT-5, pp870-876, 1987
40. A. Cutolo and M. Gallo, "Microbending optoelectronic sensor for on-line temperature measurements in high-power electrical systems", *European Trans. On Elec. Power Eng.*, vol. 1, pp. 281-287, 1991
41. J. B. Freal et al., "A microbend horizontal accelerometer for borehole deployment", *J. Lightwave Technol.*, vol. LT-5, pp. 993-996, 1987
42. R. E. Sovik, "Implementation of s in a vortex shedding flowmeter", in *Proc. ISA Digitech '85*, 1985, pp. 207-211
43. D. Varshneya et al., "Speed sensor for advanced gas turbine engine control", *Proc. SPIE*, vol. 1367, pp. 181-191, 1991
44. C. K. Kao and G. A. Hockham, "Dielectric-fiber surface waveguides for optical frequencies," *Proc. IEE London*, vol. 133, pp:1151—1158, July 1966
45. F. P. Kapron, D. B. Keck, and R. D. Maurer, "Radiation losses in glass optical waveguides," *Trunk Telecom. Guided Waves, IEE*, pp:148—153, September 1970
46. F. P. Kapron, D. B. Keck, and R. D. Maurer, "Radiation losses in glass optical waveguides," *Appl. Phys. Lett.*, vol. 17, pp:423—425, Nov 1970
47. T. Miya, Y. Terunuma, T. Hosaka, and T. Miyoshita, *Electron. Lett.* Vol. 15, pp: 106, 1979
48. Govind P. Agrawal, *Fiber-Optic Communication Systems*, 2nd edition, John Wiley & Sons, Inc, 1997
49. Hiroshi Murata, *Handbook of optical fibers and cables*, 2nd edition, Marcel Dekker, Inc, New York, 1996
50. D. Marcuse, "Loss Analysis of Single-Mode Fiber Splices," *Bell System Technical Journal*, vol. 56, pp. 703-718, 1977
51. Alok. K. Das and Satyabrata Bhattacharyya, "Low-Loss Fusion Splices of Optical Fibers," *Journal of Lightwave Technology*, vol 3, no. 1, February 1985, pp83—92

52. Yuichi Usui, Toshio Ohshima, Yuichi Toda, Yasuyuki Kato and Mitsuhiro Tateda, "Exact Splice Loss Prediction for Single-Mode Fiber," *IEEE Transactions on Microwave Theory and Techniques*, vol 30, no. 4, April 1982, pp601-604
53. David W. Peckham, Charles R. Lovelace, "Multimode Optical Fiber Splice Loss: Relating System and Laboratory Measurements," *Journal of Lightwave Technology*, vol. 5, no. 11, November 1987
54. Ken-Ichi Kitayama, Masaharu Ohashi, and Shigewki Seikai, "Mode Conversion at Splices in Multimode Graded-Index Fibers," *IEEE Journal of Quantum Electronics*, VOL. QE-16, NO. 9, SEPTEMBER 1980 pp971—978
55. John T. Krause, W. A. Reed, and K. L. Walker, "Splice Loss of Single-Mode Fiber As Related to Fusion Time, Temperature, and Index Profile Alteration," *Journal of Lightwave Technology*, vol. 4, no. 7, July 1986, pp: 837-840
56. Q. Bing, G. Pickrell, J. Xu, Z. Huang et al., 'Novel data processing techniques for dispersive white light interferometer', *Optical Engineering*, vol.43, no.11, 3165-3171 November 2003
57. Wang Q, Ning YN, Palmer AW, Grattan KTV, "Central Fringe Identification in A White-light Interferometer using a Multi-stage-squaring Signal-processing Scheme", *Optics Communications*
58. Yuan LB, Ansari F."White-light interferometric fiber-optic distributed strain-sensing system", *Sensors and Actuators A-Physical* 63 (3): 177-181 1997
59. J. Tapai-Mercado, A.V.Khomenko, And A. Garcia-Weidner. "Precision and Sensitivity Optimization for White-Light Interferometric Fiber-optic Sensors", *Journal of Lightwave Technology*, 19(1): 70-74, 2001
60. Wang A, Miller MS, Plante AJ, Gunther MF, Murphy KA, Claus RO. "Split-spectrum intensity-based optical fiber sensors for measurement of micro displacement, strain, and pressure" *Applied Optics* 35 (15): 2595-2601 1996
61. Yuan LB, Zhou LM, Jin W, Chan CC."Recent progress of white light interferometric fiberoptic strain sensing techniques", *Review of Scientific Instruments* 71 (12): 4648-4654 2000
62. David. N. Nikogosyan, *Properties of Optical and Laser-Related Materials A Handbook*, John Wiley & Sons, Chichester, UK, 1997

63. Marvin J. Weber, *Handbook of Optical Materials*, CRC Press, Florida, USA, 2003
64. Joseph H. Simmons, Kelly S. Potter, *Optical Materials*, Academic Press, San Diego, USA, 2000
65. J. H. Wray, J. T. New: *J. Opt. Soc. Am.* Vol. 59, pp774-776, 1969
66. Max Born, Emil Wolf, *Principles of Optics, Electromagnetic Theory of Propagation, Interference and Diffraction of Light*, 5th edition, 1975, Pergamon Press, Oxford
67. M. K. Barnoski and S. M. Jensen, "Fiber waveguides: A novel technique for investigating attenuation characteristic," *Appl. Opt.* vol 15, no. 9, pp 2112-2115, 1976
68. P. Healy, " Multichannel photon-counting backscatter measurements on mono-mode fiber," *Electron lett.*, vol 17 no. 20 pp 751-852 1981
69. P. Healy, P. Hensel, "Optical time domain reflectometry by photon counting," *Electron. Lett.*, vol 16, no 16, pp631-633, 1980
70. P. Healy, "Optical time domain reflectometry –A performance comparison of the analog and photon counting techniques," *Opt. Quantum Electron.*, vol 16, pp267-276, 1984
71. A. Tapia-Mercado, J. Khomenko, A.V. Garcia-Weidner, "Precision and sensitivity optimization for white-light interferometric fiber-optic sensors," *J. Lightwave Technol.* Vol: 19 no:1, 2001, pp: 70 -74

VITA

Zhengyu Huang was born in China, 1975. He received his B.S. degree in Optical Instrumentation in 1999 from Tsinghua University, China. From 1999 to 2000, he worked as a staff member in Optical Information Processing Lab, Department of Precision Instruments, Tsinghua University, China. He joined the Center for Photonics Technology at Virginia Polytechnic Institute and State University (Virginia Tech) in 2000, and received his M.S. degree in Electrical Engineering in 2002. Since 2000, he has worked on optical fiber sensors, optical fiber communication devices. He is the author/co-author of 10 refereed journal papers, 6 conference papers and 7 patent disclosures.